Surface Studies of Metal Oxide Catalysts and Ultrathin Films

David Charles Grinter

Thesis submitted for the Degree of Doctor of Philosophy

of the University College London

Department of Chemistry

UNIVERSITY COLLEGE LONDON

2011

I, David Grinter, confirm that the work presented in this thesis is my own. Where information has been derived from other sources, I confirm that this has been indicated in the thesis.

ABSTRACT

This thesis examines two important metal oxide systems: ultrathin CeO_2(111) films on Pt(111), and carboxylic acids on TiO_2 surfaces, both of which are significant for future energy research.

The structure and growth of ultrathin films of CeO_2(111) supported on Pt(111) have been studied with Scanning Tunnelling Microscopy (STM), Low Energy Electron Diffraction (LEED) and Auger Electron Spectroscopy (AES). The ultrathin films were grown in a number of ways and their growth mechanism, electronic structure, and domain boundaries were investigated using STM and STS. Atomically resolved STM images (filled and empty states) have been obtained on these ultrathin films permitting the identification of many defect structures.

The behaviour of individual gold atoms at room temperature on ultrathin CeO_2(111) films on Pt(111) has been investigated with STM. Simultaneous atomically resolved images of a gold adatom and the filled states of the ceria permitted the identification of two adsorption sites: (i) atop an oxygen atom and (ii) in a three-fold hollow site.

The adsorption and reactivity of acetic acid on anatase TiO_2(101) has also been investigated. It was found that at low coverage, acetic acid is observed to have a characteristic appearance con-

sistent with a dissociative bidentate binding geometry to two neighbouring Ti_{5c} sites. Deposition at elevated temperatures at saturation coverage yielded a (2 $\times$ 1) superstructure. The effects of heating, UV exposure, and tip pulsing were also investigated.

STM has been used to investigate the adsorption and photo-reactivity of benzoic acid on rutile TiO_2(110)(1 $\times$ 1) and (1 $\times$ 2). Benzoic acid binds to both surfaces dissociatively via a bridging geometry leading to a (2 $\times$ 1) overlayer on the (1 $\times$ 1) surface at saturation. Benzoate adsorbs between the added-rows of the (1 $\times$ 2) reconstruction leading to a (2 $\times$ 2) superstructure at higher coverage and demonstrated the important role of intermolecular interactions such as hydrogen bonding.

To my Parents...

ACKNOWLEDGEMENTS

Many thanks must go to my supervisor, Prof. Geoff Thornton, for all his advice and guidance during the course of my studies and for giving me the opportunity to work in such an interesting field. In addition I would like to thank all the other members of the Thornton group, current and former, for their invaluable input and help. Dr. Chi Pang in particular deserves a great deal of recognition for all his help both in carrying out experiments and also during writing-up. Dr. Greg Cabailh must also be thanked for his excellent advice in matters both practical and analytical and in the pub. Dr. (soon!) Oliver Yim deserves special praise for his patience and the assistance he has given me in many ways over the last few years for which I am truly thankful.

On the departmental side of things, I am indebted to the members of the MAPS workshop along with Len and the rest of the Technical Support Group for all their advice on how to fix all manner of equipment, from sheared bolts to ion gauge controllers. I also thank Dr. Wendy Brown, my second supervisor, and the other members of staff in Chemistry and the LCN.

Finally I thank all of my friends and family for their considerable support and patience over the last four years. It's time to stop working on Saturdays now.

PUBLICATIONS LIST

The Defect Structure of Ultra-Thin Ceria Films on Pt(111): Atomic Views from Scanning Tunnelling Microscopy.

D.C. Grinter, R. Ithnin, C.L. Pang and G. Thornton

J. Phys. Chem. C **2010**, *114*, 17036-17041

Reduction of thin film ceria on Pt(111) by supported Pd nanoparticles probed with resonant photoemission.

J. Matharu, G. Cabailh, R. Lindsay, C.L. Pang, D.C. Grinter, T. Skála and G. Thornton

Surf. Sci. **2011**, *605*, 1062-1066

Characterization Tools of Oxide Ultrathin Films

D.C. Grinter and G. Thornton

"Oxide Ultrathin Films. Science and Technology" Eds. G. Pacchioni and S. Valeri *Wiley-VCH* **2011**

In Preparation:

STM Studies of Acetic Acid on Anatase TiO_2(101)

D.C. Grinter, M. Nicotra and G. Thornton

Binding of a Dye-Molecule Analogue to Rutile TiO_2(110) Surfaces

D.C. Grinter, P. Nickels, T. Woolcot and G. Thornton

GLOSSARY

AES Auger Electron Spectroscopy

AFM Atomic Force Microscopy

CB Conduction Band

CITS Current Imaging Tunnelling Spectroscopy

CVD Chemical Vapour Deposition

DFT Density Functional Theory

ECR Electron Cyclotron Resonance

eV Electron Volt

FEL Fast Entry Loadlock

FFT Fast Fourier Transform

IMFP Inelastic Mean Free Path

LEED Low Energy Electron Diffraction

LDOS Local Density of States

LT-STM Low Temperature Scanning Tunnelling Microscope

MBE Molecular Beam Epitaxy

ML	Monolayer
MS	Mass Spectrometry
NC-AFM	Non Contact Atomic Force Microscopy
PES	Photoemission Spectroscopy
PO	Post Oxidation
PVD	Physical Vapour Deposition
QMS	Quadrupole Mass Spectrometer
RD	Reactive Deposition
RFA	Retarding Field Analysis
RGA	Residual Gas Analysis
SPM	Scanning Probe Microscopy
STM	Scanning Tunnelling Microscopy
STS	Scanning Tunnelling Spectroscopy
TSP	Titanium Sublimation Pump
UHV	Ultra-High Vacuum
UPS	Ultra-Violet Photoelectron Spectroscopy
VB	Valence Band
VT-STM	Variable Temperature Scanning Tunnelling Microscope
WGS	Water Gas Shift
WKB	Wentzel-Kramers-Brillouin
XPS	X-ray Photoelectron Spectroscopy

TABLE OF CONTENTS

LIST OF FIGURES

CHAPTER 1

INTRODUCTION

1.1 The Surface Science of Metal Oxides

There are a multitude of important chemical and physical processes that occur at surfaces and interfaces whose study has permitted not only a deeper understanding of their underlying principles, but has also driven the development of experimental techniques with unparalleled capabilities. Forming an understanding of the mechanisms of heterogeneous catalysis is one of the primary motivational factors for research into the behaviour of reactive surfaces on the atomic level. The degree to which such work is recognised in the larger scientific community was demonstrated by the award of the 2007 Nobel Prize in Chemistry to Gerhard Ertl *"for his studies of chemical processes on solid surfaces"*. The work of Ertl towards understanding the mechanism of iron

catalysis of the Haber process for ammonia production, as well as carbon monoxide oxidation over platinum, is a great example of the power of the techniques developed. In general, the catalytic systems of interest are extremely complex and since studying them at the atomic level is required for clear mechanistic understanding, a number of simplifications are usually applied. The majority of surface science experiments are undertaken on single crystal surfaces under ultra high vacuum (UHV) conditions at room or even cryogenic temperatures. Such conditions are obviously far removed from the real operating environment of most catalysts, and this has been termed a *"pressure"* or *"materials"* gap which must be considered when comparing results for the model systems under examination. Recently there has been a drive to bridge these gaps by performing experiments at more relevant temperatures and pressures closer to ambient and, with improvements to experimental techniques, some progress is being made in this direction.[1, 2]

A prerequisite for the study of the chemical and physical properties of surfaces are high-quality experimental techniques, and perhaps the most important of these in recent years has been the development of scanned probe microscopy (SPM). The scanning tunnelling microscope (STM) invented by Gerd Binnig and Heinrich Rohrer in the 1980s, [3, 4] which earned its founders the 1986 Nobel Prize in Physics, and the closely related atomic force microscope (AFM) have allowed real-space imaging and manipulation of surfaces on the single atom scale, revolutionising surface science. The iconic image of "IBM" spelled out in individual xenon atoms on nickel by Don Eigler et al. [5] illustrated the power of STM in dramatic fashion and its unparalleled ability to image single defects and adsorbates in and on surfaces positions STM as one of the key tools in the surface scientist's arsenal.

Surface science and its experimental techniques are not limited to the study of catalysts by any means, and have a wide array of applications within the burgeoning field of nanotechnology

including chemical sensors, corrosion coatings, superconductors, data-storage materials, solar cells and electronic devices.[1, 6, 7] Electronic devices in particular, as they become progressively smaller, will require novel procedures for their manufacture and testing and the experience that surface scientists have of working at these small length scales is invaluable.

One of the largest and most varied classes of materials, with wide-ranging applications, are metal oxides, whose surfaces play important roles in many of the phenomena mentioned above. Examples include TiO_2 as a photocatalyst, SiO_2 and Al_2O_3 as catalyst supports, ZnO in gas sensors, and copper oxides as high-T_c superconductors amongst many others.[8] As well as the economic driving forces based mainly on their real-world applications, the study of metal oxide surfaces is also important from a more fundamental point of view of furthering our understanding of their basic properties such as phase-changes, electronic and magnetic structure and behaviour, crystal structures, and bonding.[8]

1.2 Ultrathin Oxide Films

A large number of metal oxides relevant for catalysis are electrically insulating or semiconducting and as a result present a number of challenges for their study using traditional surface science techniques.[8] Electron-based techniques such as STM and LEED, both of which are extensively used in this thesis, are therefore difficult to implement on metal oxide single crystals due to the occurrence of charging.[9, 10] One common method to overcome this is n-type doping of the oxide via reduction, often by high-temperature annealing in UHV. This method is the preferred preparation procedure for TiO_2 which has a band gap of $\sim$3 V and whose reduction can be

observed visually as the colour of the crystal changes from transparent to dark blue.[11] However this reduction process often has undesirable side-effects including the introduction of surface and sub-surface oxygen vacancies, as well as changing the electronic structure in complex ways.[12] An elegant and increasingly-popular solution to these problems is the formation of an ultrathin oxide film of thickness up to 20 Å on a conducting substrate.[13] Such a system permits the implementation of the full range of surface science characterisation techniques that require the use of charged particles and has also allowed the study of a variety of novel low-dimensional oxide structures not previously encountered.[1] The concept of an "inverse model catalyst" is an extension of an ultrathin film system and is comprised of an incomplete oxide layer supported on a single crystal of the catalyst metal. This forms the opposite situation to that encountered in the normal catalytic system of a highly dispersed metal on an oxide support and has proved a useful paradigm for the investigation of the interactions between the oxide and the metal which are proposed to be key to the activity of such systems.[14, 15]

1.3 Cerium Dioxide

Cerium dioxide, CeO_2, or ceria, is a widely used material with a vast number of proven industrial applications including automobile catalytic converters, fuel cells, dielectric materials, hydrocarbon reforming reactors and an ever increasing role as a heterogeneous catalysis for a large number of oxidation and reduction processes.[16–18] One application that has particular importance has been the recent discovery that gold supported on ceria is a powerful catalyst for the low temperature water-gas-shift reaction, widely used for the production of hydrogen for use as an alternative to fossil fuels.[19] The basis of ceria's activity lies in its accommodation of variable

charge states (Ce^{3+} and Ce^{4+}) that permits facile oxidation and reduction at the surface as well as high mobility of oxygen within the lattice leading to efficient oxygen storage and release during reactions.[20, 21] Bulk CeO_2 is insulating with a band gap of approximately 6 eV, and therefore the application of charged-particle based surface science techniques is not usually possible. Solutions to this in the past have included increasing the conductivity of the bulk crystal by doping; reduction of the sample by sputtering or annealing cycles; and by application of the techniques at elevated temperatures (above 300° C).[11, 22] The formation of well-ordered and crystalline CeO_2(111) ultrathin films on conducting substrates has been extensively studied with a number of preparation procedures identified. In this thesis, some of these various procedures have been compared with the intention of discovering the optimal conditions for films suitable for atomically resolved SPM investigations. There exists a wide range of substrates that have been successfully employed as supports for ceria films including Ru(0001) [23, 24] Pd(111) [25], Rh(111) [26, 27], Ni(111) [25], Re(0001) [28], Cu(111) [29, 30] and Pt(111) [31–34] for a variety of thicknesses ranging from complete oxide coverages to "inverse model catalyst" systems.

1.4 Titanium Dioxide

The surfaces of titanium dioxide, TiO_2, have been some of the most investigated of all oxides, especially rutile TiO_2(110) which is regarded as a prototypical metal oxide surface with a vast number of studies and reviews in the literature regarding its structure, reactivity and catalytic action.[11, 35–40] Interest in titania was prompted by the discovery by Fujishima and Honda in 1972 of its photocatalytic activity for water splitting [41] and it has a multitude of proven applications in a diverse range of fields including heterogeneous catalysis, solar cells, pigments,

gas sensors and even electronic devices. The review by Diebold [11] provides a comprehensive summary of these applications as well as the chemistry and structure of many of the surfaces of titania. Of the three polymorphs of TiO_2, rutile, anatase and brookite; the thermodynamically most stable rutile TiO_2(110) surface has been by far the most popular for study, despite not displaying the highest catalytic activity.[42] As with ceria, titania is also commonly used in catalysis as a support for metal particles and the system of Pt/TiO_2 in particular is a model for the study of the strong metal substrate interaction (SMSI).[43]

Anatase TiO_2 is of particular interest with regards to photocatalysis as it displays higher activities than the other polymorphs and forms a higher fraction of the industrially produced catalysts in use.[44] Experimental data on anatase surfaces are scarce in comparison to rutile however, due primarily to the difficulty in growing large anatase single crystals or mining natural samples with sufficient purity.[45] One approach that has proved successful in a number of instances has been the growth of ultrathin films of anatase TiO_2 on suitable substrates, but in general there is a great need for more research on anatase single crystal surfaces. In powder materials, the surfaces most commonly found are the (101), (100) and (001), of these the thermodynamically most stable and that which forms the major fraction in active catalysts is the (101) which is the focus of some of this thesis.[11]

1.5 Thesis Structure

The next chapter of this thesis contains a brief overview of the fundamental background of the theory behind of a number of the experimental techniques used for the investigation of the oxide

ultrathin films and single crystal surfaces. A relatively thorough understanding of these techniques is vital when it comes to the analysis of the results obtained from experiments, particularly in the case of Scanning Tunnelling Microscopy and Spectroscopy (STM/STS) which will be examined in some detail. The theoretical background of the supplementary techniques of Low Energy Electron Diffraction (LEED) and Auger Electron Spectroscopy (AES) will also be covered in this chapter mainly from the perspective of analysis of their experimental results rather than a purely academic approach.

Chapter 3 details the experimental apparatus used for this research, predominantly contained within two Ultra-High Vacuum (UHV) systems and focuses on the elements that were optimised for the study of the ultrathin films and surfaces in this work. An explanation of the operation and features of the two STMs employed is provided, along with details of sample preparation techniques and the implementation of the auxiliary analytical techniques.

Chapter 4, the first section of results, is a summary of the growth and characterisation of ultrathin CeO_2(111) films on Pt(111). A number of preparation procedures for these films have been examined and compared, with the results analysed by STM, LEED and AES. The large and atomic scale structure of such films is presented and discussed in addition to placing the work in the context of ultrathin film and single crystal metal oxide surface studies.

Chapter 5 shows the results of experiments on a model catalyst for the low temperature water-gas-shift reaction; gold supported on ceria. The structure and behaviour of single atoms and small gold particles on an ultrathin ceria film have been analysed with STM.

Chapter 6 is a study of the adsorption and reaction properties of acetic acid on anatase TiO_2(101)

using STM and LEED. A model for the binding geometry is proposed and results of both sub-monolayer and saturated coverages are examined. The desorption behaviour of acetic acid is also investigated along with the effects of illumination with ultraviolet light and co-adsorption with water.

The final section of results, chapter 7, is an investigation of the adsorption and reaction properties of benzoic acid on rutile TiO_2(110). Both the (1×1) and (1×2) surfaces were investigated, with important implications for the elucidation of the structure of sub-stoichiometric TiO_2 surfaces.

References

[1] Bowker, M., Ed. *Scanning Tunneling Microscopy in Surface Science. Nanoscience and Catalysis;* Wiley VCH, 2010.

[2] Hendriksen, B. L. M.; Bobaru, S.; Frenken, J. W. M. *Top. Cat.* **2005**, *36*, 43–54.

[3] Binnig, G.; Rohrer, H.; Gerber, C.; Weibel, E. *Appl. Phys. Lett.* **1982**, *40*, 178–180.

[4] Binnig, G.; Rohrer, H.; Gerber, C.; Weibel, E. *Phys. Rev. Lett.* **1982**, *49*, 57–61.

[5] Eigler, D.; Schweizer, E. *Nature* **1990**, *344*, 524–526.

[6] Ertl, G.; Freund, H.-J. *Phys. Today* **1999**, *1*, 32–38.

[7] Venables, J. A. *Introduction to Surface and Thin Film Processes;* Cambridge University Press, 2000.

[8] Henrich, V. E.; Cox, P. A. *The Surface Science of Metal Oxides;* Cambridge University Press, 1994.

[9] Freund, H.-J. *Farad. Disc.* **1999**, *114*, 1–31.

[10] Baumer, M.; Freund, H.-J. *Prog. Surf. Sci.* **1999**, *61*, 127–198.

[11] Diebold, U. *Surf. Sci. Rep.* **2003**, *48*, 53–229.

[12] Yim, C. M.; Pang, C. L.; Thornton, G. *Phys. Rev. Lett.* **2010**, *104*, 036806.

[13] Freund, H.-J.; Pacchioni, G. *Chem. Soc. Rev.* **2008**, *37*, 2224–2242.

[14] Chambers, S. *Surf. Sci. Rep.* **2000**, *39*, 105–180.

[15] Henry, C. R. *Surf. Sci. Rep.* **1998**, *31*, 231–325.

[16] Trovarelli, A. *Catalysis by Ceria and Related Materials*, Catalytic Science Series; Imperial College Press, 2002.

[17] Trovarelli, A.; de Leitenburg, C.; Boaro, M.; Dolcetti, G. *Cat. Today* **1999**, *50*, 353–367.

[18] Gorte, R. J. *AIChE J* **2010**, *56*, 1126–1135.

[19] Fu, Q.; Saltsburg, H.; Flytzani-Stephanopoulos, M. *Science* **2003**, *301*, 935–938.

[20] Bernal, S.; Calvino, J.; Cauqui, M.; Gatica, J.; Larese, C.; Omil, J. P.; Pintado, J. *Cat. Today* **1999**, *50*, 175–206.

[21] Liu, Z.; Jenkins, S. J.; King, D. A. *Phys. Rev. Lett.* **2005**, *94*, 196102.

[22] Esch, F.; Fabris, S.; Zhou, L.; Montini, T.; Africh, C.; Fornasiero, P.; Comelli, G.; Rosei, R. *Science* **2005**, *309*, 752–755.

[23] Lu, J.; Gao, H.-J.; Shaikhutdinov, S.; Freund, H.-J. *Surf. Sci.* **2006**, *600*, 5004–5010.

[24] Mullins, D. R.; Radulovic, P.; Overbury, S. H. *Surf. Sci.* **1999**, *429*, 186–198.

[25] Alexandrou, M.; Nix, R. *Surf. Sci.* **1994**, *321*, 47–57.

[26] Eck, S.; Castellarin-Cudia, C.; Surnev, S.; Ramsey, M.; Netzer, F. P. *Surf. Sci.* **2002**, *520*, 173–185.

[27] Wilson, E. L.; Chen, Q.; Brown, W.; Thornton, G. *J. Phys. Chem. C* **2007**, *111*, 14215–14222.

[28] Xiao, W.; Guo, Q.; Wang, E. *Chem. Phys. Lett.* **2003**, *368*, 527–531.

[29] Matolín, V.; Libra, J.; Matolínová, I.; Nehasil, V. *Appl. Surf. Sci.* **2007**, *254*, 153–155.

[30] Staudt, T.; Lykhach, Y.; Hammer, L.; Schneider, M. A.; Matolín, V.; Libuda, J. *Surf. Sci.* **2009**, *603*, 3382–3388.

[31] Berner, U.; Schierbaum, K.-D. *Thin Sol. Films* **2001**, *400*, 46–49.

[32] Berner, U.; Schierbaum, K.-D. *Phys. Rev. B* **2002**, *65*, 235404.

[33] Wilson, E. L.; Grau-Crespo, R.; Pang, C. L.; Cabailh, G.; Chen, Q.; Purton, J. A.; Catlow, C. R. A.; Brown, W.; de Leeuw, N. H.; Thornton, G. *J. Phys. Chem. C* **2008**, *112*, 10918–10922.

[34] Grinter, D. C.; Ithnin, R.; Pang, C. L.; Thornton, G. *J. Phys. Chem. C* **2010**, *114*, 17036–17041.

[35] Pang, C. L.; Lindsay, R.; Thornton, G. *Chem. Soc. Rev.* **2008**, *37*, 2328–2353.

[36] Pang, C. L.; Thornton, G. *Surf. Sci.* **2006**, *600*, 4405–4406.

[37] Henderson, M. A. *Surf. Sci. Rep.* **2011**, *66*, 185–297.

[38] Thompson, T. L.; Yates, J. T. *Chem. Rev.* **2006**, *106*, 44284453.

[39] Yates, J. T. *Surf. Sci.* **2009**, *603*, 1605–1612.

[40] Fujishima, A.; Zhang, X.; Tryk, D. *Surf. Sci. Rep.* **2008**, *63*, 515–582.

[41] Fujishima, A.; Honda, K. *Nature* **1972**, *238*, 37–38.

[42] O'Regan, B.; Graetzel, M. *Nature* **1991**, *353*, 737–740.

[43] Bowker, M.; Stone, P.; Morrall, P.; Jr, R. L. S.; Bennett, R.; Perkins, N.; Kvon, R.; Pang, C. L.; Fourre, E.; Hall, M. *J. Cat.* **2005**, *234*, 172–181.

[44] Linsebigler, A.; Lu, G.; Jr, J. Y. *Chem. Rev.* **1995**, *95*, 735–758.

[45] Diebold, U.; Ruzycki, N.; Herman, G.; Selloni, A. *Cat. Today* **2003**, *85*, 93–100.

CHAPTER 2

THEORETICAL ASPECTS OF INSTRUMENTATION

Abstract

This chapter aims to provide a theoretical examination of the techniques used in this work, focussing primarily on scanning probe microscopy and spectroscopy, especially in relation to their application on metal oxide and ultrathin film surfaces, but also examining the two other surface characterisation techniques that were implemented; Low Energy Electron Diffraction (LEED) and Auger Electron Spectroscopy (AES).

2.1 Scanning Tunneling Microscopy (STM)

2.1.1 Introduction and Basic Principles

The development of the scanning tunnelling microscope (STM) in the 1980s by Gerd Binnig and Heinrich Rohrer [1, 2] revolutionised the fields of surface science and nanotechnology. Over the last few years it has become routine to image samples with atomic resolution, carry out spectroscopic measurements on adsorbates, and even manipulate single atoms.[3–5]

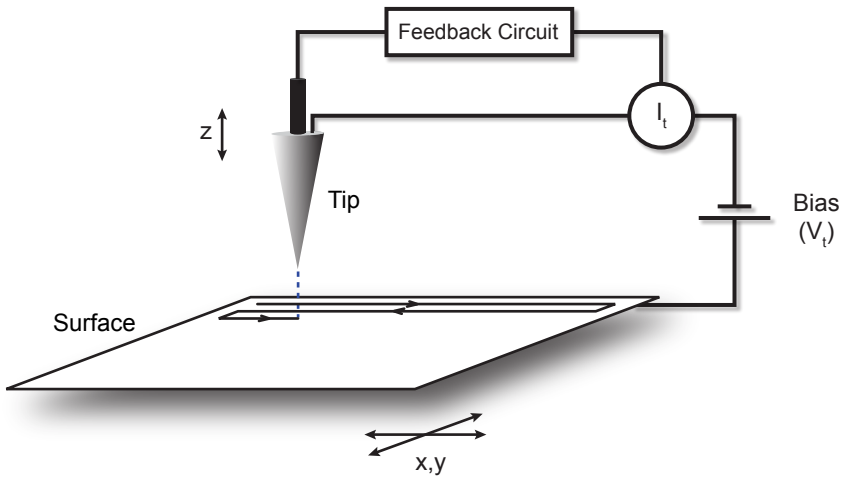

Figure 2.1: Schematic illustration of the basic experimental setup of an STM depicting the rastering of a sharp tip across a surface under the control of a current feedback loop.

The experimental setup of STM, demonstrated schematically in Figure 2.1, displays the relative simplicity of the technique. An atomically sharp tip is moved to within a few Å of a conducting or semi-conducting surface and a small potential difference is applied between the two. The resultant small tunnelling current, which is a function of the tip-surface separation, is measured and the tip

is rastered over the surface, building up a map approximating the topography of the surface. With refinement this technique is able to image with atomic resolution, as first demonstrated by Binnig et al. on the Si(111) (7 × 7) surface.[6] The technological and engineering challenges that must be overcome to implement STM with this resolution are by no means trivial and some of these obstacles and solutions to them will be reviewed in the third chapter of this work.

In the experimental setup of STM there exists a potential barrier between the tip and sample which an electron cannot cross from a classical viewpoint unless it has kinetic energy greater than the barrier height. From a quantum mechanical perspective however, there is a small, finite transmission probability which may be easily calculated as described below. The band structure at such a tunnel junction is illustrated in Figure 2.2 for a metallic surface and tip separated by a short distance d_t, (a) before and (b) after a bias voltage V is applied.

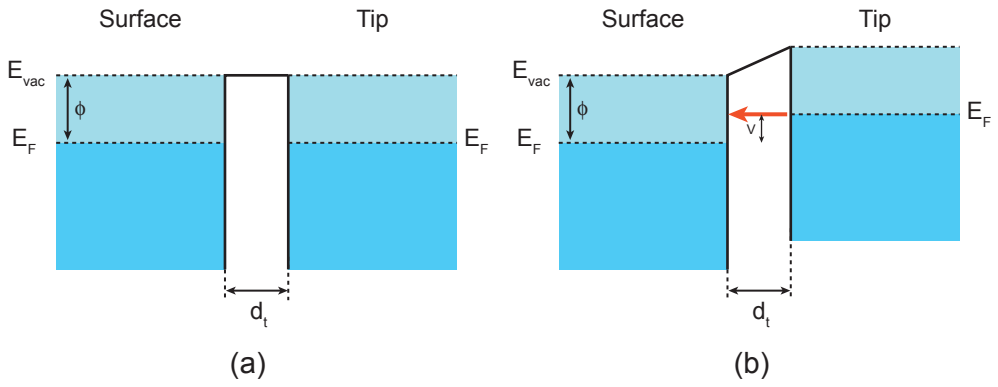

Figure 2.2: Diagram depicting the band structure and potential barrier between a metallic tip and sample tunnel junction as present in STM at: (a) zero bias (b) an applied voltage, V. d_t is the tip-sample separation, and E_{vac} and E_F the vacuum and Fermi levels respectively.

If we consider a one-dimensional wave in the z-direction and a rectangular barrier, the solutions to the Schrödinger equation inside it are of the form in equation 2.1:

$$\psi \propto e^{-\kappa z} \tag{2.1}$$

$$\kappa = \sqrt{\frac{2m(V_B - E)}{\hbar^2}} \tag{2.2}$$

Where κ is the decay constant and is a function of the barrier height, V_B, the energy of the state, E, and the mass of the electron, m. Obviously the barrier height, V_B, is not constant across the gap as shown in Figure 2.2b but assuming a small bias voltage this approximation holds and an average value can be used. For the simplest case, V_B is the vacuum level of the system and hence the difference $V_B - E$ is equal to the workfunction of the surface for states at the Fermi level, E_F. At low bias voltages and temperature, the tunnelling current, I_t, is exponentially decaying with the barrier width, d_t, and given by equation 2.3[2–4]:

$$I_t \propto e^{-2\kappa d_t} \tag{2.3}$$

If we consider a typical workfunction of a few eV, 2κ is approximately 2 Å^{-1}, meaning that a variation in the separation of the tip and sample of 1 Å will lead to an order of magnitude change in the tunnelling current. This exponential current-distance relationship leads to the enormous sensitivity of the STM and also means that in most cases the tunnelling can be considered to occur predominantly through a single atom on the end of the tip. This very simple description can provide a simple explanation of the behaviour of STM on the nanometer scale, suitable for large scale topographical features, however for a better understanding of the process it is necessary to examine more complex formalisms, such as those constructed by Tersoff and Hamann [7, 8], Chen [9], Lang [10–12] and Wentzel-Kramers-Brillouin (WKB) [4, 13].

2.1.1.1 Tersoff and Hamann

The simple exponential relationship for the tunnelling current derived above was not able to adequately explain the observed atomic resolution of the first experiments of Binnig et al. [6] and as such a more rigorous theory was required. It is possible to calculate the transmission coefficient for an electron incident on the barrier between the tip and sample but this is computationally expensive even when applied to very simplistic surface models and not feasible for more realistic systems.[4] However, due to the dominance in STM imaging of the relative change in tunnelling current rather than its absolute value, it is suitable to apply Bardeen's perturbation formula, where the wavefunction tail and the electron transfer coefficient are not rigorously treated [14]. The tunnelling current by first-order perturbation theory is given by equation 2.4

$$I = \frac{2\pi e}{\hbar} \sum_{\mu,\nu} \left[f(E_\mu) - f(E_\nu) \right] |M_{\mu\nu}|^2 \delta(E_\nu + V - E_\mu) \tag{2.4}$$

where $f(E)$ is the Fermi function, V the applied voltage bias, $M_{\mu\nu}$ the tunnelling matrix between the states ψ_μ of the tip and ψ_ν of the surface, and E_μ and E_ν are the energy of the two states in the absence of tunnelling. In the small voltage and low temperature limit this reduces to equation 2.5

$$I = \frac{2\pi}{\hbar} e^2 V \sum_{\mu,\nu} |M_{\mu\nu}|^2 \delta(E_\nu - E_F) \delta(E_\mu - E_F) \tag{2.5}$$

where E_F is the Fermi level. Bardeen demonstrated that the matrix elements $M_{\mu\nu}$ can be expressed

as equation 2.6: [14]

$$M_{\mu\nu} = \frac{\hbar}{2m} \int dS \cdot \left(\psi_\mu^* \nabla \psi_\nu - \psi_\nu \nabla \psi_\mu^*\right) \tag{2.6}$$

In this, Tersoff and Hamann treat the tip as a point probe which gives the ideal measurement device with maximum possible resolution, and leads to a matrix element that is proportional to the amplitude of ψ_ν at the position r_0 of the tip and hence the following relationship:

$$I \propto \sum_\nu |\psi_\nu(\mathbf{r}_t)|^2 \delta(E_\nu - E_F) \equiv \rho(\mathbf{r}_t, E_F) \tag{2.7}$$

This shows the approximation (only valid at low bias) that the tunnelling current is proportional to the surface local density of states (LDOS) at E_F, $\rho(\mathbf{r}_t, E_F)$, which is equivalent to the surface charge density at E_F.[4] As a result of this it can be considered that an STM image is a contour map of constant surface LDOS. At more realistic, higher, bias voltages this simple approximation no longer holds and it might be expected that the expression could be generalised to:

$$I \sim \int_{E_F}^{E_F+V} \rho(\mathbf{r}_t, E)\, dE \tag{2.8}$$

This expression (2.8) does not take into account the energy dependence of the matrix element and tip DOS, but it is still a reasonable approximation at higher bias voltages (assuming $V \ll \phi$) and is much better than the simple relationship in equation 2.7.[4] Although this model is simplistic

in its treatment of the tip as a point probe, the result anticipates the basic feature that the current is proportional to the integrated LDOS as shown in more realistic models found elsewhere.[7, 8]

2.1.1.2 Chen Model

The first s wave tunnelling models predicted a resolution of about 6 Å which were in clear disagreement to the experimentally obtained results demonstrating that features with spacings as low as 2 Å were resolved [15]. An explanation of this increased resolution was provided by Chen who removed this s wave approximation and predicted atomic resolution on metal substrates.[9] The approximation seems unlikely to be valid for most tip materials such as tungsten and platinum-iridium, which are both d band metals, and have a Fermi level DOS containing mostly contributions from d states. In addition to this, W is often considered to have highly localised dangling bonds which play a major role in tunnelling. One of the most important results of Chen is illustrated in Figure 2.3, which is that of the reciprocity principle showing that a d_{z^2} tip scanning an s wave sample is exactly equivalent to an s wave tip scanning a d_{z^2} sample.

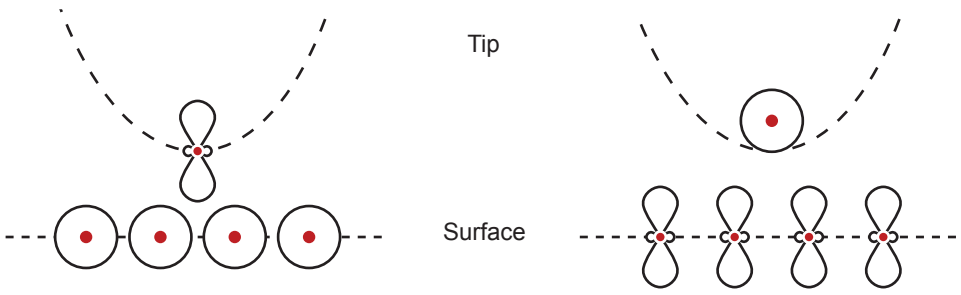

Figure 2.3: Illustration of the reciprocity principle demonstrating the equivalence during STM operation of a d_{z^2}-terminated tip scanning an s sample and an s-terminated tip scanning a d_{z^2} sample as proposed by Chen.[9]

Chen's approach is also generally considered to be the first attempt to model the STM from a chemical perspective. In it he considers the fact that the tip-sample separation is the range of 4-6 Å and hence it is within the region where there is significant covalent overlap between the tip and sample. As a result it can be imagined that the process of a tip scanning is a series of bond making and breaking steps, and is therefore chemically interacting with the surface. This ability of the tip to take part in reactions at the surface has been demonstrated by Lyo and Avouris who showed that individual Si atoms could be transferred from tip to sample and vice-versa with electrical pulsing of the tip [16] and by Bikondoa et al. who demonstrated selective desorption of hydrogen adatoms on TiO_2 by electrical tip pulsing.[17].

2.1.1.3 Lang Model

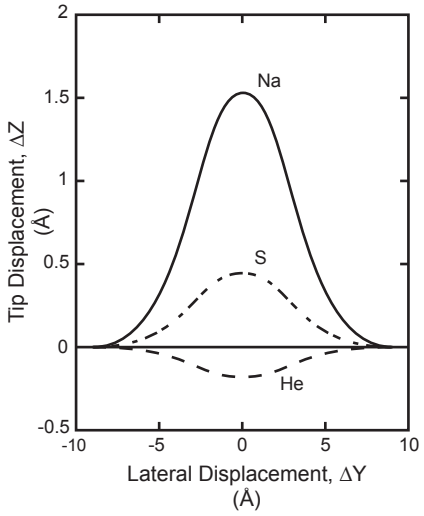

Figure 2.4: Calculated tip displacement (ΔZ) vs. lateral displacement (ΔY) for an STM scan of adsorbate atoms (Na, S, and He) on a jellium surface at small bias voltages, highlighting the importance of electronic structure on the appearance in STM. Figure adapted from [11].

As shown previously, STM effectively measures the LDOS at the surface and as a result any adsorbates will have a large effect on the imaging. Lang carried out a series of calculations [10–12] on imaging different atoms using the Bardeen tunnelling formalism and considering two flat electrodes; one with a Na atom on it as a tip, and the other with adsorbate atoms (He, Na and S). He calculated the state density, and it showed that the Na *3s* and S *2p* resonances create an increase in the LDOS at the Fermi level, whereas the He causes a reduction by polarising the metal states away from the Fermi level. This change in the LDOS results in the following way in the constant current STM mode; the adsorbates appear as protrusions (Na, S) or depressions (He) depending on whether there is an increase or decrease in the LDOS as illustrated in Figure 2.4. The ramification of this is that the analysis of STM images can often be non-trivial, particularly for atomically resolved images and it is important to compare with calculations such as simulated STM images in order to accurately interpret them. An example of the importance of this is displayed in Figure 2.5, where a typical STM image of rutile TiO_2(110) is displayed, along with a model of the surface structure.

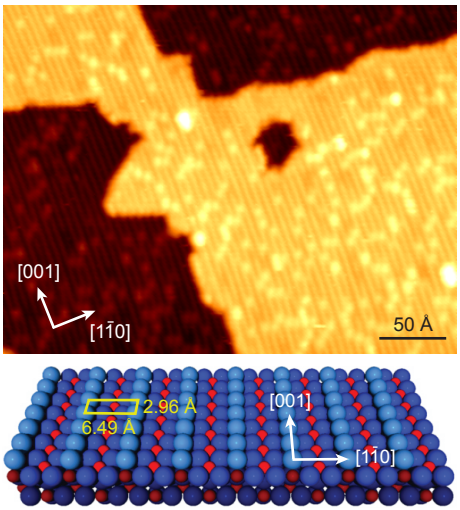

Figure 2.5: A typical STM image (30×24 nm^2, V_s = +1.50 V, I_t = 0.10 nA) and associated structural model of the rutile TiO_2(110) surface. The bright rows in the [001] direction are attributed to Ti^{4+} ions (red atoms in model).

In the STM image of the rutile $TiO_2(110)$ surface shown in Figure 2.5 the bright lines which are normally suggestive of a higher part of the surface in fact originate from the Ti^{4+} ions rather than the bridging O^{2-} ions due to the tunnelling conditions used. As a positive bias is applied to the sample, tunnelling occurs into the empty states and as such they appear brighter in the final image, contrary to their topographic locations on the surface as shown in the structural model of the surface also displayed in Figure 2.5. The bright features between these rows are attributed to oxygen vacancies and hydroxyls located on the bridging oxygen rows (light blue atoms in model) and again highlight the importance of electronic effects on the correct analysis of topographic STM images.

2.1.1.4 WKB Approximation

One of the assumptions of the Tersoff-Hamann theory is the use of a low bias voltage, which is contrary to the usual operation of STM especially as utilised on metal oxides where it is common to use voltages in the range 1-3 V, or even higher. Under such conditions it is not suitable to only consider states at the Fermi level and instead a range of states will have an effect on the tunnelling current. The semi-classical Wentzel-Kramers-Brillouin (WKB) approximation, shown in equation 2.9 is a useful model in such situations, especially when extended to scanning tunnelling spectroscopy (STS) as will be discussed later in this chapter. The tunnelling probability is calculated between two planar electrodes at zero temperature and the resultant tunnelling current is the integral over the energy range where both filled-initial and empty-final states are available for elastic tunnelling.[4, 13]

$$I = \int_0^{eV} \rho_s(r, E)\rho_t(r, \pm eV, \mp E)T(E, eV, r)\, dE \tag{2.9}$$

The upper and lower signs correspond to positive ($eV > 0$) and negative ($eV < 0$) sample biases respectively, and $\rho_s(r, E)$ and $\rho_t(r, E)$ are the density of states of the sample and tip at location r and energy E measured with respect to their Fermi levels. The transmission probability, T, for electrons with energy E and bias voltage V at a tip-sample separation of z is given by equation 2.10 which has a dependence on the average of the tip and surface workfunctions $\left(\frac{\phi_s+\phi_t}{2}\right)$:

$$T(z, E, V) = exp\left(-\frac{2z\sqrt{2m}}{\hbar}\sqrt{\frac{\phi_s + \phi_t}{2} + \frac{eV}{2} - E}\right) \tag{2.10}$$

Although the integral in equation 2.9 sums across all the filled-empty state pairs in the energy window provided by the bias voltage V, the tunnelling probability T has a maximum when $E = 0$ which is at the Fermi level (E_F) of the emitter, and as such electronic states close to E_F contribute most to the tunnel current.[18]

2.1.2 STM of Semiconductors

The theory examined previously can strictly only be applied to metal substrates, whereas for semiconductors the Fermi level is located within the bulk band gap. Unless there are metallic surface states, tunnelling must occur from high lying valence band states, or low lying conduction band states as shown in Figure 2.6, and hence high bias voltages (of the order of 2 V) are commonly used to image semiconductors.[3]

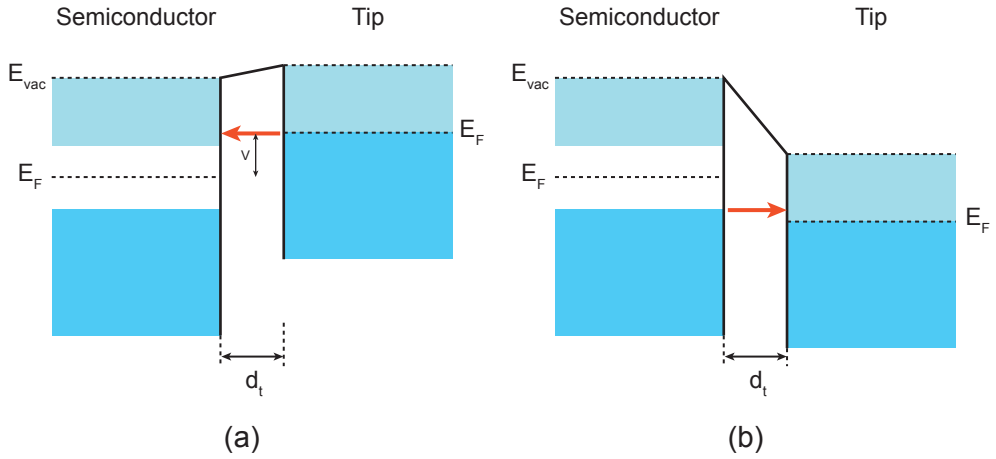

Figure 2.6: A diagram showing the band structure and tunnel junction for tunnelling to and from a semiconductor surface at (a) positive and (b) negative tip biases.

As a result of this, the tunnelling current is no longer proportional to the LDOS at a given energy level, and contributions from transitions from or into energy levels in the sample must also be considered. Another important consideration is the limit on spatial resolution due to the limited conductivity of the sample, and the usual assumption made in STM theory that all the applied voltage is dropped within the vacuum. In low conductivity materials however, there is some voltage drop across the sample in the space charge region directly below the tip. The size of the zero bias space charge region, s, is given by equation 2.11: [19]

$$s = \sqrt{\frac{2\varepsilon kT}{q^2 n}} \tag{2.11}$$

where ε is the sample permittivity, q the charge on an electron and n the number density of charge carriers. We can therefore see that as the local charge carrier concentration increases, the space charge size decreases. This space charge diameter can vary a lot between different materials, for example in Si(111)(7 $\times$ 7), it has been calculated to be 2 Å, whereas for ZnO it can range from 2-200 Å. As a result, atomic resolution is not limited by large band gaps, but rather by large space

charge diameter, a good example of which is seen in the comparison between TiO_2 on which atomic resolution can be readily achieved, and ZnO on which it is much more difficult, despite both samples having similar band gap sizes.[19–21]

2.1.3 STM of Ultrathin Metal Oxide Films

As mentioned in the introductory chapter, one motivation for the study of an oxide surface as a thin film rather than a termination of the bulk is to alleviate charging problems due to the insulating nature of most metal oxides. A high conductivity is vital for STM and the use of thin films on conducting substrates has enabled the study of a wide range of oxides not previously accessible to the technique. Other strategies attempted to provide enhanced conductivity include doping for narrow band-gap oxides such as TiO_2 [21] and high-temperature studies on wider gap oxides including CeO_2 (800 K) [22, 23] and NiO (500 K) [24]. These approaches have limitations though, notably in the case of TiO_2, where the procedure for increasing the conductivity by annealing in UHV generates additional defects and changes the electronic structure of the surface considerably.[25] The application of raised-temperature STM is also not ideal as it restricts studies of adsorbate-oxide interactions and may induce undesired surface reconstructions. In particular cases, conducting surface states may permit the required conduction for STM study as in the case of metallized ZnO$(10\bar{1}0)$ achieved after H_2 exposure.[26] For direct tunnelling through a non-conductive film, the thickness is critical, with a maximum of $\sim$1 nm so that sufficient overlap between tip and substrate states occurs at low bias voltages. Alternatively, some oxides with small band gaps, such as Fe_3O_4 and V_2O_3 have sufficient carrier density to allow conduction of low currents through a thicker film even at room temperature. Doping of films to increase their conductivity is achieved either with intrinsic defects (as in the case of oxygen vacancies in

TiO_2) or with impurity atoms for other semiconductors.[18] The importance of bias voltage in determining image contrast is illustrated in Figure 2.7a and 2.7b, where schematics of the tunnel junction for a thin oxide film are shown. In Figure 2.7a, the applied bias voltage is lower than the onset of the film conduction band (CB) and as such the film acts as an additional vacuum barrier and only slightly perturbs the tunnelling process. Figure 2.7b in contrast, depicts a bias high enough to allow tunnelling into states within the CB of the film dramatically changing the observed contrast in STM and permitting atomically resolved imaging of the oxide film.[27]

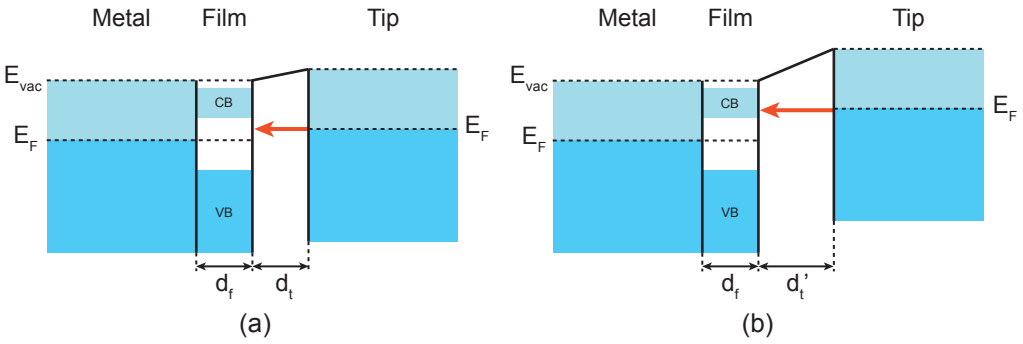

Figure 2.7: A schematic of the tunnelling junction for an ultrathin film of insulating oxide (thickness d_f) on a metal surface for two bias voltages.

Explanation of the observed contrast in STM when tunnelling through an ultrathin oxide film is often complex, for a number of reasons. If a low bias voltage is used for imaging, the observed morphology may be a result of the electronic structure of the oxide-film interface whose states have the most influence on the tunnelling current; whereas at biases closer to the conduction band of the oxide, there may be a large increase in the contrast due to the availability of oxide states into/from which tunnelling may occur. An example of the imaging of a buried interface is seen in the study of thin alumina films on NiAl(110) where the interface between the metal and oxide is imaged with atomic resolution despite being three atomic layers down.[28] The main result of

this bias-dependent imaging is that the apparent height in STM of any features of ultrathin films is often due predominantly to electronic rather than topographical effects and as such analysis of the true morphology is often not easy.[18] Despite these difficulties, the voltage dependence leads on nicely to the use of scanning tunnelling spectroscopy (STS) where the electronic structure of films can be probed very effectively by STM and which will be examined in more detail further on in this chapter.

2.1.3.1 Metal Particles Supported on Ultrathin Films

Metal single atoms and nanoparticles supported on ultrathin oxide films are important catalytic systems for a number of reactions and are an ideal candidate for study with STM which is one of the few techniques that has the resolution to examine their morphology, bonding, electronic structure and in some cases reactivity. (See [27] and references within) Small metal particles of the order of ~ 20 atoms in size often have interesting electronic structures and the use of STM as a probe of these results in a number of effects that must be considered. The charge states of such metal particles may be extremely influential on their catalytic action and techniques that are able to probe this on the individual scale rather than as an average are very desirable. A schematic depicting the tunnel junctions involved is depicted in Figure 2.8 where two biases are displayed (a) lower than the conduction band (CB) onset of the film and (b) higher than the CB onset.

The electrical isolation of such clusters, screened by the oxide film on one side and the vacuum gap on the other, leads to a so-called double tunnel junction and therefore a more complicated formulation is required for the tunnelling current during STM. One effect of this isolation is Coulomb charging leading to a build-up of electrons within the metal cluster states and which has

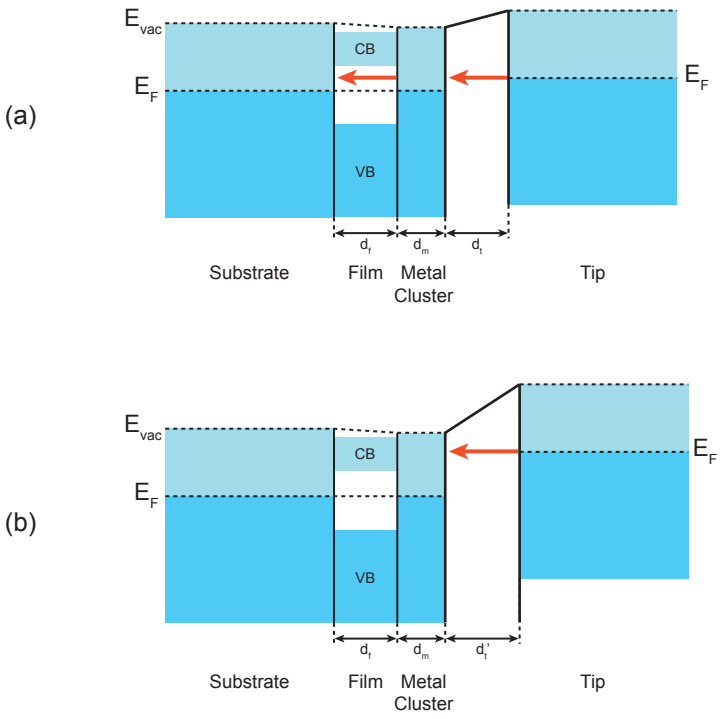

Figure 2.8: A depiction of the tunnelling junctions and band structure for a metal cluster (thickness d_m) supported on an ultrathin film (thickness d_f) of insulating oxide on a metal surface.

a characteristic effect on the tunnelling.[29, 30] If the bias is too low, then electrons from the tip will not have enough energy to overcome the coulomb repulsion and enter the metal resulting in no tunnel current through the cluster (visible as a region of zero conductance during I/V spectroscopy - see following section for more details). As the bias voltage is increased and the energy of the electrons is greater than that required to overcome the coulomb repulsion, then tunnelling through the cluster can occur and a peak would be observed in the differential conductance. In terms of the appearance in STM imaging, the height of such metal clusters is likely to be highly bias dependent and comparison with simulated STM is often vital in order to understand the results obtained. The system shown schematically in Figure 2.8 depicts the metal cluster as having a continuous band structure when the reality is often very different as, due to confinement effects, very small metal clusters may have discrete states which may be suitable for investigation with scanning tunnelling spectroscopy.

2.1.4 Scanning Tunnelling Spectroscopy

The influence of the local density of states (LDOS) at the surface on the tunnelling current in STM permits the development of powerful spectroscopic tools. It is possible to determine such information as band gaps of semiconductors, band onsets in insulating oxide films [29], electronic structures of single atoms and clusters [30], and even magnetic and vibrational structure.[31, 32] Many of these parameters can of course be measured by traditional spectroscopic techniques such as PES and IRAS, but these yield an average value across the surface and it is the unparalleled spatial resolution provided by STM that permits spectroscopy on the scale of individual atoms or molecules. To see the relationship between the tunnelling current and the LDOS of the surface under investigation, it is useful to consider its derivative, dI/dV, (also known as the differential conductance); in this case we shall use the WKB approximation for I given in Equation 2.9, which differentiates to:

$$\frac{dI}{dV} = \rho_s(r, eV)\rho_t(r, 0)T(E, eV, r) + \int_0^{eV} \rho_s(r, E)\rho_t(r, \pm eV, \mp E)\frac{dT(E, eV, r)}{dV}\, dE \quad (2.12)$$

The first term in Equation 2.12 is simply the product of the sample DOS (ρ_s), the tip DOS (ρ_t) and the transmission probability (T, given by Equation 2.10), and the second describes the voltage dependence of the transmission probability. The transmission probability, T, is a monotonic function and therefore contributes a smooth background to dI/dV and as a result most structure in the plot of differential conductance versus V is due primarily to the first term in 2.12. For a metallic tip, the DOS is generally considered to be constant and therefore it can be considered that dI/dV is simply proportional to the LDOS of the surface.

The simplest mode of operation of STS is in so-called point current/voltage (I/V) spectroscopy, where the tunnelling current is measured as a function of bias voltage at a fixed tip-sample separation. To achieve these spectra a scan is interrupted and, with the feedback loop switched off (to keep the tip-sample separation constant), the voltage ramped whilst monitoring the current. Typically a number of such spectra are obtained at various points on the surface and then averaged to increase the signal-to-noise ratio. To obtain the differential conductance (dI/dV) which is proportional to the LDOS as described earlier, the I/V curves are either numerically differentiated after acquisition or obtained using a lock-in amplifier during measurement of the tunnelling current. Current Imaging Tunnelling Spectroscopy (CITS) is a commonly used combination of I/V point spectroscopy with the imaging ability of the STM to obtain atomically resolved spectroscopy of a desired surface. The implementation of CITS is conceptually simple; at each pixel within a scan the feedback loop is switched off and a point I/V spectrum obtained before switching on the loop again and moving to the next pixel. In such a way a current image is built up at all the bias voltages in the range of the I/V curve and by differentiating the individual spectra, a 2-D map of the LDOS can be obtained, with atomic resolution. [31] Obtaining good quality data in this way is far from trivial and requires an extremely stable tip and very low noise levels within the STM. STS is therefore often performed at cryogenic temperatures and careful thought must be given to reducing vibrational and electronic noise in the design of the STM and its environment.

2.1.5 Tip Convolution

The preceding theoretical section has examined the use of various ideal tips for STM. In reality the assumption that the majority of tunnelling occurs through the terminating atom of an atomically sharp tip holds only for perfectly flat surfaces. In most cases this is not applicable and the shape

of the tip apex plays an import role in image formation and analysis of all results must take this into account. When a tip is scanned across a surface there is a convolution of its shape with any features on the surface. The magnitude and effect of this convolution is dependent on the relative sizes of the features being scanned and the curvature of the tip. The most common results of such convolution are illustrated in Figure 2.9.

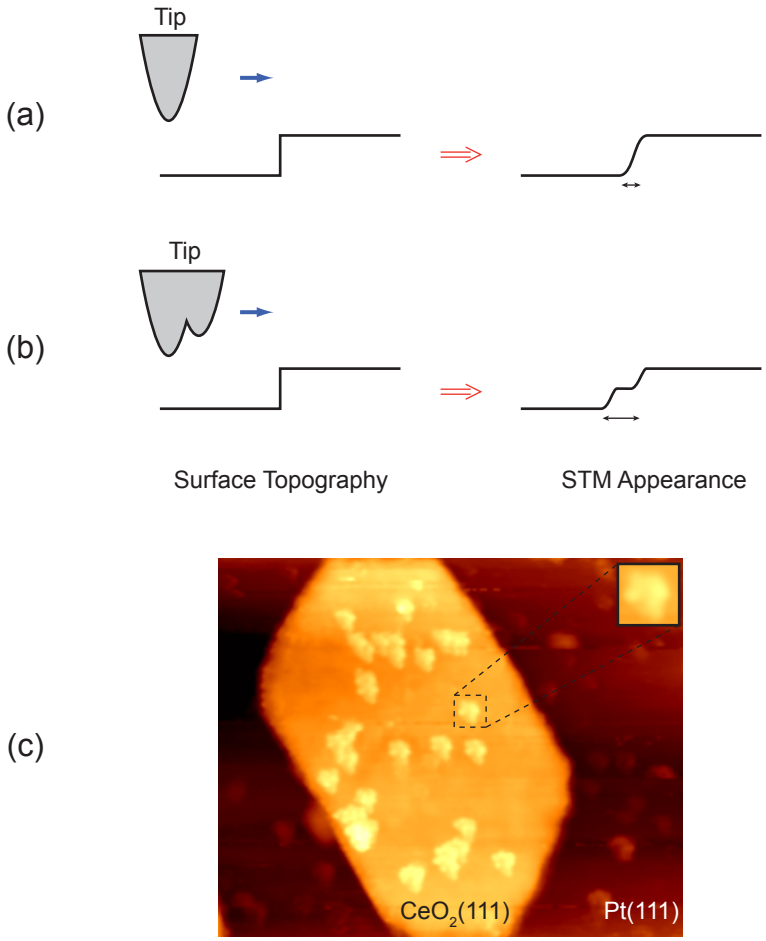

Figure 2.9: An illustration of the effects of tip convolution during STM for (a) a symmetric tip and (b) a "double", or multiple tip and (c) an STM image (50×35 nm^2, V_s = -3.20 V, I_t = 0.05 nA) of Au clusters on a 0.6 nm thick island of CeO_2(111) on Pt(111).

The tips shown in Figure 2.9 may indeed be suitable for atomic resolution imaging on an atomically

flat surface, as it is possible that they are terminated by a single atom that is bound tightly enough to permit stable tunnelling. Figure 2.9a, shows a typical tip scanning over a sharp, vertical feature on the surface (e.g. a monoatomic step edge) and it is observed that when the tip reaches the step edge, tunnelling occurs simultaneously from the side of the tip and its apex when they are the same distance from the surface. The resultant STM appearance is therefore a convolution of the real vertical step and the slope (curvature) of the tip. Real tips often have a second apex close to the endmost one as illustrated in Figure 2.9b. Such an occurrence is often termed a "double" tip, as it results in the imaging of features on the surface twice due to tunnelling from both apexes. As displayed in Figure 2.9b, if the tips are at different heights there is a shadow effect and the step edge in the example appears twice, at a reduced height and with a lateral displacement dependent on the relationship between the two tip apexes. As in Figure 2.9a, the step edge appears sloped in the STM image due to the finite curvature of the tips. A clear demonstration of such tip convolution effects is displayed in Figure 2.9c, an STM image of Au clusters on a CeO_2(111) island on Pt(111). The bright features on the island are approximately 0.2 nm tall at their maximum and display a clear motif that is repeated across the image and shown in more detail in the top right corner. Although convolution of this scale is readily apparent during scanning, it is not always so obvious and there are instances in the literature of works failing to account for such effects and drawing unsupportable conclusions based on such results.[33]

2.2 Low Energy Electron Diffraction (LEED)

The experiments of Clinton Davisson [34] and George Thomson [35–37] during the 1920s into the diffraction of electron beams by nickel and gold paved the way for an important technique

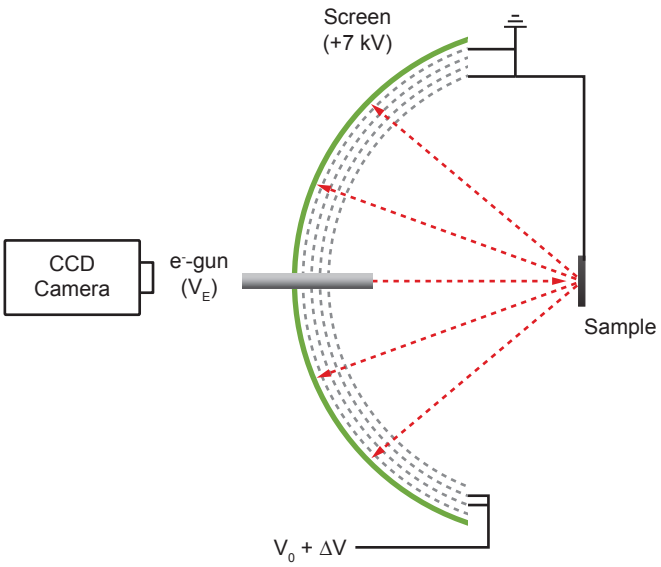

Figure 2.10: A diagram of a typical reverse-view LEED setup, highlighting the positions of the sample, electron gun, grids and phosphor screen as well the CCD camera.

for the study of the structure of surfaces. Low Energy Electron Diffraction (LEED) has proved to be a very useful tool for the elucidation of the structure of many surfaces, and Davisson and Thomson were honoured for their discoveries by their award of the Nobel Prize in Physics in 1937. The practical setup for a typical LEED experiment is illustrated in Figure 2.10. In LEED, a monochromatic electron beam of energy a few hundred eV, and current of $\sim 1\mu$A is incident on a grounded sample where it is diffracted by the crystal lattice. The diffracted beams travel through a number of grids to remove any inelastically scattered electrons and form a pattern on a phosphor screen whose spatial distribution reflects the underlying symmetry of the surface. LEED is a good demonstration of the wave-particle duality of electrons; at the energies normally employed, 20-200 eV, the electrons will have de Broglie wavelengths of between 2.74 Å and 0.87 Å as given by Equation 2.13. This is of the same order of magnitude as the interatomic spacing of the surfaces of many crystalline materials and hence are an excellent probe of structure on this scale.[38–40]

$$\lambda(\text{Å}) = \left(\frac{150.6\ \text{Å}^2\text{eV}}{E(\text{eV})}\right)^{\frac{1}{2}} \tag{2.13}$$

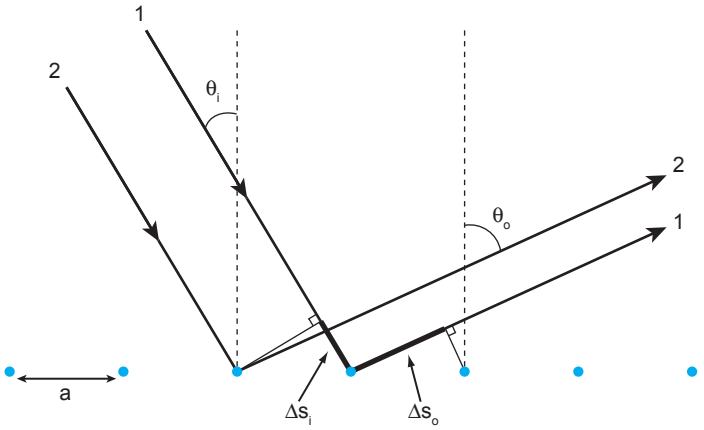

Figure 2.11: An illustration of diffraction from a 1-D lattice of atoms separated by a distance a. Two parallel incoming and outgoing beams are shown, at an incident angle of θ_i.

Figure 2.11 sets up the simple model of a line of atoms, separated by a distance a, to examine the conditions for Bragg diffraction by a periodic array. By considering two parallel incoming beams, it is seen that the path difference, Δs between the two is given by equation 2.14:

$$\Delta s = \Delta s_o - \Delta s_i = a(\sin\theta_o - \sin\theta_i) \tag{2.14}$$

The Bragg conditions for constructive interference are that this path difference is equal to an integer number of wavelengths and hence:

$$\Delta s = a(\sin\theta_o - \sin\theta_i) = n \cdot \lambda \tag{2.15}$$

$\therefore$

$$a\left(\frac{\sin\theta_o}{\lambda} - \frac{\sin\theta_i}{\lambda}\right) = n \tag{2.16}$$

Substituting in the projected wavevectors for the incoming and outgoing beam, $k_{\|i,o}$:

$$k_{\|i,o} = \frac{2\pi}{\lambda}\sin\theta_{i,o} \tag{2.17}$$

gives the following Bragg condition, with the result that the projected distance between diffraction spots in k-space is $a^* = \frac{2\pi}{a}$:

$$\begin{aligned} \Delta k_{\|} &= k_{\|i} - k_{\|o} \\ &= n \cdot \frac{2\pi}{\lambda} \\ &= n \cdot a^* \end{aligned} \tag{2.18}$$

This distance, a^*, is known as the reciprocal lattice vector and is inversely proportional to the lattice spacing of the periodic array. This simple 1-D example can be easily be extended to 2-D and allows us to see that by measurement of the diffraction pattern, the surface structure of a crystal lattice may be found. Modelling of LEED patterns from first principles, in combination with I-V LEED, where both the position and intensity of the diffraction peaks are measured at different beam energies; allows the precise determination of both the vertical and horizontal

arrangement of atoms in the first few atomic layers of a surface. In this work however, such investigations are not required.

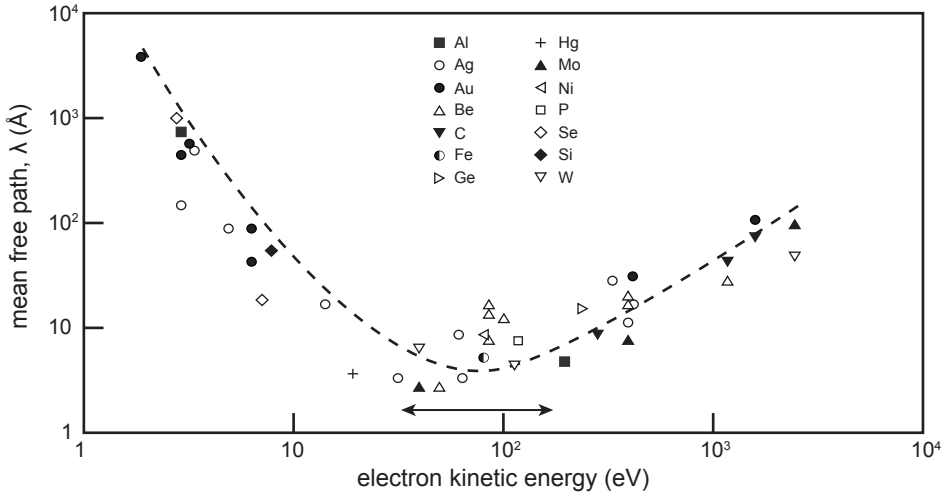

Figure 2.12: A plot of electron mean free paths versus energy for a selection of elements along with that calculated from theory (dashed line), illustrating the surface sensitivity inherent in using electrons with energies in the range 10-1000 eV such as for LEED and AES. Adapted from data in [41].

An important consideration for any technique involved in the study of surfaces is its sensitivity to the atoms in layers close to the surface. Electrons moving within a sample are susceptible to both elastic and inelastic scattering via a number of mechanisms, which leads to an attenuation length dependent on their energy. By examining the attenuation length for various energy electrons in a variety of materials, the plot shown in Figure 2.12 can be drawn up. We can see that for electrons in the range 10-1000 eV, which encompass those employed in LEED and Auger Electron Spectroscopy (AES), discussed later, the attenuation length less than 10 Å. This has the result that both techniques show a good degree of surface sensitivity as the probe electrons only travel a few atomic layers into the sample even with the incoming beam at normal incidence to the surface. By comparison, Reflection High Energy Electron Diffraction (RHEED) which employs electrons of energy of the order of keV and therefore have much longer attenuation lengths, must be carried out

at grazing incidence to the surface in order to attain the same degree of surface sensitivity.[38, 39]

2.3 Auger Electron Spectroscopy (AES)

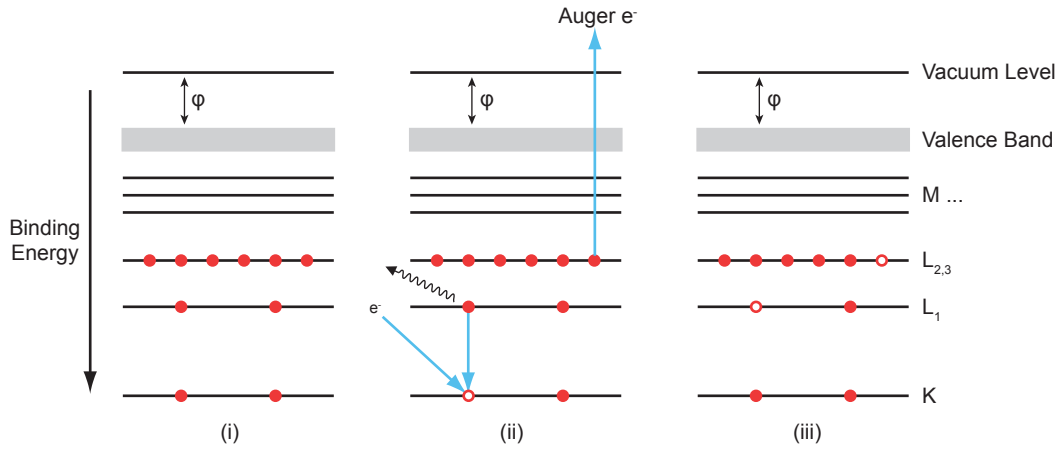

Figure 2.13: Energy level diagram of the Auger process showing (i) the initial state, (ii) the electron transitions, and (iii) the final state. In AES an incoming electron beam causes the emission of a core electron; the resultant hole is filled by an electron from a higher level, and an Auger electron is emitted. This emitted electron has an elementally specific energy that allows chemical identification of species on, or in the top few atomic layers of a sample surface.[42]

Auger Electron Spectroscopy (AES) discovered independently by Lise Meitner in 1923 [43, 44] and Pierre Auger in 1925 [45], is a widely implemented technique for determining the elemental composition of surfaces due to its relative ease of application and its sensitivity. An outline of the process is illustrated in Figure 2.13 where (i) and (iii) display the initial and final states of the system and (ii) describes the electron transition steps.[42] The first step in the Auger process is the emission of a core electron by an incident photon or electron, causing hole formation within an atom at, or near the surface. This is followed by autoionization where the vacancy is filled by an electron transition from a level with lower binding energy (down electron) as shown in Figure

2.13(ii). As a result of this there is a quantum of energy available, ΔE, equal to the difference in binding energies between the core hole and the down electron, which can be removed by a photon (X-ray fluorescence) or by transfer to a third electron (the Auger electron) which escapes into the vacuum with energy E_{kin} given by equation 2.19:

$$E_{kin} = E_k - E_{L_1} - E_{L_{2,3}} - \phi \tag{2.19}$$

Auger peaks are designated by the letters which describe the levels of the three electrons involved, in the example in Figure 2.13 for instance, the transition is termed $KL_1L_{2,3}$. As the energy of the Auger electron is dependent on the chemical structure of the atom it is elementally specific, and all elements with three or more electrons will have a characteristic spectrum. As shown in Figure 2.12, the energy of the electrons involved in AES are such that they have relatively short attenuation lengths and as such a high degree of surface sensitivity.[38]

Retarding Field Analysis

The detection method for AES used in this work was retarding field analysis (RFA) which has the great advantage of employing the LEED optics already present in most UHV systems for surface science studies.[38, 42] A schematic diagram of the LEED optics in this mode is presented in Figure 2.14. As with LEED, the inner and outer grids and the sample itself are all earthed to ensure that any electrons leaving the sample travel in a field free space and hence do not change their trajectories. In the Retarding Field Analysis (RFA) arrangement the screen acts as the current collector and the central (retarding) grids are used to form a band pass filter. A beam of electrons of energy E_p incident on a surface will result in an emitted electron energy distribution, $N(E)$,

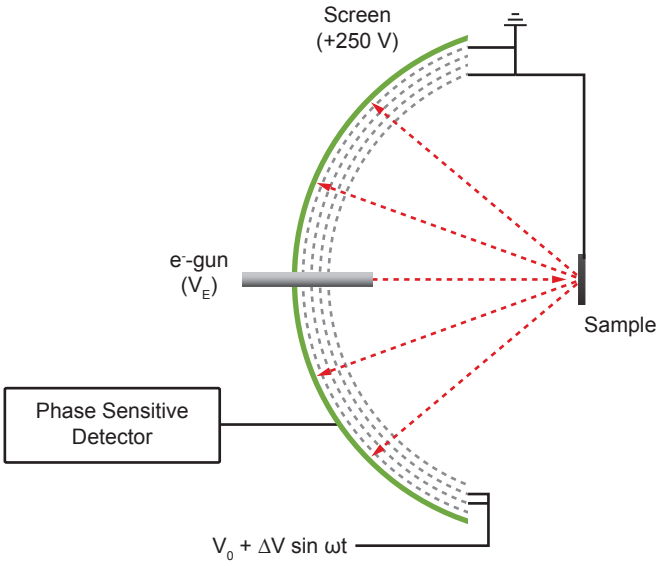

Figure 2.14: A diagram of a typical reverse-view LEED setup in use for AES using retarding field analysis (RFA). The inner grids form a band pass filter and the screen acts as the current collector attached to a phase sensitive detection system.

as seen schematically in Figure 2.15a. The large peak on the left is due to secondary electrons, the Auger peaks of interest are superimposed on this, but have a much smaller amplitude. The sharp peak at E_p is due to elastically scattered electrons. The current at the detector (screen) if the retarding grids are at a potential V_0, corresponding to a minimum pass energy $E_0 = eV_0$, is therefore $\int_{E_0}^{E_p} N(E)\,dE$. If this current is then differentiated, the signal will therefore be the energy distribution, as desired. Comparing the two cases where the retarding voltages are V_0 and $V_0 + \Delta V$ results in a difference between the collected currents of $\int_{E_0}^{E_0+\Delta E} N(E)\,dE$. If ΔE is small enough, this is equal to $\Delta E N(E_0)$ and therefore proportional to the required distribution as displayed in Figure 2.15b.

To improve the signal-to-noise characteristics of this method of signal detection, it is common to modulate the retarding voltage sinusoidally resulting in a voltage $V_0 + \Delta V \sin \omega t$. The screen current can then be expressed as a Taylor expansion as a sum of the DC term ($\int_{E_0}^{E_p} N(E)\,dE$) and the harmonics; $\sin(\omega t), \sin(2\omega t)$ etc. The first and second harmonics have amplitudes A_1 and

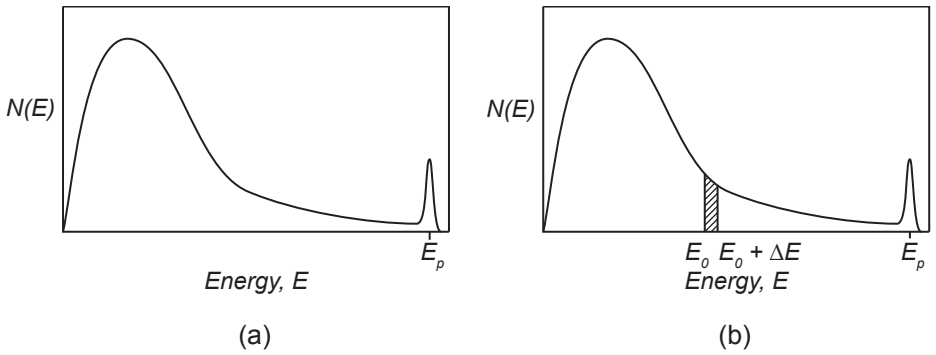

Figure 2.15: Illustration of the energy distribution ($N(E)$) of emitted electrons from a surface with an incident beam of electrons having energy E_p. In (b) the region shaded has an area of $\Delta E N(E_0)$, assuming a small enough value of ΔE. Adapted from [38].

A_2 respectively, given by:

$$A_1 = \Delta E N(E_0) + \frac{\Delta E^3}{8}\frac{dN^2}{d^2E}(E_0) + \frac{\Delta E^5}{192}\frac{dN^4}{d^4E}(E_0) + \cdots \tag{2.20}$$

$$A_2 = \frac{\Delta E^2}{4}\frac{dN}{dE}(E_0) + \frac{\Delta E^4}{48}\frac{dN^3}{d^3E}(E_0) + \frac{\Delta E^6}{1536}\frac{dN^5}{d^5E}(E_0) + \cdots \tag{2.21}$$

As long as ΔE remains small, the higher order terms can be neglected and hence, using a phase-sensitive technique employing a lock-in amplifier, the current at the screen will be proportional to the desired $\Delta E N(E_0)$. If the amplitude of the second harmonic (A_2) is measured using the lock-in to detect the signal at 2ω, the first differential of the energy distribution, $\frac{dN}{dE}(E)$ can be extracted.

The advantage of this approach is illustrated in Figure 2.16, as a small broad peak on a large constant background (a) is amplified and much more clearly defined once differentiated (b). This is of particular importance as many of the Auger peaks of interest are superimposed on a large background arising from secondary electrons undergoing other energy loss mechanisms. Also

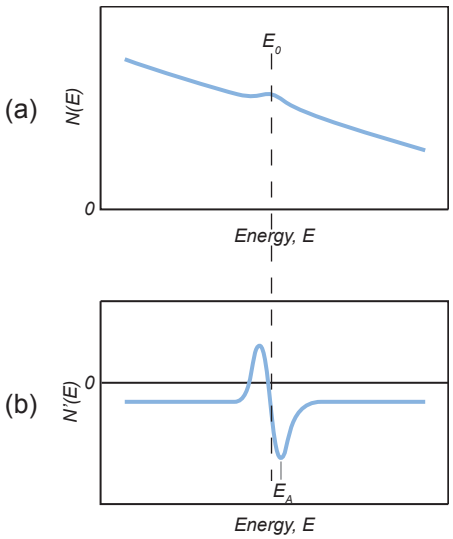

Figure 2.16: Schematic illustrating the effect of differentiating the AES signal to more clearly display those peaks that are superimposed on a large secondary electron background. The small peak in (a) is much easier to identify once the spectrum is differentiated (b).

shown in Figure 2.16 is the common practice of referencing the Auger line energy as E_A, the minimum of $N'(E)$, which of course corresponds to the maximum gradient of $N(E)$ rather than the maximum itself (E_0).[40]

References

[1] Binnig, G.; Rohrer, H.; Gerber, C.; Weibel, E. *Appl. Phys. Lett.* **1982**, *40*, 178–180.

[2] Binnig, G.; Rohrer, H.; Gerber, C.; Weibel, E. *Phys. Rev. Lett.* **1982**, *49*, 57–61.

[3] Wiesendanger, R. *Scanning Probe Microscopy and Spectroscopy: Methods and Applications;* Cambridge University Press, 1994.

[4] Bonnell, D. A. *Scanning probe microscopy and spectroscopy: Theory, techniques, and applications;* Viley-VCH, 2001.

[5] Eigler, D.; Schweizer, E. *Nature* **1990**, *344*, 524–526.

[6] Binnig, G.; Rohrer, H.; Gerber, C.; Weibel, E. *Phys. Rev. Lett.* **1983**, *50*, 120–123.

[7] Tersoff, J.; Hamann, D. *Phys. Rev. B* **1985**, *31*, 805–813.

[8] Tersoff, J.; Hamann, D. *Phys. Rev. Lett.* **1983**, *50*, 1998–2001.

[9] Chen, C. *Phys. Rev. Lett.* **1990**, *65*, 448–451.

[10] Lang, N. *Phys. Rev. Lett.* **1985**, *55*, 230–233.

[11] Lang, N. *Phys. Rev. Lett.* **1986**, *56*, 1164–1167.

[12] Lang, N. *Phys. Rev. B* **1986**, *34*, 5947–5950.

[13] Hamers, R. *Ann. Rev. Phys. Chem.* **1989**, *40*, 531–559.

[14] Bardeen, J. *Phys. Rev. Lett.* **1961**, *6*, 57–59.

[15] Wintterlin, J.; Wiechers, J.; Brune, H.; Gritsch, T. *Phys. Rev. Lett.* **1989**, *62*, 59–62.

[16] Lyo, I.; Avouris, P. *Science* **1991**, *253*, 173–176.

[17] Bikondoa, O.; Pang, C. L.; Ithnin, R.; Muryn, C. A.; Onishi, H.; Thornton, G. *Nat. Mat.* **2006**, *5*, 189–192.

[18] Nilius, N. *Surf. Sci. Rep.* **2009**, *64*, 595–659.

[19] Bonnell, D. *Prog. Surf. Sci.* **1998**, *57*, 187–252.

[20] Flores, F.; García, N. *Phys. Rev. B* **1984**, *30*, 2289–2291.

[21] Diebold, U. *Surf. Sci. Rep.* **2003**, *48*, 53–229.

[22] Esch, F.; Fabris, S.; Zhou, L.; Montini, T.; Africh, C.; Fornasiero, P.; Comelli, G.; Rosei, R. *Science* **2005**, *309*, 752–755.

[23] Norenberg, H.; Briggs, G. *Surf. Sci.* **1998**, *402*, 734–737.

[24] Castell, M.; Wincott, P.; Condon, N.; Muggelberg, C.; Thornton, G.; Dudarev, S.; Sutton, A.; Briggs, G. *Phys Rev B* **1997**, *55*, 7859–7863.

[25] Pang, C. L.; Lindsay, R.; Thornton, G. *Chem. Soc. Rev.* **2008**, *37*, 2328–2353.

[26] Wang, Y.; Meyer, B.; Yin, X.; Kunat, M.; Langenberg, D.; Traeger, F.; Birkner, A.; Wöll, C. *Phys. Rev. Lett.* **2005**, *95*, 266104.

[27] Bowker, M., Ed. *Scanning Tunneling Microscopy in Surface Science. Nanoscience and Catalysis;* Wiley VCH, 2010.

[28] Kresse, G.; Schmid, M.; Napetschnig, E.; Shishkin, M.; Kohler, L.; Varga, P. *Science* **2005**, *308*, 1440–1442.

[29] Nilius, N.; Kulawik, M.; Rust, H.-P.; Freund, H.-J. *Surf. Sci.* **2004**, *572*, 347–354.

[30] Zandvliet, H. J. W.; van Houselt, A. *Annu. Rev. Anal. Chem.* **2009**, *2*, 37–55.

[31] Wiesendanger, R. *Rev. Mod. Phys.* **2009**, *81*, 1495–1550.

[32] Ho, W. *J. Chem. Phys.* **2002**, *117*, 11033–11061.

[33] Humphrey, D. S.; Cabailh, G.; Pang, C. L.; Muryn, C. A.; Cavill, S. A.; Marchetto, H.; Potenza, A.; Dhesi, S. S.; Thornton, G. *Nano. Lett.* **2009**, *9*, 155–159.

[34] Davisson, C.; Germer, L. *Phys. Rev.* **1927**, *30*, 705–740.

[35] Thomson, G. *Proc. Roy. Soc. Lond. A* **1928**, *117*, 600–609.

[36] Thomson, G. *Proc. Roy. Soc. Lond. A* **1930**, *128*, 649–661.

[37] Thomson, G. *Proc. Roy. Soc. Lond. A* **1931**, *133*, 1–25.

[38] Woodruff, D. P.; Delchar, T. A. *Modern Techniques of Surface Science;* Cambridge University Press, 1994.

[39] Venables, J. A. *Introduction to Surface and Thin Film Processes;* Cambridge University Press, 2000.

[40] Oura, K.; Lifshits, V.; Saranin, A.; Zotov, A.; Katayama, M. *Surface Science. An Introduction;* Springer, 2003.

[41] Zangwill, A. *Physics at Surfaces;* Cambridge University Press, 1988.

[42] Briggs, D.; Seah, M. P. *Practical Surface Analysis: Auger and X-ray Photoelectron Spectroscopy;* Wiley-Blackwell, 1994.

[43] Meitner, L. *Z. Phys. A* **1923**, *5*, 54–66.

[44] Meitner, L. *Z. Phys. A* **1923**, *5*, 307–312.

[45] Auger, P. *Journal de Physique* **1925**, *6*, 205–208.

CHAPTER 3

INSTRUMENTATION

Abstract

The instrumentation used in experimental science is crucial for the acquisition of accurate and reliable results, especially in the case of the advanced techniques described in the previous chapter. Whereas chapter two examined these techniques from a theoretical perspective, this section aims to discuss the practical aspects of their implementation, focussing primarily on the scanning probe microscopes (SPM) and their operation, but also examining the peripheral instruments used for sample preparation and analysis. The experiments were all carried out under Ultra High Vacuum (UHV) and the various systems used to obtain these conditions will also be detailed.

3.1 The UHV Systems

A key requirement for studying reactive surfaces and systems at the atomic scale is an extreme degree of cleanliness and therefore this work was carried out at UHV, commonly defined as a pressure lower than 1×10^{-10} mbar. By applying simple kinetic theory we are able to make an estimate of the monolayer (ML) arrival time that demonstrates why such low pressures are necessary. Taking the example system of CO on Ag(111); a ML might be defined as $\sim 1 \times 10^{19}$ atoms m^{-2} leading to an arrival time of $\sim$10 hours at a CO pressure of 1×10^{-10} mbar, assuming unity sticking probability.[1, 2] Such an estimate, although rough and for a very specific instance, nonetheless demonstrates the need for such conditions to provide a reasonable time period in which to perform the desired experiments. To achieve these low pressures and a clean environment, a relatively complex UHV system must be employed with certain specialised features as described in the following pages.

The instruments used in this work are contained within the two UHV systems photographed in Figures 3.1 and 3.2. Both systems are composed of two main UHV chambers; the STM and other characterisation instrumentation (LEED/AES) are contained within an Analysis Chamber (left), and the sample preparation facilities in a Preparation Chamber (right). In each system the two chambers are isolated from each other by a manual gate valve, which permits the higher pressures required for sample preparation to be used without unnecessary contamination of the analysis chamber.

In order to reach UHV, a series of pumps are used to sequentially reduce the pressure. In the first instance rotary (positive displacement) pumps act as backing pumps for turbo-molecular (kinetic)

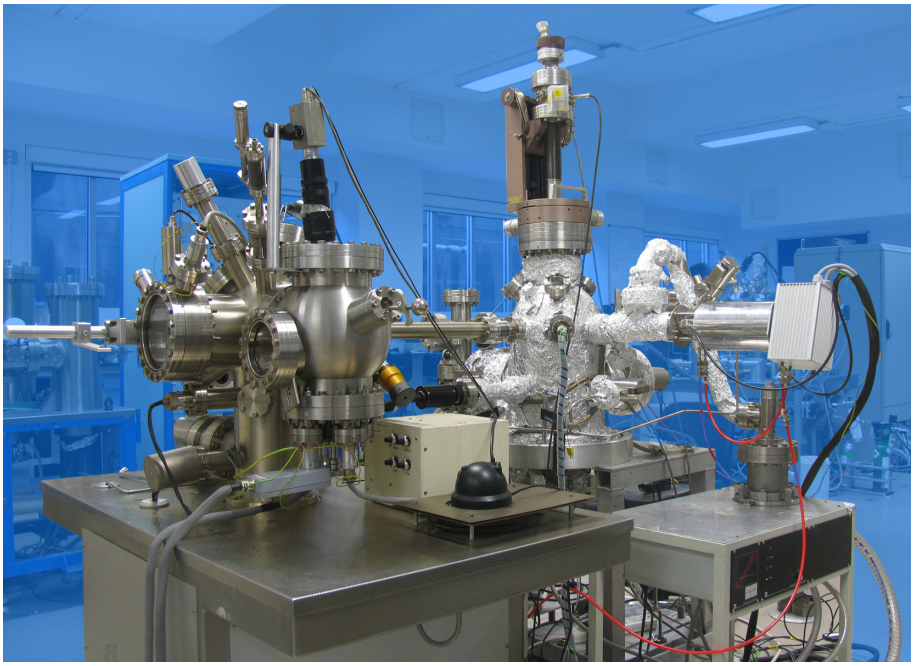

Figure 3.1: Photograph of the *Omicron* UHV AFM/STM system with separate vacuum chambers for sample preparation (right) and analysis (left).

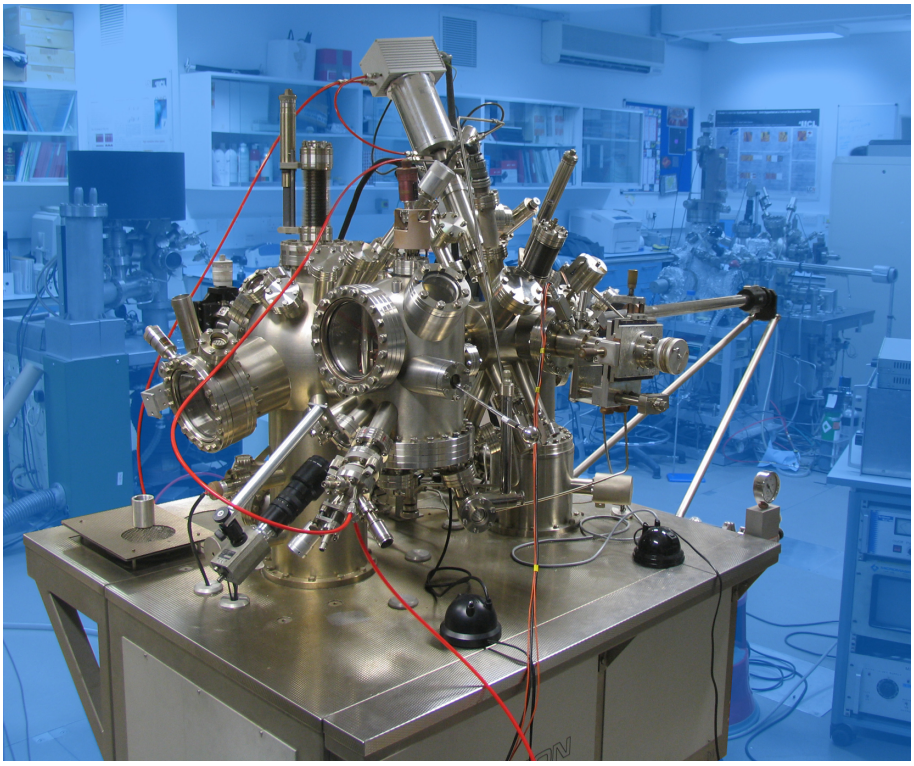

Figure 3.2: Photograph of the *Omicron* UHV VT-STM system with separate vacuum chambers for sample preparation (back) and analysis (front).

pumps attached to each chamber. These turbo-pumps handle the high gas loads encountered when bringing the system down from atmospheric pressure as well as during operations such as sputtering or oxidation when there is a significant volume of gas requiring removal from the system. To bring the pressure into the UHV domain it is necessary to bake the entire system at $\sim$400 K for $\sim$24 hours to remove gas molecules, predominantly water and hydrocarbons, that are adsorbed on the inner surfaces of the chamber. After baking, ion getter pumps and titanium sublimation pumps (TSP) are used to enable true UHV conditions to be realised. A gas line system is also present on both systems allowing high purity gases to be introduced via high precision leak valves.

To facilitate the transfer of samples and tips to and from the vacuum systems without breaking the UHV conditions, each system is equipped with a fast entry loadlock (FEL) pumped by the a turbo-pump. A chilled water system is present in the laboratory to allow cooling of the turbo-pumps, atom source, and metal evaporators. Monitoring of the extremely low residual gas pressures is achieved using Bayard-Alpert type hot-cathode ionisation gauges in each chamber which allow measurements in the range 10^{-4} to 10^{-11} mbar. For higher pressures such as in the backing lines of the turbo-pumps, Pirani gauges are employed allowing measurements down to 10^{-2} mbar. Figure 3.3 is a schematic overview of the two UHV systems showing the vacuum chambers and also the location and geometry of the various devices used for sample preparation and analysis.

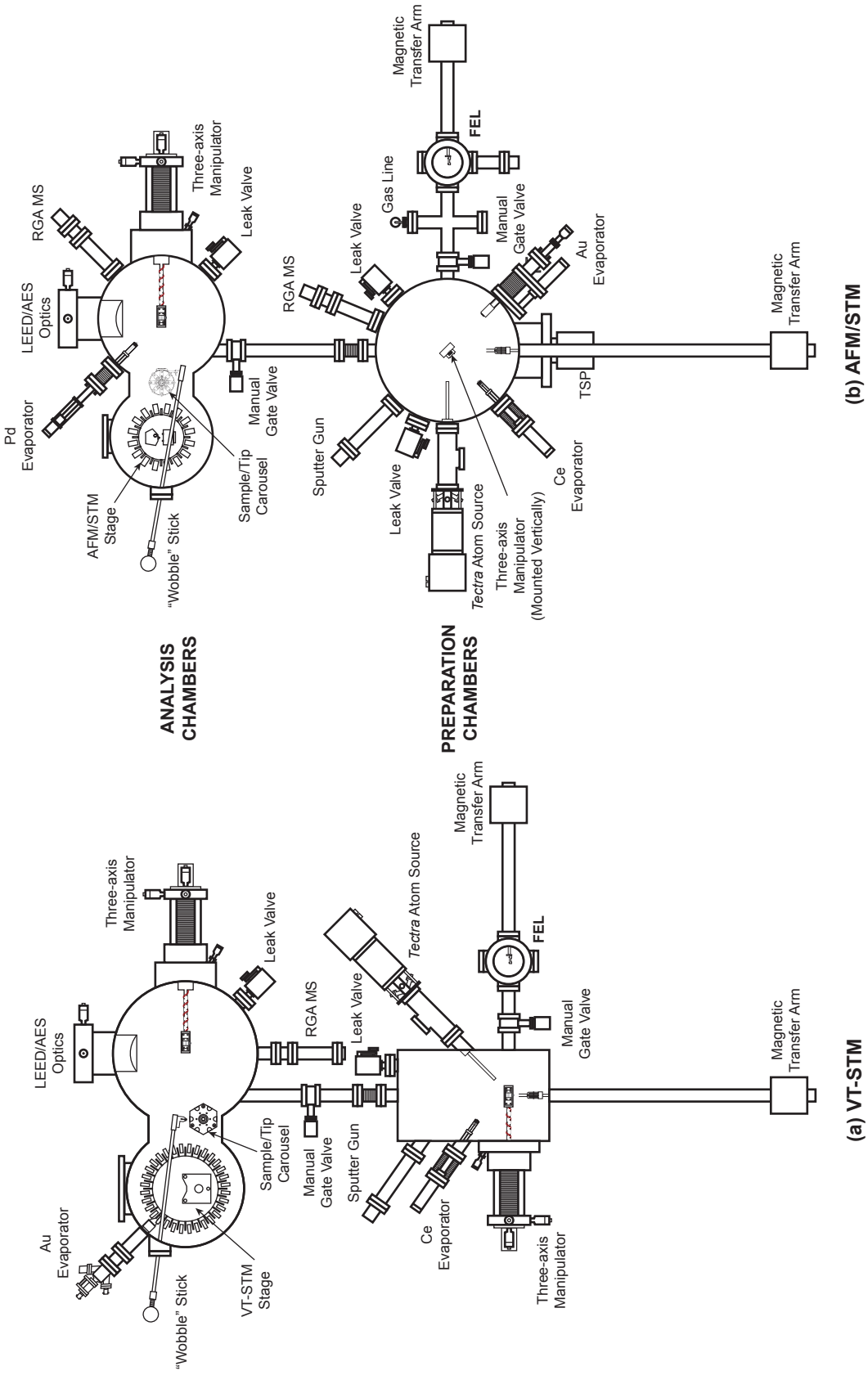

Figure 3.3: UHV system overview diagram showing the location and geometry of the principal sample preparation and analysis devices.

3.2 The Scanning Probe Microscopes

The experiments in this work were carried out using two scanning probe microscopes. The first was an *Omicron* UHV AFM/STM which is capable of acting both as a scanning tunnelling microscope (STM) and also a non-contact atomic force microscope (NC-AFM) permitting atomic resolution studies of both conducting and insulating substrates at room temperature. The second microscope was an *Omicron* UHV variable temperature scanning tunnelling microscope (VT-STM) capable of operation at sample temperatures between 25-1500 K as well as in-situ dosing.[3] Photographs of the AFM/STM (a) and VT-STM (b) stages are presented in Figure 3.4 showing the locations of the sample holders and tips for both instruments.

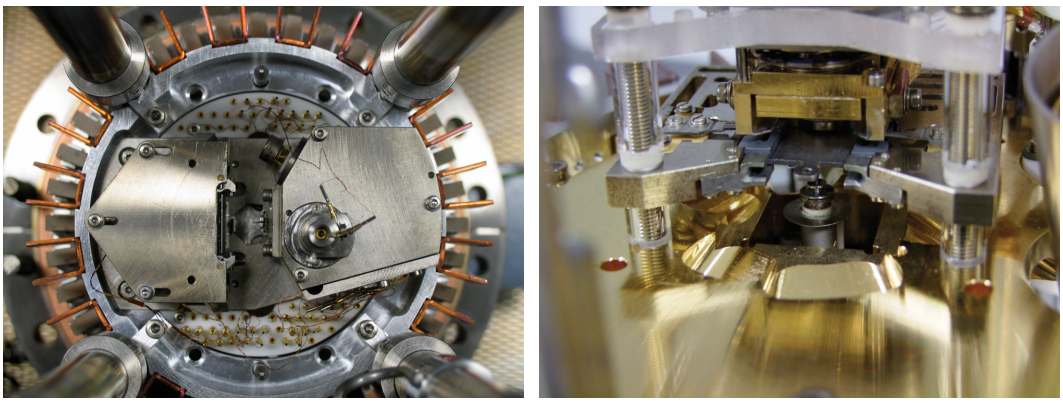

(a) (b)

Figure 3.4: The STM sample stages of the microscopes used in this study (a) Top view of the AFM/STM; the tip is on the right hand side, and the copper fins and magnets of the eddy-current damping system are clearly visible (b) Side view of the VT-STM; the tip is pointing upwards, the evaporants during in-situ dosing travel through the channel visible on the base of the stage.

3.2.1 Microscope Operation

The VT-STM and AFM/STM have slightly different operating methods during scanning. In the case of the AFM/STM the tip is kept stationary whilst the sample is moved, contrasting with the VT-STM where the sample position is fixed and the tip moved, a result of the complex optical detection system required for AFM operation. To position and move the sample with sufficient precision to achieve atomic resolution imaging, the sample plate holder (or tip) is mounted on a piezoelectric drive. This drive permits motion in the z direction (towards the tip) for coarse approach on the millimetre scale using a slip-stick inertial mechanism, as well as fine movement on the sub-Å scale required during scanning. The piezoelectric tube also provides motion in the x and y directions during image acquisition allowing a raster scan to be built-up. A typical image consists of a 400×400 point scan which provides a good level of detail without requiring an excessively long acquisition time (typical scan rates are a couple of lines per second).

To allow optimal imaging the microscope stages are carefully designed to minimise the effects of vibrations and thermal drift. The stages are suspended by thin vertical springs, and copper fins on the base are positioned within permanent magnets for eddy-current damping. Vibrations are further minimised by mounting the UHV systems on active vibration dampers (*Halcyonics*) and by isolation of the analysis and preparation chambers from each other by sections of edge-welded bellows. Careful design of individual components of the microscopes to have high resonant frequencies serves to lessen their susceptibility to low frequency noise from the building and local environment. Both systems are located in the basement to reduce the magnitude of any building noise, and all mechanical sources of noise such as rotary pumps and water chillers are situated outside of the laboratory. In order to minimise thermal drift, the SPMs are constructed

from materials with matching thermal expansion coefficients, and there is climate control within the laboratory to provide good temperature stability of the surrounding environment. During microscope operation it is also standard procedure to cover the viewports of the UHV chambers in order to lessen the effects of drift caused by infra-red radiation from the lighting within the lab or sunlight.

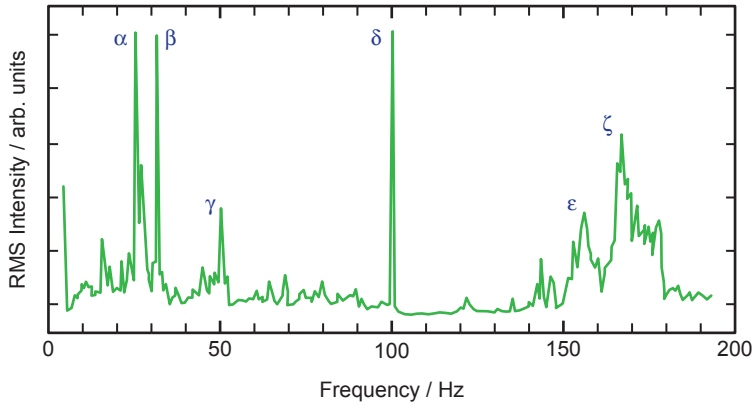

Figure 3.5: A power spectrum of the vibrational noise present during AFM/STM operation obtained using an accelerometer (*Wilcoxon*) bolted to the STM chamber and detected with a spectral analyser (*Hewlett Packard*).

As part of the recommissioning and testing of the AFM/STM, vibration measurements were conducted within the laboratory to identify sources of noise and eliminate them where possible. A typical power spectrum of the noise is displayed in figure 3.5 obtained using a piezoelectric accelerometer (*Wilcoxon*) bolted to the AFM/STM chamber with a spectral analyser (*Hewlett Packard*) as the detector. The primary peaks have the following frequencies $\alpha = 25$ Hz, $\beta = 32$ Hz, $\gamma = 50$ Hz, $\delta = 100$ Hz, $\epsilon = 157$ Hz, $\zeta = 168$ Hz, which correspond to a variety of sources of noise. The peaks at 50 and 100 Hz (γ and δ) were mainly derived from mains-powered rotary pumps in the adjacent room but did not have a great effect on STM performance. On some occasions however, noise at the frequencies of ϵ and ζ were observed in STM images and

after a thorough search the source was found to be the chilled water recirculator used to cool the turbomolecular pumps. The addition of a longer length of flexible hose between the copper water pipes and these pumps removed the majority of these vibrations. The source of the vibrations leading to the peaks at α and β was not found, however the insertion of a section of edge-welded bellows between the preparation and analysis chambers of the AFM/STM led to a significant reduction in their intensity and they did not cause any problems during STM operation.

3.2.2 Scanning Tunnelling Microscope Modes

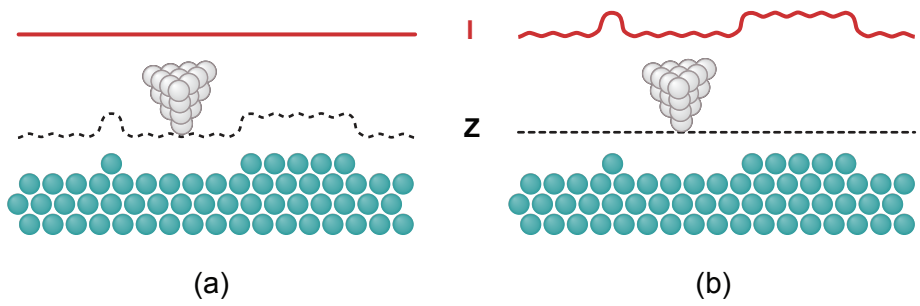

Figure 3.6: The operational modes of STM: (a) Constant current mode, where the tip-sample separation (Z) is adjusted during scanning to keep the tunnelling current (I) constant and hence form an image of the surface. (b) Constant height mode, where the tip is scanned across the surface at a uniform height and the tunnelling current is monitored to form the image.

The two common modes of operating the STM are shown schematically in Figure 3.6: (a) constant current and (b) constant height. In constant current topography mode (CCT) (Figure 3.6a) the tip-sample separation is adjusted by the z-piezo during the course of a scan in order to keep the tunnelling current constant. This is achieved by the feedback loop system as detailed in Figure 3.7. In constant height mode, the tip is rastered across the surface at a set height as depicted in Figure 3.6b, and the image is formed by the variation in the tunnelling current. The main

advantage of this mode of operation is its speed since it is not limited by the response time of the feedback loop, however it is only suitable for use on atomically smooth surfaces or the tip is likely to crash into the surface. Due to this limitation this mode is not really suitable for imaging the surfaces of interest for this work where there is a significant height variation (a few nm) across the samples.

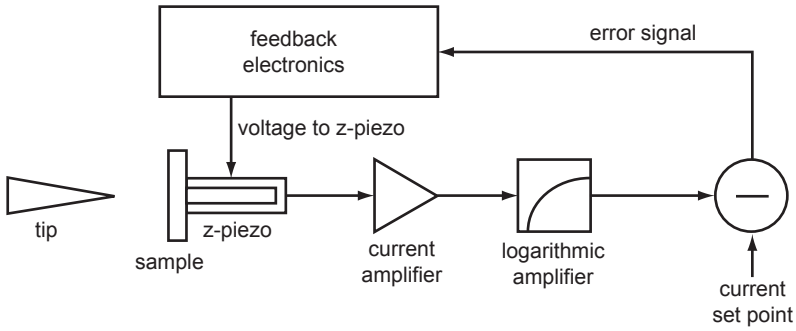

Figure 3.7: Block diagram of the constant current mode feedback system.[3]

3.2.3 Tip Fabrication

A prerequisite for atomic resolution scanning probe microscopy is the fabrication of a sharp, stable tip. The STM tips for all the work in this study were prepared in the laboratory via electrochemical etching of tungsten wire or manual cutting of platinum-iridium alloy wire (80% Pt, 20% Ir) according to well-documented methods.[4–6] Two techniques were employed for etching: the plate and immersion methods, which are shown schematically in Figure 3.8. The first of these is accomplished as shown in Figure 3.8a with a metal plate acting as the cathode and the W wire as the anode, and a small volume of 2 M NaOH held in place by surface tension. A low voltage ($\sim$2 V DC) is applied across the solution and etching occurs according to equation

3.1.[5] When the tungsten becomes very thin as a result of the etching, the weight of the wire below pulls it into a narrow neck and it fractures leaving a sharp point suitable for STM.

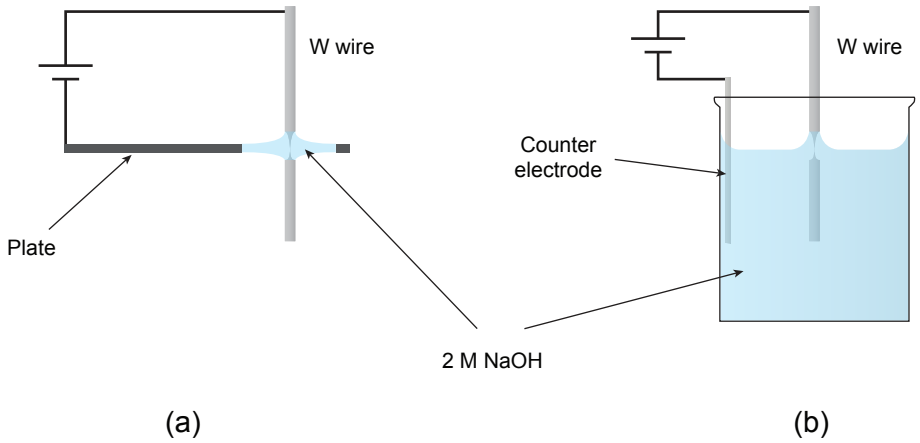

Figure 3.8: Diagram of the two etching methods used to fabricate STM tips for this work. (a) the plate method (b) the immersion method.

$$\mathrm{W_{(s)} + 2\,OH^- + 2\,H_2O \longrightarrow WO_4^{2-} + 3\,H_{2(g)}} \tag{3.1}$$

The immersion method is shown schematically in Figure 3.8b; for this a length of tungsten wire is dipped into a small beaker of the etching solution and etching occurs at the liquid-air interface. The etching current is monitored electronically so that when it drops below a certain level the etching finishes, yielding a sharp tip. To enable more reproducible fabrication of tips, a device was designed and built to allow both of the methods detailed above to be used. It allows a fine degree of control over the height of the tip and facile attachment of tip-holders designed for the *Omicron* AFM/STM as well as for *Omicron* Variable Temperature (VT) and Low Temperature (LT) STMs. Figure 3.9 shows the design plan and a photograph of the finished device.

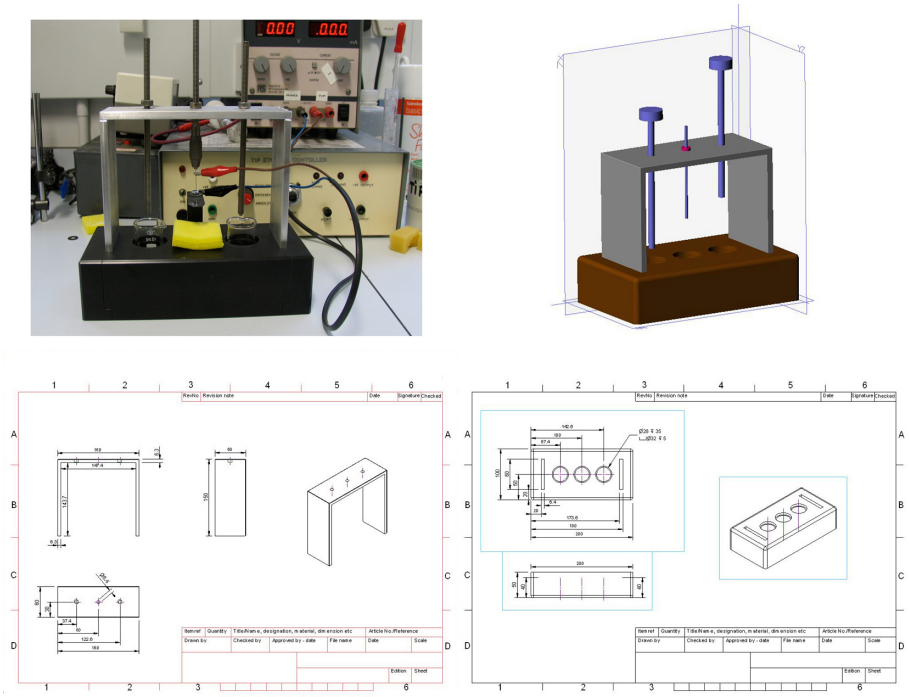

Figure 3.9: Photograph and design drawings of the tip-etching apparatus constructed to allow reproducible electrochemical etching of STM tips.

After etching, the tips are inspected with an optical microscope, washed thoroughly in distilled water and isopropanol to remove any etching solution, and transferred into the UHV system via the FEL. In-vacuum treatment of the tips include annealing at 450 K to remove contaminants and argon ion sputtering to remove tungsten oxide from the tip apex that may induce instability during scanning. In addition to this, during the course of STM operation, voltage pulses of up to 10 V are applied to tips to remove any contaminants or molecules that may have been picked up from the sample surface to permit stable atomic resolution scanning.

3.3 Sample Preparation

3.3.1 Argon Ion Bombardment

A common method of removing surface contaminants is by inert ion bombardment, or sputtering, normally with argon.[1, 2] This is achieved by the formation of a beam of ions from an ion gun (location within chamber displayed in Figure 3.3) which is incident at a variable angle to the sample. Inside the gun a hot filament emits electrons (25 mA) forming a plasma of Ar^+ ions when a high pressure of gas ($\sim 10^{-5}$ mbar) is introduced. An ion beam with energy 500-1500 eV is extracted through a lens system and focussed onto the sample where its kinetic energy is transferred to atoms at the surface, removing them and leaving a roughened surface. To smooth this surface and remove any embedded argon, the sample is annealed at high temperature in UHV. In practice, the most reliable cleaning of the Pt(111) surface used as a support for the ultrathin ceria films was obtained when the argon ion beam was directed at alternate grazing angles to the sample surface during sputtering cycles.

3.3.2 Sample Heating and Manipulation

The samples used in this study were attached to *Omicron* sample plates either with spot-welded tantalum clips or molybdenum clips fixed with bolts as depicted in Figure 3.10. The method of sample mounting with bolts was a departure from the standard of spot-welded Ta clips due to problems encountered during annealing of the Pt(111) crystal, which led to weakening of the spot-welds and caused noise during STM experiments from the resultant loose sample. As shown

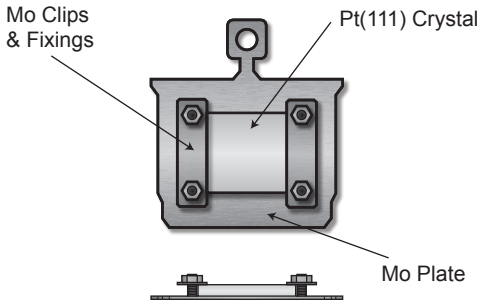

Figure 3.10: Diagram showing the mounting method of the Pt(111) crystal onto a standard Omicron sample plate.

in Figure 3.3, these plates are moved around the system by magnetic transfer arms. In each UHV chamber there is a sample manipulator that allows movement in all three axes, as well as 360° rotation. From the manipulator in the analysis chamber the sample plate can be moved either into an 8-position carousel for temporary storage or into the microscope stage with the use of a pincer grip "wobble stick". The manipulators in both UHV systems have provision for sample heating via electron bombardment (e-beam heating) up to ∼1500 K. For this method of heating electrons are emitted from a hot tungsten filament by thermionic emission and bombard the back of the sample plate which is held at a high positive bias. The temperature of the sample is monitored with a chromel-alumel thermocouple and an infrared pyrometer.

3.3.3 Metal Evaporation

An important requirement for this work is the ability to deposit metals under UHV conditions onto surfaces of interest. Physical vapour deposition (PVD) was employed to this end by heating the desired metal in an appropriate manner until sublimation was achieved. In the case of the cerium required for formation of the ultrathin films a homemade electron-beam evaporator was constructed as displayed in Figure 3.11.

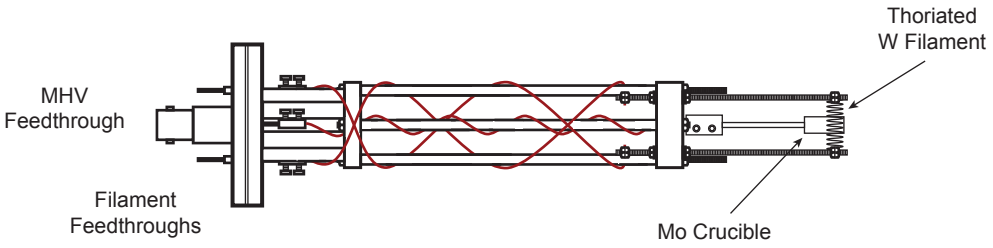

Figure 3.11: Schematic of the electron-beam evaporator constructed for PVD of cerium to form ultrathin ceria films.

In the doser, Ce metal foil (99.9%, *Advent RM*) is contained within a molybdenum crucible that is held at high positive bias relative to an earthed thoriated tungsten filament. When this filament is heated, thermionic emission occurs and electrons are accelerated towards the crucible leading to e-beam heating to ∼1500 K, sufficient to evaporate Ce. A quirk of the particular doser used was that in order to initiate stable emission from the filament, a small amount of cerium had first to be evaporated onto it. This was achieved by using a higher filament current than usual for a few seconds before dropping down to the standard dosing settings.

To evaporate gold onto the surface of the ultra-thin ceria films, two commercial evaporators were employed, schematics of which are displayed in Figure 3.12: (a) Compact Vapour Source (J. Taylor & C. Nicklin) (b) *Omicron* EFM-3. The principle of operation of the compact vapour source is slightly different to that of the e-beam evaporator used for cerium. Au wire (99.9%, Advent RM), is contained within an alumina crucible that is heated resistively up to a temperature of ∼1200 K. Other important features include water cooling, a shutter mechanism to allow precise dose timing, and a k-type thermocouple to accurately determine the temperature of the crucible. The EFM-3 is an e-beam evaporator where the Au wire is contained within a Mo crucible that is water cooled and also has a flux monitor attached to allow fine control of the evaporation rate.

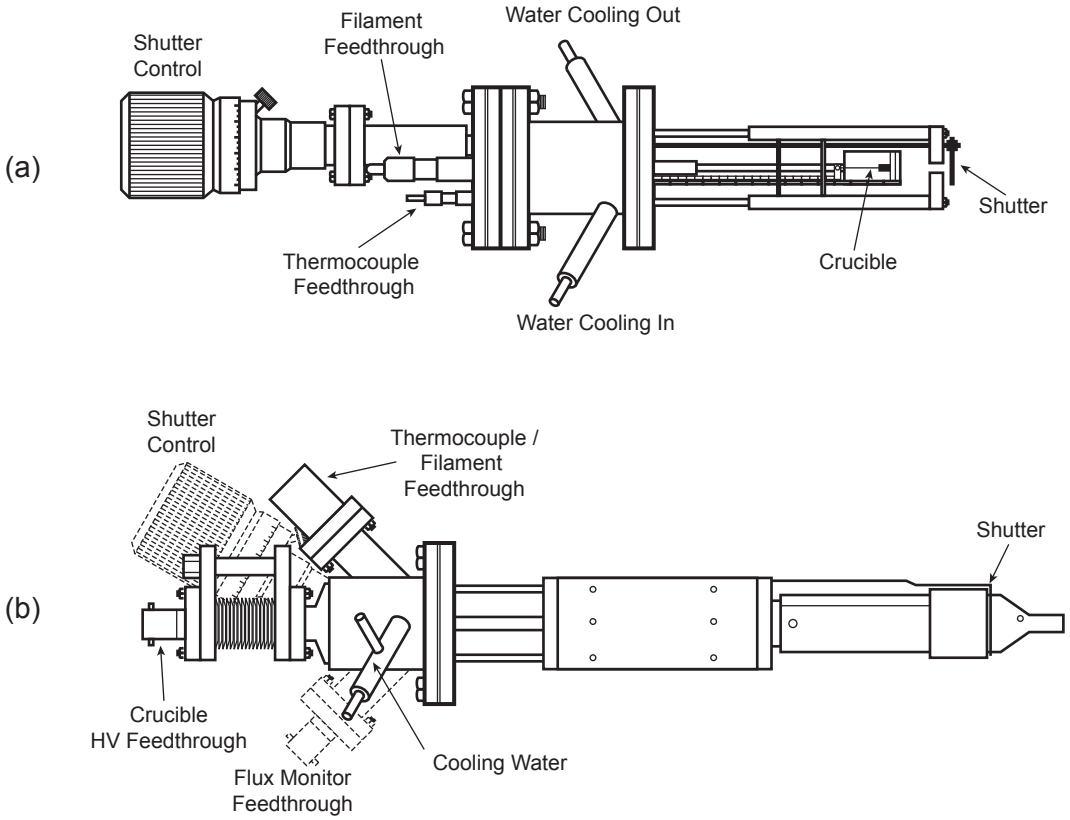

Figure 3.12: Schematic of the evaporators used for gold deposition onto the thin films: (a) Compact Vapour Source, J. Taylor & C. Nicklin (b) *Omicron* EFM-3.

3.3.4 Atomic Oxygen Source

In the majority of the experiments the oxidation steps in the formation of ultrathin ceria films were carried out using molecular oxygen (O_2) leaked into the vacuum chamber. To provide a greater degree of control over this process, atomic oxygen was employed, generated by a commercial atom source (*Tectra IonEtch*). A schematic of the device is shown in Figure 3.13 with its primary features labelled.

To form the beam of atoms, microwaves are used to generate a plasma within the required gas from which the excited atoms are extracted and travel towards the sample. A magnetron produces microwaves with wavelength 2.45 GHz, which are guided via a resonant coupler into the vacuum

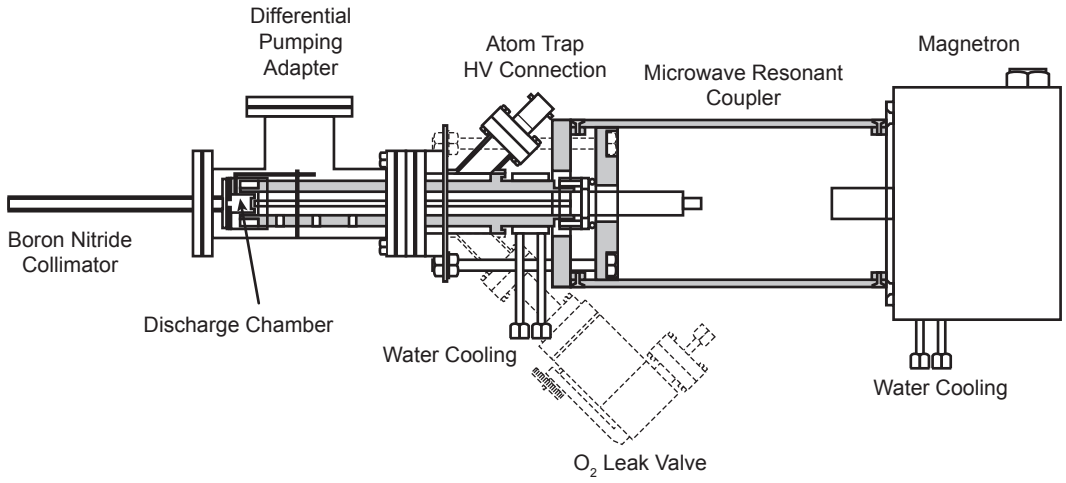

Figure 3.13: Schematic of the atom source (*Tectra IonEtch*) used to supply atomic oxygen for the oxidation of ceria ultrathin films.

chamber to a boron nitride plasma chamber where the high purity oxygen is excited and a plasma is formed. The discharge chamber is surrounded by permanent magnets which create an axial magnetic field of 87 mT, under which electrons in the microwave field undergo Electron Cyclotron Resonance (ECR), greatly enhancing their path length. This increases the probability of ionisation of more gas molecules within the chamber, and hence leads to an enhancement of the plasma density. A low-conductance boron nitride (BN) aperture at the end of the discharge chamber allows a small flux of the excited atoms out into the main vacuum chamber, with only a low residual ion current. To minimise this current further, metal plates held at high negative and positive biases surround the aperture and act as an ion trap.[7] Reasonably high pressures ($\sim 10^{-5}$ mbar) are required to sustain a plasma within the source and as a result it is necessary to employ a differential pumping stage to keep the chamber pressure around 10^{-7} mbar. A turbo-molecular pump provides this differential pumping, and is connected via an all-metal valve to the atom source.

3.4 Auxiliary Analytical Techniques

3.4.1 Low Energy Electron Diffraction (LEED)

In this work LEED is employed to check the long-range order of the surface and monitor the formation of thin films and ordered adsorbate overlayers. A sharp, intense diffraction pattern with a low background was taken to show that the surface was well-ordered and suitable for investigation by SPM. A rear view LEED optics (*Omicron*) is located in the analysis chamber as shown in Figure 3.3 and consists of a four grid system with an integral electron gun. In this system, depicted schematically in Figure 3.14a, the electron gun produces a monochromatic beam with energy in the range 30-300 eV, which is incident upon the earthed sample. The diffracted electrons then travel through the four grids toward a phosphor screen. The inner and outer grids are earthed to create a "field free region" for the scattered electrons to travel through. The middle pair of grids are at a negative potential $V = -E_p + \Delta V$, where E_p is the energy of the incident beam, and ΔV is in the range $0 - 10$ V. This forms a filter that ensures only elastically scattered electrons pass through and are accelerated to the phosphor screen (floating at 7 kV) where they cause bright spots on a dark background.[8] Images of these patterns are recorded using a digital camera and processed using conventional image analysis software (*Adobe Photoshop*).

3.4.2 Auger Electron Spectroscopy (AES)

The LEED optics were used in retarding field analyser (RFA) mode to perform Auger Electron Spectroscopy (AES) during the course of this work. This arrangement is displayed in Figure

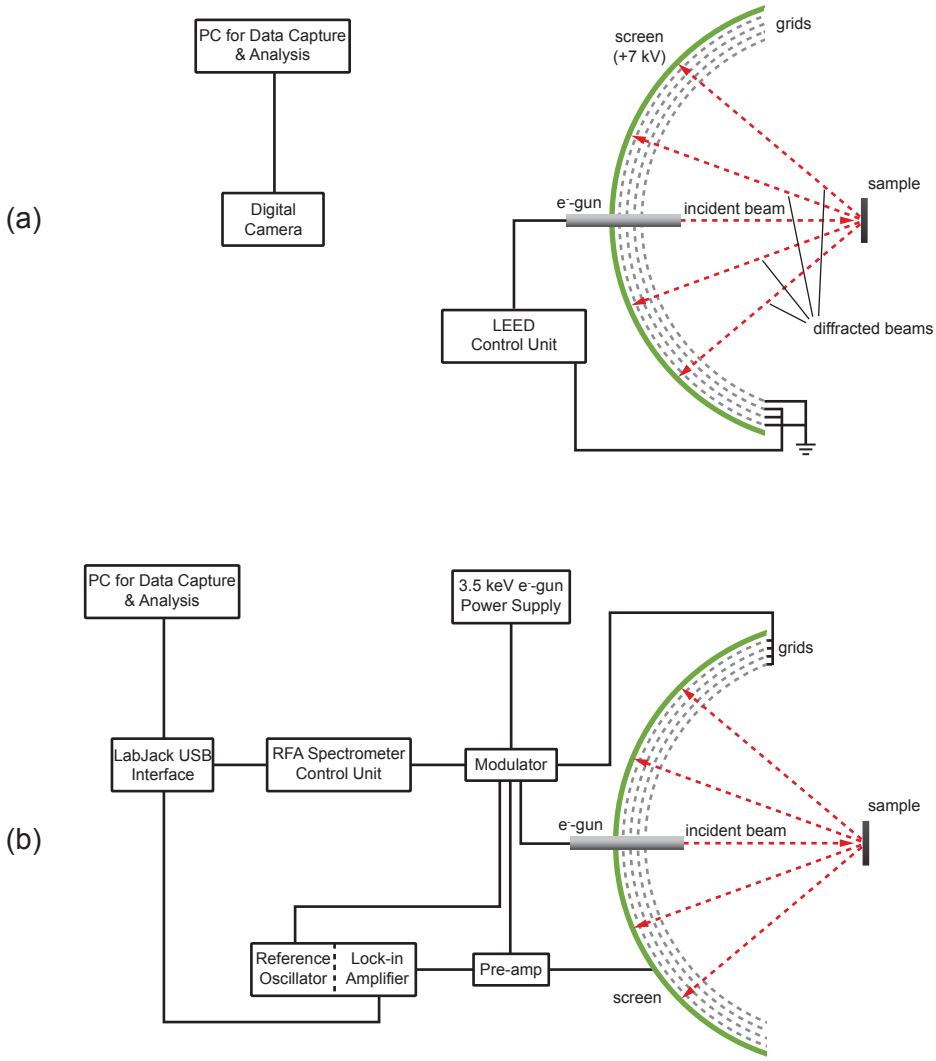

Figure 3.14: Schematic depicting the LEED optics and electronics for (a) LEED (b) AES in RFA mode.

3.14b, and has the primary advantage of not requiring a complex additional detection system, with the trade-off of a slightly poorer signal-to-noise ratio.[8, 9] To employ RFA, a modulating voltage is applied to the central grids of the LEED optics as described in the previous chapter and a lock-in amplifier provides the phase-sensitive detection to retrieve the Auger spectra in derivative mode. The primary function of AES in this work was the detection of surface contaminants and monitoring the growth and purity of the ultra-thin films.

3.4.3 Quadrupole Mass Spectrometry

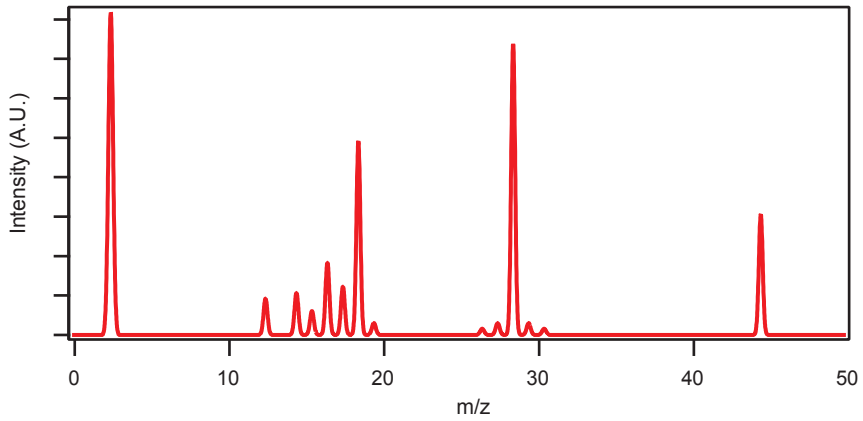

Figure 3.15: A typical RGA Mass Spectrum from a clean UHV chamber used in this work with pressure $\sim 10^{-10}$ mbar, the primary peaks of interest are those at m/z = 18, 28 and 44 from H_2O, CO/N_2, and CO_2 respectively.

As shown in Figure 3.3, a quadrupole mass spectrometer (QMS) (*Vacuum Generators*) is located in both analysis and preparation chambers. This is used to check the purity of the argon and oxygen for sputtering and oxidation processes as well as for leak checking the chamber using helium detection. A typical residual gas analysis (RGA) mass spectrum of a clean UHV chamber with pressure $\sim 10^{-10}$ mbar is displayed in Figure 3.15 with peaks for H_2 (m/z = 2), C (12), N (14), CH_4 (16), H_2O (18), CO & N_2 (28), CO_2 (44).

References

[1] Woodruff, D. P.; Delchar, T. A. *Modern Techniques of Surface Science;* Cambridge University Press, 1994.

[2] Venables, J. A. *Introduction to Surface and Thin Film Processes;* Cambridge University Press, 2000.

[3] Omicron. *VT-STM User's Guide;* Omicron Nanotechnology, 1994.

[4] Melmed, A. *J. Vac. Sci. Technol. A* **1991**, *9*, 601–608.

[5] Ibe, J.; Bey, P.; Brandow, S.; Brizzolara, R.; Burnham, N.; Dilella, D.; Lee, K.; Marrian, C.; Colton, R. *J. Vac. Sci. Technol. A* **1990**, *8*, 3570–3575.

[6] Yu, Z.; Wang, C.; Du, Y.; Thevuthasan, S.; Lyubinetsky, I. *Ultramicroscopy* **2008**, *108*, 873–877.

[7] Tectra. *IonEtch Operating Manual;* Tectra, 2001.

[8] Omicron. *SPECTALEED Optics and Electron Gun User's Guide;* Omicron Nanotechnology, 1995.

[9] Omicron. *Instruction Manual: RGLC Spectrometer Control;* Omicron Nanotechnology, 1996.

CHAPTER 4

GROWTH AND CHARACTERISATION OF ULTRATHIN CeO_2(111) FILMS ON Pt(111)

Abstract

The structure and growth of ultrathin films of CeO_2(111) supported on Pt(111) has been studied with Scanning Tunnelling Microscopy (STM), Low Energy Electron Diffraction (LEED) and Auger Electron Spectroscopy (AES). The ultrathin films were grown in two ways: by reactive deposition, and by post-oxidation of Ce/Pt surface alloys. Both molecular and atomic oxygen were employed as oxidants and the results compared to develop a repeatable recipe for films suitable for high-resolution studies. The growth mechanism, electronic-structure, and domain boundaries of these films were investigated using STM and STS. In addition, atomically resolved

STM images (filled and empty states) have been obtained on these ultrathin films and the results compared with previously reported high-temperature STM and non-contact atomic force microscopy (NC-AFM) images of the native CeO_2(111) surface. The similarity between these images is striking and allows a number of defects and adsorbates observed in our ultrathin film to be assigned. Moreover, the similarity in structure between the native oxide and the ceria ultrathin film indicates that it is an excellent topographic mimic of the native oxide.

Part of this work has been published in [1] and [2]

4.1 Introduction

The study of ceria (CeO_2) is currently of great interest, with proven technological applications arising from its wide-ranging catalytic properties. Some of its more important uses have been in exhaust gas purification in automotive catalytic converters and in the water gas shift reaction to produce H_2.[3–5] The key to these properties lies in the high mobility of lattice oxygen leading to excellent oxygen storage and release, as well as the promotion of noble metal activity.[6] Both aspects are thought to be determined by the nature, concentration and mobility of lattice defects, especially oxygen vacancies. It is well known that the defect structure of transition metal oxide surfaces is key to their reactive behaviour. For rare-earth oxides such as ceria there is the added complication that the removal of neutral oxygen to form a vacancy leaves electrons localized on previously empty f-states.[7] There is the resultant effect that the reduction of Ce^{4+} to Ce^{3+} occurs for two cations per oxygen vacancy, leading to efficient reversible oxygen release and hence a high activity for a number of catalytic systems.[4, 8] A further potentially important role of vacancies is in the binding of catalytically active metals such as Au, recently discovered to be a highly active catalyst for the water-gas-shift reaction.[9–11]

The (111) surface of CeO_2 is the thermodynamically most stable, and thought to make up a large fraction of the active catalysts, and has therefore been chosen as the focus of this work.[12, 13] Reduction of CeO_2 occurs via the straightforward equation 4.1 until complete reduction where x = 0.5, and the ceria is all stoichiometric Ce_2O_3:

$$CeO_2 \rightleftharpoons CeO_{2-x} + \frac{x}{2}O_2 \tag{4.1}$$

Since its inception in the late 1980s, scanning probe microscopy (particularly scanning tunnelling microscopy, STM) has become a hugely important tool for directly investigating the defective nature of surfaces, since the technique allows individual point defects to be probed. A key limitation to the implementation of STM in the study of ceria is the insulating nature of the native oxide. Stoichiometric CeO_2 has a band gap of about 6 eV, and as a result the use of STM has been limited mainly to high temperature (>575 K) studies.[14, 15] The complementary technique of non-contact atomic force microscopy (NC-AFM) has also been used to study the surface structure of CeO_2(111) at room and cryogenic temperatures. Although more difficult to implement, this technique has provided important insights, especially with regards to adsorbate-surface interactions not seen at the elevated temperatures required for single crystal STM.[16–21]

One means of studying insulating metal oxides using charged particle techniques is to prepare ultra-thin films on conducting substrates.[22] A number of metal supports have proved successful in this regard, including Ru(0001) [23, 24] Pd(111) [25], Rh(111) [26, 27], Ni(111) [25], Re(0001) [28], Cu(111) [29, 30] and Pt(111) [12, 31, 32] with STM having been employed in some of these cases.[12, 23, 26, 27, 30, 32]

In this study, we prepare ultra-thin ceria films on a Pt(111) substrate. Our images suggest that ultra-thin films grown in this way mimic the native surface very closely in terms of the structural elements present. In particular, a number of point defects and arrays of such defects previously observed in STM and NC-AFM of the native surfaces can be identified in the ultra-thin films produced here.

4.2 Experimental Procedure

All STM images presented here were recorded in the constant current mode, using commercial room temperature STMs (Omicron AFM/STM and VT-STM) housed in ultra-high vacuum (UHV) chambers with a base pressure of 1×10^{-10} mbar. STM tips were prepared by electrochemical etching of W wire (Advent) in 2M NaOH solution, followed by degassing at $\sim$500 K in UHV and Ar^+ sputtering. Voltage pulses and high bias scans (negative and positive) were performed during routine STM operation in order to condition the tip apex and allow stable tunnelling with atomic resolution imaging.

Samples were prepared in a preparation chamber with a base pressure of 1×10^{-10} mbar attached to the analysis chamber. The Pt(111) crystal was prepared by cycles of Ar^+ sputtering (1.5 keV) and annealing at 1100 K in UHV until a well-ordered Pt(111)(1×1) pattern was observed in LEED and impurities were below the detection limit of AES. In order to remove minor carbon contamination, cycles of annealing at 1100 K in 1×10^{-6} mbar O_2 were also occasionally performed.

There are a variety of recipes in the literature for the growth of ultrathin oxide films on metal substrates, which generally are divided into two categories: post oxidation (PO), and reactive deposition (RD). For ceria films particular schemes appear to be favoured depending on the substrate and the desired thickness of the final films. One aim of this work has been to optimise the conditions for preparing ceria films suitable for atomically resolved STM investigations which require well-ordered, atomically flat and relatively thin oxide layers, ideally with lateral dimensions as large as possible (islands or terraces with widths greater than 40 nm) so that edge effects

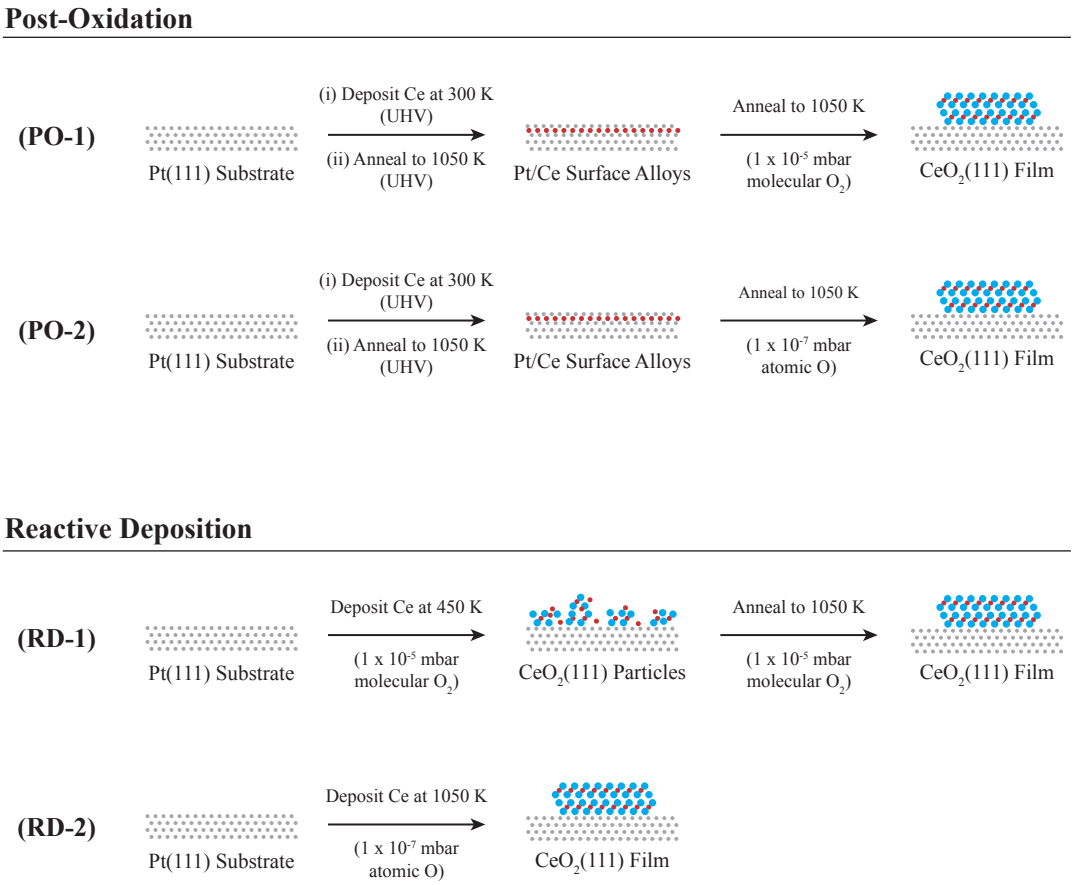

Figure 4.1: Schematic of the preparation methods compared for the growth of ultrathin ceria films. The procedures can be split into two groups: Post-oxidation of Pt/Ce surface alloys (PO-1, PO-2), and reactive deposition in molecular or atomic oxygen (RD-1, RD-2).

are minimized. As a result, a number of different procedures have been compared, and are summarised in schematic form in Figure 4.1. For the post-oxidation methods (PO-1 and PO-2) of Pt/Ce surface alloys as described by Berner and Schierbaum [12]; cerium metal (Alfa Aesar, 99.9%) was evaporated onto the clean Pt(111) substrate at 300 K via physical vapour deposition (PVD) from an electron beam evaporator and then annealed in UHV at 1050 K for 3 minutes. The oxidation step for PO-1 consisted of annealing to 1050 K in an O_2 pressure of 5×10^{-6} mbar for 2-10 minutes; for the PO-2 route, the oxidation step used an atomic oxygen source (Tectra Ion Source) with a chamber pressure of 1×10^{-7} mbar with the same temperature and time as for PO-1. The first reactive deposition scheme (RD-1) was based on that for ceria films

grown on Rh(111) in [23]. The Pt substrate was held at 450 K with the cerium metal evaporated from the same doser in 1×10^{-6} mbar O_2 . This partially formed oxide film was then annealed to 850 K in 1×10^{-6} mbar O_2 for a few minutes followed by short heating cycles at 920 K in 5×10^{-6} mbar O_2 to form a more ordered film. The other reactive deposition procedure (RD-2) has not been reported elsewhere for ceria films to date, and consisted of a single-step process where Ce metal was deposited via PVD onto the substrate which was held at 1050 K in an atomic oxygen environment at a chamber pressure of 1×10^{-7} mbar. For all of the procedures detailed above, the temperatures and durations of the annealing cycles were varied to determine the optimal growth conditions summarised in 4.1. Temperatures were monitored with an optical pyrometer (Minolta). The atomic oxygen source is estimated to produce an atom beam flux of $\sim 2.5 \times 10^{15}$ atoms $cm^{-2}s^{-1}$ at the sample.

The above procedures all led to $CeO_2(111)$ ultrathin films with (1.37 $\times$ 1.37) LEED patterns relative to Pt(111)(1 $\times$ 1) and uncontaminated Auger electron spectra which were then investigated with STM. Due to the O-Ce-O trilayer structure parallel to fluorite-type $CeO_2(111)$, we define a monolayer (ML) as one trilayer unit with a thickness of 0.31 nm. All coverages are estimated from the film thickness and the surface area fraction measured by STM.

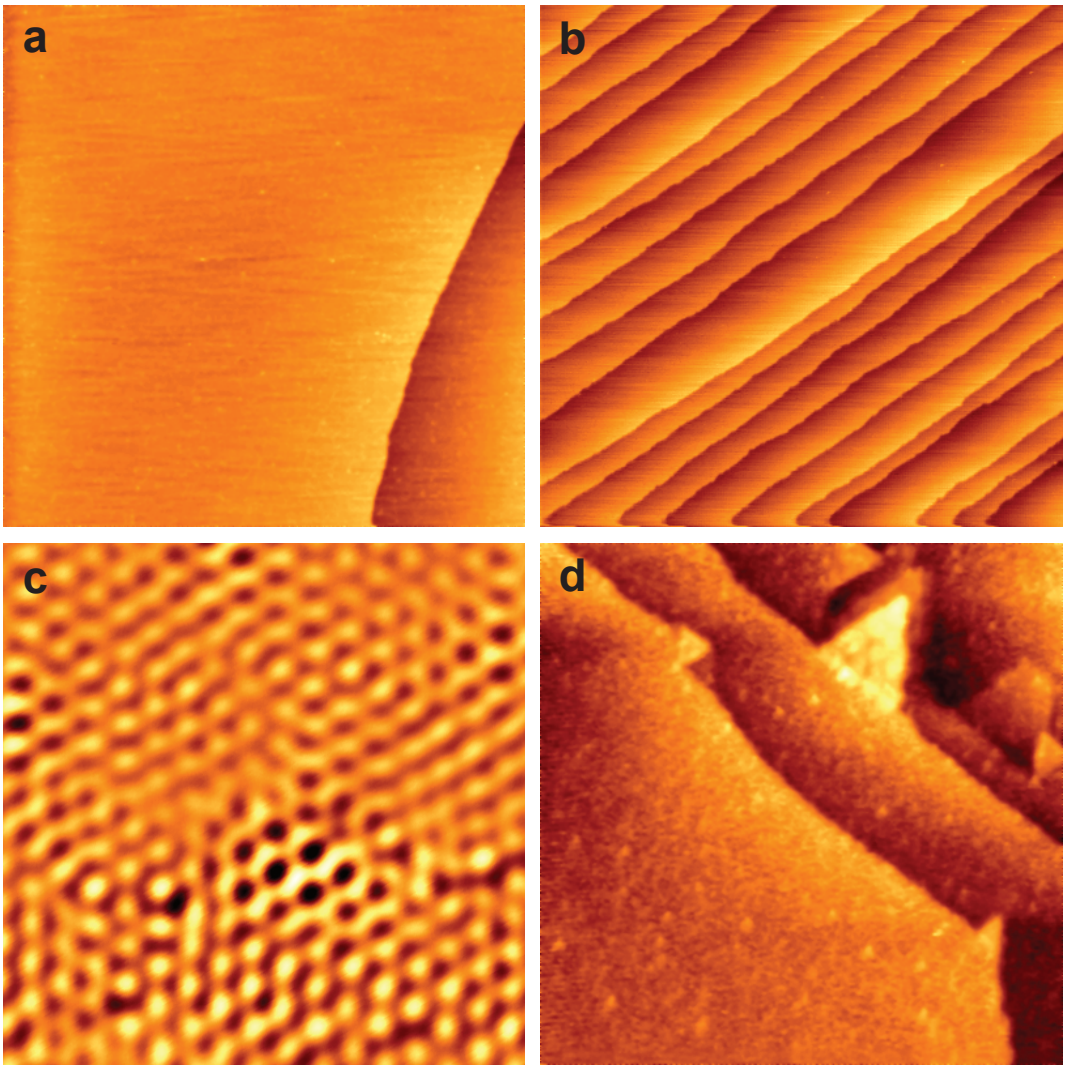

Figure 4.2: STM images of the Pt(111) substrate used for the growth of ceria ultrathin films: (a) Large area consisting of just two wide (111) terraces. (400 × 400 nm^2, V_s = -3.2 V, I_t = 0.25 nA) (b) Image from a different area of the same crystal showing a more heavily stepped area. (300 × 300 nm^2, V_s = -0.5 V, I_t = 0.25 nA) (c) Atomically resolved image of the Pt(111) filtered using FFT. (4 × 4 nm^2, V_s = -0.1 V, I_t = 0.32 nA) (d) Region of the Pt crystal after a 1000 K annealing cycle in 1×10^{-6} mbar O_2 with triangular structures on the step edges characteristic of PtO_2. (80 × 80 nm^2, V_s = +0.5 V, I_t = 0.25 nA)

4.3 Results and Discussion

4.3.1 Pt(111) Substrate

STM analysis shows that the clean Pt(111) substrates prepared consisted mainly of flat terraces separated by monatomic steps of height 0.23 nm, as demonstrated in Figure 4.2a and b. Terrace widths ranged from above 400 nm (Figure 4.2a) to a minimum of $\sim$10 nm (Figure 4.2b) depending on the particular area of the crystal examined. Atomically resolved images of the clean surface as seen in Figure 4.2c display a non-reconstructed (1 $\times$ 1) hexagonal arrangement of features with a separation of 0.28 nm as expected on the basis of previous work and consistent with the interatomic spacing of Pt(111), which is 0.2775 nm.[12] The corrugation of such metal surfaces is very low and hence achieving atomically resolved images is not easy, especially at room temperature. As a result the image presented in Figure 4.2c has been filtered via a low-pass fast fourier transform (FFT) filter in Image SXM (vers. 1.87) in order to remove high frequency noise. Low Energy Electron Diffraction from the clean surface showed a clear Pt(111)(1 $\times$ 1) pattern with the first order spots having a separation consistent with the interatomic spacing of Pt(111). As detailed in the experimental section, the Pt(111) crystal was prepared by cycles of annealing in oxygen and UHV. On some occasions this led to the formation of a small amount of PtO_2, as observed in the STM image displayed in Figure 4.2d, where triangles of PtO_2 are seen at the step edges of the Pt(111) terraces. These STM results show good agreement with the work of Krasnikov et al. in [33] where the oxidation of Pt(111) is studied in detail with LEED and STM. AES confirmed the presence of a small amount of oxygen in the surface region in these cases, but due to the lack of XPS on the UHV system it was not possible to further determine the oxidation state of the Pt. This result is an interesting illustration of how the oxidising conditions

used for substrate preparation and during film growth may affect the substrate and therefore ought to be considered when performing analysis on the ceria films. Both STM and AES were used to determine the cleanliness of the substrate before deposition as in some cases a number of small contaminants were observed in STM after the sputter/anneal cycles and despite being under the detection limit of AES may still have interfered with the growth of the ceria.

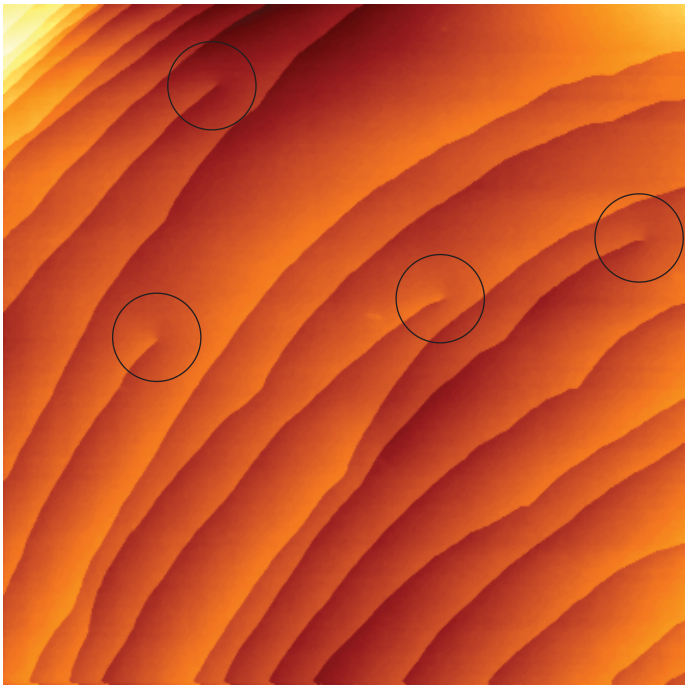

Figure 4.3: Large area STM image of the clean Pt(111) substrate with four screw dislocations marked by black circles. (1000 $\times$ 1000 nm^2, V_s = +1.0 V, I_t = 0.20 nA)

Figure 4.3 is a 1 $\times$ 1 μm^2 STM image of the bare Pt(111) substrate with a number of visible screw dislocations (marked by black circles). Such dislocations are only occasionally observed on our Pt(111) surface and as such an accurate measurement of their density is difficult to achieve and the effect they have on the ceria film growth is unknown at this point. Nucleation of the oxide film is proposed to occur at the substrate step edges and as such these dislocations may be preferred sites for this process, an examination of which could be of interest for future work and would

require an in-situ observation of the deposition and oxidation steps.

4.3.2 Post-Oxidation of Pt/Ce Surface Alloys

As described in the experimental section, post-oxidized films are grown via an intermediate Pt/Ce surface alloy. These alloy phases can be identified in LEED by the presence of (2×2) and (2×2)R30° reflexes and in STM by their characteristic moiré patterns as displayed in Figure 4.4a. STM and LEED have been used to extensively characterise such alloys by Baddeley et al. [34] and Essen et al. [35] and as such a detailed analysis has not been undertaken here, merely a confirmation of these previous results to ensure that the alloys are formed correctly as an intermediate. In Figure 4.4b, a 100×100 nm^2 STM image of the area marked with a black square in 4.4a is shown. There are three distinguishable phases, labelled I, II and III. Atomically resolved STM is possible on these phases, with examples of region I and II shown in Figures 4.4c and d, respectively. Figure 4.4c shows bright atomic-sized features in a hexagonal array with separation ~ 5 Å and a large moiré superstructure with periodicity on the order of ~ 100 Å. Figure 4.4d shows a similar hexagonal array of atomic features with separation ~ 5 Å. However, the moiré superstructure has a much larger periodicity of ~ 30 Å. By comparison of these results with the earlier studies [34, 35], it is possible to assign phase I (shown in Figure 4.4c) as an alloy with layers of composition Pt_5Ce terminated by a layer of Pt_2Ce, and phase II (shown in Figure 4.4d) as an alloy with similar composition but with a slightly contracted terminating layer of Pt_2Ce and a rotation of $\sim 30°$.[34] In both cases, the bright atomic features can be assigned to the location of Ce atoms within the Pt_2Ce terminating layer. Atomically resolved images of phase III have also been obtained (not shown) and again can be assigned via comparison with [34] as originating from a region of Pt_5Ce alloy, but with a Pt termination rather than Pt_2Ce.

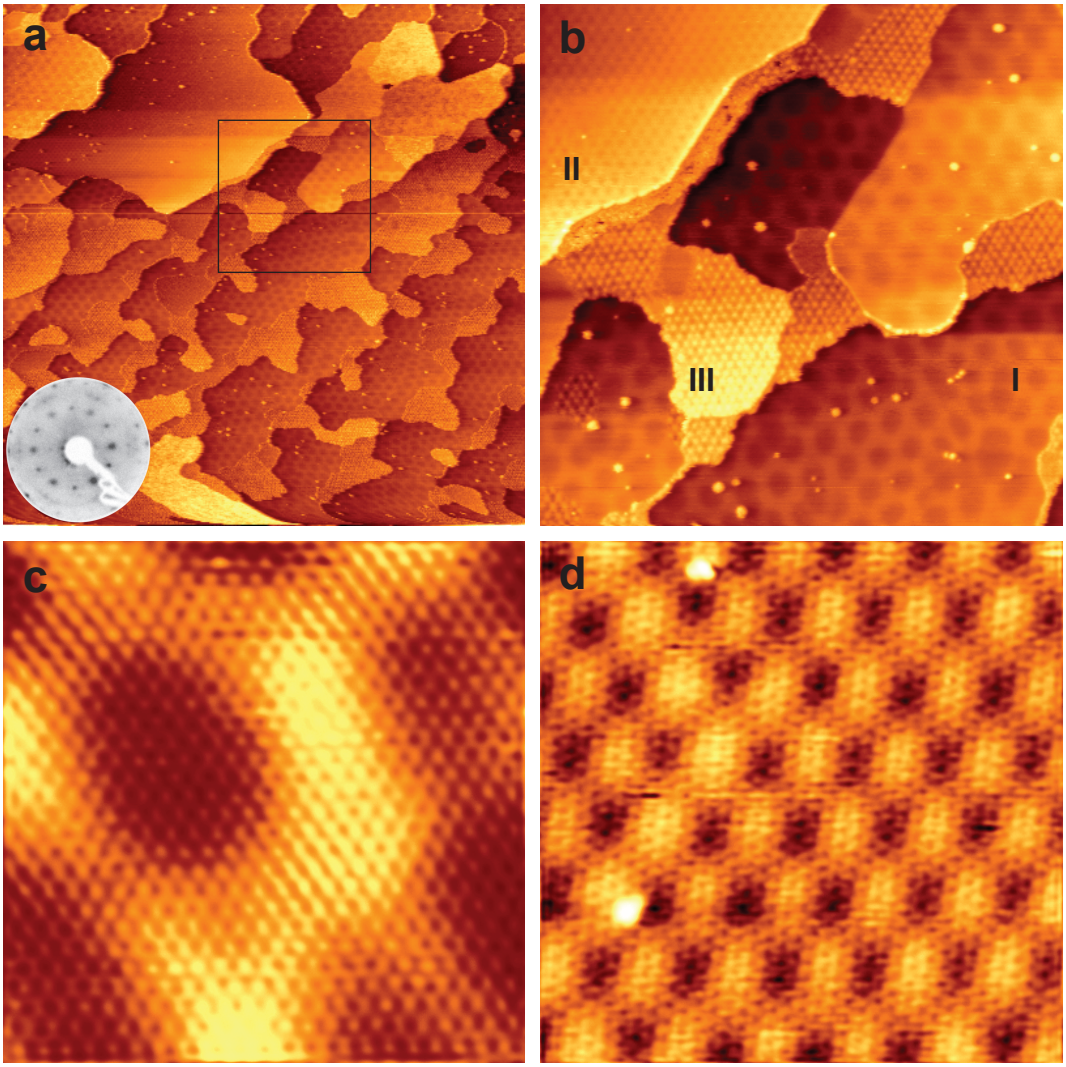

Figure 4.4: STM images of Pt/Ce surface alloys formed by PVD of Ce onto the Pt(111) substrate followed by annealing in UHV. (a) Large scale image showing the rounded terraces and moiré patterns typical of the surface alloys. (300 × 300 nm^2, V_s = -0.5 V, I_t = 0.25 nA) (inset LEED E = 43 eV) (b) Higher resolution image of the area marked with a black square in (a) with three distinct phases identified. (100 × 100 nm^2, V_s = -0.5 V, I_t = 0.25 nA) (c) Atomically resolved image of Phase I, composed of Pt_5Ce layers terminated with Pt_2Ce. (11 × 11 nm^2, V_s = -0.5 V, I_t = 0.25 nA) (d) Atomically resolved image of Phase II, composed of Pt_5Ce layers terminated with a contracted, rotated Pt_2Ce layer. (15 × 15 nm^2, V_s = -0.5 V, I_t = 0.25 nA)

Post-oxidation of these alloys by heating under a partial pressure of molecular or atomic oxygen leads to the formation of thin films of ceria, typical STM images of which are displayed in Figure 4.5 (a-molecular oxygen, b-atomic oxygen). The STM image in 4.5a shows that the film (estimated from STM to have a coverage of ∼0.5 ML) consists of isolated islands of ceria with geometric shapes (hexagonal and triangular) of lateral dimensions 30-50 nm. The apparent thickness of these islands is 0.3 nm or 0.6 nm, consistent with one or two O-Ce-O trilayers, respectively. This trilayer stacking implies that the film is oxygen-terminated $CeO_2(111)$, the thermodynamically most stable surface, and that which may form the major fraction of active catalyst surface.[12, 13] The STM image in 4.5b of a 1.4 ML ceria film formed via oxidation in atomic oxygen has a very similar appearance and consists of islands 0.3 and 0.6 nm tall, but with smaller lateral dimensions and slightly less angular edges.

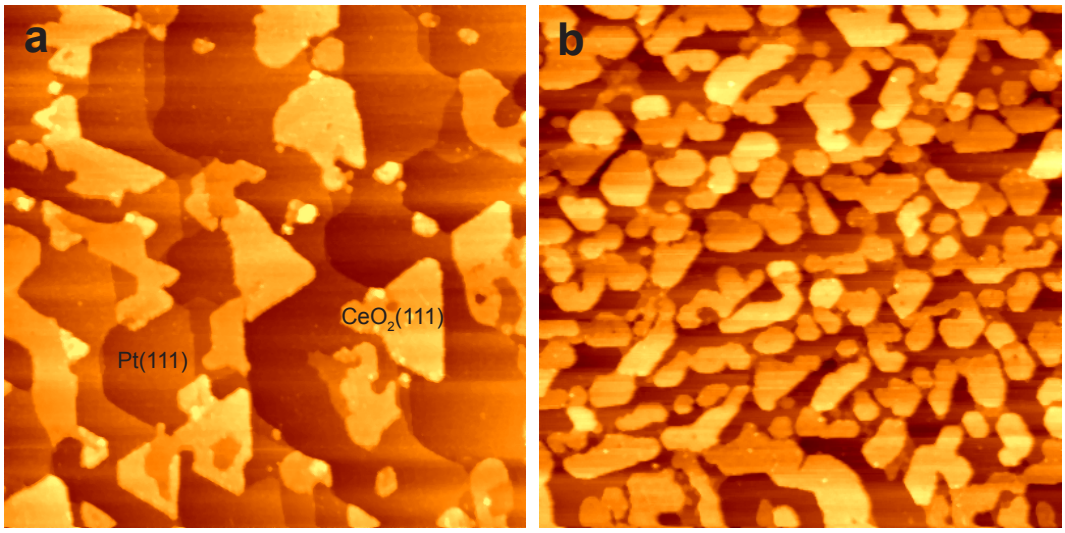

Figure 4.5: STM images of ultrathin $CeO_2(111)$ films prepared by post oxidation of Pt/Ce surface alloys in: (a) molecular oxygen (200 × 200 nm^2, V_s = -3.0 V, I_t = 0.10 nA) (b) atomic oxygen (200 × 200 nm^2, V_s = -3.2 V, I_t = 0.10 nA). Both films consist of islands of ceria one or two trilayers thick with estimated coverages of 0.5 ML (a) and 1.4 ML (b). The Pt(111) substrate is still visible in both cases.

4.3.3 Reactive Deposition Methods

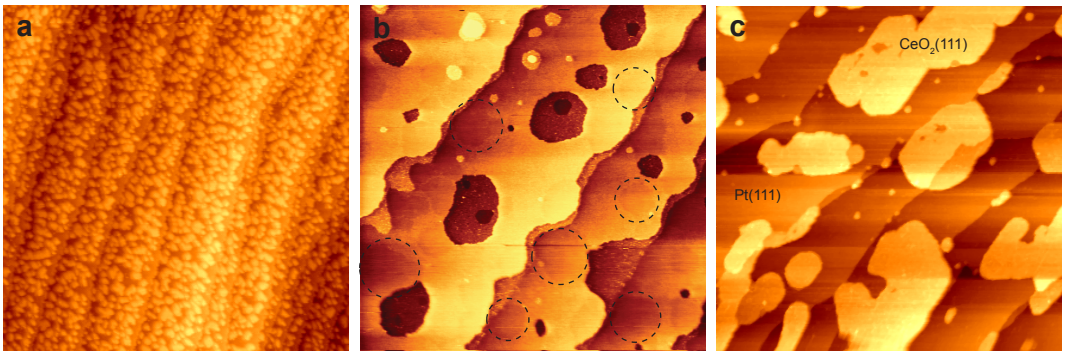

Figure 4.6: STM images showing the stages in growth of ceria films via a reactive deposition process in molecular oxygen (RD-1). (a) STM image (200 × 200 nm^2, V_s = +2.0 V, I_t = 0.25 nA) of small ceria particles after reactive deposition of cerium in 1×10^{-5} mbar O_2 at a temperature of 450 K. (b) STM image (200 × 200 nm^2, V_s = -0.5 V, I_t = 0.25 nA) of a 0.8 ML ceria film after post-oxidation of (a) at 850 K in 1×10^{-5} mbar O_2. The ultrathin ceria film of thickness 1 trilayer (0.3 nm) covers ∼80% of surface. A few holes in the ceria are observed revealing the Pt substrate and/or some partially formed oxide. The dashed circles indicate regions of Ce_2O_3(0001). (c) STM image (200 × 200 nm^2, V_s = -3.2 V, I_t = 0.15 nA) of a 0.8 ML ceria film after oxidation of (b) at 1050 K in 5×10^{-5} mbar O_2. Regions of bare Pt(111) are observed with isolated CeO_2(111) islands of thickness 1 or 2 trilayers as for films prepared via post-oxidation methods.

Figure 4.6 shows STM images taken from ceria films grown via reactive deposition by the scheme detailed in Figure 4.1 RD-1. An STM image (Figure 4.6a) taken after Ce dosing in an O_2 pressure of 1×10^{-5} mbar with the sample held at 450 K shows a nearly complete coverage of the Pt surface by small (∼10 nm diameter) particles of ceria. These particles are uniformly distributed over the surface, with no preference for step-edges. Upon annealing at 850 K in 1×10^{-5} mbar O_2 for 5 minutes, a near complete film is formed, as shown in Figure 4.6b. This large area STM image shows the presence of a ceria film across the Pt substrate covering about 80% of the surface. Individual steps on this film have a height of 0.3 nm, consistent with a single trilayer of CeO_2. There are a number of dark holes within the terraces. Although atomic resolution imaging was not possible within these holes, their appearance in STM is visibly different to that of the ceria and

their depth is approximately one trilayer. As such, it is assumed that these holes correspond either to the underlying Pt or a region of partially formed oxide. A number of other bright features with geometric shapes and lateral sizes of a few nm are visible on the terraces and are likely related to the start of the formation of a second ceria trilayer. Upon annealing the film in Figure 4.6b to 1050 K in 5×10^{-5} mbar O_2 for 4 minutes, the structure of the ceria film is changed dramatically, as displayed in Figure 4.6c. The ceria coalesces to form isolated islands with a layered structure consistent with 1 or 2 trilayers of CeO_2 and a total film coverage of 0.8 ML. These islands are very similar to those formed via the post-oxidation routes in Figure 4.5 with angular shapes close to that observed in the results of PO-2 (Figure 4.5b). However, the shape of the islands varies depending on the precise oxidation temperatures and times used.

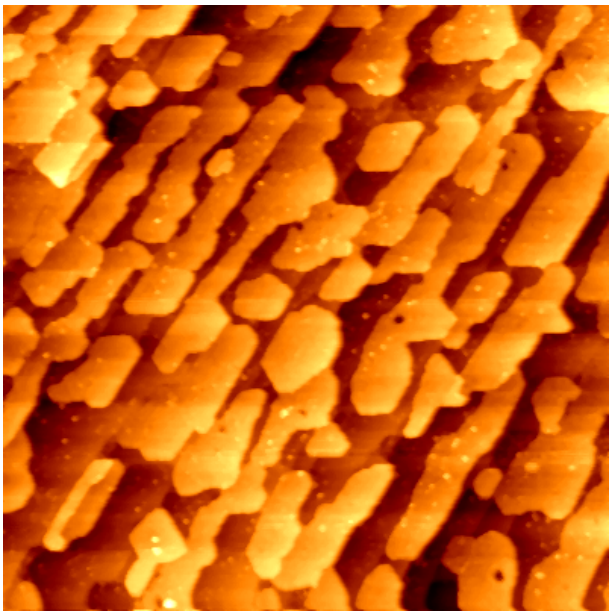

Figure 4.7: STM image (200 $\times$ 200 nm^2, V_s = -3.2 V, I_t = 0.10 nA) of a 1.3 ML ceria ultrathin film prepared via a single step reactive deposition process (RD-2). Ce metal is evaporated onto the Pt substrate which is held at 1050 K in a atomic oxygen pressure of 1×10^{-7} mbar. The appearance of this film is very similar to those formed by the other methods, with islands of ceria two trilayers thick across the surface of the Pt.

The final film growth procedure was the single step reactive deposition process (RD-2 in Figure 4.1) in atomic oxygen, a typical STM image of which is displayed in Figure 4.7. Although the film is of a slightly higher coverage (∼1.3 ML) compared to those displayed in Figure 4.6, it has the same general structure of all the other ceria films in this study, with islands of ceria ∼0.6 nm tall formed epitaxially on the platinum substrate.

4.3.4 CeO_2(111) Film Large-Scale Structure

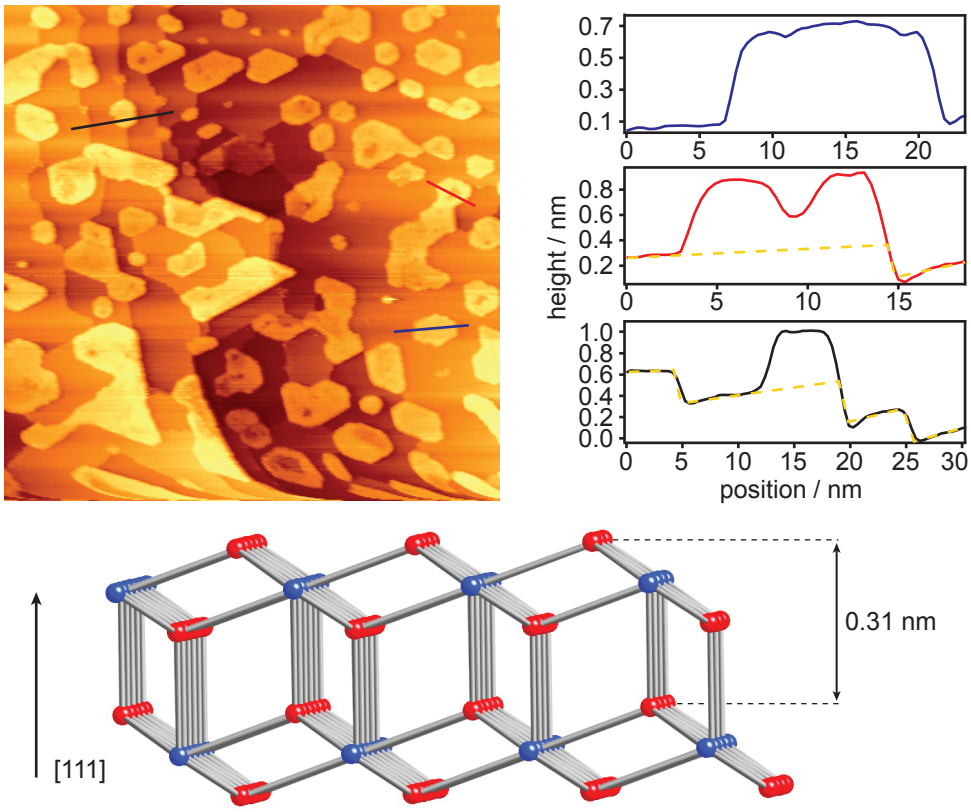

Figure 4.8: STM image (150 × 150 nm^2, V_s = +1.76 V, I_t = 0.50 nA) and associated line profiles of a 0.6 ML ultrathin ceria film formed via oxidation of surface alloys. The film has a layered structure, with layer thicknesses of 0.3 nm, corresponding to an O-Ce-O trilayer. Also shown is a ball-and-stick model of CeO_2, highlighting the trilayer structure. (red atoms: O^{2-}, blue atoms: Ce^{4+})

Bulk CeO_2 has the fluorite crystal structure and the (111) surface is thermodynamically most stable surface [13], which is expected to be oxygen terminated under the conditions used for all the films grown during the course of this work.[12] A ball-and-stick model clearly showing the trilayer structure of ceria is displayed in Figure 4.8, where one trilayer is defined as: O^{2-} - Ce^{4+} - O^{2-}, and has a height of 0.31 nm. [12] This layered structure is evident in the films as mentioned above, with the steps on ceria islands in Figures 4.5, 4.6 and 4.7 all measured to be multiples of $\sim$0.3 nm. A clear demonstration of this can be seen in the STM image and associated line profiles in Figure 4.8 of a 0.6 ML ceria film formed by post-oxidation of the Pt/Ce surface alloys in molecular oxygen. The blue line profile is over a hexagonal-shaped island located in the middle of a Pt terrace with its edges aligned with the primary azimuths of the substrate, and can be seen to be $\sim$0.6 nm tall, or two trilayers. The red line profile is over an island that is 2 trilayers thick in places, but with a depression in the middle corresponding to a single trilayer; the step edge of the Pt substrate is shown as a dashed yellow line (the step height of the Pt is 0.23 nm). The black line profile is over a ceria island nucleated at a step edge of the Pt, and again has a height corresponding to two trilayers. It is observed that there are no ceria islands composed exclusively of a single trilayer although some have an incomplete second layer, suggesting that a double trilayer structure is the most stable for the growth conditions used.

A typical low energy electron diffraction pattern (60 eV) from a 1.5 ML ceria film is displayed in Figure 4.9 and shows a low background with sharp reflexes from the Pt(111)(1 $\times$ 1) substrate with CeO_2(111) (1.37 $\times$ 1.37) commensurate with it. This 1:1.37 ratio of lattice spacings of Pt(111):CeO_2(111) measured from LEED is a deviation from the ideal ratio of the respective single crystal parameters of 1:1.4.[36] This discrepancy may arise from the large lattice mismatch between support and film, which gives rise to a strain-induced contraction of the ceria ultrathin film lattice relative to the single crystal. This may have an important effect regarding the defect

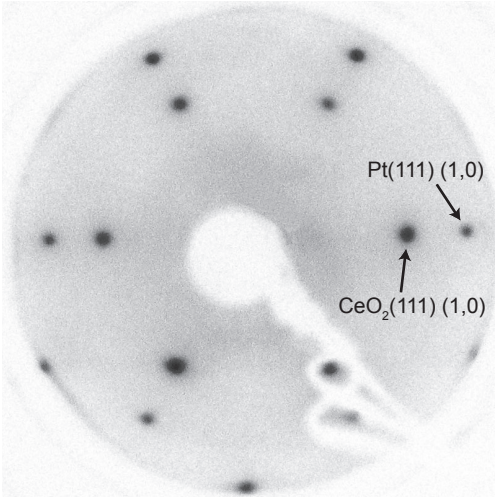

Figure 4.9: Typical Low Energy Electron Diffraction pattern (60 eV) of a 1.5 ML ultrathin ceria film, displaying reflexes from Pt(111)(1 × 1) and CeO_2(111)(1.37 × 1.37).

structure present in the film, as suggested by Castellarin et al. [37] who report strain-induced ordering of defects at the surface of a similar CeO_2(111) film. Such a large lattice mismatch leading to a strained interface between oxide and support is often not ideal if it is desired that the film mimic the bulk as closely as possible. Substrates for other oxide ultrathin films such as TiO_2 are often chosen to allow less strained interfaces.[38]

Auger electron spectroscopy was used to ensure the cleanliness of the ceria films, typical spectra are shown in Figure 4.10 for the clean Pt(111) substrate (blue) and a 1.5 ML ceria film (black) grown by reactive deposition in atomic oxygen (AES spectra for all growth procedures are almost identical). The spectra are plotted in derivative mode using RFA detection, and show clearly the Pt LMM peak groups, as well as for O KLL and Ce LMM. A common method for determining the coverage of an adsorbate layer is to measure the attenuation of the substrate Auger peaks with increasing adsorbate thickness.[39] However, due to the poor signal-to-noise ratio of the Pt peaks and low film coverages in this work it was not possible to get an accurate estimate in this way. As all of the films in this study still expose the substrate, the thickness of the oxide layers can

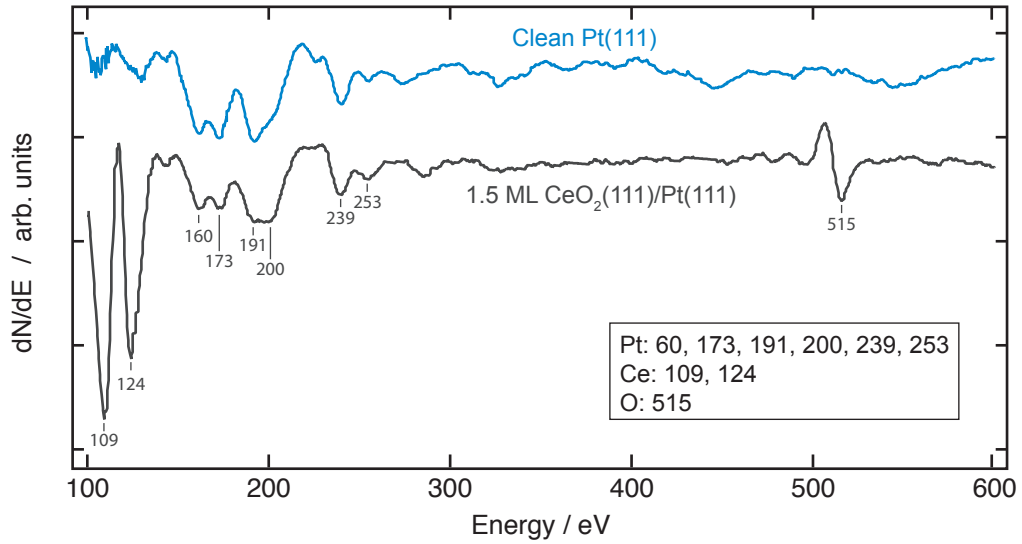

Figure 4.10: Derivative Auger Electron Spectra for the clean Pt(111) substrate (blue) and a 1.5 ML CeO_2(111) film (black), spectra vertically offset for display purposes.

be measured directly from the STM images, allowing an estimate of the total oxide present by combination with the fractional surface area, also measured with STM.

The growth mechanisms of ultrathin oxide films are another area of much interest and our results back-up the assertions of previous studies of ceria films.[23, 37] The oxide islands are observed to preferentially nucleate at step edges and other dislocations on the substrate and grow via a Volmer-Weber type mechanism, irrespective of whether the preparation procedure was via post-oxidation or reactive deposition. A clear example of this preference for step edges is displayed in Figure 4.11 which is a composite of four STM images allowing a view of a 1200 $\times$ 400 nm^2 area of a 0.5 ML ceria film. The majority of the ceria islands are observed to decorate the step edges of the substrate and only a few are found in the middle of the (111) terraces. This film was prepared by post-oxidation of alloys using molecular oxygen, and although it is not trivial to investigate the intermediate steps of the oxidation process using STM, an interesting avenue of future research may be to use a chemically sensitive microscopy technique such as XPEEM to

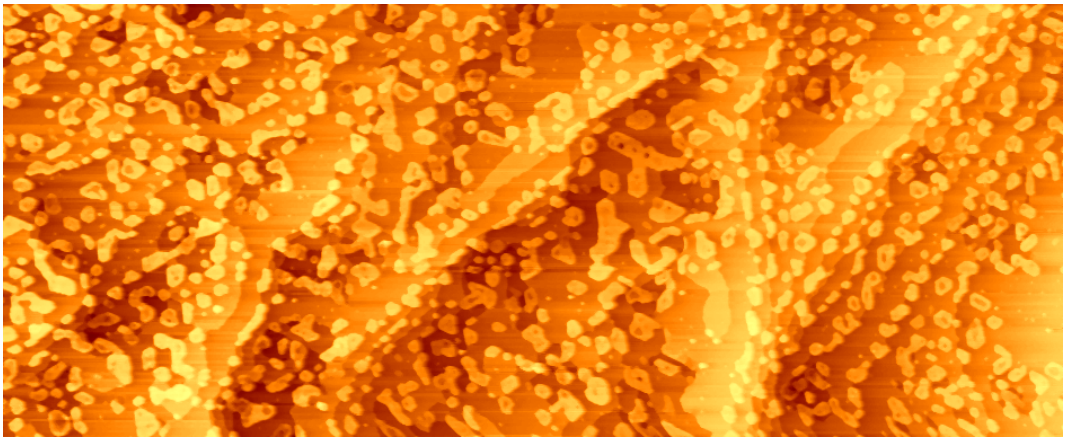

Figure 4.11: Composite STM image (1200 × 400 nm^2, V_s = +1.5 V, I_t = 0.28 nA) of a 0.5 ML CeO_2(111) film formed by post-oxidation. The small ceria islands are observed to decorate the step edges of the substrate, indicating preferential oxidation at the edges of the surface alloys or preferential initial adsorption sites.

monitor this growth in an in-situ fashion.

The Volmer-Weber growth mechanism expected due to the large lattice mismatch between ceria and platinum, favours independent growth of 3-D oxide islands in preference to a wetting layer of oxide and has the added result that many of the ceria islands are observed to contain lines of depressions, some of which are irregularly shaped and others which are aligned along the principal crystallographic directions of the oxide. Such depressions have been observed for CeO_2(111) films on Ru(0001) [23] and were assigned to domain boundaries, but not investigated in depth. Domain boundaries on oxide ultrathin films have been examined using NC-AFM, a good example of which is the work of Simon et al. in [40] on the antiphase domain boundaries of ultrathin alumina on NiAl(110).

Figure 4.12a is an STM image showing a 0.6 nm thick ceria island grown via post-oxidation in atomic oxygen that displays a number of such features, visible as bright and dark lines in inverted V shapes, parallel to the edges of the island. An atomically resolved image of the area marked

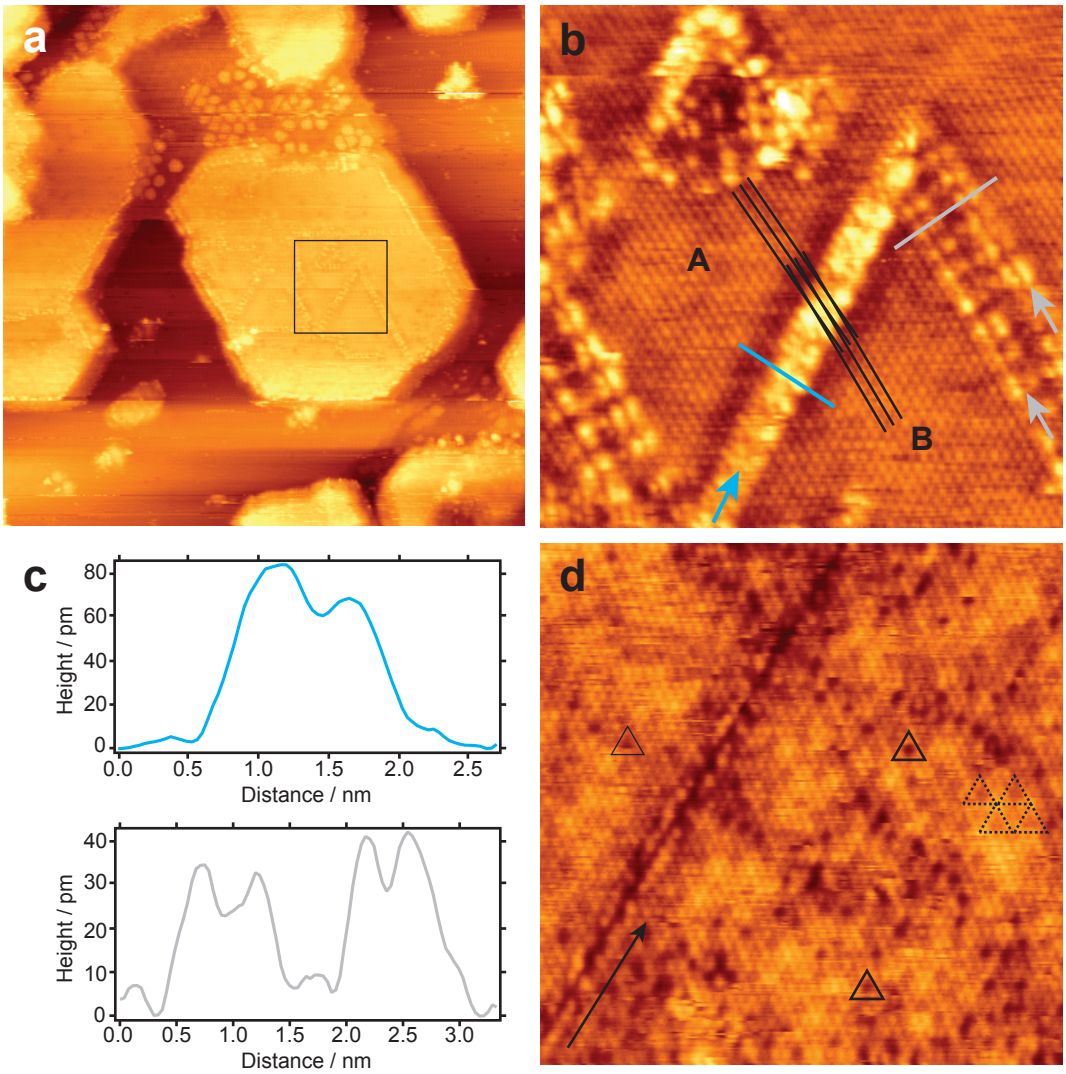

Figure 4.12: STM images and associated line profiles of domain boundary features observed on ceria ultrathin films. (a) Partially formed CeO_2 film (1.2 ML) with a number of bright features aligned with the island edges observed on top. (90 $\times$ 90 nm^2, V_s = -3.2 V, I_t = 0.10 nA) (b) Atomically resolved image of the area in (a) marked with a black square. The lines are found to be domain boundaries separating A and B whose lattices are rotated $\pm 2^\circ$ with respect to the substrate. (15 $\times$ 15 nm^2, V_s = -3.2 V, I_t = 0.10 nA) (c) Line profiles across the domain boundaries observed in (a) & (b). (d) Atomically resolved image of another ceria film with a domain boundary visible running from the bottom left to the top right of the frame. Oxygen vacancies are marked with black triangles. (20 $\times$ 20 nm^2, V_s = -3.2 V, I_t = 0.10 nA)

with the black square is shown in Figure 4.12b which allows closer analysis of these features. A bright ridge (marked with a blue arrow) approximately 1.5 nm wide and 80 pm tall (blue line profile in Figure 4.12c) is observed going from the bottom left to the top right of the island, with some further structure visible on its top. At $\sim 60^{\circ}$ to this ridge are a number of other parallel ridge features marked with grey arrows, a line profile across one of these is displayed in Figure 4.12c. Each ridge, of width 1 nm, consists of a pair of bright features spaced by 0.5 nm in the direction of the line profile and distributed every 1 nm along the length of the ridge. The two ridges have a separation (centre to centre) of 1.5 nm and have a maximum height of $\sim$40 pm, about half of that of the ridge marked with blue. Filled states atomic resolution images of the island, as shown in Figure 4.12b, allow us to see that the bright ridges divide the island into two domains labelled A and B which have a very small rotation ($\pm 2^{\circ}$) of their lattices with respect to the substrate (to aid visual identification of this rotation, guidelines have been superimposed onto Figure 4.12b). Such a rotation is not visible in LEED most likely due to the small angle between the domains which would likely lead just to a broadening of the diameter of the oxide spots. It can also be observed from Figure 4.12a that there is a region at the top middle of the image where the oxide is only partially formed, and appears as bright rounded shapes on the substrate, an intermediate stage in the oxidation process of the Pt/Ce alloys discussed earlier in this chapter.

In addition to these boundaries separating rotated domains of the ceria, there are also boundaries such as that shown in Figure 4.12d, which appear as a depression along the direction indicated by the black arrow and separate regions that are otherwise identical in appearance. Such boundaries may originate from the coalescence of islands of ceria that had separate oxidation nucleation points on the Pt/Ce alloys. Figure 4.12d is obtained at negative sample bias, and hence oxygen atoms are imaged as bright spots, permitting the observation of a number of oxygen vacancies (marked with solid black triangles) as well as some ordered surface oxygen vacancies (marked

with dashed black triangles). The appearance and nature of such vacancies will be discussed later on in this chapter, when the defect and adsorbate structure of the ceria films is analysed in more detail. One of the key aims of this study has been to identify ceria film growth procedures that yield very flat surfaces suitable for high-resolution STM studies. As part of this, the effect of multiple oxidation steps was investigated and it was discovered that rather than promoting growth in a 2-D fashion, further annealing led to 3-D growth creating taller ceria islands with smaller lateral dimensions, less suitable for examination with STM.

4.3.5 CeO_2(111) Film Electronic Structure

The electronic structure of such ultrathin oxide layers is of great interest as they are often thought to be quite different to those of the bulk due to interactions with the substrate and also confinement effects due to the short (few nm) lengthscales involved.[38] There are many surface sensitive spectroscopic techniques in use which provide information on the macro-scale, but the application of scanning tunnelling spectroscopy (STS) can potentially allow a much higher resolution right down to the atomic scale. The highest quality STS data requires the stability provided by operation at cryogenic temperatures, however, the instrument used in this work is limited to room temperature studies and as such, only semi-quantitative results have been obtained.

Figure 4.13a is an STM image of the 1.5 ML CeO_2(111) film from which I/V point spectra were obtained. The I-V point spectra presented in Figure 4.13b correspond to the ceria (blue line) and the platinum substrate (red line) and are an average of seven separate curves obtained at locations within the blue square on top of a ceria island and the red square on the substrate as displayed in Figure 4.13a. Spectra were obtained by ramping the bias voltage from -3.2 V to +3.0 V, with

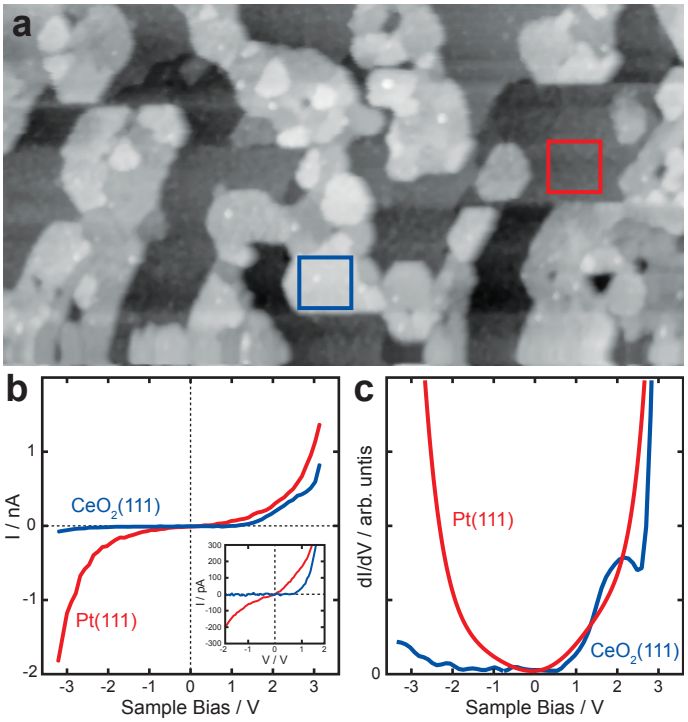

Figure 4.13: STS investigations of a 1.5 ML CeO_2(111) film on Pt(111). (a) STM image of the area of the ceria film from which conductance spectra were obtained. (200 × 100 nm^2, V_s = +2.0 V, I_t = 0.05 nA) (b) I/V spectra for the clean Pt(111) substrate (red line) and the CeO_2(111) film (blue line). The spectra are an average of 7 points taken from the regions of the STM image in (a) marked with red and blue squares. The curve from the Pt substrate shows a finite non-zero current for all bias voltages, whereas the curve from the ceria displays a region of zero current between -2.5 V and +1.5 V. (c) Differential Conductance (dI/dV) spectra for the Pt(111) substrate (red) and CeO_2(111) film (blue) obtained by numerically differentiating the data in (b) (polynomial fit was applied to the Pt data before differentiation). The ceria spectrum displays a valence band onset at around -2.5 V and a conduction band onset at +3.0 V, with a peak located inside the band gap originating from Ce *4f* states at +2.0 V.

the feedback loop switched off. The red line from the Pt shows a finite, symmetric non-zero current for all bias voltages as expected for a metallic tunnelling junction due to the continuous density of states at the Fermi level (see inset for expanded view of the origin). On the ceria film a region of zero current is observed between around -2.5 V and +1.5 V. The data presented in Figure 4.13b was numerically differentiated to find the differential conductance (dI/dV), and is shown in Figure 4.13c. The curve corresponding to the Pt(111) substrate in Figure 4.13b was fitted with a polynomial prior to differentiation. Although rather noisy, the ceria film displays a region of zero conductance that corresponds to the oxide band gap ranging from -2.5 V (VB) to

+3.0 V (CB) with a peak inside the gap observed at +2 V. Bulk ceria has a band gap of ∼6 V [7] which is slightly larger than our observed gap, although the valence band onset for our data is not well pronounced leading to a potential source of this discrepancy. A recent publication by Shao et al. [41] observes a narrowing of the ceria band gap with reducing film thickness although a quantitative analysis is not provided. The additional peak at around +2.0 V has been observed in previous STS investigations of ceria thin films [41, 42] and by comparison with EELS and PES data [7, 43] is assigned to the Ce *4f* band, unoccupied in stoichiometric CeO_2 but partially filled in our reduced CeO_{2-x} films.

4.3.6 Reduced Ceria Phases

Although we are unable to directly monitor the oxidation state of the ceria within the prepared films in situ, examination of the STM images allows a number of conclusions to be drawn. A minority area ($25 \pm 3\%$) of the terraces seen in Figure 4.14a (same image as Figure 4.6b; a partially oxidised ceria film prepared by reactive deposition in molecular oxygen) displays a noticeably different contrast in STM (some of these areas are highlighted by dashed circles). An atomically resolved image of which is shown in Figure 4.14b corresponding to the area with the black square in 4.14a and shows the edge of one of these minority areas, inside of which a characteristic hexagonal motif is observed with a surface unit cell rotated 15° with respect to the majority $CeO_2(111)$. This motif is very similar to that assigned to surface $Ce_2O_3(0001)$ by Berner and Schierbaum [12] and we make the same assignment here. Ce_2O_3, like the other rare-earth sesquioxides, can crystallise with one of three crystal structures (hexagonal, monoclinic, or body-centered cubic) of which the hexagonal La_2O_3 structure is the most frequently observed.[44] It is important to note that although the structure we image in STM is similar to that of Berner and

Schierbaum, the Ce_2O_3 phase was formed in a different way. In the previous study, Ce_2O_3 was only seen after the majority CeO_2 ultra-thin film was annealed for 10 min at 1000 K in UHV [12], whereas here it has been observed as an intermediate in the growth of the oxide from the surface alloys.

The image in Figure 4.14c is of the area of Ce_2O_3 marked with the black square in Figure 4.14b and was taken at a quite different bias voltage of -0.22 V. A number of regions with different contrast are seen (labelled I to IV) between which the tip has clearly undergone a number of termination changes as marked with the black arrows. A filtered and expanded image of the region labelled III is displayed in Figure 4.14d and displays a hexagonal lattice with the same spacing (0.38 nm) as observed for $CeO_2(111)$, but with a quarter of the oxygen atoms missing (dark spots). This structure agrees with the relatively simple transformation between $CeO_2(111)$ and $Ce_2O_3(0001)$ proposed by Berner and Schierbaum in [12] and is another indication of the ability of ceria to store and release oxygen without major structural changes, key to its catalytic behaviour. The bias voltage used to obtain Figures 4.14c and d (-0.22 V) is much less negative than that normally required for atomic resolution imaging of filled states on $CeO_2(111)$ which is typically -3.2 V. The latter value is thought to arise from tunnelling from O *2p* orbitals. The less negative value of -0.22 V indicates a different origin of the STM contrast, possibly involving substrate states, although it is still likely to have a significant contribution from the oxygen atoms.

4.3.7 Defect and Adsorbate Structure

An understanding of the interaction of adsorbate molecules with $CeO_2(111)$, particularly with regards to surface defects, may be key to gaining insight into the mechanism of ceria catalysis.

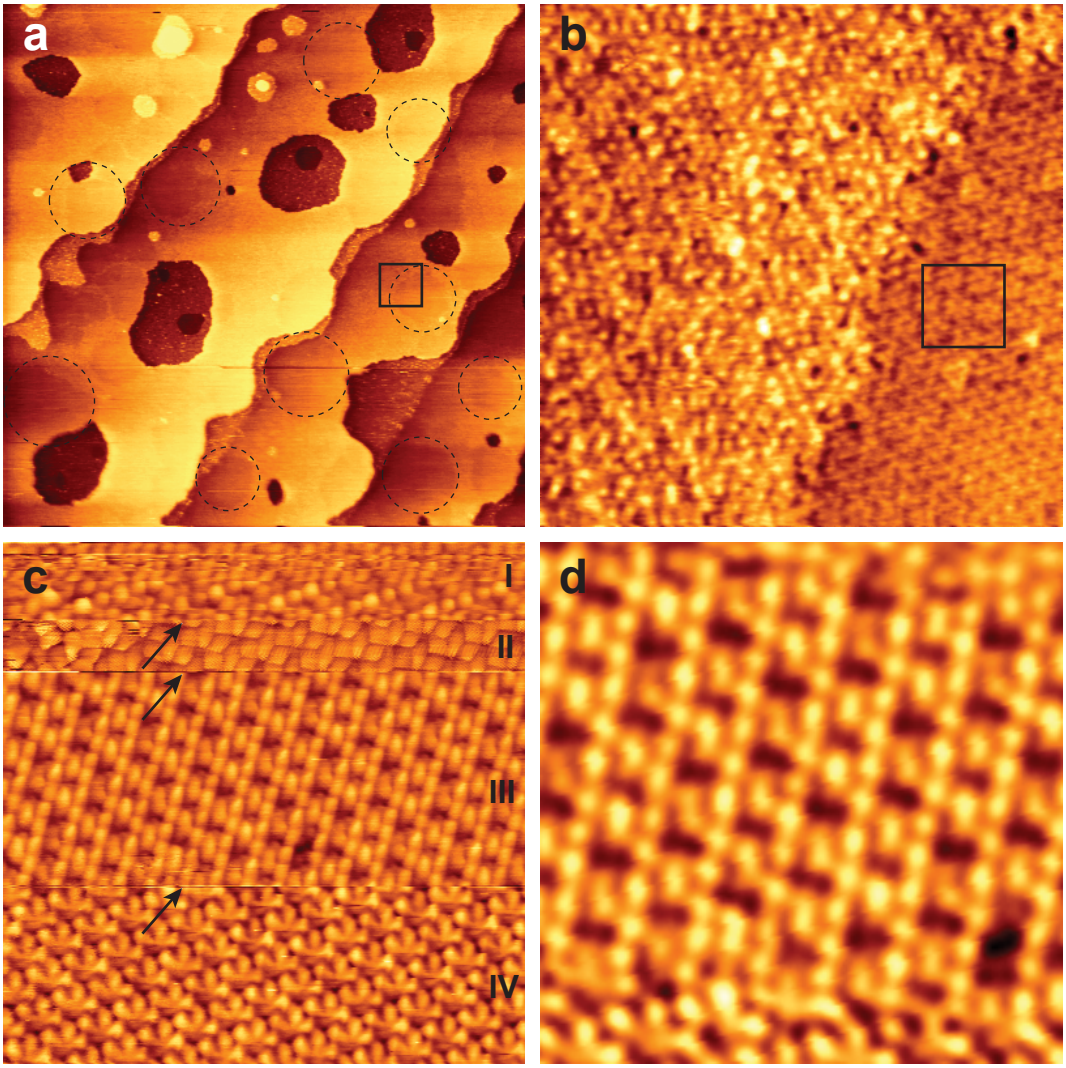

Figure 4.14: STM images showing areas of ceria ultrathin films that are of Ce_2O_3 stoichiometry. (a) Large scale image (same as Figure 4.6) (200 $\times$ 200 nm^2, V_s = -3.2 V, I_t = 0.20 nA) of partially oxidised ceria film, regions of different contrast are highlighted with dashed circles. (b) Expanded image (20 $\times$ 20 nm^2, V_s = -3.2 V, I_t = 0.20 nA) of the region in (a) marked with a black square; the area on the left hand side is of a 1 trilayer thick ceria film with a high density of oxygen vacancies, and the area on the right displays contrast assigned to Ce_2O_3. (c) Atomically resolved image of the area in (b) marked with a black square (10 $\times$ 10 nm^2, V_s = -0.22 V, I_t = 0.20 nA). A number of different tip contrast modes are visible (I-IV) with spontaneous tip changes occuring at the lines marked with arrows. (d) Atomically resolved image (7 $\times$ 7 nm^2, V_s = -0.22 V, I_t = 0.20 nA) of the area in (c) labelled III, the bright spots are assigned to oxygen atoms, a quarter of which are observed to be missing leading to identification of this phase as Ce_2O_3.

This next section of results focuses on atomically resolved imaging of the ultra-thin films. In order to obtain good-quality atomically resolved STM images it is necessary to have large (ideally at least 30 nm wide), flat ceria islands such as those shown in Figure 4.15 from where Figures 4.16 and 4.17 are taken. The terrace marked with the dashed rectangle in Figure 4.15 is approximately 90 nm wide and 0.9 nm tall (corresponding to three ceria trilayers) grown by post-oxidation in molecular oxygen and is an ideal location for high-resolution studies.

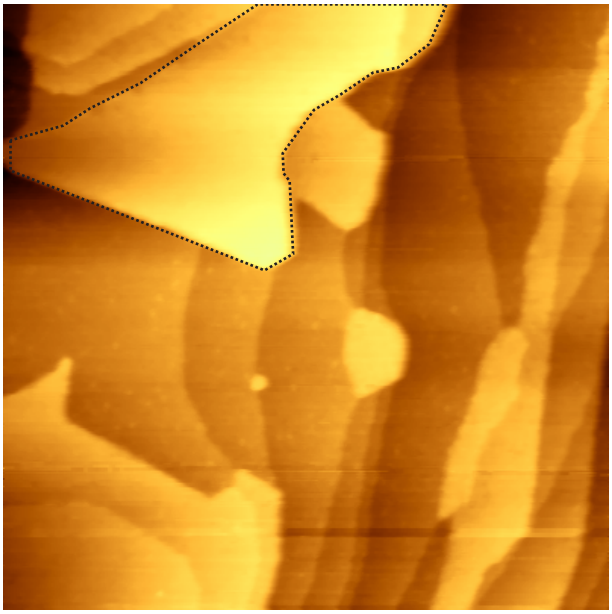

Figure 4.15: STM image (200 $\times$ 200 nm^2, V_s = +1.5 V, I_t = 0.10 nA) showing an area of a ceria ultrathin film with large flat terraces best suited to atomically resolved measurements. The atomically resolved images in Figures 4.16 and 4.17 were obtained on top of the island marked with a dashed rectangle, which is 0.9 nm thick (three trilayers).

In the majority of the images presented here, the sample is held at negative bias relative to the tip during scanning so that filled sample states are imaged. As such, the bright spots in all of the atomically resolved images obtained at this bias are assigned to oxygen atoms, due to the dominant tunnelling contributions from O *2p* orbitals at the high biases used for best contrast.[14]

Measurement of the interatomic spacing between these bright spots yields a value of 0.38 $\pm$0.03 nm, consistent with the ideal parameters for both CeO_2(111) (0.3826 nm) and Ce_2O_3(0001) (0.3888 nm) [12] and agreeing with our measured LEED ratio of 1:1.37 with respect to the Pt(111) substrate. As oxygen vacancies are thought to be critical in determining the catalytic properties of ceria, we have chosen to use filled states imaging so that surface oxygen vacancies should appear simply as dark spots. Such filled states imaging also facilitates comparison with NC-AFM images, which also show surface oxygen atoms as bright features and vacancies as dark spots.[16–21] The use of such a large negative bias is not without problems, and a large number of tips that were tried proved unable to image the ceria with atomic resolution under these conditions, and were very unstable even during large-scale scans. The interaction between tip and sample is relatively large at these settings as exemplified by the case of hydroxyls on TiO_2(110) which are observed to desorb from the surface when pulsed or scanned at + 3 V bias.[45] The vast majority of other STM studies on ceria ultrathin films to date have used small (1-2 V) positive sample biases,[12, 23, 26, 27, 30, 32] in which case it is assumed that the Ce^{4+} cations provide most of the empty states for image formation and as such appear as bright protrusions in atomically resolved STM.

Figure 4.16 is an atomically resolved STM image and associated structural model recorded from the highlighted area of the ceria film shown in Figure 4.15, and displays a number of characteristic features. The bright spots are assigned to the terminating oxygen atoms as described above and the dashed circles are drawn around depressions that are surrounded by six slight protrusions. By comparison with high temperature STM images by Esch et al. [14] and 80 K NC-AFM images by Torbrugge et al. [20] taken from single crystal CeO_2(111), we assign these depressions to surface oxygen vacancies (O_{vac}) and the surrounding protrusions to oxygen atoms. The magnitude of the outwards relaxation of the surrounding O atoms is not as pronounced in our thin film as that

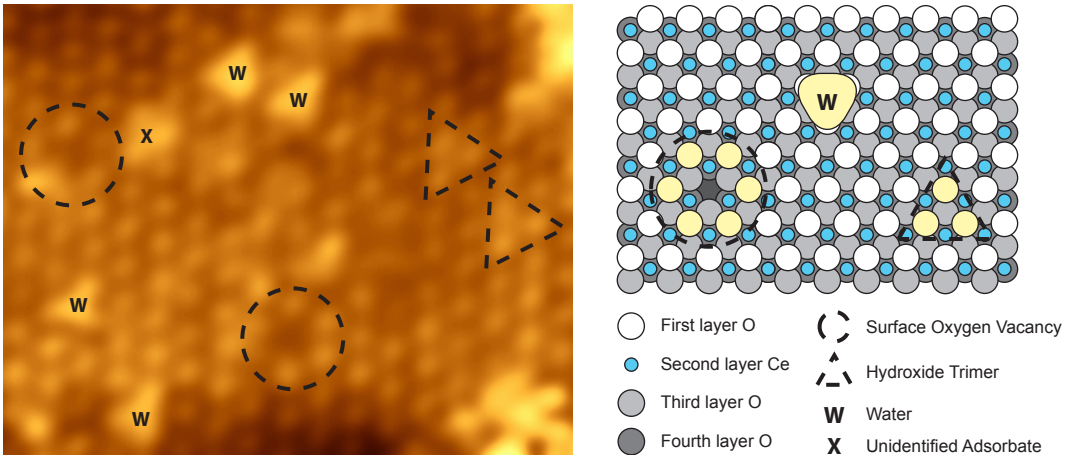

Figure 4.16: Atomically resolved, filled states, STM image (5 × 4 nm^2, V_s = -3.2 V, I_t = 0.20 nA) and structural model of vacancies and adsorbates on an ultrathin film of CeO_2(111) on Pt(111). Bright spots correspond to top oxygen layer, with identification of adsorbed water, hydroxyl trimers and surface oxygen vacancies, by comparison with NC-AFM [20, 21] and high temperature STM [14]. The assignments are highlighted in the structural model. Water molecules are observed exclusively above second layer Ce atoms.

observed on the single crystal and in some cases no protrusion is observed at all. When a neutral surface O_{vac} is formed by removal of a lattice oxygen atom, two electrons are left behind resulting in the reduction of two second layer Ce^{4+} ions underneath the vacancy as described in Equation 4.2 according to the Kroger-Vink notation.[46] This negative charge is expected to be localised on the Ce ions closest to the vacancy as shown by the combined STM and DFT study on native CeO_2(111) in [14], although the situation for ultrathin film ceria is not known and requires further theoretical consideration.

$$\mathrm{O_o^x} + 2\,\mathrm{Ce_{Ce}^x} \longrightarrow \mathrm{V_o^{\cdot\cdot}} + 2\,\mathrm{Ce_{Ce}^{'}} + \tfrac{1}{2}\,\mathrm{O_2} \tag{4.2}$$

A number of bright triangular features (marked **W** in Figure 4.16) are seen across the surface of the film and are centred at three-fold hollow positions between three top layer oxygen sites. From room temperature NC-AFM studies of single crystal CeO_2(111) [17], water has been shown to

adsorb solely in these same three-fold hollow sites, as illustrated in the model of Figure 4.16. Thus by comparison with the NC-AFM images, we can assign these triangular features to adsorbed water molecules, the source of water being the residual vacuum. Such adsorbed water has not previously been seen in STM studies of the $CeO_2(111)$ single crystal surface, presumably due to the elevated temperatures employed, illustrating an advantage of study at room temperature. The adsorption of water solely on the three-fold hollow sites above the Ce ions can be rationalised by considering the attraction between the partial negative charge on the polarisable water molecule and the cerium cations. Also highlighted in Figure 4.16 are a number of triangular arrangements of bright spots (marked by dashed triangles), each of which lie atop three adjacent top layer oxygen ions. The orientation of these triangular features is the opposite to that found for adsorbed water, indicating that they are centred on the third layer oxygen sub-lattice, as illustrated in the model in Figure 4.16. An analogous feature present in NC-AFM [17] was assigned as triple hydroxide clusters and we make the same assignment here. A similar feature can also be seen in Figure 4.16, marked **X**. It is also composed of a triangular protrusion centred on a third layer oxygen site. However, in this case, the triangle does not resolve into individual spots, suggesting the presence of an as yet unexplained surface feature.

The formation of multiple surface oxygen vacancies has also been observed in our films, for example in Figure 4.17, where a number of such features are highlighted. The most common multiple vacancy formation seen in our films is that of a trimer of three missing surface oxygen atoms, as seen on single crystal $CeO_2(111)$ [14, 15, 17] and also on ultra-thin ceria films grown on Rh(111) [37]. The vacancy trimers in Figure 4.17 are all oriented in the same direction, consistent with the observation by Esch et al. [14] that the only trimer arrangement seen is that which is centred on a third layer oxygen site. This arrangement results in just six Ce^{3+} cations in the second layer being exposed rather than an additional Ce^{4+} cation, and hence is a more

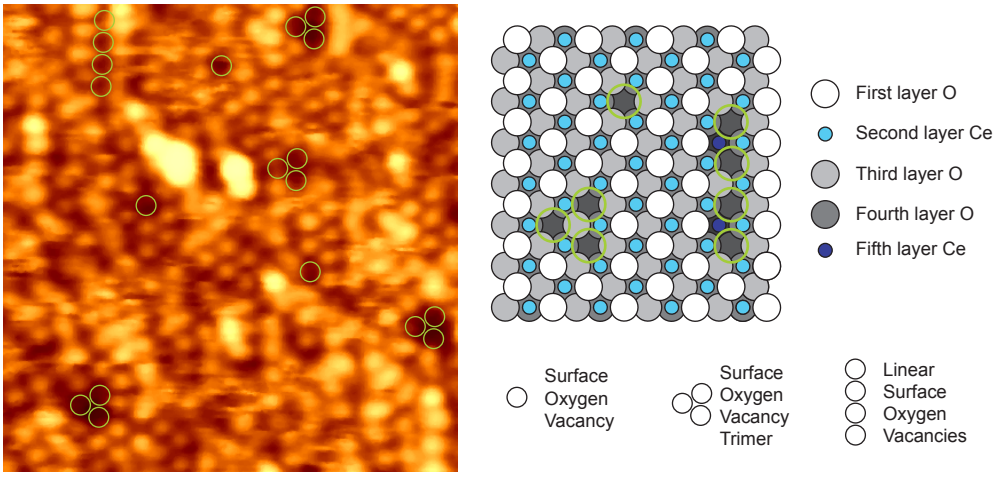

Figure 4.17: Atomically resolved, filled states, STM image (6 × 6 nm^2, V_s = -3.5 V, I_t = 0.09 nA) and structural model depicting surface oxygen vacancies on an ultrathin film of CeO_2(111) on Pt(111). Bright spots correspond to top oxygen layer, and surface O_{vac} are observed as isolated individuals, trimers, and linear arrangements as highlighted by yellow circles superimposed on the STM image. Trimers of surface oxygen vacancies are oriented such that they are centred above a third layer oxygen site for energetic reasons. The model shows the presence of additional sub-surface vacancies in a linear array as proposed by Esch et al. in [14].

stable arrangement.[47] As well as these trimers, linear surface oxygen vacancies comprising four vacancies can also be observed in Figure 4.17, and have been seen in many other images not shown here. As seen for the individual surface O_{vac} in Figure 4.16, the protrusion of the surrounding top layer oxygen atoms around these multiple vacancies is not as prominent on the ceria film compared to the single crystal, perhaps due to electronic effects of the thin film affecting the localisation of the charge that leads to such protrusions. Such multiple vacancies are proposed to be potential active sites for catalytic reactions [48] due to the large numbers of Ce^{3+} cations that are exposed to gas phase molecules.

Another common form of defect observed in images of the single crystal surface is that of a subsurface oxygen vacancy, which appears in STM and NC-AFM as three protrusions of top layer oxygen sites separated by two lattice spacings in a triangular arrangement and centred above a third layer oxygen site. [14, 20] We have also observed this type of defect as illustrated

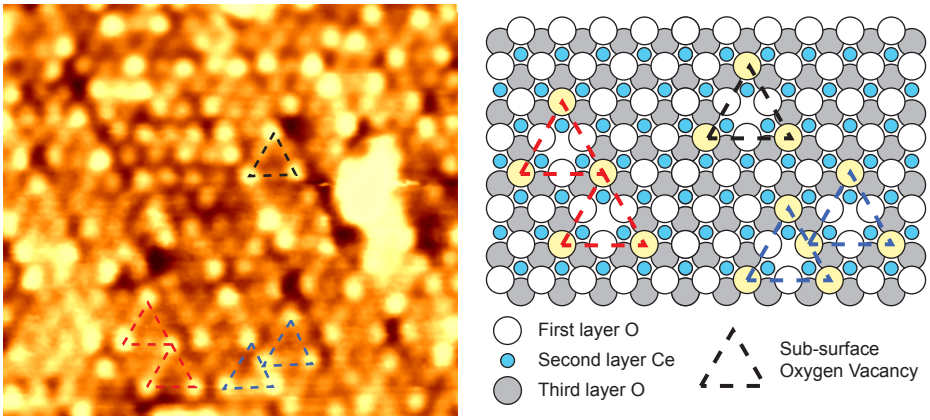

Figure 4.18: Atomically resolved, filled states, STM image (7 × 6 nm^2, V_s = -3.0 V, I_t = 0.25 nA) and structural model depicting subsurface oxygen vacancies on a single trilayer ultrathin film of CeO_2(111) on Pt(111). Bright spots in the STM correspond to top layer oxygen termination of the surface, and oxygen vacancies in the third layer result in a characteristic triangular arrangement of protrusions as highlighted by dashed triangles and bright atoms in the structural model. The coloured dashed triangles superimposed on the STM image and model highlight common configurations of the sub-surface vacancies observed: isolated (black) and adjacent (orange and red).

in Figure 4.18, where much of the surface of a ceria film is seen to display this triangular superstructure indicating a high density of such defects. The image in Figure 4.18 was taken from a region of the 0.3 nm thick ceria film shown in Figure 4.6b formed via reactive deposition in molecular oxygen. A number of these subsurface defects are highlighted in Figure 4.18 by dashed triangles with their vertices centred on the protruding oxygen atoms, demonstrating isolated vacancies (black), and two forms of adjacent vacancies (orange and red). An additional characteristic signature of these subsurface vacancies is a small inward relaxation of the other three surface oxygen ions that make up the triangular shape, [14, 20] some evidence of which is present in our images. There are a number of depressions also visible in the STM, likely surface oxygen vacancies, but due to the enhanced contrast of the subsurface vacancies, it is not possible to assign these with a high degree of confidence. Given that this film is only a single trilayer thick, the high density of these subsurface vacancies indicates the highly reduced nature of the film formed by reactive deposition under the preparation conditions used.

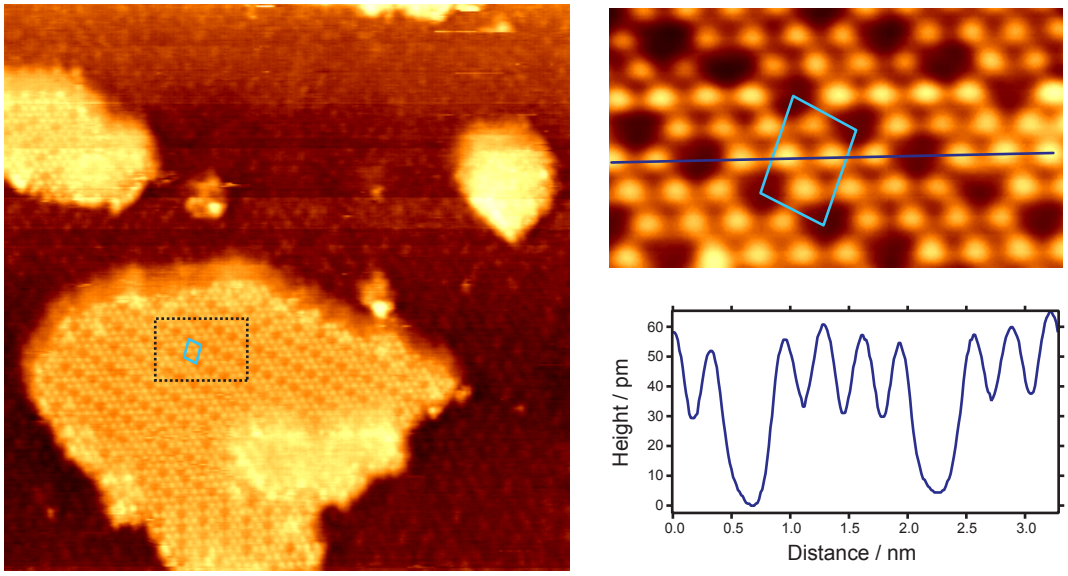

Figure 4.19: STM image (25 $\times$ 25 nm^2, V_s = -3.2 V, I_t = 0.25 nA) of a heavily reduced ceria thin film formed via reactive deposition. The majority of the surface visible is a single trilayer CeO_2(111) ultrathin film with a high concentration of subsurface oxygen vacancies (as depicted with atomic resolution in figure 4.18). Islands of the next ceria trilayer on top are observed to have linear arrays of ordered surface oxygen vacancies as shown clearly in the atomically resolved, inset 4 $\times$ 2 nm^2 STM image. The unit cell corresponding to these arrays is highlighted in blue, and indicates that a quarter of the terminating surface oxygen atoms are missing. A line profile is also presented, showing that the corrugation of oxygen atoms is measured at 20 pm, with the vacancies having an apparent depth of 50 pm.

In the partially oxidised films such as displayed in Figure 4.6b, there are a number of island structures on top of the films, which can be imaged with atomic resolution as shown in Figure 4.19. These islands which are the start of a second ceria trilayer, display an interesting structure not previously observed, that contrasts with that of the surrounding film. The surrounding film is similar in appearance to the area shown in Figure 4.18 and is a single trilayer thick. On top of the islands we observe the terminating oxygen layer with ordered single surface oxygen vacancies, their unit cell is shown in blue. This is highlighted in the inset image in Figure 4.19 and the array of defects is assigned in matrix notation as:

$$\mathrm{CeO_2}\{111\} - \begin{bmatrix} 2 & 1 \\ -1 & 2 \end{bmatrix} - \mathrm{O}_{vac} \tag{4.3}$$

A line profile across some of these defects is also displayed in Figure 4.19 and shows that the corrugation of the oxygen atoms is approximately 20 pm, with a depression of depth 50 pm observed at the vacancy site. Such a depth is consistent for a single vacancy as seen in Figure 4.16 and many others obtained on these films, as well as STM of the native single crystal $CeO_2(111)$ surface by Esch et al. in [14]. Along with this majority structure, we also observe arrays of these vacancies with rotations of 120° and 240° with respect to the above orientation on both the larger and smaller-sized islands on the film. The presence of such areas reinforces the view that ceria films formed in this way are quite highly reduced from stoichiometric CeO_2. Similar 2-dimensional arrays of triple oxygen vacancies have been previously observed for CeO_{2-x} films on Rh(111) [37] attributed to strain between the oxide and the metal support.

As mentioned before, the majority of previous STM investigations on ceria ultrathin films have been performed at positive sample biases. A primary reason for this is the instability of tips at high negative biases which in our experience means that only a small percentage of the tested tips were able to reproducibly image filled states. Empty states imaging was also attempted on our films as displayed in the series of STM images shown in Figure 4.20. Figure 4.20a shows a large area (200 $\times$ 200 nm^2) of a 0.9 ML ceria film formed by post oxidation in atomic oxygen mostly composed of ceria islands 2 trilayers thick. Figure 4.20b is an image of one of these islands (marked with a dashed square in 4.20a) that shows an interesting inversion of contrast half-way up the image due to a spontaneous tip change at the line marked with an arrow. The region marked with a dashed square is shown with atomic resolution in Figure 4.20c, where the bright protrusions, assigned

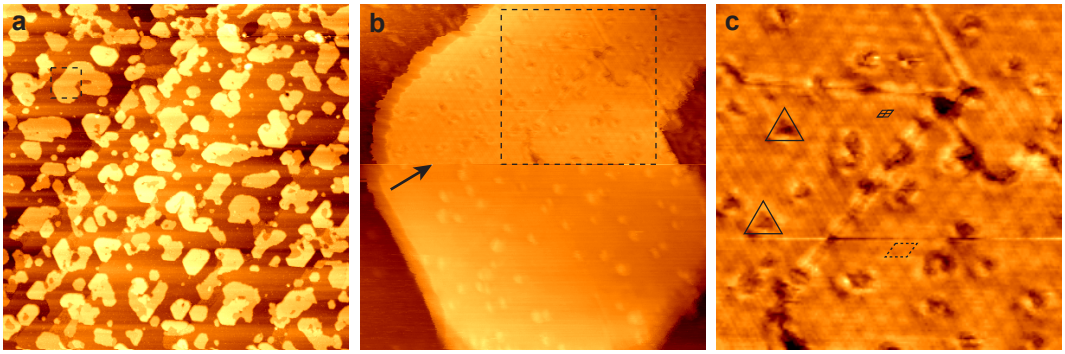

Figure 4.20: Series of STM images showing progressive stages towards achieving atomically resolved, empty states images. (a) Large scale (200 × 200 nm^2, V_s = +2.2 V, I_t = 0.10 nA) image showing general structure of a 0.9 ML ceria film formed by post oxidation in atomic oxygen. (b) STM image (30 × 30 nm^2, V_s = +2.2 V, I_t = 0.10 nA) of one of the islands on the film in (a), a tip change occurs at the line marked with an arrow leading to an inversion of contrast. (c) Atomically resolved empty states STM image (12 × 12 nm^2, V_s = +2.2 V, I_t = 0.10 nA) using the tip in the mode at the top of (b). The bright spots are assigned to the Ce atoms at the surface (unit cell marked with solid parallelogram), triple oxygen vacancies are marked with black triangles and a moiré superstructure with periodicity four times that of the lattice spacing (unit cell marked with dashed parallelogram).

to the Ce^{4+} cations, are in a hexagonal lattice with spacing of ∼0.38 nm (unit cell marked with a solid black parallelogram). Also visible is a moiré superstructure with periodicity four times that of the lattice spacing, whose unit cell is marked with a dashed parallelogram similar to what has been observed for ultrathin ceria films on Rh(111) and attributed to strain between the oxide and the metal substrate. [37] Also highlighted in 4.20c are a number of defects, most likely triple surface oxygen vacancies, marked by black triangles.

For a true comparison between the filled and empty states data in the above examples and those found in previous studies in the literature, images of the same area are required at the two bias voltages necessary to give atomic resolution for both cases. We have achieved this for a brief part of a scan, the results of which are displayed in Figure 4.21. This is a so-called dual mode image where data is recorded simultaneously both forwards and backwards along the fast scan direction (horizontal) with separate bias voltages for each. To allow us to image both filled and empty states the sample biases chosen were -3.2 V in the forward direction (lower images) and

+2.0 V in the backwards (upper images), corresponding to regions in the LDOS derived from the O^{2-} and Ce^{4+} ions respectively. For clarity the images are shown twice, one set with highlights of the salient features and the other unmarked.

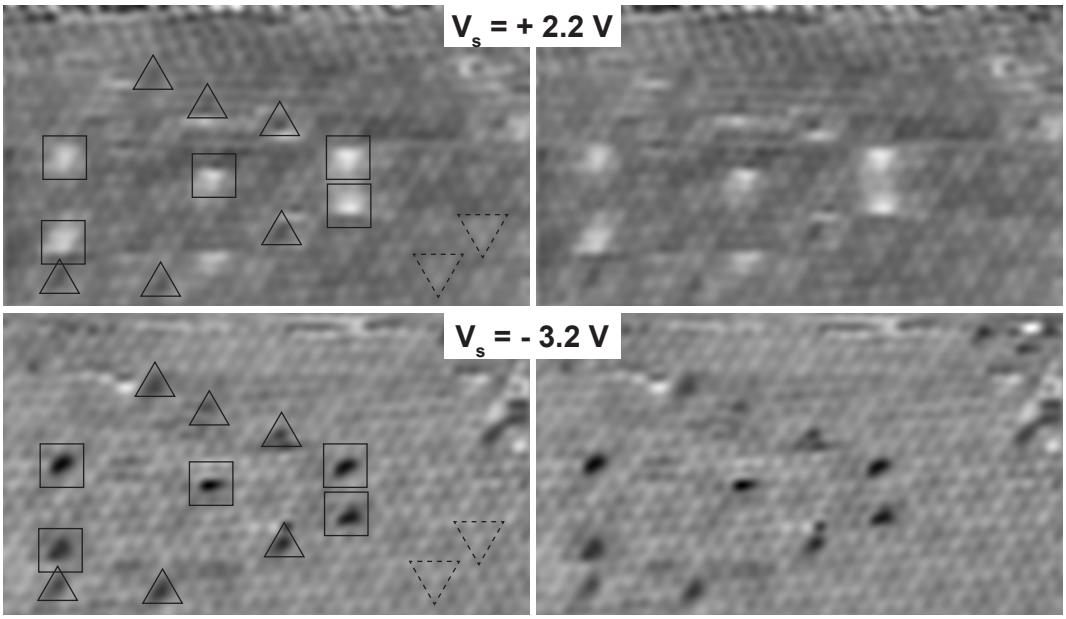

Figure 4.21: Atomically resolved, dual-mode, STM images obtained at sample biases of - 3.2 V (bottom frames) and + 2.2 V (top frames). The two sample biases chosen permit both filled and empty states imaging corresponding to states derived from the O^{2-} and Ce^{4+} ions, respectively. Various oxygen vacancies are observed and the images are displayed twice for clarity; once unaltered and once with highlighted features. (7×6 nm^2, V_s = -3.2 / + 2.2 V, I_t = 0.25 nA)

Both images have a hexagonal lattice of bright spots, with spacings of 0.38 nm, consistent with LEED and earlier STM results. By superimposing the two frames (not shown) it is possible to see that the bright features in one coincide with the dark holes in the other, allowing us to assign the bright features in the filled states image (lower) to the O^{2-} anions, and the bright features in the empty states image (upper) to the Ce^{4+} cations. There is a repeating motif of a triangle of slightly brighter spots visible in the empty states images (marked by inverted dashed triangles) with a slightly different pattern in the filled states, likely some sort of moiré interference

pattern commonly found on such films. The imaging quality of the defects is not great and firm identification is not possible at this stage, although a number of preliminary observations can be made. In the filled states images we observe a number of dark depressions similar to single surface O_{vac} observed elsewhere on the ceria films and highlighted by the solid triangles and squares. At the corresponding locations in the empty states image, there are two types of feature observed. The first is an increased brightness of three of the Ce ions underneath the proposed O_{vac} (as observed by Esch et al. on native CeO_2(111) [14]) and marked in our images by black squares. The second feature is characterised by dark spots in the empty states image between the positions of the Ce ions at the same location as the depression in the filled states image. The origin of this contrast is not known. Clearly the identification of the precise nature of the defects observed in Figure 4.21 is far from complete - this is primarily due to a lack of good quality data; finding a tip that is able to scan in this dual mode is extremely rare (a voltage switch of magnitude 5.2 V is occurring at the start and end of each line of the scan, requiring an extremely stable tip). One method of improving this sort of work would be to carry out STM at low temperatures, possibly permitting more stable tunnelling conditions. As commonly seen in STM results on TiO_2 surfaces, the imaging mode of the tip plays an important role in determining the contrast observed in the images; to fully understand the nature of the point defects observed in Figure 4.21, a full theoretical model of the system is required along with calculated STM images, a good avenue for further work.

4.3.8 Mobility of Defects and Adsorbates

The behaviour of small molecules, especially water, with the various point defects on the ceria surface is of vital importance in understanding the basic reactivity of the surface, as can be seen

with the great amount of work dedicated to the understanding of such effects on another important catalyst surface, that of rutile TiO_2(110) including examples found in [45, 49, 50]. There are no studies on defects and molecular adsorbates on the surface of ceria ultrathin films using STM and the picture when it comes to the native CeO_2(111) surface is also still not clear, providing great opportunities for future investigations. The mobility of defects on ceria is somewhat disputed: Namai et al. [18] appeared to observe the diffusion of surface O_{vac} across the native CeO_2(111) surface at room temperatures, whereas Esch et al. [14] did not observe any such diffusion for temperatures below 673 K. This discrepancy was explained by adsorbate-mediated diffusion. [14, 20] Theoretical studies have predicted that water molecules should dissociate rapidly in the presence of O_{vac} on the ceria surface such that the two species should not be found simultaneously [51], a claim contrary to the observations by NC-AFM on the native CeO_2(111) [16] where adsorbed water molecules show low mobility and coexist with vacancies, although are observed to undergo dissociation on occasion.

In our experiments, we do not observe significant movement of single or multiple, surface or subsurface O_{vac} for the duration of scanning (minutes) at room temperature. There is, however, some movement of water molecules and other adsorbate species. This mobility is demonstrated in Figure 4.22 which is a series of three sequential, atomically resolved, STM images of the same 8×8 nm^2 area of a ceria film taken at 400 s intervals. For clarity the images are presented as the raw data on top and with highlighted features on the bottom. The fast scan direction is horizontal for all these images. Due to slight thermal or piezo drift during the course of each scan, the images are slightly out of registry with each other and an individual surface O_{vac} (marked with a yellow circle) as well as a line of surface O_{vac} (marked with a yellow line) have been highlighted to provide common points across all three images. Whilst these O_{vac} remain unaltered throughout the scan, the surface O_{vac} marked with a blue hexagon and labelled ‘a’ is observed to move a

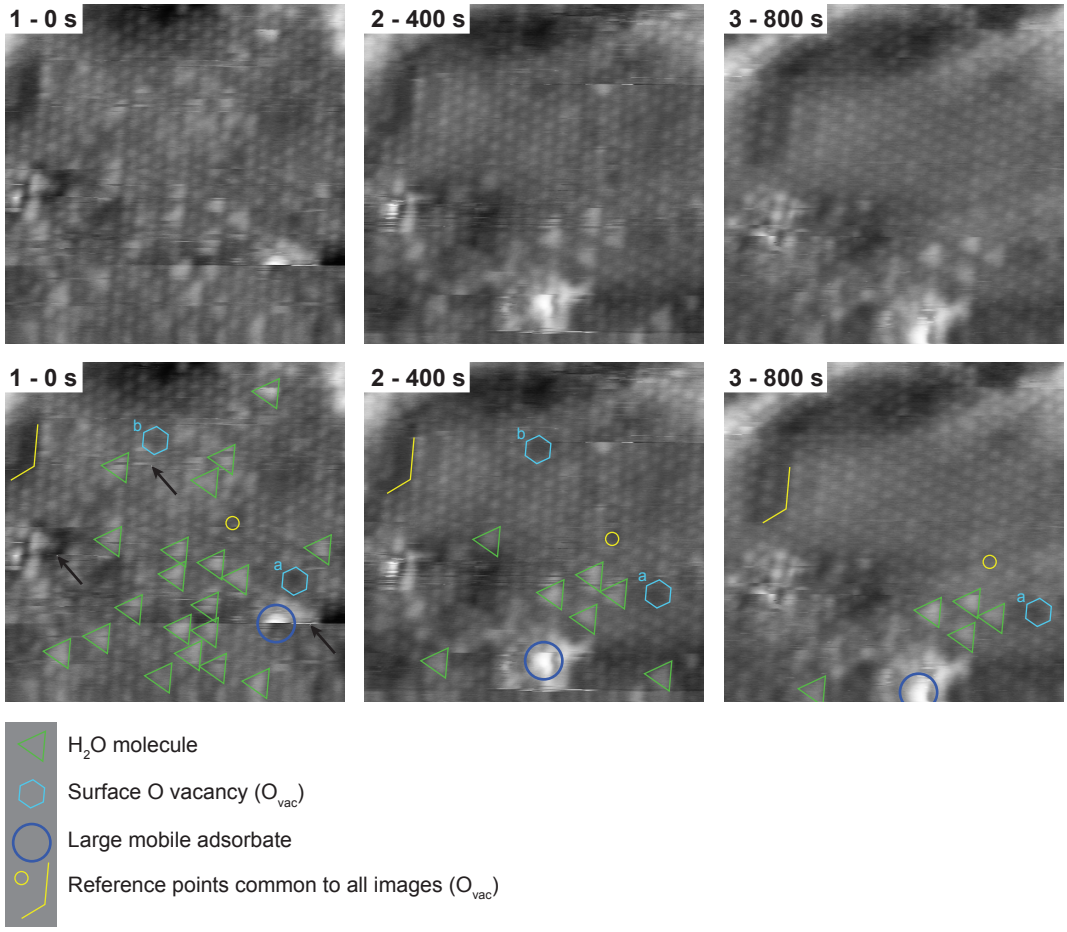

Figure 4.22: Sequence of STM images obtained at 400 second intervals displaying the tip-enhanced mobility of water molecules and other adsorbates on an ultrathin CeO_2(111) film. The density of water molecules (marked with green triangles) is observed to dramatically reduce after two frames, likely by interaction with the STM tip as evidenced by the heavy streaking in the fast scan direction (horizontal). A surface oxygen vacancy (marked with hexagon labelled b) is observed to become filled during the course of these scans probably by one of these water molecules. A large adsorbate (marked with purple circle) is also observed to move down the frame. (8×8 nm^2, V_s = -3.2 V, I_t = 0.24 nA)

single lattice spacing to the left between the first and second images. The origin of such movement is not clear, and this movement of O_{vac} has not been observed in our other experiments due primarily to the difficulty in achieving stable atomic resolution imaging for sequential areas at the bias voltages used. As mentioned earlier, such hopping of oxygen atoms is thought to be either tip or adsorbate mediated. The other O_{vac} marked with a blue hexagon (labelled 'b') is observed to be filled between frames two and three, again the mechanism of this is not clear, but it could be the result of an encounter with an adsorbed water molecule, perhaps with dissociation as observed on TiO_2(110) [45] although there is no sign of the resultant hydrogen atoms that are expected and are observed in NC-AFM studies of the native surface.[16].

The interaction of water with ceria surfaces is important, especially in consideration of the action during the water-gas-shift reaction. It was shown earlier in Figure 4.16, that water from the residual background is observed to adsorb on our ultrathin films and appear as bright triangles above three lattice oxygens always oriented in the same direction, consistent with their binding only on sites directly above the Ce ions underneath. In the first image (0 s) of Figure 4.22, 20 such molecules can be clearly identified (highlighted with green triangles), with a number of other possible candidates obscured by tip-induced streaking. On most of the these molecules there is clear tip interaction characterised by streaks and scanning instability (indicated by black arrows) in the fast-scan direction and by the second frame (400 s), there are only seven molecules in this area of the film. By the third frame (800 s) of scanning over the same location, only five water molecules can be identified, and the top half of the image is completely clear of adsorbates. Such a sequence of images provides a clear demonstration that water can be moved easily across the ceria surface by the tip and such a considerable interaction also manifests itself in instability while scanning, such that tips are often only capable of atomic resolution imaging for a few hours at most. Indeed after this sequence of three images, the tip underwent a change such that it was no

longer able to provide a clear image of this part of the surface. In addition to this tip influenced mobility of water, a tall adsorbate of unknown identity (marked by a purple circle) is also observed to move during the course of these scans, interestingly the major movement is not in the direction of fast-scan (horizontal) but rather at right angles to this.

4.4 Summary and Conclusions

We have used scanning tunnelling microscopy in combination with low energy electron diffraction and Auger electron spectroscopy, to characterize ultrathin films of CeO_2(111) supported on Pt(111). The films were prepared in a number of ways to identify the most appropriate growth procedure to form films suitable for high-resolution STM measurements. Post-oxidation of Pt/Ce surface alloys was employed using molecular and atomic oxygen, whilst multi- and single-stage reactive deposition in atomic and molecular oxygen was compared and contrasted. All methods gave films with similar structure although in general the use of atomic oxygen proved more controllable and allowed reproducible growth of films with large terraces best suited for STM. Atomically resolved images (of both filled and empty states) of films prepared by these methods revealed remarkable similarities to images recorded in previous studies on CeO_2(111) single crystals using NC-AFM and high temperature STM. Surface oxygen vacancies were imaged both individually, as trimers, and in linear arrays. Subsurface oxygen vacancies were also detected. Adsorbed water molecules and surface hydroxide trimers were also imaged, again with a similar appearance to that seen on native CeO_2(111). The mobility of such adsorbates at room temperature was investigated and shown primarily to be due to interactions with the STM tip. The electronic structure of such ultrathin films was investigated with scanning tunnelling spectroscopy and a clear band gap was observed with a slightly lower size than for bulk CeO_2. As a result of these studies, we conclude that ultrathin ceria films supported on Pt(111) make excellent topographic models for the native oxide as well as interesting materials in their own right.

References

[1] Grinter, D. C.; Ithnin, R.; Pang, C. L.; Thornton, G. *J. Phys. Chem. C* **2010**, *114*, 17036–17041.

[2] Matharu, J.; Cabailh, G.; Lindsay, R.; Pang, C. L.; Grinter, D. C.; Skála, T.; Thornton, G. *Surf. Sci.* **2011**, *605*, 1062–1066.

[3] Deluga, G.; Salge, J.; Schmidt, L. *Science* **2004**, *303*, 993–997.

[4] Trovarelli, A. *Catalysis by Ceria and Related Materials*, Catalytic Science Series; Imperial College Press, 2002.

[5] Gorte, R. J. *AIChE J* **2010**, *56*, 1126–1135.

[6] Bernal, S.; Calvino, J.; Cauqui, M.; Gatica, J.; Larese, C.; Omil, J. P.; Pintado, J. *Cat. Today* **1999**, *50*, 175–206.

[7] Pfau, A.; Schierbaum, K.-D. *Surf. Sci.* **1994**, *321*, 71–80.

[8] Mullins, D. R.; Overbury, S. H.; Huntley, D. *Surf. Sci.* **1998**, *409*, 307–319.

[9] Fu, Q.; Saltsburg, H.; Flytzani-Stephanopoulos, M. *Science* **2003**, *301*, 935–938.

[10] Liu, Z.; Jenkins, S. J.; King, D. A. *Phys. Rev. Lett.* **2005**, *94*, 196102.

[11] Zhang, C.; Michaelides, A.; King, D. A.; Jenkins, S. J. *J. Phys. Chem. C* **2009**, *113*, 6411–6417.

[12] Berner, U.; Schierbaum, K.-D. *Phys. Rev. B* **2002**, *65*, 235404.

[13] Conesa, J. *Surf. Sci.* **1995**, *339*, 337–352.

[14] Esch, F.; Fabris, S.; Zhou, L.; Montini, T.; Africh, C.; Fornasiero, P.; Comelli, G.; Rosei, R. *Science* **2005**, *309*, 752–755.

[15] Norenberg, H.; Briggs, G. *Phys. Rev. Lett.* **1997**, *79*, 4222–4225.

[16] Gritschneder, S.; Iwasawa, Y.; Reichling, M. *Nanotech.* **2006**, *18*, 044025.

[17] Gritschneder, S.; Reichling, M. *Nanotech.* **2007**, *18*, 044024.

[18] Namai, Y.; Fukui, K.; Iwasawa, Y. *Cat. Today* **2003**, *85*, 79–91.

[19] Fukui, K.; Namai, Y.; Iwasawa, Y. *Appl. Surf. Sci.* **2002**, *188*, 252–256.

[20] Torbrügge, S.; Reichling, M.; Ishiyama, A.; Morita, S.; Custance, O. *Phys. Rev. Lett.* **2007**, *99*, 056101.

[21] Torbrügge, S.; Cranney, M.; Reichling, M. *Appl. Phys. Lett.* **2008**, *93*, 073112.

[22] Freund, H.-J. *Farad. Disc.* **1999**, *114*, 1–31.

[23] Lu, J.; Gao, H.-J.; Shaikhutdinov, S.; Freund, H.-J. *Surf. Sci.* **2006**, *600*, 5004–5010.

[24] Mullins, D. R.; Radulovic, P.; Overbury, S. H. *Surf. Sci.* **1999**, *429*, 186–198.

[25] Alexandrou, M.; Nix, R. *Surf. Sci.* **1994**, *321*, 47–57.

[26] Eck, S.; Castellarin-Cudia, C.; Surnev, S.; Ramsey, M.; Netzer, F. P. *Surf. Sci.* **2002**, *520*, 173–185.

[27] Wilson, E. L.; Chen, Q.; Brown, W.; Thornton, G. *J. Phys. Chem. C* **2007**, *111*, 14215–14222.

[28] Xiao, W.; Guo, Q.; Wang, E. *Chem. Phys. Lett.* **2003**, *368*, 527–531.

[29] Matolín, V.; Libra, J.; Matolínová, I.; Nehasil, V. *Appl. Surf. Sci.* **2007**, *254*, 153–155.

[30] Staudt, T.; Lykhach, Y.; Hammer, L.; Schneider, M. A.; Matolín, V.; Libuda, J. *Surf. Sci.* **2009**, *603*, 3382–3388.

[31] Berner, U.; Schierbaum, K.-D. *Thin Sol. Films* **2001**, *400*, 46–49.

[32] Wilson, E. L.; Grau-Crespo, R.; Pang, C. L.; Cabailh, G.; Chen, Q.; Purton, J. A.; Catlow, C. R. A.; Brown, W.; de Leeuw, N. H.; Thornton, G. *J. Phys. Chem. C* **2008**, *112*, 10918–10922.

[33] Krasnikov, S. A.; Murphy, S.; Berdunov, N.; McCoy, A. P.; Radican, K.; Shvets, I. V. *Nanotech.* **2010**, *21*, 335301.

[34] Baddeley, C.; Stephenson, A.; Hardacre, C.; Tikhov, M. *Phys. Rev. B* **1997**, *56*, 12589–12598.

[35] Essen, J.; Becker, C.; Wandelt, K. *e-J. Surf. Sci. Nanotech.* **2009**, *7*, 421–428.

[36] Schierbaum, K.-D. *Surf. Sci.* **1998**, *399*, 29–38.

[37] Castellarin-Cudia, C.; Surnev, S.; Schneider, G.; Podlucky, R.; Ramsey, M.; Netzer, F. P. *Surf. Sci.* **2004**, *554*, L120–L126.

[38] Nilius, N. *Surf. Sci. Rep.* **2009**, *64*, 595–659.

[39] Briggs, D.; Seah, M. P. *Practical Surface Analysis: Auger and X-ray Photoelectron Spectroscopy;* Wiley-Blackwell, 1994.

[40] Simon, G. H.; Koenig, T.; Rust, H.-P.; Heyde, M.; Freund, H.-J. *New J Phys* **2009**, *11*, 093009.

[41] Shao, X.; Jerratsch, J.-F.; Nilius, N.; Freund, H.-J. *Phys. Chem. Chem. Phys.* **2011**, (27), 12646–12651.

[42] Jerratsch, J.-F.; Shao, X.; Nilius, N.; Freund, H.-J.; Popa, C.; Ganduglia-Pirovano, M. V.; Burow, A. M.; Sauer, J. *Phys. Rev. Lett.* **2011**, *106*, 246801.

[43] Wuilloud, E.; Delley, B.; Schneider, W.; Baer, Y. *Phys. Rev. Lett.* **1984**, *53*, 202–205.

[44] Silva, J. L. F. D. *Phys. Rev. B* **2007**, *76*, 193108.

[45] Bikondoa, O.; Pang, C. L.; Ithnin, R.; Muryn, C. A.; Onishi, H.; Thornton, G. *Nat. Mat.* **2006**, *5*, 189–192.

[46] Nolan, M.; Parker, S. C.; Watson, G. W. *Surf. Sci.* **2005**, *595*, 223–232.

[47] Zhang, C.; Michaelides, A.; King, D. A.; Jenkins, S. J. *Phys. Rev. B* **2009**, *79*, 075433.

[48] Campbell, C. T.; Peden, C. H. F. *Science* **2005**, *309*, 713–714.

[49] Diebold, U. *Surf. Sci. Rep.* **2003**, *48*, 53–229.

[50] Pang, C. L.; Sasahara, A.; Onishi, H.; Chen, Q.; Thornton, G. *Phys. Rev. B* **2006**, *74*, 073411.

[51] Watkins, M.; Foster, A.; Shluger, A. *J. Phys. Chem. C* **2007**, *111*, 15337–15341.

CHAPTER 5

GOLD SUPPORTED ON CeO_2(111) ULTRATHIN FILMS

Abstract

The behaviour of individual gold atoms at room temperature on ultrathin CeO_2(111) films on Pt(111) has been investigated with scanning tunnelling microscopy and their adsorption sites identified. The ceria films were prepared by post-oxidation of Pt/Ce surface alloys in atomic oxygen, yielding high quality surfaces with high densities of surface oxygen vacancies proposed as good nucleation sites for gold adsorption. The application of atomically resolved STM of a gold adatom simultaneously with the filled states of the ceria permitted observation that the gold adatoms interact heavily with the tip and exist on two types of adsorption site: (i) atop an oxygen and (ii) in a three-fold hollow oxygen site, and are generally immobile at room temperature.

5.1 Introduction

Prized for thousands of years for its stability and unreactiveness, gold would seem to be an unlikely candidate for use as a catalyst. Surprisingly, gold single-atoms and nanometre-sized particles have shown great catalytic activity for a number of applications ranging from CO oxidation to the hydrogenation of alkenes.[1–3] Many of these promising catalytic systems rely on a metal-oxide support such as TiO_2 and SiO_2, raising interesting questions regarding the role of the oxide support and the nature of any interactions between it and the gold.[4] Of particular interest is the recent discovery that Au nanoparticles supported on ceria are a highly active catalyst at low temperatures for the water-gas-shift reaction, important for the economic production of hydrogen.[5] The catalytic properties of ceria are well-documented with applications including exhaust gas purification in automotive catalytic converters amongst many others.[6–9]

Many of the advantageous properties of ceria are a result of the high mobility of lattice oxygen which leads to excellent oxygen storage and release during catalysis due to the facile reduction and re-oxidation of Ce^{4+} to Ce^{3+}, as well as the promotion of noble metal activity. [10] This mobility is in part determined by the defect structure of the oxide, including oxygen vacancies which are well known to be key to the reactivity of metal oxides and are also important in the binding of metal nanoparticles. [5, 11–13]

The origin of the catalytic properties of gold is not fully understood although it is now generally accepted that key factors influencing such activity include the size and shape of the particles, the degree of unsaturation and the interaction with the oxide support.[14, 15] There is a large body of both theoretical [11, 12, 16–23] and experimental work [3–5, 13, 24–37] examining the

mechanism of action of the Au/CeO_2(111) system. The limitations in accurately modelling the strongly-correlated Au/CeO_2(111) system with density functional theory (DFT) are also well-documented [16] and as such a definitive description of the relative stabilities of the possible nucleation sites and oxidation states of single gold atoms is not possible. One observation of these calculations has been that single gold atoms are rather weakly bound to the CeO_2(111) surface and therefore we might expect that at the temperature of our experiments (300 K) they are highly mobile. STM results of Au/CeO_2(111) have so far indicated a preference for nucleation of gold at step edge sites on fully oxidised films and terrace sites (likely oxygen vacancies) on more reduced ones,[24, 37, 38] although there are no high-resolution studies on the binding of single atoms to date. Another key area of debate has been regarding the oxidation state of the gold within the active catalyst and there is conflicting experimental evidence in the literature as to whether the gold is neutral or cationic during reactions.[2, 5, 16]

Scanning tunnelling microscopy (STM) is a very useful tool for the study of surfaces and adsorbates with the resolution required for investigating the individual point defects that are suspected to be key to the catalytic activity. Stoichiometric CeO_2 is insulating with a band gap of $\sim$ 6 eV and although some high-temperature STM studies have been carried out, [39, 40] a successful approach for studies at room temperatures has been to use an ultrathin film on a conducting metal substrate.[41] A number of metal supports have been demonstrated to be suitable for the growth of CeO_2(111) and its investigation by STM including Ru(0001) [42, 43], Rh(111) [44, 45], Cu(111) [46] and Pt(111) [47–50]. The suitability of such ultrathin films as models for the true oxide surface is often debated, especially with regards to differences in the electronic structure.[51] Thin films of CeO_2(111) have been shown to display similar point defect structures [52], notably those of surface and sub-surface oxygen vacancies [49] that suggest a good topographical match with those found on the surface of the bulk oxide.

The first efforts at forming an understanding of the behaviour of Au on $CeO_2(111)$ surfaces has been to study the behaviour of large clusters on the surface, in what can perhaps be termed a "top-down" approach. [24, 37, 38] In contrast to this, we have analysed the behaviour of single atoms of gold on reduced, highly defective, $CeO_2(111)$ in order to understand their bonding and properties. Ultrathin films of $CeO_2(111)$ were prepared on a Pt(111) substrate via a post-oxidative procedure and characterised by STM, AES and LEED. Gold atoms were then adsorbed onto the film via PVD and STM used to examine the results.

5.2 Experimental Procedure

The experiments were carried out on a commercial AFM/STM (*Omicron*) situated in a UHV system with a base pressures of 1×10^{-11} mbar. STM images were recorded in constant current mode at room temperature with electrochemically etched tungsten tips conditioned in-vacuum by annealing to 400 K, Ar^+ sputtering (0.5 keV) and by voltage pulses during scanning.

The Pt(111) substrate was prepared by cycles of Ar^+ sputtering (1.5 keV) and annealing at 1100 K in UHV until a well-ordered Pt(111)(1×1) pattern was observed in LEED and impurities were below the detection limit of AES. Occasional cycles of annealing at $\sim$1000 K in 1×10^{-7} mbar O_2 were also performed in order to remove minor carbon contamination. The ceria ultrathin film was prepared by a post-oxidative route, found to be the most reliable route for the formation of large, flat terraces of $CeO_2(111)$ suitable for high-resolution STM investigations. For this method cerium metal (*Alfa Aesar*, 99.9%) was evaporated onto the clean Pt(111) substrate at 300 K via physical vapour deposition (PVD) from an electron-bombardment type evaporator and

then annealed in UHV at 990 K for 5 minutes. Further annealing to 970 K in an atomic oxygen pressure of 1.7×10^{-7} mbar (*Tectra Ion Source*) for 2 minutes led to the formation of an epitaxial $CeO_2(111)$ ultra-thin film with a (1.37 $\times$ 1.37) LEED pattern in registry with Pt(111)(1 $\times$ 1). Temperatures were monitored with an optical pyrometer (*Minolta*).

Gold was deposited onto these ultrathin ceria films at room temperature via PVD from a commercial evaporator (Compact Vapour Source, J. Taylor & C. Nicklin) where gold wire (Advent RM, 99.9%) is contained within an alumina crucible, heated by a tungsten filament. The doser was calibrated by STM measurements after deposition onto rutile $TiO_2(110)$ and the purity of the evaporated gold checked by Auger electron spectroscopy. Due to the O-Ce-O trilayer structure of $CeO_2(111)$, we define a film monolayer (ML) as one trilayer unit with a thickness of 0.31 nm. The films do not completely cover the Pt substrate and therefore the coverage is estimated from the film thickness and the surface area fraction measured by STM. For the gold atoms and clusters it is useful to define the coverage in terms of that of the Au(111) surface, leading to a ML being defined as 1.4 $\times 10^{-15}$ atoms cm^{-2} as in [24].

5.3 Results and Discussion

The growth and characterisation of ultrathin ceria films on platinum has been extensively covered in the previous chapter of this work, including their defect structure. Due to the importance of oxygen vacancies on the reactivity of oxides, and especially for the nucleation of adsorbed metal atoms and clusters, the post-oxidative preparation method using atomic oxygen and short oxidation times gave a good combination of large ceria terraces with a high density of surface

oxygen vacancies, including the ordered arrays as observed in [49].

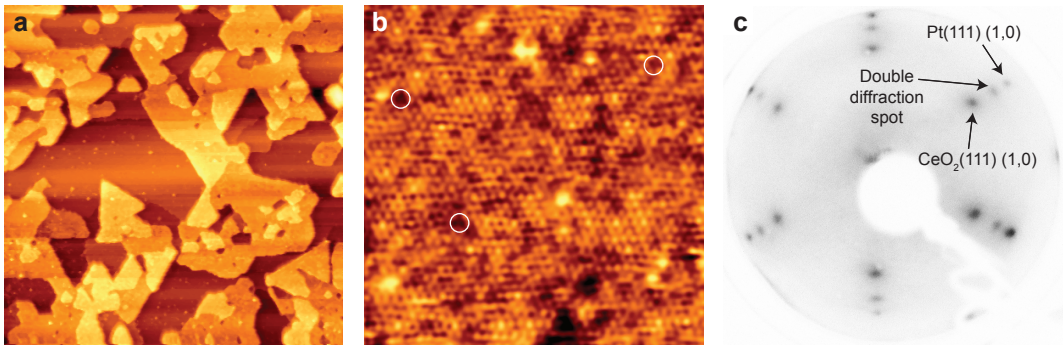

Figure 5.1: STM and LEED images of a 1.5 ML ultrathin CeO_2(111) film on Pt(111) before dosing with Au. (a) Large scale STM image of the film displaying geometric ceria islands two trilayers thick. (200 × 200 nm^2, V_s = -3.2 V, I_t = 0.10 nA) (b) Atomically resolved STM image with a high density of surface oxygen vacancies (highlighted with circles). (15 × 15 nm^2, V_s = -3.2 V, I_t = 0.10 nA) (c) 62.3 eV LEED image displaying Pt(111)(1 × 1), CeO_2(111) (1.36 × 1.36) and double diffraction spots at (1.15 × 1.15).

Figure 5.1 shows the results of this preparation method, with an 1.5 ML CeO_2(111) ultrathin film formed whose large-scale structure can be seen in the STM image in Figure 5.1a. The film consists of well ordered, geometric islands of CeO_2(111) 0.6 nm thick, corresponding to 2 Ce-O-Ce trilayers. An atomically resolved image on top of one of the islands is presented in Figure 5.1b, with the bright spots in the filled states image corresponding to the oxygen atoms that terminate the oxide. The high density of surface oxygen vacancies characterised by dark spots on the oxygen lattice, some of which have been marked with circles, provides a large number of possible nucleation sites for the gold. A low energy electron diffraction pattern of this film (62.3 eV) is shown in Figure 5.1c and shows the expected reflexes from the substrate Pt(111)(1 × 1) and CeO_2(111)(1.36 × 1.36) commensurate with it. There exists a slight contraction from the ceria bulk lattice parameter due to the strain within the film, as often observed for such low-coverage films. An interesting additional feature of the LEED pattern for this film was the presence of intermediate reflexes at (1.15 × 1.15) relative to Pt(111)(1 × 1). These are likely due either to

multiple scattering or the presence of some un-oxidised Pt/Ce alloy.

5.3.1 Large-Scale Imaging and Tip Convolution Effects

The results of a short dose of Au onto the ceria film shown in Figure 5.1 are displayed in Figure 5.2 which shows a raw STM image of the gold-dosed film (a) and an image with the evaporated gold clusters highlighted (b). All of the ceria islands on this section of the film are 2 trilayers thick, and there is an even distribution of gold clusters (small bright features) across the top surface of the islands with no preferential nucleation at their edges. The gold is observed to adsorb almost exclusively on the ceria islands rather than the Pt(111) substrate, possibly due to its increased mobility on the metal surface inhibiting their appearance in STM.

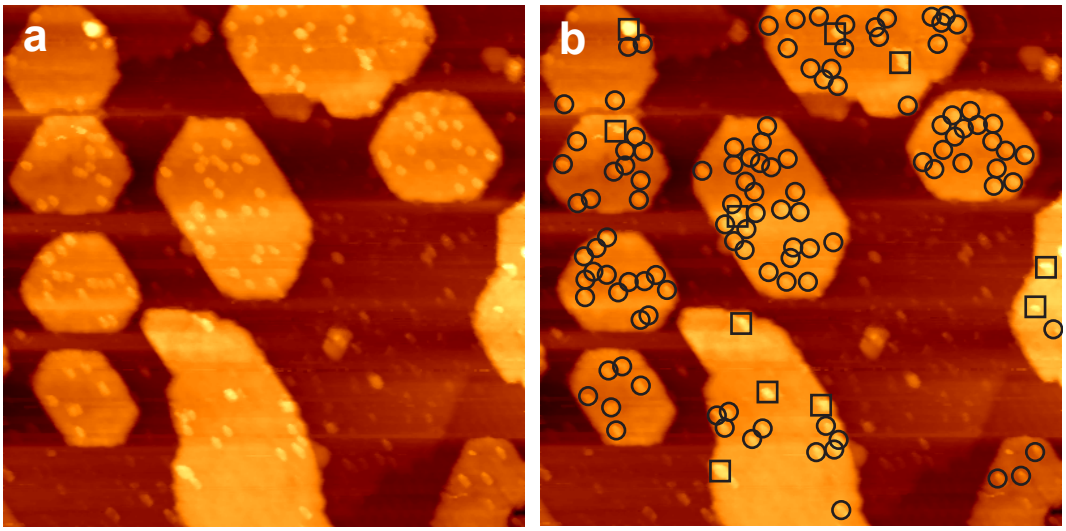

Figure 5.2: (a) Large scale STM images of 0.07 ML Au on a 1.5 ML ultrathin CeO_2(111) film on Pt(111) (100 $\times$ 100 nm^2, V_s = -3.2 V, I_t = 0.05 nA) The same image is shown in (b) with 0.2 nm high gold adatoms highlighted with black circles and larger clusters marked with black squares. The atoms are observed to nucleate evenly across the top of the ceria islands with no preference for step edges.

The gold adsorbates can be divided into two different groups dependent on their height - those marked with circles in Figure 5.2b, which make up the vast majority, have a height of ∼0.2 nm; and those marked with squares are larger with heights between 0.3-0.8 nm. The width of all the features is ∼2 nm, however this is much increased from their true size due to tip-convolution effects. The features with heights ∼0.2 nm have a density of 0.01 nm^{-2} which, assuming each is an individual gold atom, corresponds to an approximate total coverage of ∼0.07 ML. We assign the larger features to clusters of a few gold atoms, whose behaviour has been studied in some detail in previous works.[24, 35, 38] The lack of nucleation at step edge sites on our films contrasts with the observations of Baron et al. of Au deposition on reduced ceria films where despite preferential nucleation on top of the terraces compared with the fully oxidised films, there was still a significant number of particles at the edges.[24] As mentioned previously, our films are heavily reduced and contain many oxygen vacancies which are proposed to stabilise the nucleation and trap the gold atoms and particles leading to nucleation on top of the terraces. It must also be considered that the films in [24] are significantly thicker and completely cover the metal substrate and as a result the step edges are single ceria trilayers onto a lower terrace of CeO_2(111) in comparison to our islands which are two trilayers thick and lead straight to the metal. Due to the low coverage of gold investigated, no change was apparent in the LEED pattern of the Au/CeO_2(111)/Pt(111) system, and in AES measurements the Au LMM and KLL peaks are superimposed on those of the Pt substrate preventing clear assignment.

When making STM measurements of adsorbed atoms and small clusters it is important to always consider the effects of tip-convolution due to the similar sizes of the tip apex and the features on the surface. Such convolution often manifests itself as a broadening of the observed width of the feature, in some cases upto double the actual size. In our STM observations we had many difficulties avoiding such effects, and even more dramatic widening as demonstrated in Figure

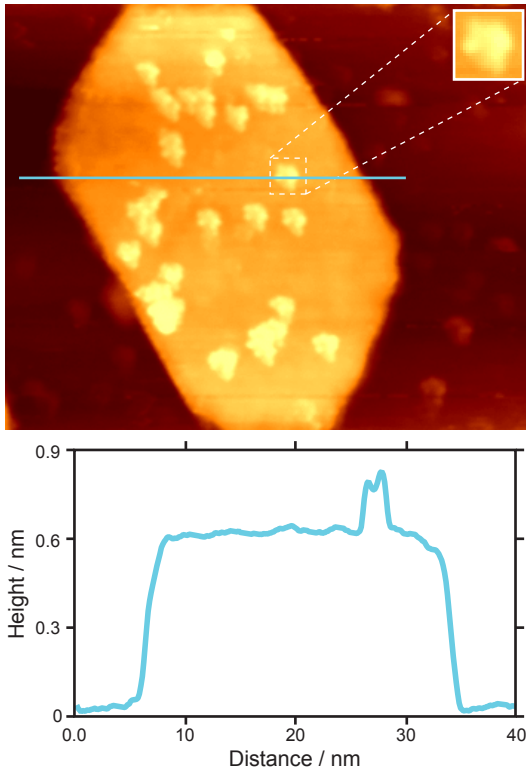

Figure 5.3: STM image and associated line profile of Au adatoms on a 1.5 ML ultrathin CeO_2(111) film on Pt(111) demonstrating the effects of tip convolution with the gold adatoms. The repeated motif is shown in the inset image and leads to overestimation of width and coverage at larger scan sizes. From the line profile, the ceria island is observed to be two trilayers thick (0.6 nm) and the gold atom ~0.2 nm tall. (40 × 40 nm^2, V_s = -3.2 V, I_t = 0.05 nA)

5.3, a zoomed-in image of one of the ceria islands with Au atoms on top. A repeated motif (as shown in inset image) is visible on top of each individual atom, and it is clear that in effect the gold atoms are scanning the tip, and it is the tip apex itself which is imaged. Also presented in Figure 5.3 is a line profile across the island and one of the clusters, clearly showing that the ceria is 0.6 nm thick (2 trilayers) and the tallest point of the gold is ~0.2 nm tall. Such tip convolution is often not apparent at large scan sizes and can often lead to over-estimation of coverage and particle size. Such tip convolution artefacts were extremely common on this system, due to the significant interactions between the tip and the gold adatoms. One of the methods to clear up a tip causing significant convolution is to perform voltage pulses with the tip. An example of the results of such a pulse is presented in Figure 5.4 where a + 10 V pulse has been applied on top of

one of the ceria islands near the centre of the frame, and an STM image taken of the surrounding area immediately afterwards.

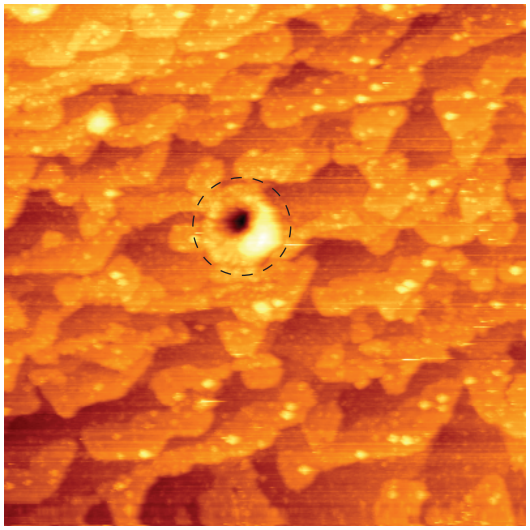

Figure 5.4: Large scale STM image of 0.07 ML Au on a 1.5 ML ultrathin CeO_2(111) film on Pt(111) after a + 10 V tip pulse has been applied to the centre of the frame. The voltage pulse makes a hole in the surface (likely due to a tip crash) and deposits a large amount of material within the area of the dashed circle. (200 × 200 nm^2, V_s = -3.2 V, I_t = 0.10 nA)

The effects of the tip pulse are relatively dramatic - the tip appears to have crashed into the surface, making a hole $\sim$ 2 nm deep, and affecting an area $\sim$ 25 nm in diameter (shown by dashed circle). A significant amount of material has been deposited by the tip and forms a small pile to the bottom right of the hole $\sim$ 1 nm tall. The shape of the tip apex will have been changed a lot by such pulsing and it is hoped that the resultant apex will be more stable and display less convolution with adsorbates although this is not always the case. The STM image in Figure 5.4 is the first frame obtained after the pulse, and it can be seen that the image quality is relatively poor as evidenced by the low resolution on the gold adatoms and the lack of sharpness in imaging the edges of the ceria islands. In this case, further tip conditioning by pulsing was carried out before the imaging had stabilised and it was possible to attempt to obtain atomically resolved images.

5.3.2 Gold Single Atoms - Nucleation and Mobility

After many hours of scanning and conditioning tips it was possible to obtain images of isolated gold adatoms that are immobile on the CeO_2(111) surface with minimal tip convolution, as shown in Figure 5.5. This image was obtained by scanning at an extremely slow rate (20 seconds per line) as part of a current imaging tunnelling spectroscopy (CITS) measurement.

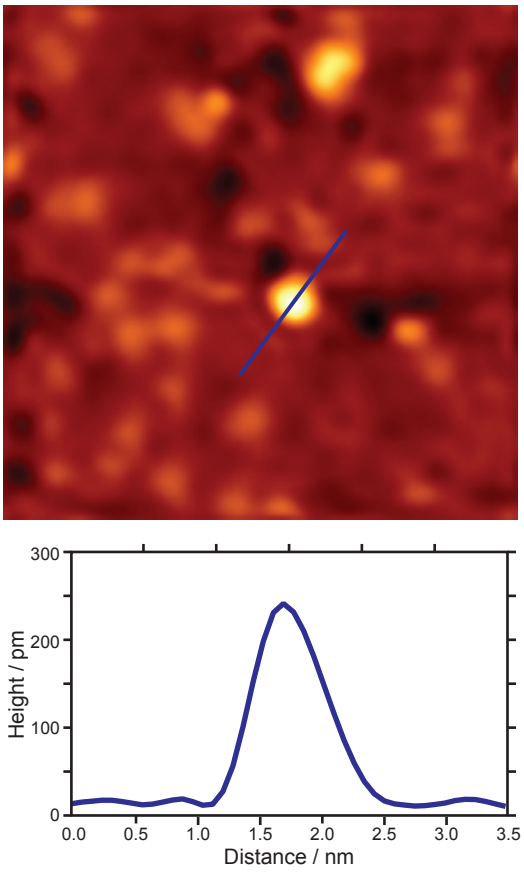

Figure 5.5: Empty states STM image and associated line profile of an isolated Au atom on a 1.5 ML ultrathin CeO_2(111) film on Pt(111) obtained using very slow scan speed. The gold adatom is measured to be 240 pm tall and have a width of 1.4 nm, typical of a single atom under STM. (10×10 nm^2, V_s = +2.0 V, I_t = 0.05 nA)

The size of the adsorbed gold atom can be measured as shown in the line profile shown in Figure

5.5; it appears 240 pm tall and 1.4 nm wide. This compares well with measurements of single gold atoms adsorbed on other oxide surfaces including Au/FeO/Pt(111) where they appear ∼180 pm tall.[53] Although the STM image presented in Figure 5.5 permits us to make a number of observations about the gold adatoms, there is no atomic resolution on the ceria substrate. At the bias voltage used to obtain this image (V_s = + 2.00 V) we are imaging the empty states of the CeO_2(111), however it is perhaps more useful to consider the filled states, with which we have considerable experience having imaged a number of defect structures on ultrathin ceria films (see previous chapter and [49]). Experimentally, the optimum bias voltage for such atomically resolved images of the top oxygen layer of CeO_2(111), allowing clear identification of oxygen vacancies, is V_s = - 3.2 V. Operation at this high a voltage causes significant interactions with the surface adsorbates and was noticeably less stable than lower, positive biases during STM operation on the Au/CeO_2(111) system. In addition, a range of tunnelling currents were tested to draw the tip away from the surface to minimise interactions between the gold adatoms and the tip, and the scan speed slowed down to further reduce interactions with the surface and generally stabilise scanning.

Presented in Figure 5.6 is an STM image and associated line profile and structural models of an instance where it proved possible to image a single gold atom without significant tip convolution whilst simultaneously achieving atomic resolution (including defects) of the ceria film. The bright lattice corresponds to the oxygen terminated film in the filled states images, and surface oxygen vacancies (O_{vac}) are present in a high density (∼20 %), one of which is marked with a black circle. The single gold adatom is the bright feature in the upper left of the frame and can be seen to change position in the course of the scan due to interactions with the tip occurring along the lines marked with black arrows. The STM fast scan direction is indicated with a white arrow.

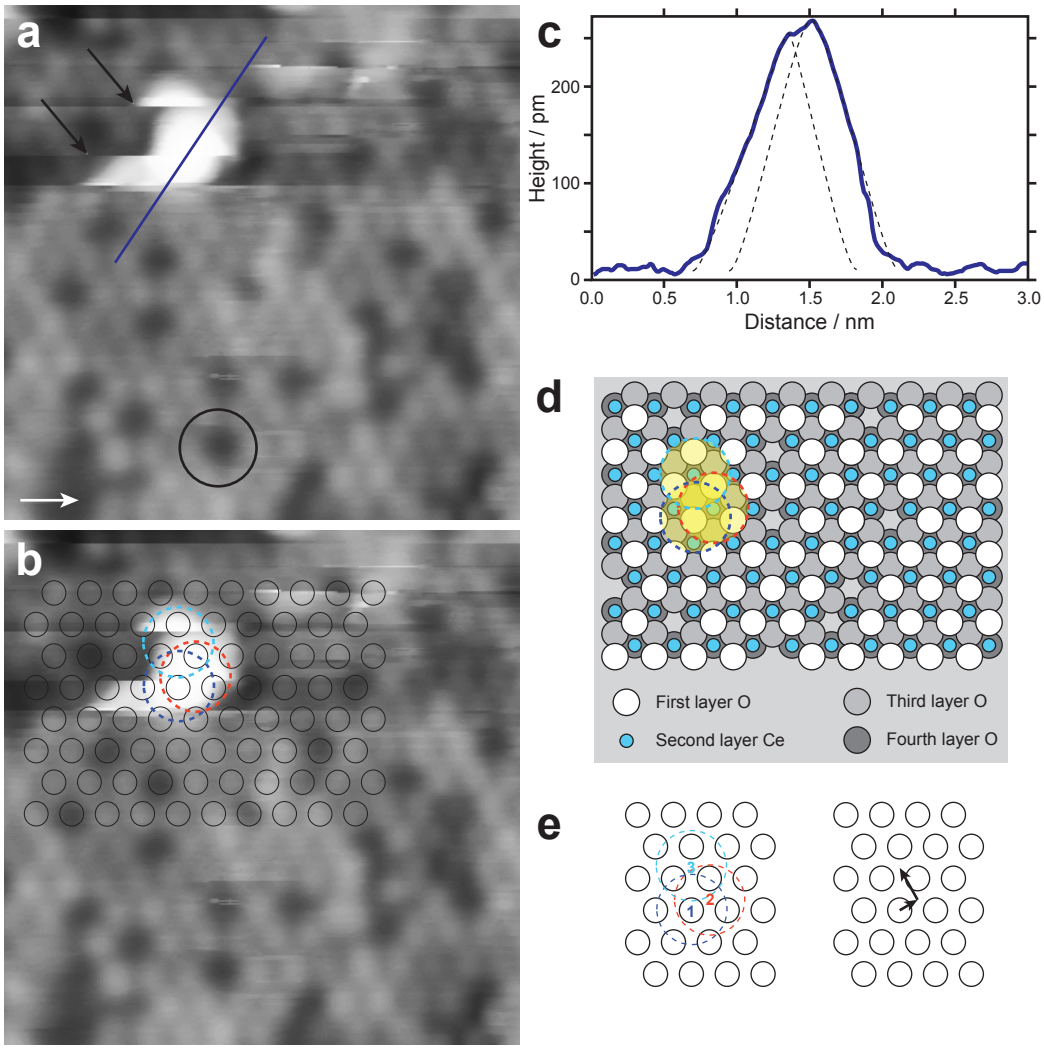

Figure 5.6: Atomically resolved STM image (a,b) (6 × 6 nm^2, V_s = -3.2 V, I_t = 0.10 nA) with associated line profile (c) and structural models (d,e) of an individual Au atom on a 1.5 ML ultrathin CeO_2(111) film on Pt(111). The CeO_2(111) film has a high density of surface oxygen vacancies one of which is highlighted with a black circle in (a), and the gold adatom is observed to move during the course of the scan as a result of interactions with the STM tip. (b) shows the same STM image as (a) but with a grid superimposed to mark the positions of the top oxygen layer allowing identification of the adsorption sites of the gold atom. Two such sites can be identified, on top of an oxygen lattice position (dark blue dashed circle), and in a three-fold hollow site (red and light blue dashed circles). It is unknown whether an oxygen vacancy is present underneath the adatom. The structural models in (d) and (e) show the movement of the gold atom from the positions marked 1-3 during the scan, the black arrows in the STM image in (a) mark the scan lines at which the hopping occurs. The line profile displayed in (c) is across two of the sites, the gold atom is measured to be ∼250 pm tall and ∼1.2 nm wide. The dashed lines show the approximate profiles of the atom in the two positions, the distance between the sites is measured to be ∼0.16 nm, consistent with the distance between a top and hollow site on the CeO_2(111) surface.

The line profile drawn across the gold atom allows the height to be measured at ∼250 pm, as observed for the gold adatom (different atom on a separate ceria island on the same ultrathin film) in Figure 5.5. As the position of the adatom changes over the profile, a guide has been added to the line profile plot to permit the approximate width to be measured (indicated with dashed line). As in Figure 5.5, the gold atom is seen to be ∼ 1.2 nm wide (not accounting for tip-broadening). The apparent slight difference (∼10 pm) in height of the atom between the two positions is a scanning artefact occurring when the tip drags the atom across the surface of the film and is not observed when line profiles are taken at a different angle. The distance between the centres of the two positions as measured from this line profile is ∼0.16 nm, consistent with the distance between the top and hollow sites on the CeO_2(111) surface.

Figure 5.6b shows the same STM image as 5.6a but with a grid superimposed to mark the positions of the top oxygen layer. The gold adatom is observed to sit on three positions during the course of the scan, these are marked by the coloured dashed circles around their base (purple-red-blue). The centres of these circles permit precise identification of the site where the adatom is located by comparison with the model structures also shown in Figure 5.6d and e. The first position (1, dark blue) is directly atop an oxygen site, there is then a movement of ∼0.16 nm to the second site (2, red); one of the three-fold hollow sites, followed by a movement of a single lattice distance (0.38 nm) to the third site (3, light blue); another three-fold hollow site. From this image we cannot determine whether there are any oxygen vacancies underneath the adatom and also cannot identify whether the hollow sites are those above a second layer Ce atom or a third layer O. Due to the considerable interaction between the tip and the gold adatoms, it was observed many times that after consecutive scans over the same area the adatoms were moved to form large clusters which induced further tip instability and poorer imaging quality. Due to the magnitude of the tip-adatom interactions it was not possible to investigate whether the thermal energy alone of the gold

adatoms (all STM was carried out at room temperature) was sufficient to cause their movement across the ceria surface.

A key question regarding the Au/CeO_2(111) system and its activity is that of the oxidation state of the gold. There is no clear consensus as to the state of the gold in the industrial WGS catalysts although it has been proposed that positively charged gold may be responsible [5] although the stability of such species during the reaction is not clear. Due to the design of the evaporator used for the PVD of the gold, it can be assumed that all atoms are neutrally charged before adsorption however from our STM data alone it is not possible to determine whether there is any charge transfer once adsorbed onto the surface of the ceria. Such charge transfer has been previously observed for the Pd/CeO_2(111)/Pt(111) system, where XPS was used to determine that Pd deposition leads to reduction of the ceria substrate.[48] Photoemission spectroscopy was also employed by Škoda et al. to study gold on ceria thin films, and their results show a similar reduction of Ce^{4+} to Ce^{3+} explained by the formation of cationic gold species.[32] Such charge transfer may also occur for single gold adatoms, and may also provide an explanation as to their surprising stability and appearance as isolated individuals even at room temperature. An additional effect that may play a role in the stability of the gold adatoms on our ceria films is the possibility of charge transfer through the ultrathin oxide film to the Pt(111) substrate. Such an effect has been observed in a number of cases including gold on MgO/Mo(100) [54, 55] and alumina/NiAl [56].

The issue of strain in the ceria film may also play an important role in the nucleation and possibly charge properties of any adsorbed metal atoms and particles. We have observed in LEED (see Figure 5.1c) that the CeO_2(111) lattice spacing in our ultrathin films has a contraction of $\sim$3 % with respect to the bulk value due to the lattice mismatch with the Pt(111) substrate which has the

further effect of causing the formation of ordered arrays of oxygen vacancies.[49] It is therefore likely that the adsorption of single gold atoms may also be affected by this strain, perhaps leading to slightly different behaviour compared with that on the unstrained native $CeO_2(111)$ surface. With increasingly thicker ceria films this strain appears to be reduced [50] until eventually there is no contraction of the lattice[42, 57]) suggesting that it would be of interest in future to compare the adsorption behaviour of single atoms on such films which may approximate the bulk more closely.

5.4 Summary and Conclusions

Scanning tunnelling microscopy has been employed to investigate the adsorption of single atoms of gold on ultrathin CeO_2(111) films on Pt(111), an important model catalytic system. The ultrathin ceria films were prepared by a post-oxidation method in atomic oxygen, and characterised with STM, LEED and AES. The films formed an incomplete layer on the Pt substrate and consisted of large, atomically flat terraces with a high concentration of surface oxygen vacancies, ideal for atomically resolved STM measurements. Low coverages ($\sim$0.07 ML) of gold were evaporated onto the films at room temperature and observed to nucleate evenly across the ceria islands with no step edge decoration. The majority of the adsorbed gold consisted of individual single atoms, which could be imaged with atomic resolution for the first time simultaneously with the top oxygen layer of the ceria. Heavy interaction between the STM tip and the gold adatoms led to unstable scanning and tip-induced movement of the adsorbates and it was possible to identify two different adsorption sites; (i) atop an oxygen atom (possibly a vacancy site), and (ii) in a three-fold hollow site.

Many future investigations are possible on the Au/CeO_2 system, of particular interest would be to carry out in-situ evaporation of gold to examine whether adsorption is favoured on oxygen vacancy sites. In addition, cooling to cryogenic temperatures could be of interest and also permits the application of scanning tunnelling spectroscopy which may aid identification of the oxidation state of the gold adatoms. The behaviour of gold atoms and the CeO_2(111) surface in conditions closer to those encountered in the real catalysts is also deserving of attention, a first step towards this may be an examination of the sintering or other effects at increased temperatures as well as exposure to CO and water.

References

[1] Haruta, M. *Cattech* **2002**, *6*, 101–116.

[2] Hashmi, A. S. K.; Hutchings, G. J. *Ange. Chem.* **2006**, *45*, 7896 – 7936.

[3] Meyer, R.; Lemire, C.; Shaikhutdinov, S.; Freund, H.-J. *Gold Bull.* **2004**, *37*, 72–120.

[4] Risse, T.; Shaikhutdinov, S.; Nilius, N.; Sterrer, M.; Freund, H.-J. *Acc. Chem. Res.* **2008**, *41*, 949–956.

[5] Fu, Q.; Saltsburg, H.; Flytzani-Stephanopoulos, M. *Science* **2003**, *301*, 935–938.

[6] Trovarelli, A. *Catalysis by Ceria and Related Materials*, Catalytic Science Series; Imperial College Press, 2002.

[7] Trovarelli, A.; de Leitenburg, C.; Boaro, M.; Dolcetti, G. *Cat. Today* **1999**, *50*, 353–367.

[8] Gorte, R. J. *AIChE J* **2010**, *56*, 1126–1135.

[9] Deluga, G.; Salge, J.; Schmidt, L. *Science* **2004**, *303*, 993–997.

[10] Bernal, S.; Calvino, J.; Cauqui, M.; Gatica, J.; Larese, C.; Omil, J. P.; Pintado, J. *Cat. Today* **1999**, *50*, 175–206.

[11] Liu, Z.; Jenkins, S. J.; King, D. A. *Phys. Rev. Lett.* **2005**, *94*, 196102.

[12] Zhang, C.; Michaelides, A.; King, D. A.; Jenkins, S. J. *J. Phys. Chem. C* **2009**, *113*, 6411–6417.

[13] Rodriguez, J.; Wang, X.; Liu, P.; Wen, W.; Hanson, J. C. *Top. Cat.* **2007**, *44*, 73–81.

[14] Chen, M.; Goodman, D. W. *Acc. Chem. Res.* **2006**, *39*, 739–746.

[15] Chen, M.; Cai, Y.; Yan, Z.; Goodman, D. W. *J. Am. Chem. Soc.* **2006**, *128*, 6341–6346.

[16] Branda, M. M.; Castellani, N. J.; Grau-Crespo, R.; de Leeuw, N. H.; Hernandez, N. C.; Sanz, J.; Neyman, K. M.; Illas, F. *J. Chem. Phys.* **2009**, *131*, 094702.

[17] Branda, M. M.; Hernandez, N. C.; Sanz, J. F.; Illas, F. *J. Phys. Chem. C* **2010**, *114*, 1934–1941.

[18] Hernandez, N. C.; Grau-Crespo, R.; de Leeuw, N. H.; Sanz, J. *Phys. Chem. Chem. Phys.* **2009**, *11*, 5246–5252.

[19] Nolan, M.; Verdugo, V.; Metiu, H. *Surf. Sci.* **2008**, *602*, 2734–2742.

[20] Varganov, S.; Olson, R.; Gordon, M.; Mills, G.; Metiu, H. *J. Chem. Phys.* **2004**, *120*, 5169–5175.

[21] Zhang, C.; Michaelides, A.; King, D. A.; Jenkins, S. J. *J. Chem. Phys.* **2008**, *129*, 194708.

[22] Chen, Y.; Cheng, J.; Hu, P.; Wang, H. *Surf. Sci.* **2008**, *602*, 2828–2834.

[23] Castellani, N. J.; Branda, M. A.; Neyman, K. M.; Illas, F. *J. Phys. Chem. C* **2009**, *113*, 4948–4954.

[24] Baron, M.; Bondarchuk, O.; Stacchiola, D.; Shaikhutdinov, S.; Freund, H.-J. *J. Phys. Chem. C* **2009**, *113*, 6042–6049.

[25] Bond, G.; Thompson, D. *Gold Bull.* **2009**, *42*, 247–259.

[26] Guzman, J.; Carrettin, S.; Fierro-Gonzalez, J.; Hao, Y. *Ange. Chem.* **2005**, *117*, 4856 –4859.

[27] Guzman, J.; Carrettin, S.; Corma, A. *J. Am. Chem. Soc* **2005**, *127*, 3286–3287.

[28] Kung, M. C.; Davis, R. J.; Kung, H. H. *J. Phys. Chem. C* **2007**, *111*, 11767–11775.

[29] Liu, P.; Rodriguez, J. A. *J. Chem. Phys.* **2007**, *126*, 164705.

[30] Naya, K.; Ishikawa, R.; Fukui, K. *J. Phys. Chem. C* **2009**, *113*, 10726–10730.

[31] Rodriguez, J.; Liu, P.; Hrbek, J.; Evans, J.; Perez, M. *Ange. Chem.* **2007**, *46*, 1329 –1332.

[32] Škoda, M.; Cabala, M.; Matolínová, I.; Prince, K. C.; Skála, T.; Šutara, F.; Veltruská, K.; Matolín, V. *J. Chem. Phys.* **2009**, *130*, 034703.

[33] Venezia, A.; Pantaleo, G.; Longo, A.; Carlo, G. D.; Casaletto, M.; Liotta, F.; Deganello, G. *J. Phys. Chem. B* **2005**, *109*, 2821–2827.

[34] Wang, X.; Rodriguez, J.; Hanson, J. C.; Perez, M.; Evans, J. *J. Chem. Phys.* **2005**, *123*, 221101.

[35] Weststrate, C. J.; Westerström, R.; Lundgren, E. *J. Phys. Chem. C* **2008**, *113*, 724–728.

[36] Weststrate, C. J.; Resta, A.; Westerström, R.; Lundgren, E.; Mikkelsen, A.; Andersen, J. N. *J. Phys. Chem. C* **2008**, *112*, 6900–6906.

[37] Zhou, Y.; Zhou, J. *J. Phys. Chem. Lett.* **2010**, *1*, 609–615.

[38] Lu, J.; Gao, H.-J.; Shaikhutdinov, S.; Freund, H.-J. *Cat. Lett.* **2007**, *114*, 8–16.

[39] Esch, F.; Fabris, S.; Zhou, L.; Montini, T.; Africh, C.; Fornasiero, P.; Comelli, G.; Rosei, R. *Science* **2005**, *309*, 752–755.

[40] Norenberg, H.; Briggs, G. A. D. *Phys. Rev. Lett.* **1997**, *79*, 4222–4225.

[41] Freund, H.-J. *Farad. Disc.* **1999**, *114*, 1–31.

[42] Lu, J.; Gao, H.-J.; Shaikhutdinov, S.; Freund, H.-J. *Surf. Sci.* **2006**, *600*, 5004–5010.

[43] Mullins, D. R.; Radulovic, P.; Overbury, S. H. *Surf. Sci.* **1999**, *429*, 186–198.

[44] Eck, S.; Castellarin-Cudia, C.; Surnev, S.; Ramsey, M.; Netzer, F. P. *Surf. Sci.* **2002**, *520*, 173–185.

[45] Wilson, E. L.; Chen, Q.; Brown, W.; Thornton, G. *J. Phys. Chem. C* **2007**, *111*, 14215–14222.

[46] Staudt, T.; Lykhach, Y.; Hammer, L.; Schneider, M. A.; Matolín, V.; Libuda, J. *Surf. Sci.* **2009**, *603*, 3382–3388.

[47] Berner, U.; Schierbaum, K.-D. *Phys. Rev. B* **2002**, *65*, 235404.

[48] Wilson, E. L.; Grau-Crespo, R.; Pang, C. L.; Cabailh, G.; Chen, Q.; Purton, J. A.; Catlow, C. R. A.; Brown, W.; de Leeuw, N. H.; Thornton, G. *J. Phys. Chem. C* **2008**, *112*, 10918–10922.

[49] Grinter, D. C.; Ithnin, R.; Pang, C. L.; Thornton, G. *J. Phys. Chem. C* **2010**, *114*, 17036–17041.

[50] Luches, P.; Pagliuca, F.; Valeri, S. *J. Phys. Chem. C* **2011**, *115*, 10718–10726.

[51] Bowker, M., Ed. *Scanning Tunneling Microscopy in Surface Science. Nanoscience and Catalysis;* Wiley VCH, 2010.

[52] Castellarin-Cudia, C.; Surnev, S.; Schneider, G.; Podlucky, R.; Ramsey, M.; Netzer, F. P. *Surf. Sci.* **2004**, *554*, L120–L126.

[53] Giordano, L.; Pacchioni, G.; Goniakowski, J.; Nilius, N.; Rienks, E. D. L.; Freund, H.-J. *Phys. Rev. Lett.* **2008**, *101*, 026102.

[54] Sterrer, M.; Risse, T.; Pozzoni, U. M.; Giordano, L.; Heyde, M.; Rust, H.-P.; Pacchioni, G.; Freund, H.-J. *Phys. Rev. Lett.* **2007**, *98*, 096107.

[55] Pacchioni, G.; Giordano, L.; Baistrocchi, M. *Phys. Rev. Lett.* **2005**, *94*, 226104.

[56] Nilius, N.; Ganduglia-Pirovano, M. V.; Brazdova, V.; Kulawik, M.; Sauer, J.; Freund, H. J. *Phys. Rev. Lett.* **2008**, *100*, 096802.

[57] Farmer, J. A.; Baricuatro, J. H.; Campbell, C. T. Jan **2010**, *114*, 17166–17172.

CHAPTER 6

ACETIC ACID ADSORPTION ON ANATASE TiO_2(101)

Abstract

The adsorption and reactivity of acetic acid on anatase TiO_2(101) has been investigated with scanning tunnelling microscopy (STM), low energy electron diffraction (LEED), and Auger electron spectroscopy (AES). At low coverages acetic acid is observed to have a characteristic appearance in STM consistent with a dissociative bidentate binding geometry. At room temperature acetic acid has a relatively strong interaction with the anatase (101) surface and a near-unity sticking probability. When deposited onto the anatase at elevated temperatures (420 K) a saturated coverage displayed an ordered superstructure with two domains across small regions of the surface. The periodicity of these domains was found to be (2×1), again consistent with a bidentate binding geometry of the acetate to two neighbouring Ti_{5c} sites along the [010] direction. Heating the

acetate-covered surface to 570 K in UHV resulted in clean desorption of $\sim$90 % of the molecules, the majority of those which were undesorbed were situated at the step edges of the anatase. Tip pulsing at + 6 V was also found to desorb the acetate molecules from the surface. Illumination of the acetate-covered surface with ultraviolet light under UHV conditions was not found to have a great effect on the structure of the adsorbates. A co-adsorption of water and acetic acid in a 1:1 mix was found to show an identical structure to pure acetic acid at saturation coverage but a number of differing adsorbates were observed at sub-monolayer coverages.

6.1 Introduction

Applications of TiO_2 are numerous and well-documented, with important examples including heterogeneous catalysis, die-sensitized solar cells, pigments, optical coatings, gas sensing, and even gate materials in semiconducting devices.[1–6] The photocatalytic behaviour of TiO_2 in particular, first discovered by Fujishima and Honda [7], has driven research into the various surfaces of titania leading to the rutile (110) (1 $\times$ 1) becoming the prototypical metal-oxide surface for studies of surface reconstructions, defects, adsorbates, and many other phenomena. In spite of the wealth of work in the literature on rutile TiO_2; the most active polymorph for catalysis and that which is found in most nanomaterials employed in commercial TiO_2 applications is actually the anatase form. Reasons for the relative paucity of detailed experimental work on the surfaces of anatase TiO_2 include difficulty in preparing good quality, large artificial crystals and the poor availability of large natural mineral crystals with suitably low levels of contaminants. As a result, an alternative approach has been to grow thin films of anatase TiO_2 via molecular beam epitaxy (MBE) or chemical vapour deposition (CVD) on suitable substrates; examples of which include $SrTiO_3$(100) and $LaAlO_3$(100).[8, 9]

The unit cells of anatase and rutile TiO_2 are displayed in Figure 6.1, with the red and blue representing oxygen and titanium atoms respectively. The two polymorphs display quite different chemistry at their surfaces, one example of which is their behaviour towards water which adsorbs molecularly on the anatase (101) but dissociates at low coverages on rutile (110).[10, 11] The (101) surface of anatase is the most stable and frequently observed, and the basic structure including its interaction with water and metal adsorption has been studied previously using STM and LEED.[10, 12, 13] An interesting point to note is the relatively low density of point defects

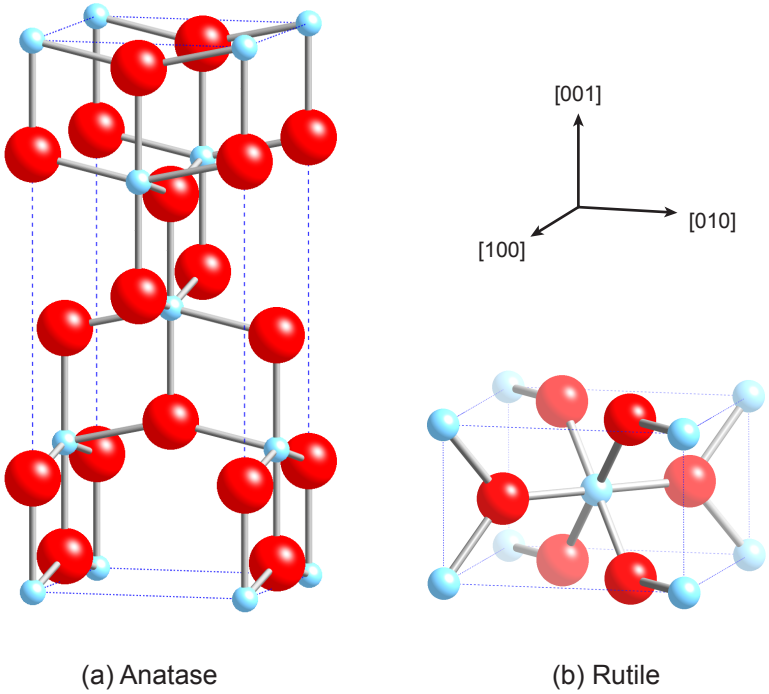

Figure 6.1: Ball and stick models of the unit cells of two of the polymorphs of TiO_2; (a) Anatase (b) Rutile (Red atoms: O, Blue atoms: Ti).

such as surface oxygen vacancies observed on anatase (101) in comparison to rutile (110) and the importance of step edges towards the reactivity of anatase.[14] Step edges are very important features generally in the study of oxide surfaces and are involved in a number of processes such as adsorption of molecules, nucleation sites for metal particles and crystal growth.

The adsorption of small molecules on the surfaces of metal oxides, and TiO_2 in particular, is of great interest both from the standpoint of investigating catalytic behaviour as well as their fundamental adsorption properties. One important class of molecules for these studies is carboxylic acids whose functionality and strong bonding to oxide surfaces plays a role in linking dye molecules to TiO_2 for use in solar cells, the formation of self assembled monolayers and as organic linkers in large organic-inorganic frameworks.[15–20] The behaviour of carboxylic acids is well documented on rutile TiO_2 surfaces [3], but there is a lack of experimental data for their adsorption on anatase

bar some studies on polycrystalline samples.[21, 22]

A photograph of the natural mineral anatase $TiO_2(101)$ crystal used in this study is shown in Figure 6.2, its dimensions are approximately 4×4 mm^2 and is observed to be translucent and dark blue in colour, similar to a heavily reduced rutile crystal after a number of cycles of sputtering and annealing. A slight contamination of unknown origin manifests itself as an orange tint to some parts of the crystal although it does not appear to affect our studies and does not show up in Auger spectroscopy of the surface.

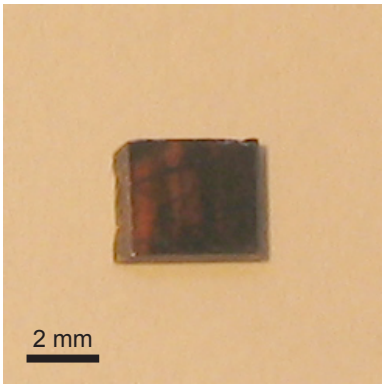

Figure 6.2: Photograph of the natural mineral anatase $TiO_2(101)$ crystal used for this work. (*Pi-Kem*) Prior to any preparation cycles the crystal was translucent and dark blue in colour with some orange patches.

6.2 Experimental Procedure

The STM, LEED and AES experiments were all conducted in a UHV chamber with a base pressure of 1×10^{-11} mbar attached to a separate sample preparation chamber equipped for Ar^+ sputtering, electron bombardment heating, RGA mass spectrometry and gas and metal dosing.

The STM employed was an *Omicron* UHV AFM/STM operated in constant current mode at room temperature using electrochemically etched tungsten tips that were conditioned during scanning with voltage pulses (up to 10 V) and high negative/positive bias scans to obtain stable atomic-resolution imaging. The natural mineral anatase TiO_2(101) crystal (*Pi-Kem*) was attached to a standard sample plate with spot-welded tantalum clips and the temperature during annealing monitored using an infra-red pyrometer (*Land*). Temperatures lower than the minimum limit of the pyrometer ($\sim$750 K) were measured by a K-type thermocouple attached to the manipulator arm and positioned near to the sample plate. Cycles of Ar^+ sputtering (20 min, 1 keV, 10 μA) and UHV annealing (5-20 min, 880-1000 K) were employed to clean the sample until any contamination was below the detection limit of AES and a well-ordered LEED pattern with low background was observed yielding a surface suitable for atomic resolution STM imaging. The STM data was calibrated by comparison with atomically resolved images of the rutile TiO_2(110)(1 $\times$ 1) surface obtained just prior to these experiments, and in all cases STM measurements were performed after allowing the sample temperature to equilibrate to that of the STM stage to minimise the effects of thermal drift.

Acetic acid (99.99 %, *Sigma-Aldrich*) was contained within a glass vial attached to the gas line of the UHV system and admitted into the preparation chamber via a high-precision leak valve. Several freeze-pump-thaw cycles were carried out to purify the acetic acid, all exposures are nominal and quoted in Langmuirs (1 L = 1.33×10^{-6} mbar s) based on the uncompensated pressure within the preparation chamber during dosing. For the coadsorption experiments of water and acetic acid, a solution was prepared with the ratio of water to acetic acid of 39:61 to yield a ratio of 1:1 for the partial pressures of the two components at 300 K assuming no deviation from Raoult's law.[23] This solution was purified by freeze-pump-thaw cycles as for the pure acid. In this work a monolayer (ML) is defined by the number of Ti_{5c}-O_{2c} pairs on the ideal surface, a

density of 5.17 nm^{-2}. For exposures in the range 0.05-0.5 L an uncompensated chamber pressure of 1.0×10^{-9} mbar was used, similarly for the range 1.0-15 L the chamber pressure was 5×10^{-8} mbar, and the time of exposure altered to give the desired dose for each case.

UV irradiation was achieved from a 365 nm lamp shone through a silica glass UHV window, with a radiating power of 1.3 $mWcm^{-2}$ at a sample distance of $\sim$28 cm from the lamp. The window was measured to absorb 50 % of the light, with the resultant photon flux on the sample under the operating conditions being 4.3×10^{16} cm^{-2} s^{-1}.

6.3 Results and Discussion

6.3.1 Clean Anatase TiO_2(101)

The (101) surface of anatase TiO_2 has been characterised previously by LEED and STM [14, 24], and shown to display a non-reconstructed (1 x 1) termination of the bulk as displayed in the ball-and-stick model displayed in Figure 6.3. Red atoms are oxygen, blue titanium. Flat terraces of anatase (101) have a sawtooth corrugation as seen in the lower panel of Figure 6.3 composed of five- and six-fold coordinated Ti atoms, (Ti_{5c}, Ti_{6c}) and two- and three-coordinated O atoms (O_{2c}, O_{3c}). The surface unit cell is also displayed in Figure 6.3, with dimensions of 10.24 Å $\times$ 3.78 Å.

After an initial sputter/anneal cycle, a dim (1 $\times$ 1) LEED pattern with a high background was observed from the anatase (101). Further cycles (5 min Ar^+ sputter, 20 min anneal at 950 K) produced a more intense and sharper pattern with a lower background as displayed in Figure 6.4.

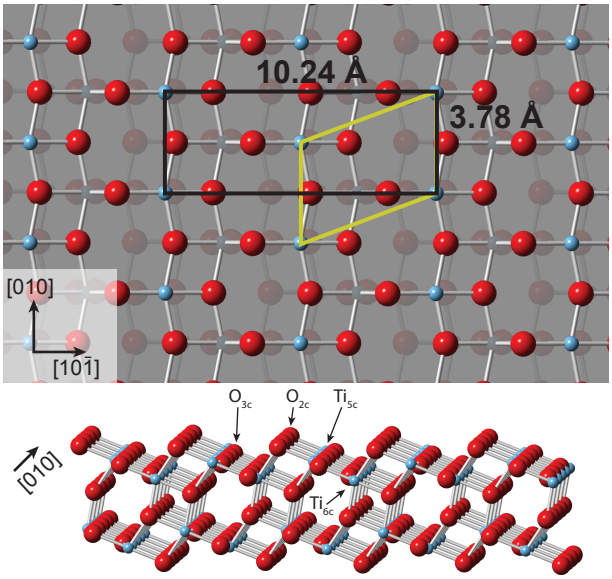

Figure 6.3: Ball and stick models (top and side views) of the anatase TiO_2(101) surface (Red atoms: O, Blue atoms: Ti) The surface unit cell is marked with a black rectangle, and has dimensions of 10.24 Å × 3.78 Å. The primitive unit cell is marked in yellow. Models prepared in *CrystalMaker 8.3* using data from [25].

The centred surface unit cell is marked with a black rectangle and the primitive unit cell marked in yellow to allow easy comparison with the model of the surface displayed in Figure 6.3. Also displayed in Figure 6.4 is an Auger electron spectrum from the clean surface, with the Ti LMM and O KLL peaks marked and no surface contamination detected.

After LEED and AES indicated that the surface was suitable for STM investigations, initial large-scale images were collected as displayed in Figure 6.5. Figure 6.5a was obtained after sputter/anneal cycles at 880 K and displays a heavily stepped structure with small (∼5 nm) terrace widths and step edges primarily oriented parallel to the [$\bar{1}$11] and [11$\bar{1}$] directions with some shorter edges oriented parallel to [010]. After further sputter/anneal cycles at 950 K, the surface was observed to become smoother as displayed in Figure 6.5b, with larger terrace widths (up to 30 nm in places). Our observations mirror those made in previous STM investigations of the anatase (101) surface.[13, 14, 24, 26] Figure 6.5c is a 50 × 50 nm^2 image and line profile of an area within

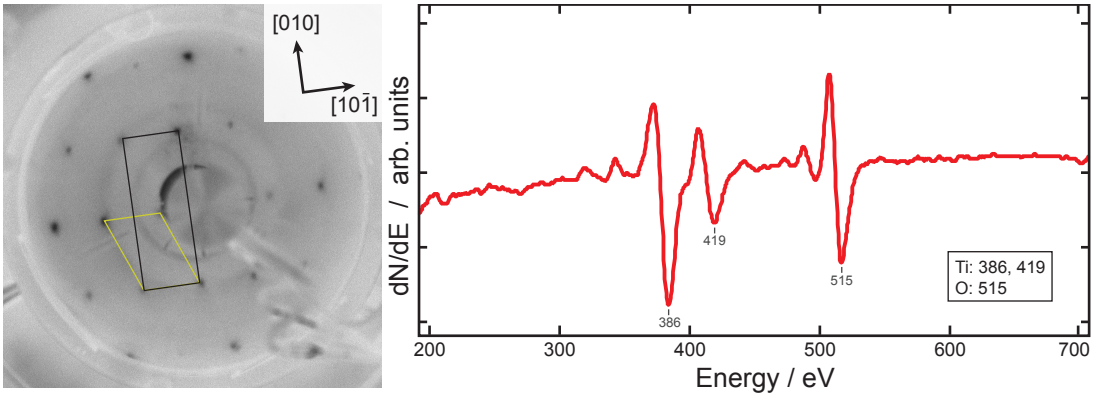

Figure 6.4: Low energy electron diffraction (LEED) (112 eV) of prepared anatase TiO_2(101) displaying a clear (1 × 1) pattern. The surface unit cell is marked with a black rectangle, and the primitive cell with a yellow rhombus to permit clear comparison with the model presented in Figure 6.3. A derivative mode Auger electron spectrum (AES) of the prepared surface is also presented with the Ti LMM (386 and 419 eV) and O KLL (515 eV) peaks marked and any contamination below the detection limit of the RFA spectrometer.

6.5b, it can be seen that the steps on the (101) surface are ∼3.8 nm tall, and monoatomic. Faintly visible in 6.5c is some atomic-sized contrast from the underlying lattice, which is examined in more detail in Figure 6.6.

Once a suitably wide terrace is identified, atomically resolved images were obtained, as displayed in Figure 6.6a & b. Both images are of empty states, and the atomic lattice is clearly visible. The origin of the contrast of this lattice has been identified by He et al. [14] and it was shown that the bright features are actually derived from a Ti_{5c} and O_{2c} pair, as shown in the model in Figure 6.6c highlighted by yellow ovals. The unit cell is marked both on the model and the STM images with a black rectangle, and the spacing as measured by STM is consistent with this explanation. An early observation of anatase TiO_2 surfaces has been the low concentration of point defects at the surface, especially in comparison with rutile TiO_2.[14] The images displayed in Figure 6.6 back this up, and only a few atomic-sized imperfections are visible with a total estimated coverage of ∼0.002 ML. Water from the background vacuum is observed as a dark depression centred on the lattice, and marked in Figure 6.6b with a solid circle. A few subsurface impurities

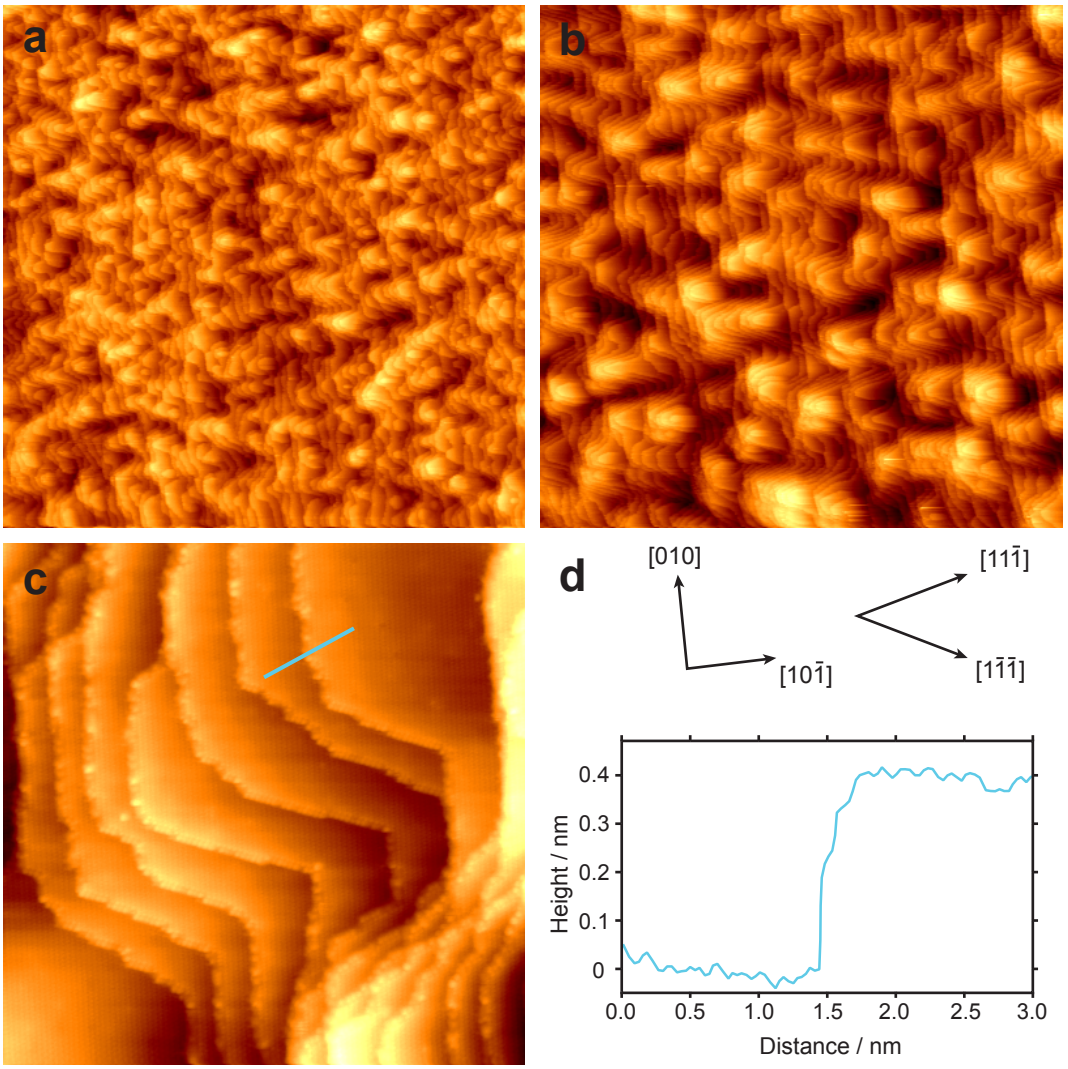

Figure 6.5: STM images of clean anatase TiO_2(101) (a) Large scale image (300 × 300 nm^2, V_s = +1.5 V, I_t = 0.20 nA) obtained after only a couple of preparation cycles, and showing a very high density of steps with narrow terrace widths. (b) Large scale image (300 × 300 nm^2, V_s = +1.2 V, I_t = 0.4 nA) obtained after further preparation cycles displaying larger (101) terraces more suited to high-resolution STM investigation. (c) Small scale image (50 × 50 nm^2, V_s = +1.2 V, I_t = 0.20 nA) of an area in (b) with step edges oriented parallel to [010], [$\bar{1}$11], and [11$\bar{1}$]. (d) A line profile of a single monoatomic step from the STM image in (c) showing a step height of ∼3.8 nm.

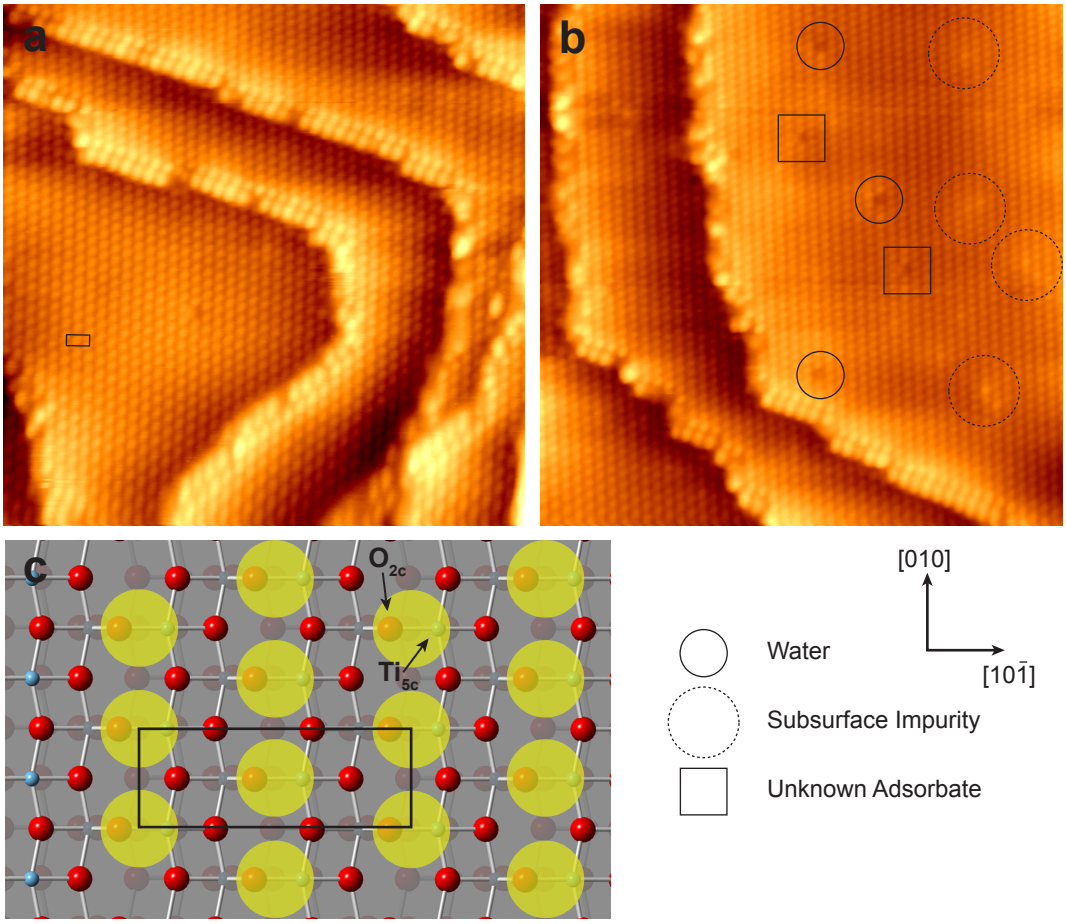

Figure 6.6: Atomically resolved empty states STM images of anatase TiO_2(101) and associated model showing the origin of the observed contrast. (a) Atomically resolved image (23 × 23 nm^2, V_s = +1.2 V, I_t = 0.20 nA) with the bright features corresponding to Ti_{5c} - O_{2c} pairs and the surface unit cell marked with a black rectangle (b) Atomically resolved image (24 × 24 nm^2, V_s = +1.2 V, I_t = 0.20 nA) with a number of point defects identified including water (marked with solid circle), subsurface impurities (dashed circles), and some unknown adsorbates (black squares) (c) Model of the (101) surface with the Ti_{5c} - O_{2c} pairs highlighted in yellow which lead to the observed atomic-sized features in (a) and (b).

are also observed, marked with dashed circles, and characterised by a protruding Ti_{5c} - O_{2c} oval and a surrounding area of brightness a few nm across. Such impurities were observed to become less common with additional sputtering and annealing suggesting migration towards the bulk or removal by the successive preparation cycles. The defects marked with black squares appear similar to water consisting of a dark oval but with an extra bright feature in the [$\bar{1}$01] direction. The origin of these features is not known, but they have been previously observed on a heavily reduced anatase (101) crystal and assigned to unidentified adsorbates.[14]

It is important to note that a unique assignment of the direction of $[10\bar{1}]$ cannot be determined from these LEED and STM results alone. To overcome this, Gong et al. conducted combined STM and first-principles calculations of the step structures on anatase (101).[13] In this study they found that the favoured trapezoidal island and step structures was reflective of the underlying symmetry of the surface and permits assignment of the crystallographic directions. We have identified the same step structures in our STM images and have applied the results of [13] in our analysis, resulting in the assignment of the direction of $[10\bar{1}]$ as shown in all of the figures.

6.3.2 Low Coverage Acetic Acid on Anatase TiO_2(101)

The adsorption and bonding of carboxylic acids to TiO_2 is of great interest and extensive work has already been carried out on rutile surfaces, the (110) (1×1) in particular. There are a number of configurations by which such acids bind to surfaces, some of which are summarised in the schematic shown in Figure 6.7. The adsorption can be split into two main schemes; molecular and dissociative, depending on whether or not the carboxylic hydrogen is transferred to the oxide surface. On rutile TiO_2, acetic acid has been shown to adsorb dissociatively at room temperature on the (110) (1 x 1) surface with a number of possible bidentate binding geometries depending on the concentration of vacancies and other adsorbates on the surface. The most common geometry is found to be bidentate between adjacent Ti_{5c} sites along the rows in the [001] direction, leading to a (2×1) acetate overlayer at saturation coverage.[3, 27]

There is conflicting experimental and theoretical data regarding carboxylic acid adsorption on anatase surfaces, with both molecular and dissociative adsorption proposed. A key limitation for experimental studies has been the availability of good quality anatase single crystals, instead TiO_2

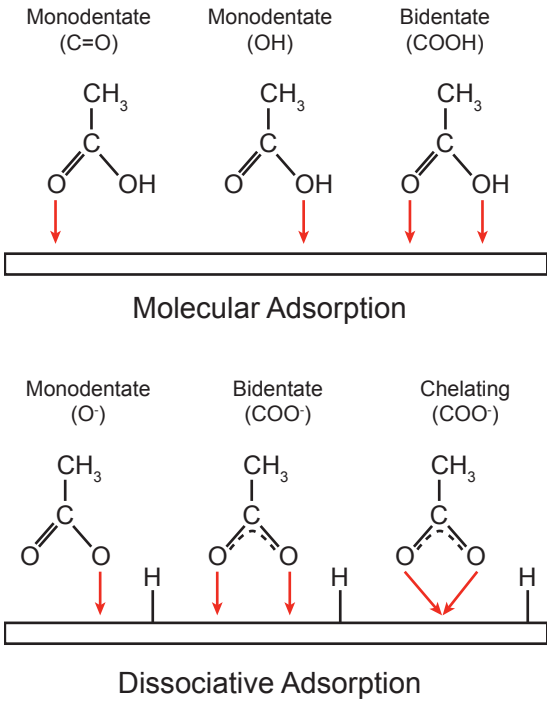

Figure 6.7: Schematic of the possible adsorption configurations for acetic acid, split into two main groups: molecular and dissociative adsorption.

films or nanoparticles have been more-widely investigated leading to results that are aggregates of many different faces and therefore require further deconvolution.[28] An example of such work was the study by Mattsson and Osterlund [21] of acetic acid adsorption on anatase nanoparticles using FTIR spectroscopy where signatures of both molecular and dissociative adsorption were observed. In [8, 22] Tanner et al. used a combination of SPM and spectroscopic techniques to study formic and acetic acid on anatase $TiO_2(001)(1 \times 4)$, and identified dissociated carboxylates forming a (2×4) acetate superstructure, but the binding geometry of individual molecules could not be satisfactorily explained with the data available. A number of DFT studies of formic acid adsorption on anatase (101)[29–31] report different behaviour, with no dissociation observed and molecular monodentate geometry most favoured, through the C=O oxygen to a Ti_{5c} site, with further stabilisation provided by hydrogen bonding of the OH group to a neighbouring O_{2c} atom.

In this first section of results, we present atomically resolved STM images of low coverages of

acetic acid on anatase (101) and propose a model for their binding.

Figure 6.8 shows a number of STM images of the anatase (101) surface after exposure to 0.1 L acetic acid. The adsorbates appear as bright features $\sim$170 pm tall evenly distributed across the terraces and step edges as seen in Figure 6.8a, with the atomic lattice of the anatase faintly visible underneath. There is no apparent preference for adsorption on step edges and the molecules are observed to exist as 2-D clusters and and as isolated individuals, with a measured coverage of 0.06 ML indicating a high sticking probability ($\sim$70%). The mobility of the acid seems very low on the timescale of our experiment (hours) although quite significant tip interactions are observed, characterised by streaking above the molecules in the fast scan direction (horizontal).

The tip termination is well-known to have a large effect on the contrast observed in STM as evidenced in Figure 6.8b, where a spontaneous tip-change occurs about half-way up the frame (marked with an arrow). In the lower half of the frame the acid molecules appear as seen in Figure 6.8a - bright round protrusions, but in the upper half a marked difference is observed. Figure 6.8c is an atomically resolved STM image taken a couple of minutes later on the same area. In this imaging mode the adsorbates are characterised by an enhanced intensity (corresponding to a height of $\sim$120-150 pm) of two neighbouring Ti_{5c} - O_{2c} pairs in the [010] direction, with two further lobes of brightness pointing along the diagonals of the centred unit cell to the Ti_{5c} - O_{2c} pairs in the $[11\bar{1}]$ and $[1\bar{1}\bar{1}]$ directions with a dark spot between them. A drift-corrected image at higher resolution of this is shown in Figure 6.8d, with the bright spots of the lattice (unit cell marked with black rectangle) originating from the Ti_{5c} - O_{2c} pairs as observed on the clean surface. Some of these pairs have been highlighted with yellow circles, showing clearly the plane of symmetry present within the molecules (marked with red dashed line). All of the adsorbate molecules are observed to have identical structures with the same orientation suggesting only a

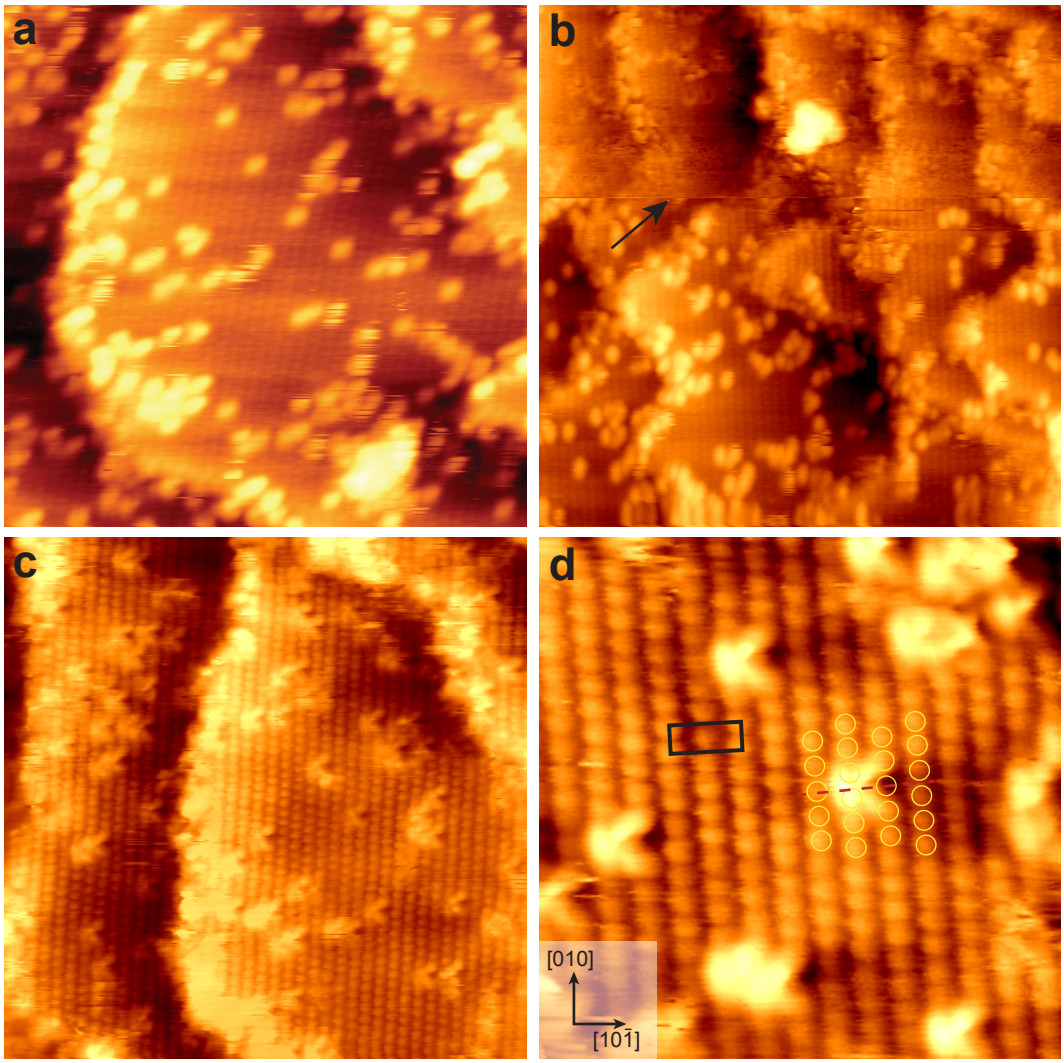

Figure 6.8: STM images of 0.06 ML acetic acid on anatase TiO_2(101) (a) The normal imaging mode where individual acetic acid molecules are imaged as bright features 170 pm tall distributed evenly across the anatase (101) surface (20 × 20 nm^2, V_s = +1.5 V, I_t = 0.10 nA) (b) STM image showing a spontaneous tip change resulting in a different imaging mode and contrast of the acetic acid molecules (29 × 29 nm^2, V_s = +1.5 V, I_t = 0.10 nA) (c) Atomically resolved image of the acetic acid molecules in the high-contrast mode. The adsorbates are characterised by enhanced intensity of two neighbouring Ti_{5c} - O_{2c} pairs in the [010] direction, with two further lobes of brightness pointing along the diagonals of the centred unit cell to the Ti_{5c} - O_{2c} pairs in the [11$\bar{1}$] and [1$\bar{1}\bar{1}$] directions with a dark spot between them (20 × 20 nm^2, V_s = +0.8 V, I_t = 0.10 nA) (d) Drift-corrected image of individual and paired acetic acid adsorbates, the surface unit cell is marked and some Ti_{5c} - O_{2c} pairs are highlighted in yellow. The plane of symmetry of the acetic acid molecules is marked with a red dashed line. (7 × 7 nm^2, V_s = +1.0 V, I_t = 0.10 nA)

single binding configuration. At the bottom-centre of Figure 6.8d, it is observed that two adsorbate molecules are bound on adjacent rows in the $[10\bar{1}]$ direction, leading to the start of an ordered string pointing along $[1\bar{1}\bar{1}]$. Dissociative adsorption of acetic acid results in hydrogen adatoms on the surface however their appearance in STM on anatase TiO_2 (101) is not known, and we cannot identify any features in our images that could be assigned to any such species.

Figure 6.9 shows three possible binding geometries for acetic acid on the anatase (101) surface: (a) Molecular monodentate binding through the C=O oxygen to a Ti_{5c} site, with the stabilising hydrogen bond formed to the O_{2c} site in the same Ti_{5c} - O_{2c} pair; the *intra*-pair arrangement. (b) Molecular monodentate binding through the C=O oxygen to a Ti_{5c} site, with the stabilising hydrogen bond formed to an O_{2c} site in a different Ti_{5c} - O_{2c} pair; the *inter*-pair arrangement. (c) Dissociative bidentate to two neighbouring Ti_{5c} sites in the [010] direction, with the dissociated hydrogen bonded to a separate O_{2c} site. Due to the symmetry observed in the STM appearance of the individual molecules (see Figure 6.8d), the inter-pair molecular adsorption geometry can be ruled out, leaving dissociative bidentate and the intra-pair molecular monodentate as the two most likely configurations at this stage. This is contrary to theoretical modelling of formic acid on the anatase (101) surface, which suggests that (b) is the most stable arrangement, although it must be remembered that such calculations are performed at low temperatures, unlike our experiments.[29–31]

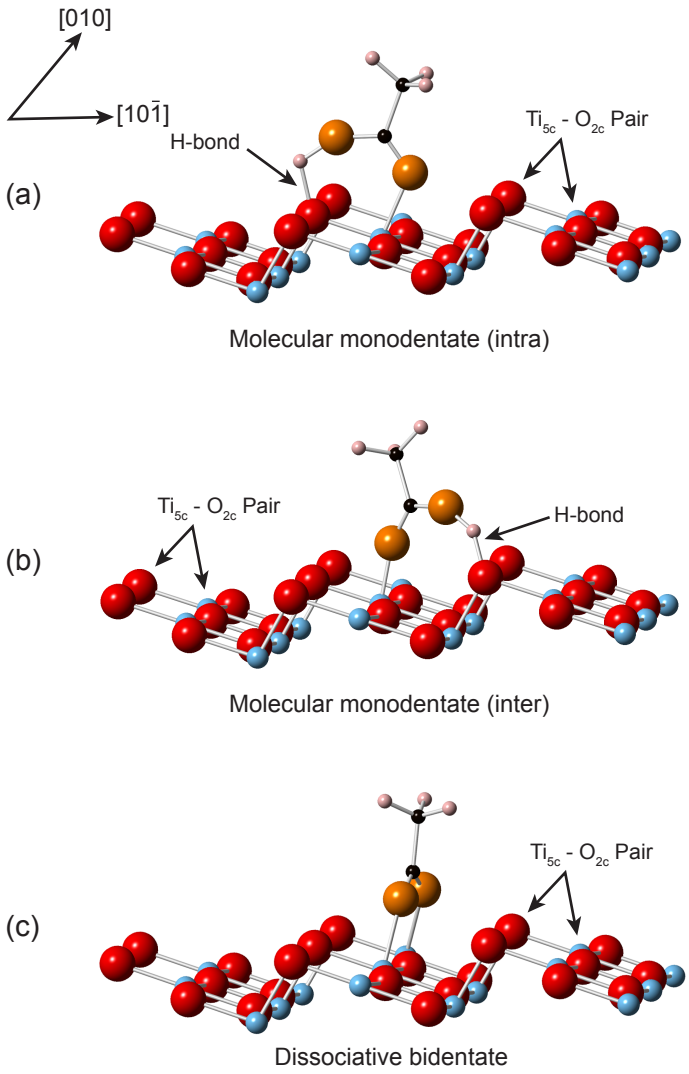

Figure 6.9: Ball-and-stick models showing possible binding configurations for acetic acid on anatase TiO_2(101) (a) Molecular monodentate (intra) binding through the C=O oxygen to a Ti_{5c} site, with the stabilising hydrogen bond formed to the O_{2c} site in the same Ti_{5c} - O_{2c} pair. (b) Molecular monodentate (inter) binding through the C=O oxygen to a Ti_{5c} site, with the stabilising hydrogen bond formed to an O_{2c} site in a different Ti_{5c} - O_{2c} pair. (c) Dissociative bidentate to two neighbouring Ti_{5c} sites in the [010] direction, with the dissociated hydrogen bonded to a separate O_{2c} site. (Red: O, Orange: Acetate O, Blue: Ti, Black: C, Pink: H) Models based on those predicted in [29–31].

6.3.3 High Coverage Acetic Acid on Anatase TiO_2(101)

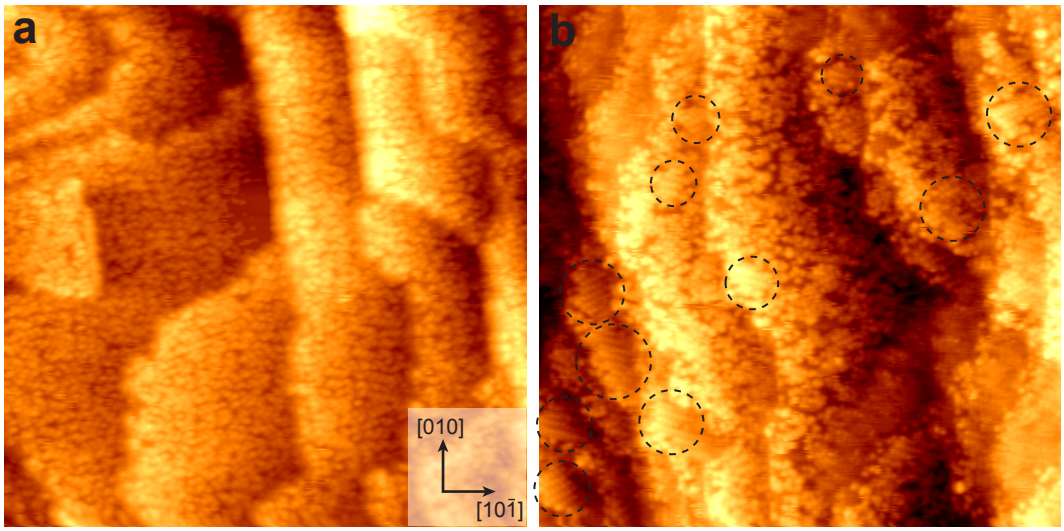

Figure 6.10: STM images of 2 L acetic acid exposure on anatase TiO_2(101) at (a) 300 K and (b) 420 K. (a) The acetic acid forms a 0.47 ML overlayer with no apparent long-range ordering. (39 $\times$ 39 nm^2, V_s = +1.2 V, I_t = 0.40 nA) (b) At higher substrate temperatures a 0.4 ML overlayer is formed with ordered domains observed in two orientations (marked with dashed circles). (50 $\times$ 50 nm^2, V_s = +1.4 V, I_t = 0.10 nA)

At higher coverages it is often observed that adsorbed molecules form ordered overlayers on TiO_2 surfaces, such as that seen for azobenzene on anatase (101).[32] Figure 6.10 shows STM images of the results of exposing the anatase (101) surface to 2 L of acetic acid at (a) 300 K and (b) 420 K. The adsorbed molecules are imaged as bright spots (the same imaging mode as in Figure 6.8a) covering the terraces of the substrate, with some small areas remaining uncovered in both cases. Analysis of the STM images yields nominal coverages of (a) 0.47 ML and (b) 0.40 ML. The small difference in coverage for these two cases despite identical exposures lies in a slightly reduced sticking probability at the higher substrate temperature. In Figure 6.10a, the result of exposure at room temperature, no long-range ordering of the adsorbates is observed. Figure 6.10b, the result of adsorption at a raised substrate temperature, has a similar general appearance to that seen in

6.10a, but there are a number of areas which display local ordering (highlighted in figure), both as short strings of molecules, and two-dimensional arrays forming two distinct domains. These ordered areas make up approximately 10 % of the total surface area as measured by STM.

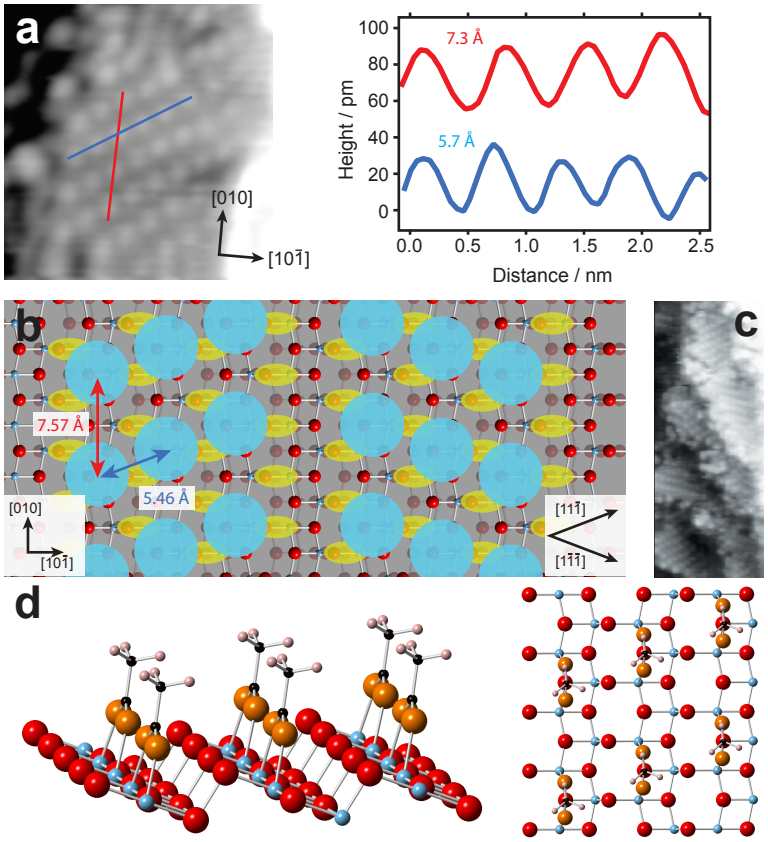

Figure 6.11: STM images and structural models explaining the origin of the ordered acetic acid domains on anatase TiO_2(101) (a) STM image (7 × 7 nm^2, V_s = +1.4 V, I_t = 0.10 nA) of one such region of ordering, the associated line profiles confirm a (2 × 1) superstructure by comparison with the model in (b) (b) Structural model of the anatase (101) surface with a (2 × 1) overlayer. The blue circles represent individual acetic acid molecules and the yellow ovals the Ti_{5c} - O_{2c} pairs that are the origin of the atomic contrast on clean anatase (101). The superstructure can be oriented in two directions along the diagonals of the centred unit cell ([11$\bar{1}$] and [1$\bar{1}\bar{1}$]) (c) an STM image (10 × 25 nm^2, V_s = +1.2 V, I_t = 0.40 nA) showing clearly the two domains of the ordered adsorbates. (d) Ball-and-stick models of acetate molecules in a dissociated bidentate geometry that form the (2 × 1) superstructure.

It is possible to image these areas of local ordering with higher resolution; images of which are presented in Figure 6.11a & c and we are able to assign these areas as having a periodicity

of (2 × 1). The red and blue line profiles across the superstructure in Figure 6.11a display intermolecular spacings of ∼7.3 Å and ∼5.7 Å respectively, which correspond reasonably well with that expected for a (2 × 1) superstructure as displayed in the model in Figure 6.11b, where the blue circles represent the acetic acid molecules. The deviation in spacing is a result of a small amount of thermal drift in the STM image which could not be compensated for. Also illustrated in the model in Figure 6.11b are the two orientations possible with (2 × 1) periodicity, along the diagonals of the centred unit cell (the $[11\bar{1}]$ and $[1\bar{1}\bar{1}]$ directions). An STM image showing a region of the sample containing adjacent overlayer domains is shown in Figure 6.11c, which is from the bottom left corner of the area displayed in Figure 6.10b. LEED investigations of this surface were carried out but due to the small surface area of the overlayer that was ordered, no additional reflexes were observed. Due to our observations at high and low coverages, we conclude that the most likely binding geometry is that of dissociative bidentate between two Ti_{5c} sites in the [010] direction.

6.3.4 Surface Modification of Acetic Acid on Anatase TiO_2(101)

STM has a unique ability to modify surfaces with extreme precision, one of the simplest ways of which is the application of voltage pulses to the tip at a certain point during scanning. Such voltage pulsing has been used to good effect on rutile TiO_2 (110) to selectively desorb H atoms by applying a +3 V pulse for 300 ms, and even induce reconstructions at higher bias voltages and currents.[33] We have used voltage pulsing in order to attempt to selectively desorb acetic acid molecules from the anatase (101) surface, the results of which are displayed in Figure 6.12. Figure 6.12a is a 20 × 20 nm^2 STM image of the anatase surface with after exposure to 2 L of acetic acid at room temperature (0.47 ML coverage). There appears to be some minor local ordering

present of the adsorbates as observed for the surface in Figure 6.10a, although tip-convolution has also lead to a broadening of all of the features making this difficult to assign. Figure 6.12b is a 20×20 nm^2 STM image of the same area after a +6 V pulse was applied at the position marked with a cross. It is observed that an area of diameter $\sim$ 6 nm has been cleared of adsorbates, with the atomic lattice now visible underneath (unit cell marked). Pulsing the tip has also induced a sharper apex, permitting higher resolution imaging of the acetic acid molecules across the rest of the surface, and confirming that the only ordering present is very short range in nature, and between nearest neighbours. Voltage pulses lower than + 6 V did not affect the overlayer, although further investigations are required to analyse the effect of the pulse duration and current.

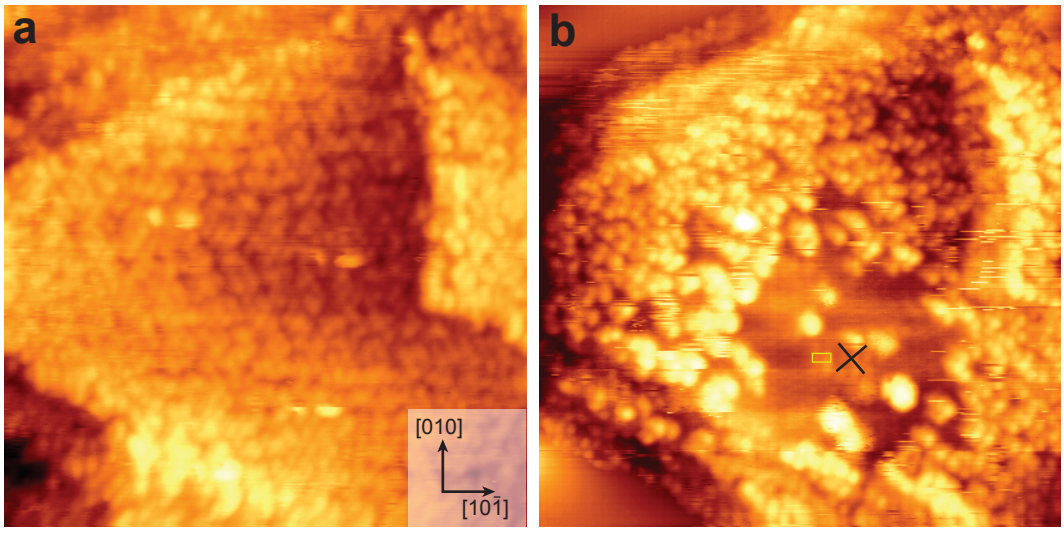

Figure 6.12: STM results of tip-pulsing of acetic acid on anatase TiO_2(101). (a) STM image of the pre-pulsed area showing a 0.47 ML coverage of acetate with some short-range strings observed. (15×15 nm^2, V_s = +1.2 V, I_t = 0.10 nA) (b) STM image after a + 6 V pulse at the position marked with a cross. An area of diameter 6 nm has been cleared of adsorbates with the atomic lattice visible in the clear area (unit cell marked in yellow). (15×15 nm^2, V_s = +1.2 V, I_t = 0.10 nA)

As seen previously, the temperature of the substrate during deposition can affect the structure of the adsorbed species, leading to a more ordered superstructure. To investigate the desorption

behaviour of acetic acid, a sample with coverage of 0.4 ML acetic acid was heated to 570 K for 10 mins. STM images before and after the heating are displayed in Figure 6.13a and b. Most of the acetic acid is observed to have been desorbed cleanly, with the coverage afterwards measured at 0.05 ML, of which 80 % of the molecules are found at the step edges. Such preferential desorption at the terrace sites over those molecules bound at step edges suggests enhanced bonding at the edges, possibly due to under-coordinated Ti atoms. The only features remaining after the desorption are observed to have the same height and width as before, and it can therefore be assumed that if any dissociation took place it did not leave any stable products on the surface. The UHV system used for this study was not equipped to perform TPD investigations and as a result it is not known whether the acetate was desorbed molecularly or if it dissociated upon heating. TPD and STM measurements by Tanner et al. of formic and acetic acid on anatase $TiO_2(001)(1 \times 4)$ showed desorption of the acetic acid upon annealing to 850 K again with only a low concentration of adsorbates or dissociation products remaining on the surface.[8, 22]

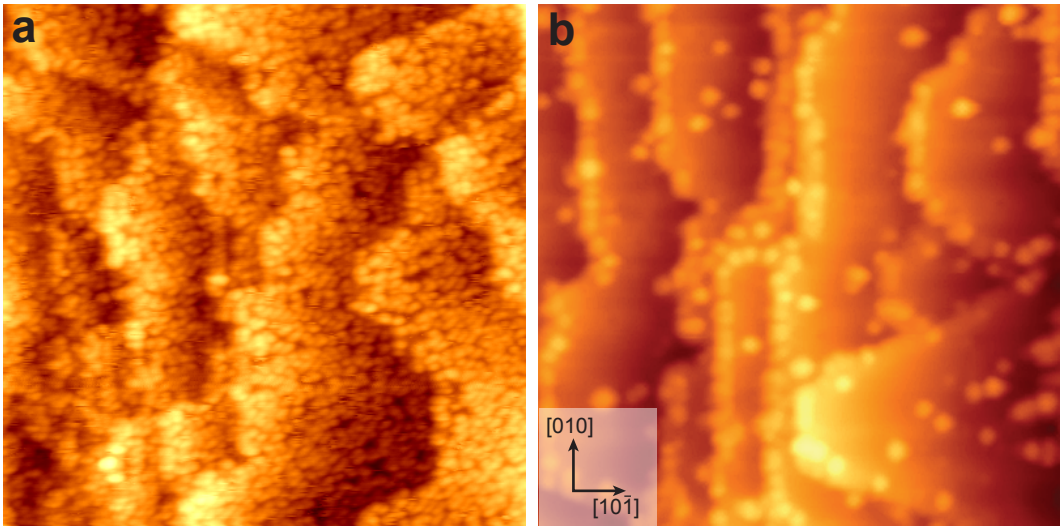

Figure 6.13: STM images showing desorption of acetic acid on anatase $TiO_2(101)$ after heating at 570 K. (a) Initial STM image of 0.4 ML acetic acid. (30×30 nm^2, V_s = +1.4 V, I_t = 0.30 nA) (b) STM image recorded after heating to 570 K for 10 mins. The coverage is measured to be 0.05 ML, predominantly located at the step edges of the anatase. (30×30 nm^2, V_s = +1.4 V, I_t = 0.10 nA)

6.3.5 UV Irradiation of Acetic Acid on Anatase TiO_2(101)

The effect of ultraviolet irradiation of TiO_2 surfaces is of much interest due to their important photocatalytic properties. Hole generation by incident photons leading to radical species that can take part in photocatalytic oxidation and decomposition is a vital process that underpins many of the mechanisms of catalysis.[1] There have been many photocatalytic studies on the various polymorphs of TiO_2 but very limited data exists of studies at the molecular and atomic scales. In our experiment, we examine the effects of illuminating an acetic-acid covered anatase (101) surface with UV light. A previous study comparing the photoinduced decomposition of acetic acid on anatase, rutile, and brookite nanoparticles reports facile dissociation into a number of intermediate species including formate, carbonate and water.[21]

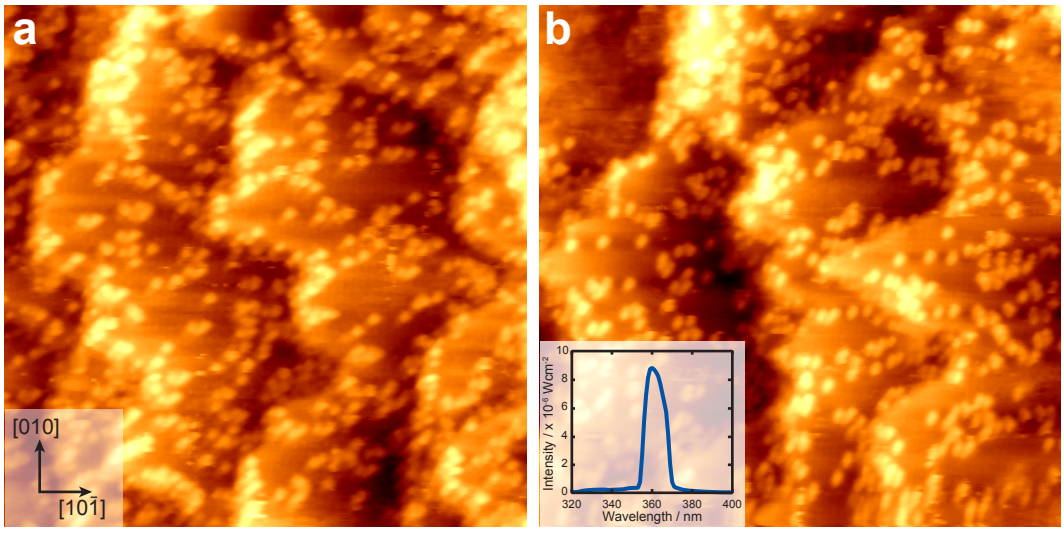

Figure 6.14: STM images showing the effect of UV irradiation of acetic acid on anatase TiO_2(101). The bright features on the terraces and step edges are individual acetic acid molecules (a) 0.08 ML acetate on anatase (101) before exposure to UV, the molecules are distributed evenly across the substrate (39 $\times$ 39 nm^2, V_s = +1.7 V, I_t = 0.10 nA) (b) After 2 hours illumination with 365 nm UV light, the system displays an almost identical appearance with a slightly lower coverage (0.07 ML) All molecular-sized features have the same height and width in STM as before illumination. (35 $\times$ 35 nm^2, V_s = +1.2 V, I_t = 0.10 nA) The power spectrum of the UV lamp used is displayed as an inset in (b).

The STM image in Figure 6.14a, shows a 0.08 ML coverage of acetate on the anatase (101) surface before illumination with UV. This sample was illuminated in the preparation chamber for 2 hours with the 365 nm UV light (power spectrum displayed as inset in Figure 6.14) with a photon flux of 4.3×10^{16} cm^{-2} s^{-1}. This wavelength light corresponds to a photon energy of 3.40 eV, larger than the bandgap of TiO_2 of 3.1 eV and hence above the threshold for photoexcitation. [1, 4] During illumination, a slight temperature increase was measured on the sample (5 K) accompanied with a pressure increase of 3×10^{-11} mbar. An STM image of the surface after illumination is presented in Figure 6.14b. The image is almost identical to that in Figure 6.14a, with the molecules having an identical appearance and only a very slightly lower coverage of 0.07 ML implying that any reaction has only occurred to a very small number of the molecules. The expected reaction products of full dissociation of acetate are CO_2 and H_2O, both of which should not adhere well to the anatase (101) surface at room temperature explaining the lack of additional features in the STM images. One reason for the apparent low reactivity may be the lack of available oxygen; the only source is the anatase surface itself. An interesting future experiment to confirm this hypothesis may therefore be to expose the same system to UV irradiation in the presence of O_2.

6.3.6 Water and Acetic Acid Co-adsorption

Water is almost ever-present in industrial applications of TiO_2 and as such it is of great interest to study its effects not only on clean surfaces, but also in combination with other adsorbates and during reactions. The rate of photocatalytic oxidation and decomposition of formic acid on Pt/TiO_2 is known to be inhibited or increased depending on the concentrations of water and as such fundamental studies of water/carboxylic acid mixtures are vital to furthering our understanding of the mechanisms behind these processes.[29, 34]

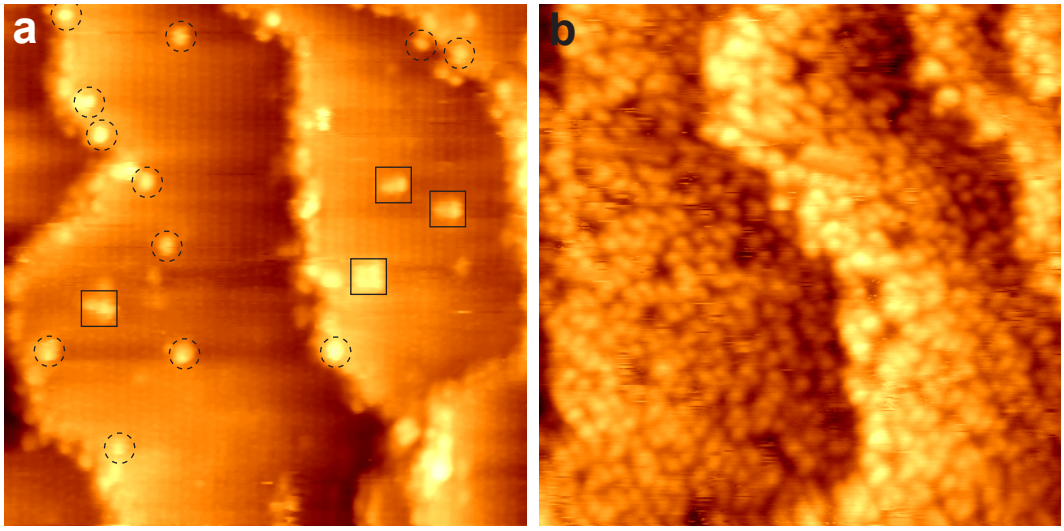

Figure 6.15: STM images of anatase TiO_2(101) after coadsorption of (a) 0.25 L and (b) 15 L water and acetic acid (1:1 ratio). (a) At low coverages (0.02 ML) a number of different features are seen including some identical in size to the acetate molecules observed for pure acetic acid exposure (marked with dashed circles) and other unidentified adsorbates with quite different shapes. (black squares) (24 $\times$ 24 nm^2, V_s = +1.0 V, I_t = 0.20 nA) (b) At saturation coverage (0.4 ML) the overlayer is identical in appearance to that observed for pure acetic acid exposure. (19 $\times$ 19 nm^2, V_s = +1.2 V, I_t = 0.20 nA)

Initial investigations of this on anatase TiO_2(101) were undertaken by exposure to 0.25 L of a 1:1 ratio of water:acetic acid at room temperature. An STM image of the result of this is displayed in Figure 6.15a, from which it can be seen that a number of different molecular-sized features are present on the surface with an estimated coverage of $\sim$0.02 ML. In contrast to a similar coverage of pure acetic acid (see Figure 6.8a) where all of the features were the same height and width and assigned to individual acetate molecules, there appear to be a number of different species present with unusual appearances (highlighted with solid squares in Figure 6.15a). A precise identification of these numerous species is not possible, but a number are found to have the same height and width as observed previously for adsorbed acetate and are bound to the same location on the lattice, some of these are highlighted with dashed circles in Figure 6.15a. In our previous experiments, pure acetic acid was found to display a sticking probability of $\sim$70% however for the co-adsorption, this has dropped to $\sim$10%. As reported by He et al. in [10] water does not adhere to anatase (101) at room temperature, so we would not expect it to appear in significant

amounts in our STM images.

Exposure of the anatase (101) surface to a further 15 L of the acetic acid solution at room temperature led to a saturated overlayer of coverage 0.4 ML as shown in Figure 6.15b. This has an almost identical appearance to that observed for high coverages of pure acetic acid (see Figure 6.10a), with no long-range ordering present and only a few occurrences of a few molecules forming short strings aligned along the $[11\bar{1}]$ and $[1\bar{1}\bar{1}]$ directions.

6.4 Summary and Conclusions

In summary, we present scanning tunnelling microscopy investigations of the adsorption properties of acetic acid on anatase TiO_2(101). A clean anatase (101) substrate was characterised with atomic resolution STM, LEED and AES. At small exposures at room temperature, acetic acid was found to adsorb evenly across the substrate terraces with no apparent preference for step edges. At saturation coverages after deposition at room temperature there was no long range ordering of the adsorbates, although exposure at raised susbtrate temperatures induced regions of highly ordered superstructure in STM. The periodicity of such overlayers was determined to be (2×1) and, along with high-resolution STM imaging of individually adsorbed molecules, the adsorption was consistent with a dissociated bidentate binding geometry of the acetate to two neighbouring Ti_{5c} atoms along the [010] direction. The acetate molecules were observed to have low mobility at the temperature of our investigations (300 K), although there was considerable interactions with the tip under certain tunnelling conditions. Voltage pulsing of + 6 V with the STM tip was able to desorb acetate molecules from the surface, as was heating to $\sim$570 K in UHV. Desorption by heating at this temperature removed the majority of the adsorbates, the remainder were observed to be located primarily at the step edges of the anatase substrate, suggesting increased bonding at these sites. Exposure of the acetate-covered surface to ultraviolet light did not have any major effect except a slight reduction ($\sim$10%) in coverage, likely due to the lack of oxygen required for photocatalytic oxidation, under the experimental conditions (UHV). The co-adsorption of water and acetic acid (1:1 ratio) was observed to have no effect on the structure of the overlayers at saturation coverage, although at lower exposures some, at-present unidentified, molecular species were observed.

There is clearly a large amount of further work that could be attempted on the acetic acid - anatase TiO_2(101) system, of particular interest would be to perform STM simulations of individual acetate molecules to determine whether the proposed dissociative bidentate binding geometry is correct. Within the deposition temperature range explored (300-420 K) only a small fraction of the saturated coverage displayed the (2×1) superstructure, it may be possible to investigate whether different deposition conditions led to increasing this fraction. In all of the experiments in this chapter, the anatase (101) substrate had an extremely low concentration of surface point defects, the effect on acid adsorption of increasing this concentration by for example, electron-beam irradiation, is another area of interest. The water/acid co-adsorption experiments require further investigation, with a multitude of possible future studies including the effect of different concentrations of water or raised or lowered deposition temperatures as well as a clear identification of the species observed in these preliminary experiments. The effects of UV irradiation of adsorbed acetate looks to be another promising route, one interesting experiment may be to examine the effect of the presence of oxygen during illumination.

References

[1] Fujishima, A.; Zhang, X.; Tryk, D. *Surf. Sci. Rep.* **2008**, *63*, 515–582.

[2] Diebold, U. *Surf. Sci. Rep.* **2003**, *48*, 53–229.

[3] Pang, C. L.; Lindsay, R.; Thornton, G. *Chem. Soc. Rev.* **2008**, *37*, 2328–2353.

[4] Henderson, M. A. *Surf. Sci. Rep.* **2011**, *66*, 185–297.

[5] Thompson, T. L.; Yates, J. T. *Chem. Rev.* **2006**, *106*, 44284453.

[6] Yates, J. T. *Surf. Sci.* **2009**, *603*, 1605–1612.

[7] Fujishima, A.; Honda, K. *Nature* **1972**, *238*, 37–38.

[8] Tanner, R.; Liang, Y.; Altman, E. *Surf. Sci.* **2002**, *506*, 251–271.

[9] Herman, G.; Gao, Y. *Thin Sol. Films* **2001**, *397*, 157–161.

[10] He, Y.; Tilocca, A.; Dulub, O.; Selloni, A.; Diebold, U. *Nat. Mat.* **2009**, *8*, 585–589.

[11] Herman, G.; Dohnalek, Z.; Ruzycki, N.; Diebold, U. *J Phys Chem B* **2003**, *107*, 2788–2795.

[12] Gong, X.-Q.; Selloni, A.; Dulub, O.; Jacobson, P.; Diebold, U. *J. Am. Chem. Soc.* **2008**, *130*, 370–381.

[13] Gong, X.-Q.; Selloni, A.; Batzill, M.; Diebold, U. *Nat. Mat.* **2006**, *5*, 665–670.

[14] He, Y.; Dulub, O.; Cheng, H.; Selloni, A.; Diebold, U. *Phys. Rev. Lett.* **2009**, *102*, 106105.

[15] O'Regan, B.; Graetzel, M. *Nature* **1991**, *353*, 737–740.

[16] Hara, K.; Horiuchi, H.; Katoh, R.; Singh, L.; Sugihara, H.; Sayama, K.; Murata, S.; Tachiya, M.; Arakawa, H. *J. Phys. Chem. B* **2002**, *106*, 374–379.

[17] Ikeda, S.; Sugiyama, N.; Pal, B.; Marci, G.; Palmisano, L.; Noguchi, H.; Uosaki, K.; Ohtani, B. *Phys. Chem. Chem. Phys.* **2001**, *3*, 267–273.

[18] Kim, Y.; Walker, J.; Samuelson, L.; Kumar, J. *Nano. Lett.* **2003**, *3*, 523–525.

[19] Nazeeruddin, M.; Kay, A.; Rodicio, I.; Humphrybaker, R.; Muller, E.; Liska, P.; Vlachopoulos, N.; Gratzel, M. *J. Am. Chem. Soc.* **1993**, *115*, 6382–6390.

[20] Villarreal, T.; Gomez, R.; Neumann-Spallart, M.; Alonso-Vante, N.; Salvador, P. *J. Phys. Chem. B* **2004**, *108*, 15172–15181.

[21] Mattsson, A.; Osterlund, L. *J. Phys. Chem. C* **2010**, *114*, 14121–14132.

[22] Tanner, R.; Sasahara, A.; Liang, Y.; Altman, E.; Onishi, H. *J. Phys. Chem. B* **2002**, *106*, 8211–8222.

[23] Ito, T.; Yoshida, F. *Journal of Chemical and Engineering Data* **1963**, *8*, 315–320.

[24] Dulub, O.; Diebold, U. *J Phys-Condens Mat* **2010**, *22*, 084014.

[25] Burdett, J.; Hughbanks, T.; Miller, G.; Richardson, J.; Smith, J. *J. Am. Chem. Soc.* **1987**, *109*, 3639–3646.

[26] Hebenstreit, W.; Ruzycki, N.; Herman, G.; Gao, Y.; Diebold, U. *Phys Rev B* **2000**, *62*, R16 334–336.

[27] Tao, J.; Luttrell, T.; Bylsma, J.; Batzill, M. *J. Phys. Chem. C* **2011**, *115*, 3434–3442.

[28] Wang, C.; Groenzin, H.; Shultz, M. *J. Am. Chem. Soc.* **2005**, *127*, 9736–9744.

[29] Miller, K. L.; Musgrave, C. B.; Falconer, J. L.; Medlin, J. W. *J. Phys. Chem. C* **2011**, *115*, 2738–2749.

[30] Miller, K. L.; Falconer, J. L.; Medlin, J. W. *J. Cat.* **2011**, *278*, 321–328.

[31] Vittadini, A.; Selloni, A.; Rotzinger, F.; Gratzel, M. *J. Phys. Chem. B* **2000**, *104*, 1300–1306.

[32] Li, S.-C.; Diebold, U. *J. Am. Chem. Soc.* **2010**, *132*, 64–66.

[33] Pang, C. L.; Bikondoa, O.; Humphrey, D. S.; Papageorgiou, A.; Cabailh, G.; Ithnin, R.; Chen, Q.; Muryn, C. A.; Onishi, H.; Thornton, G. *Nanotech.* **2006**, *17*, 5397–5405.

[34] Miller, K. L.; Lee, C. W.; Falconer, J. L.; Medlin, J. W. *J. Cat.* **2010**, *275*, 294–299.

CHAPTER 7

BENZOIC ACID ADSORPTION ON RUTILE TiO_2(110)

Abstract

Scanning tunnelling microscopy has been used to investigate the adsorption and photoreactivity of benzoic acid on the rutile TiO_2(110)(1 $\times$ 1) and reconstructed TiO_2(110)(1 $\times$ 2) surfaces. Benzoic acid binds to both surfaces dissociatively via a bridging geometry to two Ti_{5c} sites. At a slightly elevated sample temperature during deposition onto the (110)(1 $\times$ 1) surface, a well-ordered (2 $\times$ 1) overlayer was formed at saturation coverages of benzoate. On the reconstructed (110)(1 $\times$ 2) surface, benzoate was observed to adsorb between the (1 $\times$ 2) strands leading towards a (2 $\times$ 2) superstructure at higher coverage. Atomically resolved images at low benzoate coverage were consistent with the Ti_2O_3 added-row model for the TiO_2(110)(1 $\times$ 2) reconstruction.

7.1 Introduction

Ever since the discovery of TiO_2-based photocatalysis by Fujishima and Honda in the early 1970s [1], there has been remarkable interest in this field with thousands of publications regarding both the fundamental science and industrial applications.[2] There are a number of reviews of TiO_2 photocatalysis, of particular interest are those from a surface science perspective which aim to correlate the behaviour of single crystal surfaces with the activity of the bulk catalysts.[3–5]

TiO_2 is of course not limited to applications in photocatalysis with many proven applications including gas sensors, heterogeneous catalysis, pigments and electrical devices.[6–8] It is hoped that the study of single-crystalline TiO_2 surfaces will lead to increased understanding of the mechanisms behind titania's many useful properties with a view to optimising their efficiency and improving their effectiveness. The thermodynamically most stable (110) surface of rutile TiO_2 which is easily prepared has become a model system for metal oxide surface studies with a vast amount of experimental and theoretical work in the literature.[2, 6]

The rutile $TiO_2(110)(1 \times 1)$ surface has been thoroughly investigated using the full spectrum of surface science techniques and is quite well understood from the perspective of its defect structure and adsorption and reactivity of small molecules.[6, 9] The (1×2) reconstruction encountered after repeated reduction by annealing in UHV has had somewhat less attention however, with controversy still existing over its basic structure. A number of models have been proposed for the (1×2) reconstruction, the two that have had the most attention are: (i) a Ti_2O_3 added-row model which appears consistent with LEED-IV and STM data [10–14] (ii) a Ti_3O_6 added-row model that may explain NC-AFM and other STM results.[15, 16]

The absorption and behaviour of many different small molecules on rutile $TiO_2(110)$ has been studied in an attempt to understand the reactivity of the surface and its defect sites.[9] One important class of such molecules are carboxylates which have a number of practical applications, including the linking of dye molecules to titania surfaces within Grätzel type dye-sensitised solar cells.[17] On the $TiO_2(110)(1 \times 1)$ surface it has been well established that the most common binding geometry of monocarboxylic acids (formic, acetic etc.) is that of dissociative bidentate bridging to two neighbouring Ti_{5c} sites along the [001] direction.[9, 18–20] Studies on the reconstructed $TiO_2(110)(1 \times 2)$ surface are much more limited with only a couple of STM studies in the literature. Formic acid was observed by Bennett et al. to adsorb preferentially on the crosslinked sites, and even lead to re-oxidation of the surface during decomposition at raised temperatures.[21]

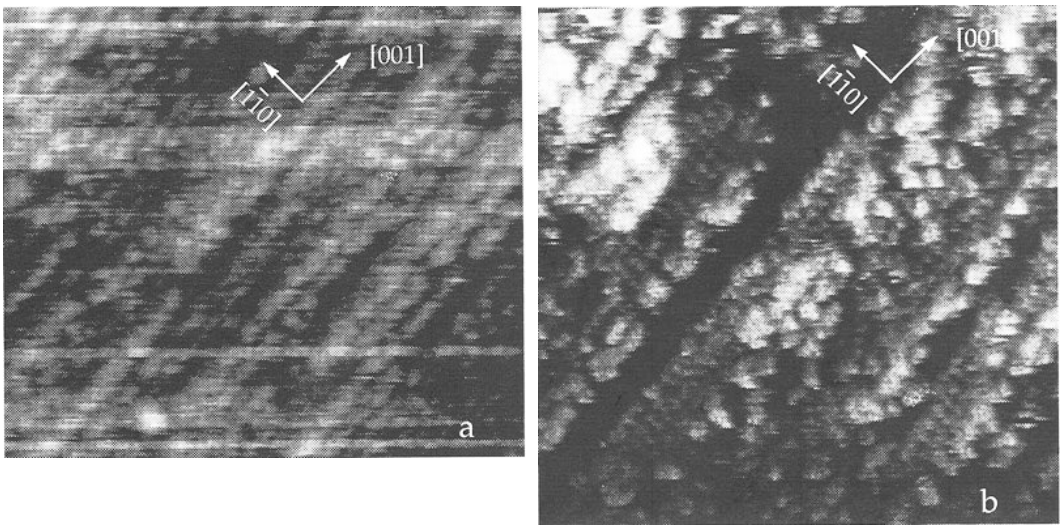

Figure 7.1: STM images of the $TiO_2(110)(1 \times 2)$ surface, reproduced from original manuscript of [22] with permission.

In an early study by Guo et al. [22] the adsorption of benzoic acid on rutile $TiO_2(110)(1 \times 1)$ and (1×2) surfaces was investigated with LEED, STM and ESDIAD and found to follow similar

behaviour to the smaller carboxylates. The STM images of benzoate on $TiO_2(110)(1 \times 2)$ (Figure 7 in [22]) have been reproduced from the original manuscript and are displayed in Figure 7.1. In our work we provide enhanced quality STM images sufficient to assign the adsorption sites.

7.2 Experimental Procedure

The experiments were conducted in a UHV system with a base pressure of 1×10^{-11} mbar and separate analysis and preparation chambers. The STM employed was an *Omicron* UHV AFM/STM operated in constant current mode at room temperature using electrochemically etched tungsten tips that were conditioned during scanning with voltage pulses (upto 10 V) and high negative/positive bias scans to obtain stable atomic-resolution imaging. All STM imaging was carried out tunnelling into empty states using positive sample bias voltages in the range 0.7-2 V. The rutile $TiO_2(110)$ crystals (*Pi-Kem*) were attached to standard sample plates with spot-welded tantalum clips and the temperature during annealing monitored using an optical pyrometer (*Land*). To prepare the $TiO_2(110)(1 \times 1)$ surface, cycles of Ar^+ sputtering (5 min, 1 keV, 10 μA) and annealing in UHV (10 min, 900 K) were employed until any contamination was below the detection limit of AES and a well-ordered (1×1) LEED pattern with a low background was observed. For the reconstructed $TiO_2(110)(1 \times 2)$ surface a separate, heavily reduced crystal was used which was dark blue in colour and had undergone a high number of annealing cycles at temperatures upto 1020 K until a well-ordered (1×2) LEED pattern was observed. The temperatures during annealing and acid exposure were measured with an optical pyrometer or a K-type thermocouple attached to the manipulator arm and positioned near to the sample plate

Benzoic acid (99.9 %, *Sigma-Aldrich*) was contained within a glass vial attached to the gas line of the UHV system and admitted into the preparation chamber via a high-precision leak valve. To purify the acid, which is a solid at room temperature, repeated melt-freeze-pump cycles were carried out. During exposure, the gas line and vial were heated to ∼400 K with the acid liquefied, RGA mass spectrometry was used to monitor the purity during dosing. All exposures are nominal and quoted in Langmuirs (1 L = 1×10^{-6} torr s) based on the uncompensated pressure within the preparation chamber during dosing. The chamber pressure during benzoic acid exposure was in the range $5 \times 10^{-8} - 2 \times 10^{-7}$ torr, with exposure times of 10-20 minutes. UV irradiation was achieved with a 365 nm lamp shone through a standard silica glass UHV window, with a radiating power of 1.3 mWcm^{-2} at a sample distance of ∼30 cm from the lamp. The window was measured to absorb 50 % of the light, with the resultant photon flux on the sample under the operating conditions being 4.3×10^{16} cm^{-2} s^{-1}. For this work we define a monolayer (ML) of adsorbates as one per primitive surface unit cell, a density of 5.2×10^{14} cm^{-2}.

7.3 Results and Discussion

7.3.1 Benzoic acid adsorption on rutile TiO_2(110)(1 × 1)

The TiO_2(110)(1 × 1) surface has been extensively studied with STM over the last decade, and is now considered to be well-understood. For our initial investigations of benzoic acid adsorption on titania surfaces it was decided to revisit the work of Guo et al. [22] and begin with TiO_2(110)(1 × 1). Figure 7.2a and b are STM images of the clean (1 × 1) surface on a large scale (a) and atomically resolved (b). The surface is characterised by flat (110)(1 × 1) terraces separated by

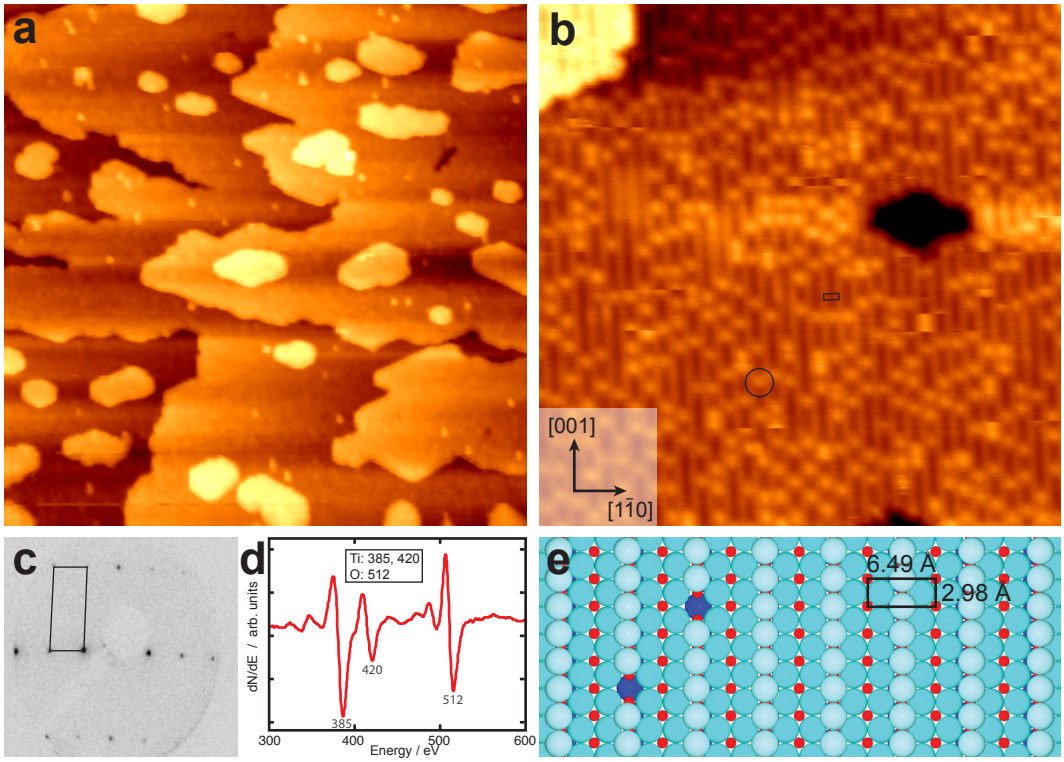

Figure 7.2: The clean rutile TiO_2(110)(1 x 1) surface. (a) Large scale area STM image (200 $\times$ 200 nm^2, V_s = +1.2 V, I_t = 0.20 nA) (b) Atomically resolved STM image (25 $\times$ 25 nm^2, V_s = +1.2 V, I_t = 0.20 nA), the bright rows in the [001] direction are assigned to Ti^{4+} ions (see model in (e)) and the bright features between these are hydroxyls. (c) LEED (80 eV) with the reciprocal-space unit cell marked. (d) Auger electron spectrum of the clean surface, peaks from Ti LMM and O KLL are shown. (e) model of the TiO_2(110)(1 $\times$ 1) surface: red atoms - Ti_{5c}, blue atoms - in plane O, light blue atoms - bridging O.

monoatomic steps of height 0.3 nm. In the atomically resolved image in Figure 7.2b, which is of empty states, the bright rows running along the [001] direction are assigned to Ti_{5c} cations as depicted in the model surface presented in Figure 7.2e (red atoms). The bright features located between the bright rows in STM (one marked with a circle) are assigned to hydroxyls.[23] The light and dark blue atoms in the model in Figure 7.2e represent bridging and surface oxygen ions respectively. The unit cell is marked on the model and the STM image (black rectangle) and has dimensions of 6.49 Å by 2.98 Å. Since the dimensions of the TiO_2(110)(1 $\times$ 1) unit cell are well-known, the STM piezos can be calibrated in all directions by comparison with such an image and applied to the other experimental results permitting more accurate measurement of distances. Displayed in Figure 7.2c is a LEED pattern (80 eV) from the clean (110)(1 $\times$ 1) surface with the

reciprocal space unit cell marked. Figure 7.2d is an Auger electron spectrum taken of the surface and shows peaks from Ti LMM (385 and 420 eV) and O KLL (512 eV) with any contamination under the detection limit of the spectrometer.

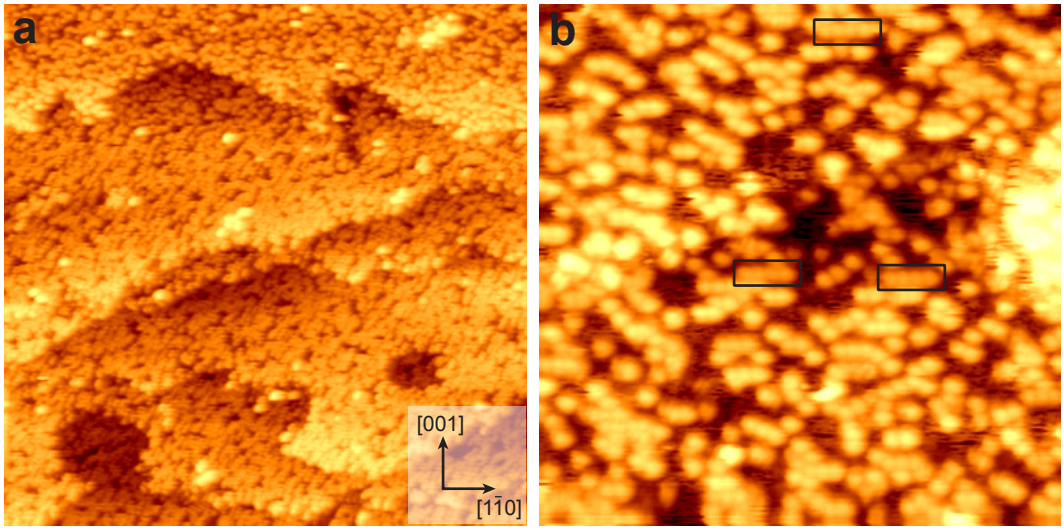

Figure 7.3: STM images of 0.2 ML benzoic acid deposited at 300 K on rutile $TiO_2(110)(1 \times 1)$. (a) Large scale area (100×100 nm^2, V_s = +1.9 V, I_t = 0.05 nA) with no long range ordering of the adsorbates visible. (b) Zoomed-in image (25×25 nm^2, V_s = +1.9 V, I_t = 0.05 nA) where the individual benzoate molecules can be seen more clearly and are observed to form short strings, some of which are highlighted.

Exposure of the clean $TiO_2(110)(1 \times 1)$ surface to $\sim$30 L of benzoic acid at room temperature led to a coverage of $\sim$0.2 ML as depicted in the STM images presented in Figure 7.3. From the large scale area in Figure 7.3a, there does not seem to be any long-range ordering of the acid molecules which appear as bright protrusions evenly distributed across the surface. In the zoomed-in image in Figure 7.3b, the adsorbed benzoate is observed to appear as bright features of height $\sim$0.30 nm and width $\sim$1.2 nm (not compensated for broadening via tip-convolution effects) and forms occasional short chains of upto 4 molecules in length oriented along the [1$\bar{1}$0] direction, some of which are highlighted with black rectangles. The previous work of Guo et al. on benzoic acid adsorption on rutile $TiO_2(110)$ surfaces observed similar dimer and trimer formations of benzoate

along the $[1\bar{1}0]$ direction which is attributed to hydrogen bonding between the aromatic ring of one benzoate molecule and a hydrogen on the neighbouring benzoate which has its aromatic ring rotated by 90° (i.e. pointing along $[1\bar{1}0]$).[22] Due to the distances involved however, it would seem more favourable for these sort of interactions to occur along the $[001]$ direction, which is not observed, leading to the conclusion that further stabilisation may be provided by hydrogen bonding between the hydrogen in the aromatic ring of the benzoate and the bridging oxygen rows of the $TiO_2(110)(1 \times 1)$ surface which would only be possible if the aromatic ring is perpendicular to the carboxylate group. In an attempt to increase the ordering of the overlayer, heating of the benzoate covered surface to 380 K in UHV was attempted but this did not have any appreciable effect on the structure of the overlayer. It has been shown that the binding geometry of formate on the $TiO_2(110)(1 \times 1)$ surface can be greatly affected by annealing to temperatures around 350 K including binding to surface oxygen vacancies.[24] We do not report any such species but it is likely that their formation is extremely sensitive to the surface preparation and defect concentration as well as the sample temperature and exposure conditions.[9]

In order to further examine the effect of sample temperature on the structure of the adsorbed layer we exposed the $TiO_2(110)(1 \times 1)$ surface to $\sim$60 L benzoic acid with the sample held at 370 K. The results are displayed in Figure 7.4. A clear (2×1) superstructure is observed in Figure 7.4a with a near-saturated coverage measured at 0.45 ML. Significant tip interaction with the benzoate is observed which is characterised by streaking in the fast scan direction (horizontal) and led to noticeable instability during STM imaging. In Figure 7.4b, a different area of the same sample, the (2×1) structure is clearly observed. A line profile (blue line) across a number of the benzoate molecules is shown in Figure 7.4d and confirms their spacing in the $[001]$ direction is $\sim$0.6 nm, twice the lattice spacing of $TiO_2(110)(1 \times 1)$. A missing benzoate molecule which appears as a dark spot permits measurement of their height to be 240 nm at the particular scanning

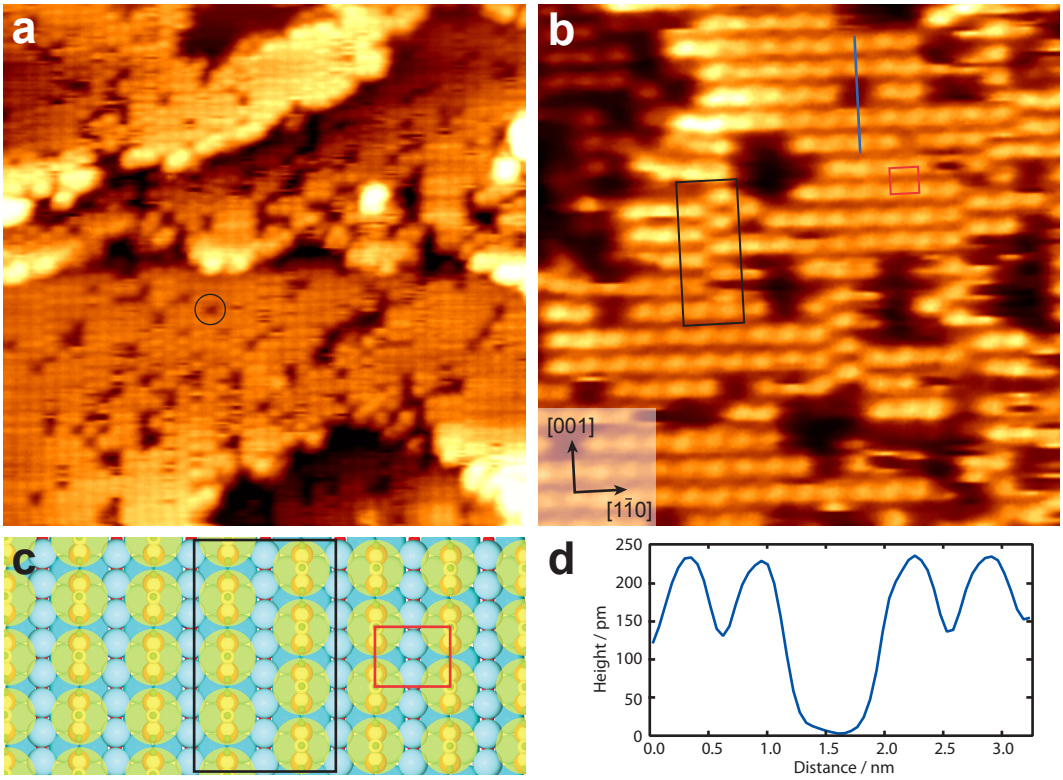

Figure 7.4: STM of 0.45 ML benzoic acid deposited at 370 K on the rutile TiO_2(110)(1 × 1) surface. (a) Large scale area STM image (25 × 25 nm^2, V_s = +1.9 V, I_t = 0.1 nA) of the saturated surface showing a (2 × 1) overlayer with an occasional missing adsorbate as highlighted. (b) STM image (15 × 15 nm^2, V_s = +1.6 V, I_t = 0.1 nA) of the overlayer showing the presence of domains offset by a lattice spacing in the [001] direction (highlighted in black). The (2 × 1) unit cell is marked in red. (c) Model of the (2 × 1) superstructure formed by the benzoate molecules bridge-binding to two adjacent Ti^{4+} cations along [001]. The black rectangle is around the junction between two (2 × 1) domains that are offset by one lattice spacing in the [001] direction. (d) Line profile from the STM image in (b) across four benzoate molecules and a missing adsorbate confirming their (2 × 1) spacing and height of ∼240 pm.

parameters used. This is slightly smaller than that measured on the unordered benzoate shown in Figure 7.3, the discrepancy is likely due to a tip convolution effects. The unit cell of the (2 × 1) overlayer is marked with a red rectangle. In the region marked with a black rectangle there exists the boundary between two domains of the (2 × 1) layer which are offset by one lattice spacing in the [001] direction. These results are all consistent with a dissociative bidentate binding geometry of the benzoate bridging two neighbouring five-fold coordinated Ti^{4+} ions in the [001] direction. A model of this binding is displayed in Figure 7.4c, where the boundary between two (2 × 1) domains with a shift of a single lattice spacing is also shown for comparison with the

region highlighted in Figure 7.4b. This (2 × 1) superstructure is identical to that observed in previous studies of small carboxylic acids on the rutile TiO_2(110)(1 × 1) surface suggesting that any intermolecular interaction between the aromatic rings of neighbouring benzoate adsorbates is minimal compared with the interaction with the surface under these deposition conditions.[9]

7.3.2 Benzoic acid adsorption on rutile TiO_2(110)(1 × 2)

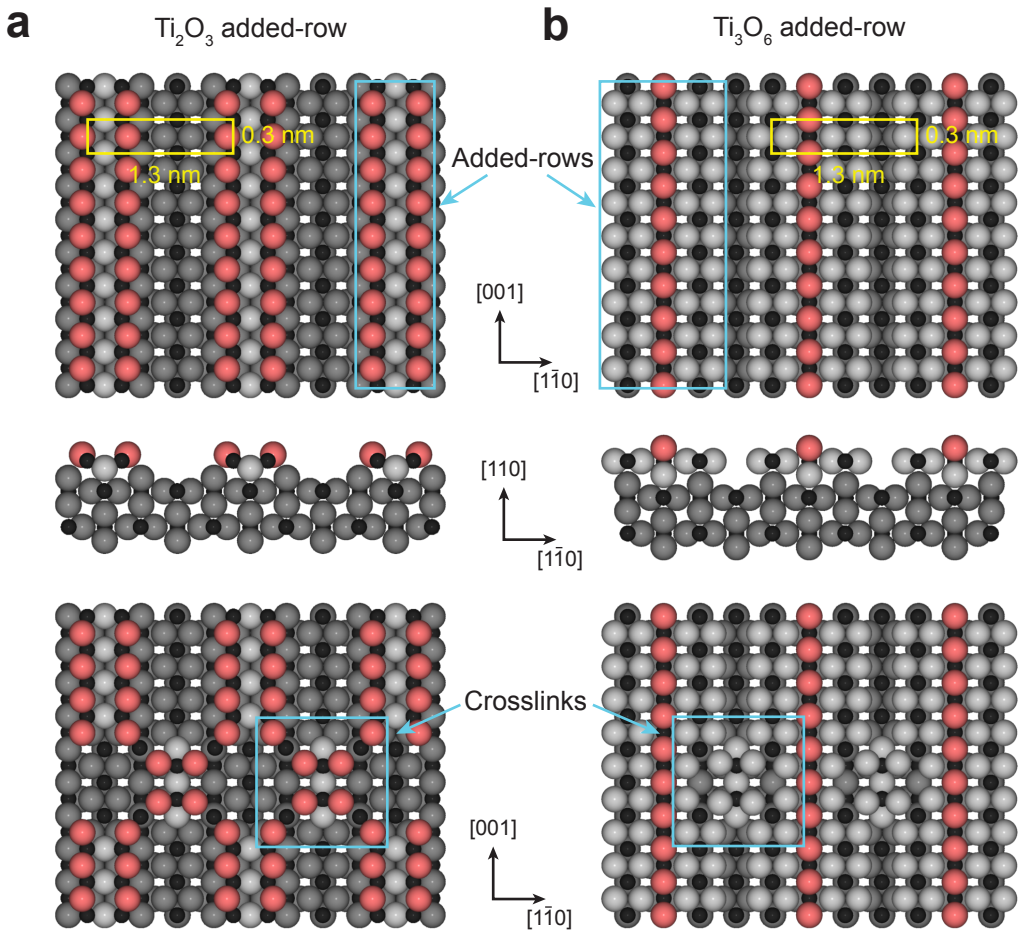

Figure 7.5: Models of the rutile TiO_2(110)(1 × 2) reconstructed surface. (a) Ti_2O_3 added-row model (b) Ti_3O_6 added-row model. Upper models show the (1 × 2) strands running along [001], the middle show a side view, and the lower depict possible cross-link structures. (Black atoms: Ti, grey and red atoms: O)

As discussed in the introduction, the structure of the cross-linked rutile $TiO_2(110)(1 \times 2)$ surface has been a matter of debate for some time now, with a number of different models proposed to explain the experimental data. The two most popular models for the reconstruction, based upon data from both scanned-probe investigations and diffraction techniques are: (a) the Ti_2O_3 added-row model and (b) the Ti_3O_6 added-row model.[11, 13, 15] Structural models for these two are displayed in Figure 7.5 in plan and cross-sectional views, the (1×2) unit cell is marked and the added rows that run along [001] are highlighted in blue. The oxygen atoms of the added rows have been shaded in light grey and red for clarity and to distinguish them from the (1×1) termination underneath. For the Ti_2O_3 model depicted in (a) the Ti cations move to octahedral sites and the oxygen anions remain near to their original positions. In the Ti_3O_6 model (b) in contrast, the atoms all stay close to their bulk positions.[13] The lower frames in Figure 7.5 depict possible structures for the cross-links (marked with blue squares) commonly observed on (1×2) reconstructed surfaces.

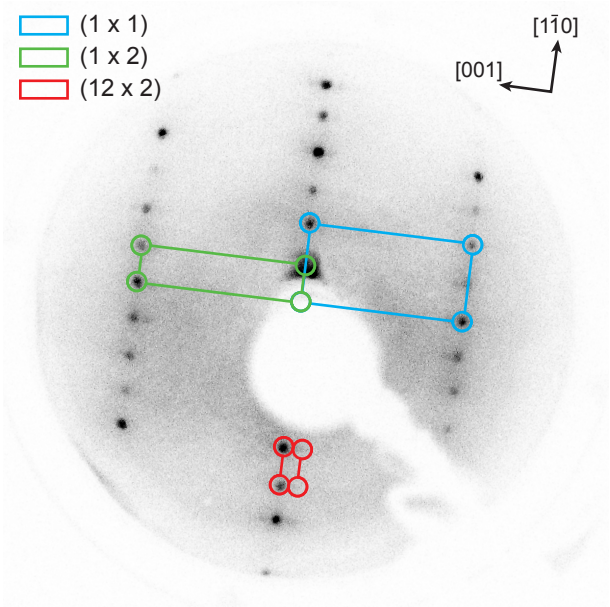

Figure 7.6: LEED (98 eV) of the rutile $TiO_2(110)(1 \times 2)$ surface. The unit cells for (1×1) (blue), (1×2) (green) and (12×2) (red) are marked.

For our experiments on the $TiO_2(110)(1 \times 2)$ surface a heavily reduced crystal was used which was dark blue in colour and had been through many annealing cycles. A typical LEED pattern (98 eV) from this crystal is displayed in Figure 7.6, with its colour inverted for clarity. Highlighted are the reciprocal unit cells with periodicities of (1×1) (blue), (1×2) (green) and (12×2) (red).

STM images of the (1×2) reconstructed surface are shown in Figure 7.7 with a number of characteristic features visible. The large scale area in Figure 7.7a shows that the surface is almost completely covered in the strands running along the $[001]$ direction with a spacing of 1.3 nm that are characteristic of the (1×2) reconstructed surface.[11] In Figure 7.7b a region close to a step edge is dislayed and the features of interest highlighted. It is observed that the additional (1×2) strands are situated on top of (1×1) terminated TiO_2 which can be seen in the region bounded in blue, with some point defects, likely hydroxyls, also visible on the (1×1) surface. The (1×2) strands are marked in red and the characteristic single- and crossed-links which run along the $[1\bar{1}0]$ direction are marked in blue and black respectively. Figure 7.7c allows more detail of these cross-links to be seen. Highlighted in black again, it is observed that they are spaced every 3.5 nm in the $[001]$ direction which is 12 times the unit cell spacing of the (1×1) surface consistent with the (12×2) reconstruction in the LEED in Figure 7.6. A few single links are also present in Figure 7.7c (highlighted in red) and are observed to point in alternating directions (up and down) and have an appearance of half that of a full crosslink. Some atomic scale contrast is visible is also apparent on the (1×2) strands which is shown more clearly in Figure 7.7d. These STM images are all obtained at positive sample biases (+ 1.2 V) and we are therefore imaging empty states and might expect the Ti^{4+} cations to appear as bright, as for the normal imaging mode on the (1×1) surface.[23] The tip termination plays an important role in image formation in STM, and it is commonly observed that spontaneous tip changes occur during scanning (often proposed to be due to the exchange of atoms with the surface) which lead to completely different contrast even at

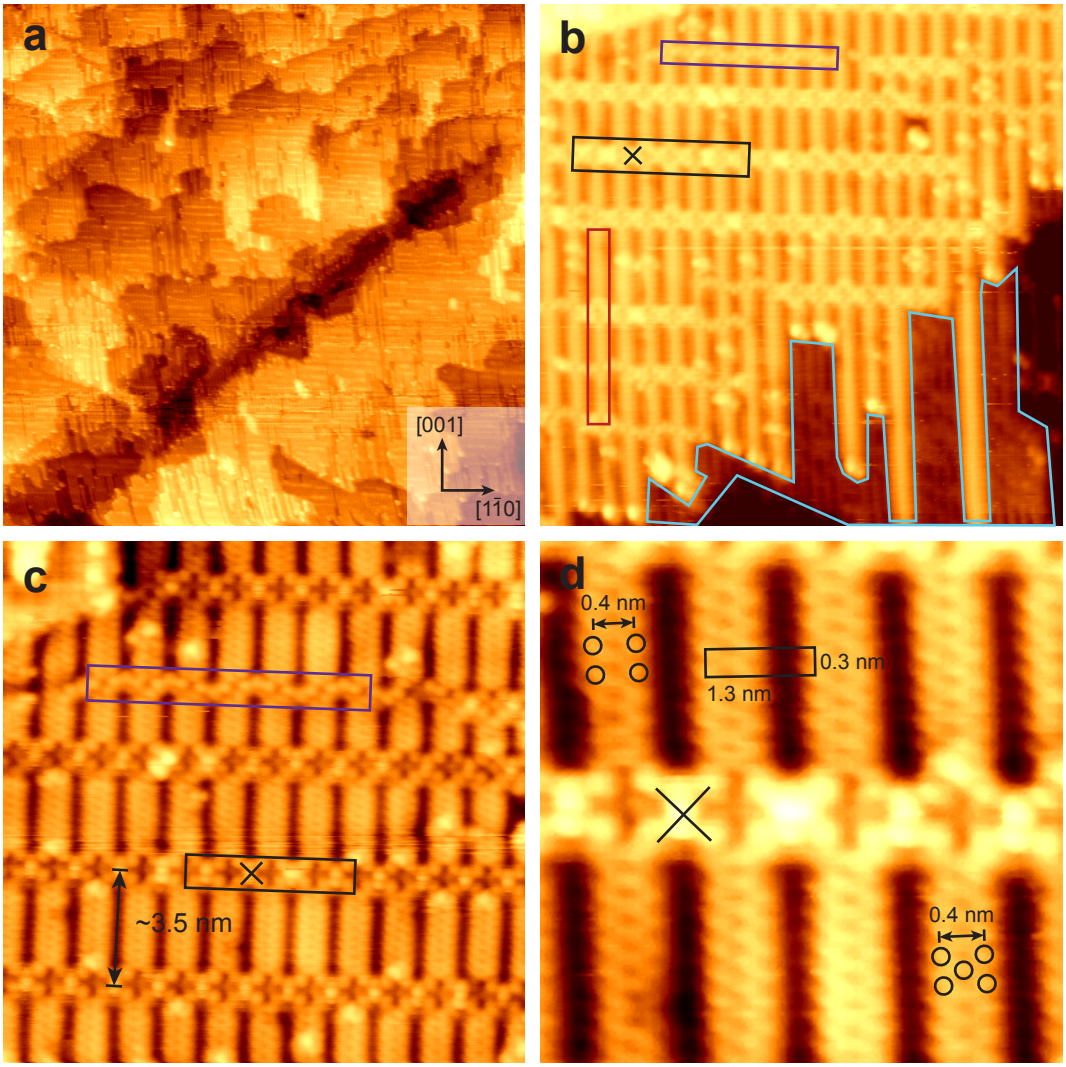

Figure 7.7: STM images of the clean rutile TiO_2(110)(1 × 2) reconstructed surface. (a) Large scale area (200 × 200 nm^2, V_s = +1.4 V, I_t = 0.2 nA) showing the general terrace structure of the surface. (b) A region of the TiO_2(110) surface showing the (1 × 2) strands in the [001] direction (red rectangle) and the single and cross links (blue and black rectangles). Underneath the (1 × 2) strands a section of (1 × 1) surface is also visible and marked with a blue border. (28 × 28 nm^2, V_s = +1.2 V, I_t = 0.3 nA) (c) A view of the (1 × 2) strands, and the cross-links spaced every 3.5 nm which give rise to the (12 × 2) pattern in LEED (see Figure 7.6). (15 × 15 nm^2, V_s = +1.0 V, I_t = 0.3 nA) (d) Atomically resolved image of the (1 × 2) strands, the unit cell is marked and the spacing of bright features which are derived mainly from Ti states is consistent with the Ti_2O_3 added-row model. (5 × 5 nm^2, V_s = +0.8 V, I_t = 0.3 nA)

identical bias voltages.[25] In the atomically resolved STM image presented in Figure 7.7d, there are two slightly different atomic contrasts observable on top of the (1 × 2) strands. In the top left of the frame there is identical contrast to that observed by Pang et al. in [11] with two bright atomic-sized spots on each strand separated by ∼0.4 nm in the $[1\bar{1}0]$ direction. Across the rest of the frame, and as highlighted in the bottom right corner, there appears a slightly different contrast with an additional bright feature in the centre of the strands. The origin of the contrast in STM is not yet fully understood in terms of either of the models presented in Figure 7.5 although the spacing of the atomic features appears to be more compatible with the Ti_2O_3 added-row model. At the present time STS experiments are being carried out in our group to try and identify the precise nature of the structure of the (1 × 2) strands and cross-links.

The cross-linked TiO_2(110)(1 × 2) surface was exposed to ∼100 L of benzoic acid while held at 350 K with STM images of the results displayed in Figure 7.8. From the large scale areas in Figure 7.8a & b, there is a clear preference for adsorption along the [001] direction with an estimated coverage of 0.12 ML and some short-range ordering visible. From the STM image displayed in Figure 7.8c it is observed that the benzoate is adsorbed between the (1 × 2) strands (one strand marked with red lines for clarity). The crosslinks (highlighted with black rectangles) are completely clear of adsorbates of the size of benzoate, a completely different behaviour to the work of Bennett et al. in [21] on formic acid adsorption on TiO_2(110)(1 × 2) where the acid was observed to favour adsorption on the cross-links with no ordering. The benzoate appears as an oval shape with its long axis along $[1\bar{1}0]$ and some regions of the molecules ordering along [001] are also apparent. A line profile across one of these is displayed in Figure 7.8d, and from this it can be seen that the intermolecular spacing is ∼6 nm, consistent with double the lattice constant along [001] and the start of a (2 × 2) superstructure. This is consistent with a bidentate bridging between two neighbouring Ti_{5c} cations along [001] as has been illustrated in Figure 7.9.

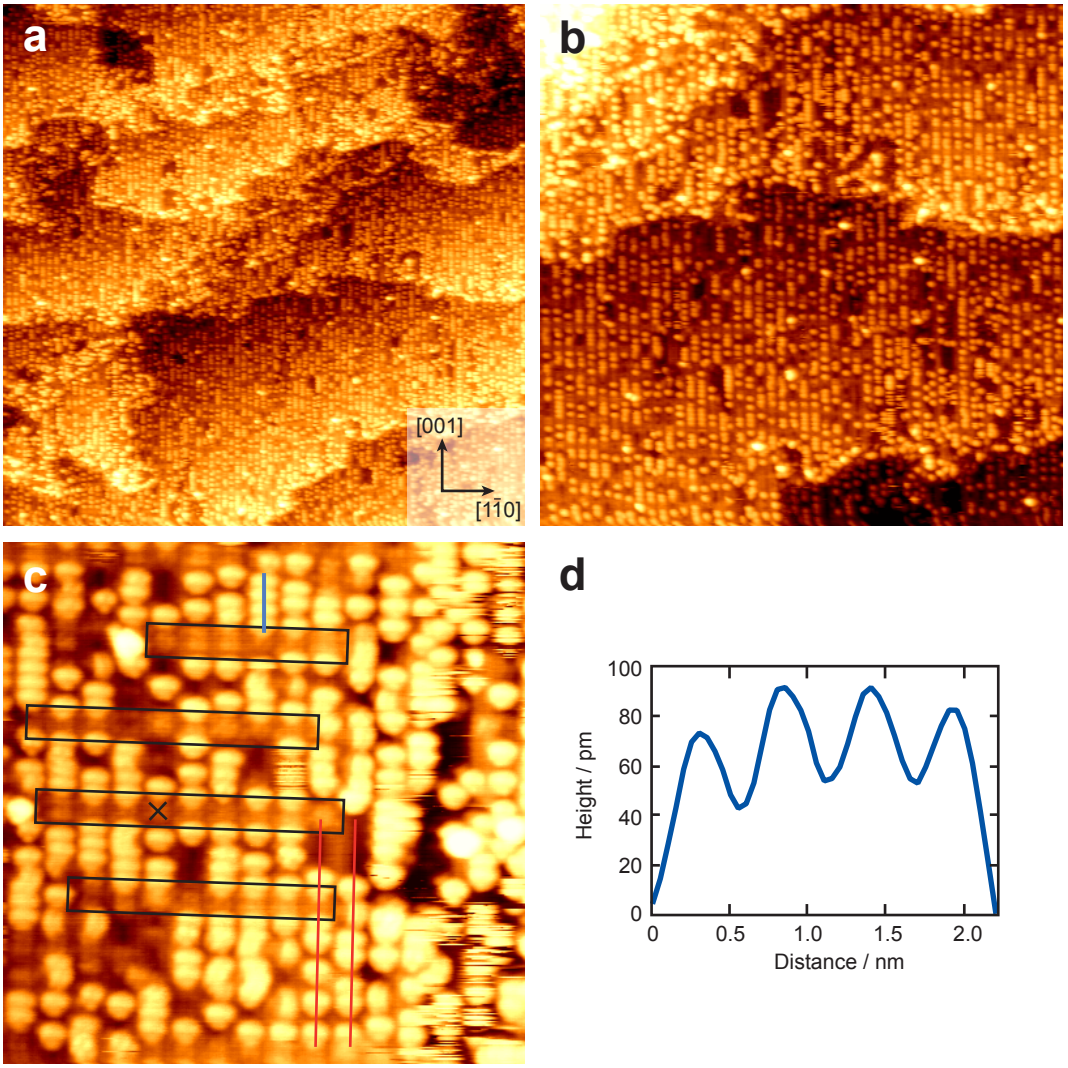

Figure 7.8: STM images of 0.12 ML BA adsorbed at 350 K on the rutile TiO_2(110)(1 × 2) surface. (a) Large scale area (100 × 100 nm^2, V_s = +1.2 V, I_t = 0.1 nA) (b) Image (60 × 60 nm^2, V_s = +1.2 V, I_t = 0.1 nA) showing that the benzoate has a preference for adsorption along the [001] direction. (c) Zoomed-in region (20 × 20 nm^2, V_s = +1.0 V, I_t = 0.1 nA) of the acid-covered surface showing that the benzoate is adsorbed between the (1 × 2) strands, one of which is marked with red lines. The cross-links (highlighted with black rectangles) are clear of any adsorbates, in contrast to the reported results of formic acid adsorption on TiO_2(110)(1 × 2).[21] (d) A line-profile across four of the benzoate molecules in (c) showing that they have a spacing in the [001] direction that is consistent with an overall (2 × 2) superstructure.

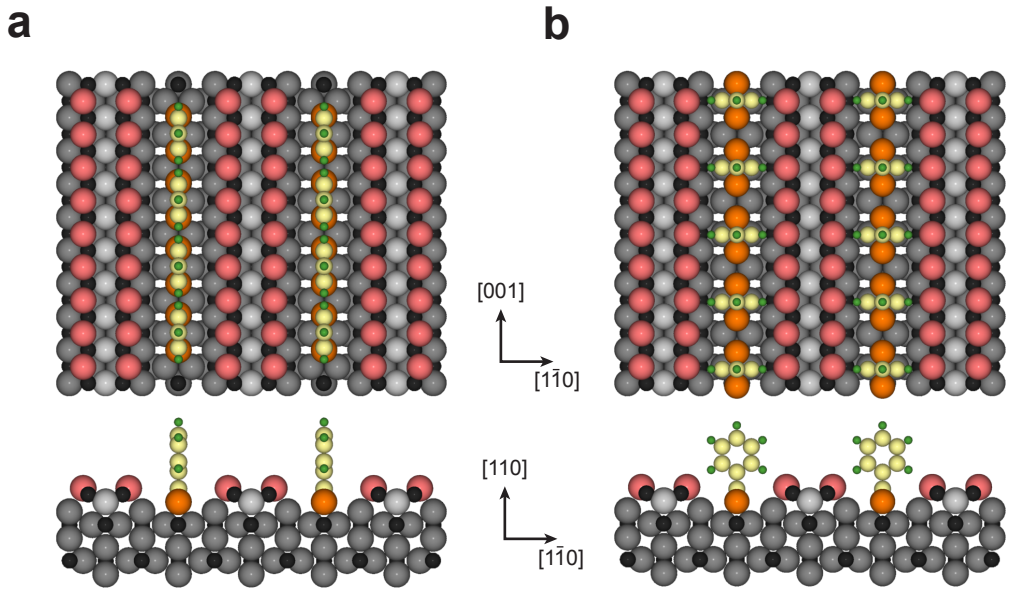

Figure 7.9: Structural models of a (2 × 2) overlayer of benzoate on the rutile TiO_2(110)(1 × 2) surface where the adsorbates bind to the Ti_{5c} sites in between the (1 × 2) strands assuming the Ti_2O_3 added-row model with two possible conformations of the benzoate shown: (a) the aromatic ring parallel to the carboxylate (along [001]), (b) the aromatic ring perpendicular to the carboxylate (along [1$\bar{1}$0]).

Figure 7.9 depicts a (2 × 2) overlayer of benzoate on a rutile TiO_2(110)(1 × 2) surface with the Ti_2O_3 added-row structure. The aromatic rings in the benzoate adsorbates are shown as: (a) co-planar with the carboxylate plane and (b) perpendicular to it.

In order to more closely identify the binding of individual benzoate molecules, the cross-linked TiO_2(110)(1 × 2) surface was exposed to ∼10 L of benzoic acid, again at 350 K, with STM images of the results displayed in Figure 7.10. A much lower coverage of benzoate can be observed, estimated as 0.005 ML from a number of images. From the large scale area in Figure 7.10a, it can be seen that there are significant areas (∼20 %) of the surface which consist of (1 × 1) terminated TiO_2(110) and are marked with a black boundary. These regions of (1 × 1) have a large number of small adsorbates, likely hydroxyls due to water dosed unintentionally during the benzoic acid exposure. Figure 7.10b details a region from the centre of the image in Figure 7.10a with a number of features highlighted. Marked with black circles are some features located

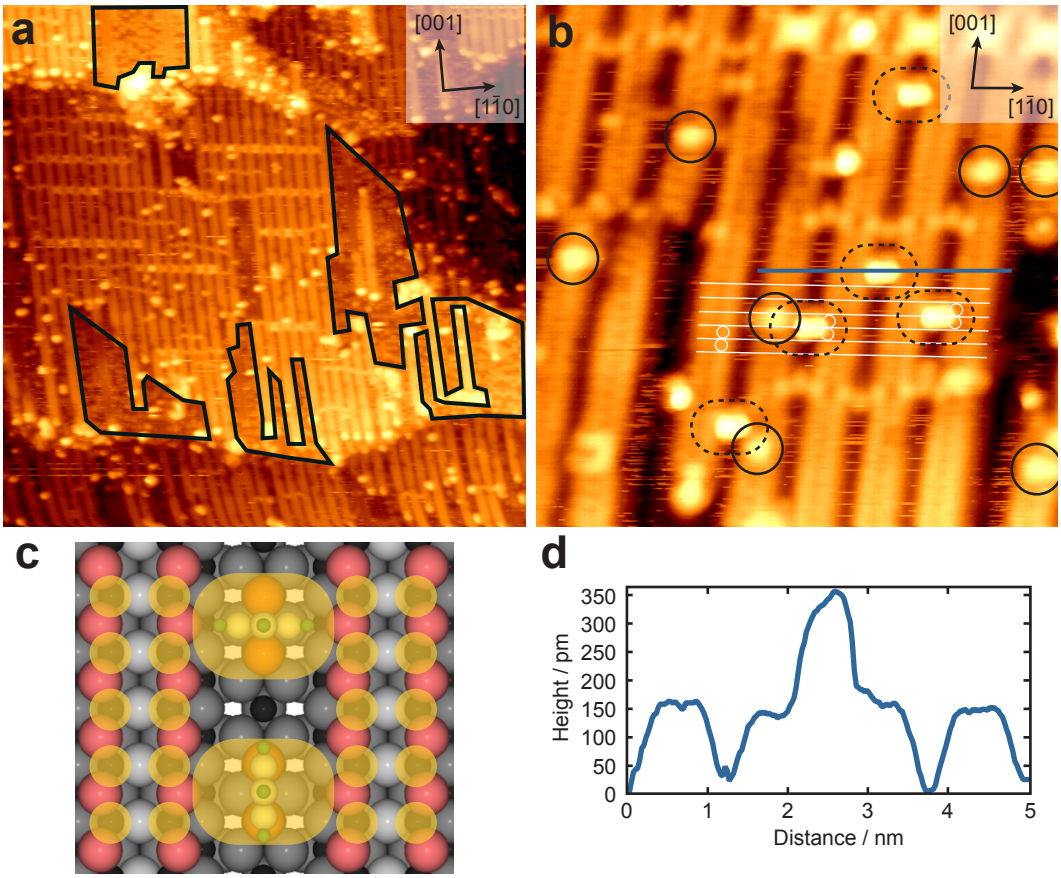

Figure 7.10: STM images of 0.005 ML BA adsorbed at 350 K on the rutile TiO_2(110)(1 × 2) surface. (a) Large scale area (100 × 100 nm^2, V_s = +1.2 V, I_t = 0.1 nA) showing the low coverage of benzoate which appear as bright features between the (1 × 2) strands. Approximately 20 % of the surface is (1 × 1) terminated with a high concentration of hydroxyls due to water that was inadvertently dosed during the benzoic acid exposure. (b) Atomically resolved image (60 × 60 nm^2, V_s = +1.2 V, I_t = 0.1 nA) showing the presence of additional adsorbates on top of the (1 × 2) strands (marked with solid circles) as well as the benzoate (dashed ovals). The atomic contrast on top of the (1 × 2) strands, although rather indistinct, is consistent with the Ti_2O_3 added-row model with the benzoate bound to two Ti_{5c} cations in between the strands. (c) Model of two benzoate molecules in the bidentate binding geometry between the Ti_2O_3 strands with the origin of the atomic contrast in STM highlighted (yellow dots correspond to the bright features in the empty states STM images). The top benzoate molecule has its aromatic ring perpendicular to [001] and the lower has it parallel to [001]. (d) A line-profile across four of the (1 × 2) strands and a benzoate molecule in (b) with an adsorbate height of ∼200 pm above the strands.(∼350 pm in total)

on top of the (1 × 2) strands that are ∼140 pm tall, and are likely to be either water molecules or hydrogen adatoms by comparison of their heights with such species on the TiO_2(110)(1 × 1) surface.[23] These are clearly distinguishable from the benzoate molecules which are located in-between the strands and marked with dashed ovals in Figure 7.10 and which have a slightly difference appearance as compared with those in Figure 7.8c which is attributed to a change in tip termination. There is some faint atomic contrast visible on the (1 × 2) strands in Figure 7.10b with a similar appearance to that observed in ref. [11] where the bright spots are assigned to the Ti^{4+} cations in the added-rows which have lateral spacing most consistent with the Ti_2O_3 model. For clarity some of these have been marked with white circles and lines on the image in Figure 7.10b, allowing it to be observed that the benzoate is indeed in a position consistent with bridge binding to two adjacent Ti_{5c} sites along [001] between the strands. A model of this binding is presented in Figure 7.10c, with the yellow highlights above the Ti_2O_3 rows correspond to the bright spots in the atomically resolved images, and two possible conformations of the aromatic ring: one perpendicular to [001] (upper) and one parallel (lower). Since the benzoate molecules appear in STM as oval shapes with their long axis along $[1\bar{1}0]$, it might be expected that the upper arrangement in Figure 7.10c is more likely. This conformation would also allow hydrogen bonding between the aromatic hydrogen atoms and the oxygen atoms in the Ti_2O_3 added-rows leading to further stabilisation of the binding. Such hydrogen bonding may also explain the different adsorption site as compared with formate on TiO_2(110)(1 × 2) observed by Bennett et al. in [21] where the cross-links are the favoured adsorption sites. In our results displayed in Figure 7.10a and b, we do not observe any nucleation on these cross-links. A line profile across four of the (1 × 2) strands and one of the benzoate molecules is displayed in Figure 7.10d showing its height is ∼200 pm above the top of the strands (∼350 pm in total), slightly taller than that recorded on the (1 × 1) terminated surface (∼300 pm) this discrepancy may be the result of different bias voltages during scanning.

7.3.3 Photodecomposition of benzoic acid on TiO_2(110)(1 × 1) and (1 × 2)

In an attempt to probe the photoreactivity of benzoic acid on TiO_2 a series of experiments were carried out by exposing the benzoate-covered TiO_2 surfaces examined earlier in this chapter to UV light (365 nm). In the first instance, the illumination was carried out under UHV conditions on both the acid-covered TiO_2(110)(1 × 1) and TiO_2(110)(1 × 2) surfaces, and although a small temperature rise (∼5 K) on the sample was observed, there was no apparent change in STM or AES carried out after illumination for times upto 1 hour with a photon flux of 4.3×10^{16} cm^{-2} s^{-1}. The saturated benzoate-covered surfaces (both (1 × 1) and (1 × 2) terminated) were exposed for an hour to the UV light in an oxygen pressure of 1×10^{-7} mbar. Even in the presence of the oxygen however, no change was observed to have taken place in either STM or AES. Similar work has been attempted for acetic acid on rutile TiO_2(110)(1 × 1) by Idriss et al. [26] where it was observed using core level PES that no reaction took place upon illumination in UHV, whereas illumination in an oxygen pressure of $\sim 5 \times 10^{-8}$ mbar led to loss of acetate from the surface via decomposition/desorption. Contrasting results were obtained by Henderson et al. on trimethylacetic acid (TMA) on rutile TiO_2(110)(1 × 1) [27, 28] using STM in combination with mass spectrometry. In this work they showed that even under UHV conditions TMA was found to decompose into CO_2 and other molecular fragments after UV irradiation. It was proposed that the C-C bond was broken via photo-excitation of the TiO_2 to produce a hole which interacted with the TMA to remove an electron from the π system which is then trapped at the surface by reducing a Ti^{4+} cation to Ti^{3+}.[28] Given these results it is not clear why we did not observe any reaction under the conditions of our experiments, either in UHV or with oxygen present, further investigation is required.

7.4 Summary and Conclusions

The adsorption of benzoic acid on rutile $TiO_2(110)$ surfaces has been studied with STM. On the near-stoichiometric $TiO_2(110)(1 \times 1)$ surface, adsorption at slightly raised temperatures (370 K) led to the formation of a saturated (2×1) overlayer. The benzoate binds in a dissociated bridging geometry to two adjacent Ti_{5c} cations in the [001] direction as has been observed for other carboxylic acids on the same surface. Evidence of intermolecular interactions between adsorbed benzoate molecules was also observed when deposited onto the $TiO_2(110)(1 \times 1)$ surface at room temperature, with some local ordering of the adsorbates attributed to hydrogen bonding. The cross-linked (1×2) reconstruction of reduced $TiO_2(110)$ was also investigated with atomically resolved, empty states STM with results appearing to fit best to the Ti_2O_3 added-row model for the reconstruction. High exposures of benzoic acid on $TiO_2(110)(1 \times 2)$ at 350 K led to ordered (2×2) superstructures of adsorbed benzoate bound to the Ti_{5c} cations between the (1×2) strands. No adsorption was observed on the crosslinks in contrast to an earlier study of formate adsorption on $TiO_2(110)(1 \times 2)$. Atomically resolved images of the (1×2) reconstruction with a low coverage of benzoate confirms this adsorption site and suggests that additional interactions between the benzoate and the surface, such as hydrogen bonding between the aromatic hydrogens and the oxygen in the substrate, may play a role in the adsorption and lead to the stable conformation of benzoate with the aromatic ring and carboxylate π systems perpendicular to each other. By extension, the binding geometries of more complex carboxylic acids may prove to be non-trivial and due to the effect of intermolecular interactions, the temperature and coverage may have important consequences for their adsorption behaviour.

Investigations into the photodecomposition of benzoic acid on rutile $TiO_2(110)$ surfaces was

carried out by illumination with 365 nm UV light under (i) UHV conditions and (ii) in the presence of molecular oxygen. No reaction was observed to occur in either case for both the (1×1) and (1×2) reconstructed surfaces. One of the main avenues of future research in this area, having found the basic properties of the adsorption, will be to further investigate the photoreactivity of the benzoate on the surfaces. By tuning the experimental conditions, and in combination with spectroscopy such as PES, it may be possible to gain a better understanding of the mechanisms of photo-induced decomposition. Of particular interest may be to explore the effects of point defects such as oxygen vacancies on the surface to examine their influence on the catalysis.

References

[1] Fujishima, A.; Honda, K. *Nature* **1972**, *238*, 37–38.

[2] Fujishima, A.; Zhang, X.; Tryk, D. *Surf. Sci. Rep.* **2008**, *63*, 515–582.

[3] Henderson, M. A. *Surf. Sci. Rep.* **2011**, *66*, 185–297.

[4] Yates, J. T. *Surf. Sci.* **2009**, *603*, 1605–1612.

[5] Linsebigler, A.; Lu, G.; Jr, J. Y. *Chem. Rev.* **1995**, *95*, 735–758.

[6] Diebold, U. *Surf. Sci. Rep.* **2003**, *48*, 53–229.

[7] Bowker, M. *Surf. Sci.* **2009**, *603*, 2359–2362.

[8] Chen, M.; Goodman, D. W. *Science* **2004**, *306*, 252–255.

[9] Pang, C. L.; Lindsay, R.; Thornton, G. *Chem. Soc. Rev.* **2008**, *37*, 2328–2353.

[10] Onishi, H.; Iwasawa, Y. *Surf. Sci.* **1994**, *313*, 783–789.

[11] Pang, C. L.; Haycock, S.; Raza, H.; Murray, P.; Thornton, G. *Phys. Rev. B* **1998**, *58*, 1586–1589.

[12] Blanco-Rey, M.; Abad, J.; Rogero, C.; Mendez, J.; Lopez, M.; Martin-Gago, J.; Andres, P. D. *Phys. Rev. Lett.* **2006**, *96*, 055502.

[13] Blanco-Rey, M.; Abad, J.; Rogero, C.; Méndez, J.; López, M.; Román, E.; Martín-Gago, J.; Andrés, P. D. *Phys Rev B* **2007**, *75*, 081402.

[14] Cocks, I.; Guo, Q.; Williams, E. *Surf. Sci.* **1997**, *390*, 119–125.

[15] Pieper, H. H.; Venkataramani, K.; Torbruegge, S.; Bahr, S.; Lauritsen, J. V.; Besenbacher, F.; Kuehnle, A.; Reichling, M. *Phys. Chem. Chem. Phys.* **2010**, *12*, 12436–12441.

[16] Bennett, R.; Stone, P.; Price, N.; Bowker, M. *Phys. Rev. Lett.* **1999**, *82*, 3831–3834.

[17] O'Regan, B.; Graetzel, M. *Nature* **1991**, *353*, 737–740.

[18] Tao, J.; Luttrell, T.; Bylsma, J.; Batzill, M. *J. Phys. Chem. C* **2011**, *115*, 3434–3442.

[19] Guo, Q.; Cocks, I.; Williams, E. *J. Chem. Phys.* **1997**, *106*, 2924–2931.

[20] Gutierrez-Sosa, A.; Martinez-Escolano, P.; Raza, H.; Lindsay, R.; Wincott, P.; Thornton, G. *Surf. Sci.* **2001**, *471*, 163–169.

[21] Bennett, R.; Stone, P.; Smith, R.; Bowker, M. *Surf. Sci.* **2000**, *454*, 390–395.

[22] Guo, Q.; Cocks, I.; Williams, E. *Surf. Sci.* **1997**, *393*, 1–11.

[23] Teobaldi, G.; Hofer, W. A.; Bikondoa, O.; Pang, C. L. *Chem. Phys. Lett.* **2007**, *437*, 73–78.

[24] Aizawa, M.; Morikawa, Y.; Namai, Y.; Morikawa, H.; Iwasawa, Y. *J. Phys. Chem. B* **2005**, *109*, 18831–18838.

[25] Sanchez-Sanchez, C.; Gonzalez, C.; Jelinek, P.; Mendez, J.; de Andres, P. L.; Martin-Gago, J. A.; Lopez, M. F. *Nanotech.* **2010**, *21*, 405702.

[26] Idriss, H.; Legare, P.; Maire, G. *Surf. Sci.* **2002**, *515*, 413–420.

[27] Henderson, M.; White, J.; Uetsuka, H.; Onishi, H. *J. Am. Chem. Soc.* **2003**, *125*, 14974–14975.

[28] White, J.; Henderson, M. *J. Phys. Chem. B* **2005**, *109*, 12417–12430.

CHAPTER 8

CONCLUSIONS AND FUTURE WORK

This thesis has examined the surfaces of a number of systems that are potentially very important with regards to future energy production and many other industrial applications. The first half of the results have focussed on ultrathin films of CeO_2(111) on Pt(111), a useful model for many oxide-based catalyst systems and when combined with gold in particular, a very promising heterogeneous catalyst for the low temperature water-gas-shift reaction for the production of hydrogen. In the second half of the results, the interaction of various TiO_2 surfaces with an important class of molecules, carboxylic acids, has been studied. This has particular relevance for anchoring of dye molecules in dye-sensitized solar cells, as well as being of interest from a fundamental scientific point of view.

STM, in combination with LEED and AES, was used to characterise ultrathin films of CeO_2(111)

supported on Pt(111). The films were prepared in a number of ways to identify the most appropriate growth procedure to form films suitable for high-resolution STM measurements. Atomically resolved images, of both filled and empty states of the ceria films revealed remarkable similarities to images recorded in previous studies on CeO_2(111) single crystals using NC-AFM and high temperature STM. Surface oxygen vacancies, subsurface oxygen vacancies and adsorbed water molecules were identified and their mobility investigated. The electronic structure of such ultrathin films was investigated with STS and a clear band gap was observed with a slightly lower size than for bulk CeO_2. As a result of these studies, it was concluded that ultrathin ceria films supported on Pt(111) make excellent topographic models for the native oxide.

The adsorption of single gold atoms on ultrathin CeO_2(111) films on Pt(111) was also investigated by evaporating low coverages ($\sim$0.07 ML) of gold onto the films at room temperature. The gold was observed in STM to nucleate evenly across the ceria islands with no step edge decoration and consisted mainly of individual single atoms which could be imaged with atomic resolution for the first time simultaneously with the top oxygen layer of the ceria. It was possible to identify two different adsorption sites; (i) atop an oxygen atom (possibly a vacancy site), and (ii) in a three-fold hollow site.

A great many future investigations are possible on the Au/CeO_2 system, of particular interest would be to carry out in-situ evaporation of gold to examine whether adsorption is favoured on oxygen vacancy sites. In addition, cooling to cryogenic temperatures could be of interest and would permit the application of STS to aid identification of the oxidation state of the gold adatoms, likely in comparison with DFT. In general there is a need for more detailed spectroscopic investigations such as could be provided by synchrotron-based techniques, but these will need to be carried out alongside STM in order to clearly correlate the structure with the behaviour of the

system. The behaviour of gold atoms and the $CeO_2(111)$ surface in conditions closer to those encountered in the real catalysts is also deserving of attention, a first step towards this may be an examination of the sintering or other effects at increased temperatures as well as exposure to CO and H_2O.

Scanning tunnelling microscopy was also employed to investigate the adsorption properties of acetic acid on anatase $TiO_2(101)$. A clean anatase (101) substrate was characterised with atomic resolution STM, LEED and AES. At small exposures at room temperature, acetic acid was found to adsorb evenly across the substrate terraces with no apparent preference for step edges. At saturation coverages after deposition at room temperature there was no long range ordering of the adsorbates, although exposure at raised susbtrate temperatures induced regions of (2×1) superstructure in STM. Along with high-resolution STM imaging of individual adsorbates, this adsorption was consistent with a dissociated bidentate binding geometry of the acetate to two neighbouring Ti_{5c} atoms along the [010] direction. Exposure of the acetate-covered surface to ultraviolet light did not have any major effect, likely due to the lack of oxygen required for photocatalytic oxidation, under the experimental conditions (UHV). The co-adsorption of water and acetic acid (1:1 ratio) was observed to have no effect on the structure of the overlayers at saturation coverage although at lower exposures some, at-present unidentified, molecular species were observed.

Surface studies of anatase TiO_2 are not widespread due to a number of practical difficulties and there is clearly a large amount of further work that could be attempted on the acetic acid on anatase $TiO_2(101)$ system alone. Of particular interest would be to perform STM simulations of individual acetate molecules to determine whether the proposed dissociative bidentate binding geometry is correct. Within the deposition temperature range explored (300-420 K) only a small fraction of

the saturated coverage displayed the (2 $\times$ 1) superstructure, it may be possible to investigate whether different deposition conditions led to increasing this fraction. In all of the experiments in this chapter, the anatase (101) substrate had an extremely low concentration of surface point defects, the effect on acid adsorption of increasing this by electron-beam irradiation for example, is another area of interest. The water/acid co-adsorption experiments require further investigation, with a multitude of possible future studies including the effect of different concentrations of water or raised or lowered deposition temperatures as well as a clear identification of the species observed in these preliminary experiments. The effects of UV irradiation of adsorbed acetate looks to be another promising route, one interesting experiment may be to examine the effect of the presence of oxygen during illumination in order to more closely examine the underlying mechanisms of photocatalysis on TiO_2.

The second carboxylic acid adsorption study was that of benzoic acid on rutile TiO_2(110). On the near-stoichiometric TiO_2(110)(1 $\times$ 1) surface, adsorption at slightly raised temperatures (370 K) led to the formation of a saturated (2 $\times$ 1) overlayer. The benzoate binds in a dissociated bridging geometry to two adjacent Ti_{5c} cations in the [001] direction as has been observed for other carboxylic acids on the same surface. The cross-linked (1 $\times$ 2) reconstruction of reduced TiO_2(110) was also investigated with atomically resolved, filled states STM. High exposures of benzoic acid on TiO_2(110)(1 $\times$ 2) at 350 K led to ordered (2 $\times$ 2) superstructures of adsorbed benzoate bound to the Ti_{5c} cations between the (1 $\times$ 2) strands. No adsorption was observed on the crosslinks in contrast to an earlier study of formate adsorption on TiO_2(110)(1 $\times$ 2). Atomically resolved images of the (1 $\times$ 2) reconstruction with a low coverage of benzoate confirms this adsorption site and suggests that additional interactions between the benzoate and the surface, such as hydrogen bonding, may play a role in the adsorption and lead to the stable conformation of benzoate with the aromatic ring and carboxylate π systems perpendicular to each

other. By extension, the binding geometries of more complex carboxylic acids may prove to be non-trivial and due to the effect of intermolecular interactions, the temperature and coverage may have important consequences for their adsorption behaviour. Investigations into the photodecomposition of benzoic acid on rutile TiO_2(110) surfaces was carried out by illumination with 365 nm UV light under (i) UHV conditions and (ii) in the presence of molecular oxygen. No reaction was observed to occur in either case for both the (1 $\times$ 1) and (1 $\times$ 2) reconstructed surfaces.

One of the main avenues of future research in this area, having found the basic properties of the adsorption, will be to further investigate the photoreactivity of the benzoate on the surfaces. By tuning the experimental conditions, and in combination with spectroscopy such as PES, it may be possible to gain a better understanding of the mechanisms of photo-induced decomposition. Of particular interest may be to explore the effects of point defects such as oxygen vacancies on the surface to examine their influence on the catalysis. As mentioned earlier in this work, the basic structure of the TiO_2(110)(1 $\times$ 2) reconstruction is still not known, and STM simulations of the clean surface as well as the acid covered surface may lead to progress on this front.